

**Image Based Fracture Prediction Diagnostic Tool for  
Avascular Necrosis of the Femoral Head**

Dipl.-Ing. Martin Preutenborbeck

Submitted in accordance with the requirements for the degree of  
Doctor of Philosophy

The University of Leeds  
School of Mechanical Engineering

January 2018

The candidate confirms that the work submitted is his/her own and that appropriate credit has been given where reference has been made to the work of others.

This copy has been supplied on the understanding that it is copyright material and that no quotation from the thesis may be published without proper acknowledgement.

The right of Martin Preutenborbeck to be identified as Author of this work has been asserted by him in accordance with the Copyright, Designs and Patents Act 1988.

© 2018 The University of Leeds and Martin Preutenborbeck

## Acknowledgements

I would like to acknowledge and thank my supervisors Dr Sophie Williams, Dr Alison Jones, Professor Richard Hall, Dr Ondrej Holub, Eleanor Freeman and Dr James Anderson for their support and guidance throughout this project. Many thanks also to the technicians at the University of Leeds, namely Phil Wood, Irvin Homan and Tony Wiese for their technical support. Finally, I would like to thank DePuy Synthes for providing the funding for this project with an iCASE studentship from the Engineering and Physical Science Research Council (EPSRC).

## Abstract

Current methods to diagnose bone diseases like avascular necrosis (AVN) are subjective and a reliable assessment of the fracture risk is not available. A diagnostic fracture prediction tool would aid clinical diagnosis, anticipate disease progression and help with the planning of subsequent interventions. The strength of bones, including the femur, can be calculated using structural mechanics with a view to ascertaining fracture risk. The aim of this thesis was to develop and validate a fracture prediction method based tomographic imaging and beam theory.

In-vitro disease models were created from additive manufacturing, explanted porcine and human femoral heads. The disease models contained a simulated lesion that was either lateral or medial to the fovea to analyse the effects of different lesion positions and to verify the ability of the developed fracture prediction tool. Current classification methods rely on the identification of the lesion volume and location to quantify the fracture risk, an approach that is purely based on geometrical information. The fracture prediction method based on structural stiffness also considered material properties which potentially added predictive capability.

The tool was subsequently validated by predicting the fracture risk of femoral heads from AVN patients to demonstrate the ability to identify necrotic lesions that were likely to progress to fracture. The predicted fracture risk was compared to the current diagnostic gold standard to diagnose AVN. The beam tool was also compared against another novel fracture prediction tool based on FEA to identify possible advantages of beam theory.

The verification tests confirmed that samples with a lesion in the weight bearing area were statistically more likely to fracture at a low load. A low fracture load meant a high fracture risk. However the experimental fracture load of porcine and human femoral heads, even among samples with similar lesions, showed variations indicating that lesion volume and location were not good predictors of fracture risk alone. There was a good correlation between the predicted fracture risk and *in-vitro* fracture loads of the human femoral head disease model indicating that the developed tool was able to objectively predict the fracture risk. The beam tool had similar good predictive capabilities as current diagnostic methods and fracture prediction methods based on FEA.

An objective *in-vivo* analysis of the mechanical fracture risk helps identifying patients whose disease is at risk of progressing, as well as stratifying surgical interventions.

## Table of Contents

|  |              |
|--|--------------|
| <b>Abstract.....</b>                                     | <b>iv</b>    |
| <b>List of Tables .....</b>                              | <b>xi</b>    |
| <b>List of Figures .....</b>                             | <b>xiii</b>  |
| <b>Abbreviations .....</b>                               | <b>xxiii</b> |
| <b>Chapter 1 Introduction.....</b>                       | <b>1</b>     |
| <b>Chapter 2 Literature review .....</b>                 | <b>3</b>     |
| 2.1 Overview of the hip .....                            | 3            |
| 2.1.1 Bony anatomy of the proximal femur.....            | 3            |
| 2.1.2 Bone metabolism.....                               | 4            |
| 2.1.3 Blood supply of the femoral head .....             | 5            |
| 2.1.4 Joint loading and muscular anatomy .....           | 6            |
| 2.2 Biomechanical model of the proximal femur .....      | 7            |
| 2.3 Avascular necrosis of the femoral head.....          | 8            |
| 2.3.1 Epidemiology.....                                  | 8            |
| 2.3.2 Aetiology (Cause).....                             | 10           |
| 2.3.2.1 Corticosteroid therapy .....                     | 11           |
| 2.3.2.2 Alcohol abuse .....                              | 12           |
| 2.3.2.3 Others causes/ associated factors .....          | 13           |
| 2.3.3 Pathophysiology .....                              | 13           |
| 2.3.3.1 Cell death.....                                  | 14           |
| 2.3.3.2 Repair process.....                              | 14           |
| 2.3.3.3 Bone fracture and collapse of femoral head ..... | 14           |
| 2.3.3.4 Asymptomatic and self-repairing necrosis .....   | 15           |
| 2.3.4 Diagnostic imaging .....                           | 16           |
| 2.3.4.1 Plain radiographs (X-ray) .....                  | 16           |
| 2.3.4.2 Computed tomography CT.....                      | 17           |
| 2.3.4.3 Magnetic resonance imaging MRI.....              | 19           |
| 2.3.5 Diagnostic Classification.....                     | 20           |
| 2.3.5.1 Ficat Arlet.....                                 | 21           |
| 2.3.5.2 Steinberg .....                                  | 22           |
| 2.3.5.3 ARCO .....                                       | 24           |

|   |           |
|---|-----------|
| 2.3.5.4 Quantifying lesion volume.....  | 25        |
| 2.3.5.5 Reliability and reproducibility of current classification systems.....                          | 27        |
| 2.3.6 Treatment options for AVN .....   | 27        |
| 2.3.6.1 Non-surgical / conservative treatments.....   | 28        |
| 2.3.6.2 Surgical treatments: Core decompression .....   | 30        |
| 2.3.6.3 Osteotomy .....   | 33        |
| 2.3.6.4 Joint reconstruction.....   | 35        |
| 2.3.6.5 Current clinical situation and management of AVN.....   | 36        |
| 2.3.6.6 Conclusion on current management of AVN.....  | 38        |
| 2.4 Material model to replicate the mechanical response of bone tissue                                  |           |
| 39  |           |
| 2.4.1 Measuring material properties of healthy and necrotic bone  | 39        |
| 2.4.2 Simulating material properties with density-modulus relationships .....                           | 43        |
| 2.4.3 Comparing isotropic and transversely isotropic material assignments on fracture simulations ..... | 49        |
| 2.4.4 Poisson's ratio .....   | 51        |
| 2.4.5 Failure criterion for bone fracture simulations.....  | 52        |
| 2.4.6 Conclusion on material model .....  | 53        |
| 2.5 Finite element analysis for avascular necrosis.....   | 54        |
| 2.6 Beam theory approaches to simulate the mechanical behaviour of the femur.....                       | 54        |
| 2.6.1 Introduction.....   | 54        |
| 2.6.2 Formulated theories.....  | 56        |
| 2.6.3 Studies using beam theory to analyse stress within the femur                                      |           |
| 57  |           |
| 2.6.4 Discussion .....  | 61        |
| 2.7 Summary .....   | 62        |
| 2.8 Aims and objectives .....   | 64        |
| <b>Chapter 3 Development of a structural mechanics model for the proximal femur .....</b>               | <b>66</b> |
| 3.1 Introduction to method development.....   | 66        |
| 3.2 Fracture Prediction methodology development.....  | 67        |
| 3.2.1 Introduction.....   | 67        |

|   |  |     |
|---|--|-----|
| 3.2.2   | Bone segmentation.....   | 67  |
| 3.2.3   | Density-modulus material model .....   | 68  |
| 3.2.4   | Beam axis and cross-sections.....  | 68  |
| 3.2.5   | Structural analysis .....  | 69  |
| 3.2.6   | Beam theory .....  | 70  |
| 3.2.7   | Tool output and quantification of the fracture risk.....   | 72  |
| 3.2.8   | Discussion of fracture prediction methodology development  | 73  |
| 3.3   | Analytical verification of the scripted structural analysis .....                                    | 74  |
| 3.4   | Material model .....   | 75  |
| 3.4.1   | Material model from literature.....  | 75  |
| 3.4.2   | Resolution dependency of density-modulus material model.   | 77  |
| 3.4.3   | Verification of the used density-modulus material model for beam simulations.....                    | 79  |
| 3.5   | Image segmentation of bone .....   | 85  |
| 3.5.1   | Introduction.....  | 85  |
| 3.5.2   | Methods.....   | 86  |
| 3.5.3   | Results .....  | 87  |
| 3.5.4   | Discussion .....   | 88  |
| 3.6   | Verification against theoretical pathology .....   | 88  |
| 3.6.1   | Introduction.....  | 88  |
| 3.6.2   | Methods.....   | 89  |
| 3.6.3   | Results .....  | 92  |
| 3.6.4   | Discussion .....   | 95  |
| 3.7   | Summary .....  | 98  |
| <b>Chapter 4 Verification of the fracture prediction tool against physical disease models .....</b> | <b>99</b>  |     |
| 4.1   | Introduction .....   | 99  |
| 4.2   | Verification against femoral head models with simulated lesions made by additive manufacturing ..... | 100 |
| 4.2.1   | Introduction.....  | 100 |
| 4.2.2   | Methods.....   | 101 |
| 4.2.2.1   | Femur model.....   | 101 |
| 4.2.2.2   | Femoral head beam model .....  | 102 |

|  |            |
|--|------------|
| 4.2.2.3 Properties of Selective Laser Sintering material .....   | 104        |
| 4.2.2.4 Experimental set-up.....   | 106        |
| 4.2.3 Results .....  | 107        |
| 4.2.4 Discussion .....   | 109        |
| 4.3 Verification against porcine femoral heads .....   | 110        |
| 4.3.1 Introduction.....  | 110        |
| 4.3.2 Methods.....   | 111        |
| 4.3.2.1 Sample preparation.....  | 111        |
| 4.3.2.2 Femoral head beam model .....  | 113        |
| 4.3.2.3 Image processing.....  | 114        |
| 4.3.2.4 Material model .....   | 114        |
| 4.3.2.5 Experimental set-up .....  | 115        |
| 4.3.2.6 Post processing of computational output .....  | 116        |
| 4.3.3 Results .....  | 117        |
| 4.3.4 Discussion .....   | 119        |
| 4.4 Verification against human femoral heads .....   | 120        |
| 4.4.1 Introduction.....  | 120        |
| 4.4.2 Methods.....   | 121        |
| 4.4.2.1 Sample preparation.....  | 121        |
| 4.4.2.2 Image capture .....  | 123        |
| 4.4.2.3 Material model .....   | 124        |
| 4.4.2.4 Beam model and fracture risk prediction.....   | 124        |
| 4.4.2.5 Experimental set-up of compression test .....  | 125        |
| 4.4.3 Results .....  | 125        |
| 4.4.4 Discussion .....   | 127        |
| 4.5 Summary .....  | 128        |
| <b>Chapter 5 Feasibility of the fracture prediction tool in assessing clinical cases of avascular necrosis .....</b>             | <b>130</b> |
| 5.1 Introduction.....  | 130        |
| 5.2 A comparison of the developed tool's ability to stratify patients for fracture risk and the ARCO classification system ..... | 131        |
| 5.2.1 Introduction.....  | 131        |
| 5.2.2 Methods.....   | 133        |

|                  |  |            |
|------------------|--|------------|
| 5.2.2.1          | Patients and disease stage .....   | 133        |
| 5.2.2.2          | Image capture and processing.....  | 134        |
| 5.2.2.3          | Material model .....   | 135        |
| 5.2.2.4          | Beam model and fracture prediction .....   | 137        |
| 5.2.3            | Results .....  | 139        |
| 5.2.4            | Discussion .....   | 144        |
| 5.3              | Comparison of the efficiency and accuracy of developed beam tool<br>with a novel fracture prediction tool based on finite element<br>analysis..... | 145        |
| 5.3.1            | Introduction.....  | 145        |
| 5.3.2            | Methods.....   | 147        |
| 5.3.2.1          | Patients and disease stage .....   | 147        |
| 5.3.2.2          | Development of patient specific disease model .....  | 148        |
| 5.3.2.3          | Beam model and fracture prediction .....   | 151        |
| 5.3.3            | Results .....  | 151        |
| 5.3.4            | Discussion .....   | 156        |
| 5.4              | Requirements for clinical application of developed tool .....  | 158        |
| 5.4.1            | User interface and input .....   | 158        |
| 5.4.2            | Density calibrated CT-scanner differences.....   | 161        |
| 5.5              | Summary .....  | 161        |
| 5.6              | Conclusion .....   | 162        |
| <b>Chapter 6</b> | <b>Other applications for the developed beam theory tool....</b>   | <b>164</b> |
| 6.1              | Introduction .....   | 164        |
| 6.2              | Possibilities for use of tool outside AVN .....  | 165        |
| 6.2.1            | Osteoporosis .....   | 165        |
| 6.2.2            | Skeletal metastasis.....   | 166        |
| 6.2.3            | Discussion .....   | 166        |
| 6.3              | Curved beam theory for fracture prediction of long bones .....   | 167        |
| 6.3.1            | Introduction.....  | 167        |
| 6.3.2            | Method .....   | 168        |
| 6.3.2.1          | Biomechanical loading model .....  | 168        |
| 6.3.2.2          | Curved beam theory and fracture risk prediction .....  | 169        |
| 6.3.2.3          | Image processing.....  | 175        |

|   |  |     |
|---|--|-----|
| 6.3.2.4   | Material model .....   | 176 |
| 6.3.3   | Results .....  | 178 |
| 6.3.3.1   | Computational results .....                                  | 178 |
| 6.3.4   | Discussion .....   | 181 |
| 6.4   | Verification against additive manufactured femur models..... | 184 |
| 6.4.1   | Introduction.....  | 184 |
| 6.4.2   | Method .....   | 184 |
| 6.4.2.1   | Beam model.....  | 184 |
| 6.4.2.2   | Experimental set-up .....                                    | 185 |
| 6.4.3   | Results .....  | 186 |
| 6.4.4   | Discussion .....   | 187 |
| 6.5   | Summary .....  | 188 |
| <b>Chapter 7 Overall discussion and conclusion.....</b>   | <b>189</b>   |     |
| 7.1   | Discussion .....   | 189 |
| 7.1.1   | Introduction.....  | 189 |
| 7.1.2   | Development of a novel fracture prediction tool .....        | 189 |
| 7.1.3   | Effectiveness of developed tool.....                         | 190 |
| 7.1.4   | Future use .....   | 192 |
| 7.1.5   | Limitations .....  | 192 |
| 7.2   | Overall conclusion .....                                     | 193 |
| <b>References.....</b>  | <b>195</b>   |     |
| <b>Appendix A Proximal femur model with simulated cone shaped AVN<br/>Lesion .....</b>                                      | <b>217</b>   |     |
| <b>Appendix B Drawing Tensile bar ISO527 .....</b>  | <b>219</b>   |     |
| <b>Appendix C Drawing Instron Cement Mould .....</b>  | <b>221</b>   |     |
| <b>Appendix D SOP.07.17 Standard Operating Protocol. Simulating an<br/>AVN-lesion within an in-vitro porcine model.....</b> | <b>223</b>   |     |
| <b>Appendix E Compression data additive manufactured proximal femur<br/>models .....</b>                                    | <b>230</b>   |     |

## List of Tables

|  |    |
|--|----|
| Table 1 Proportion of total hip replacements that are due to avascular necrosis. AVN is more prevalent among the Asian populations .....   | 9  |
| Table 2 Likelihood of severe acute respiratory syndrome (SARS) patients receiving steroid treatment to develop AVN .....   | 12 |
| Table 3 Comparison of sensitivity of different image modalities to detect changes resulting from AVN in an early stage .....   | 16 |
| Table 4 Evolution of classification systems used for AVN .....   | 21 |
| Table 5 Classification of AVN according to Ficat and Arlet (Ficat, 1985).<br><i>Adopted from Steinberg and Steinberg (2004)</i> .....  | 22 |
| Table 6 Staging and Grading of AVN according to Steinberg et al. (1995)<br>(University of Pennsylvania).....   | 23 |
| Table 7 Methods to estimate the extent of lesion involvement in the femoral head as proposed by Steinberg et al. (1995). .....   | 24 |
| Table 8 ARCO classification system for AVN (Gardeniers, 1993) .....  | 25 |
| Table 9 Literature review of outcomes of non-surgical treatments. Failure was assumed when a THA was necessary (clinical failure) or the femoral head collapsed.....   | 29 |
| Table 10 Literature review of outcomes of core decompressions stratified by the disease stage at the beginning of the treatment. Failure was assumed when a patients required additional surgery (clinical failure) or the femoral head collapsed..... | 32 |
| Table 11 Literature review of outcomes of osteotomy stratified by the presented disease stage or lesion extend. Failure was assumed when a patients required additional surgery (clinical failure) or the femoral head collapsed.....                  | 34 |
| Table 12 Literature review of outcomes of hip replacements stratified by the presented disease stage or lesion extend. Failure was assumed when a patient required revision surgery. ....  | 35 |
| Table 13 Treatment algorithm according to Ficat and Steinberg classification systems based on literature (M. A. Mont et al., 1996; Lieberman et al., 2003; Beaulé and Amstutz, 2004; Ha et al., 2011; Issa et al., 2013; Mont et al., 2015).....       | 38 |
| Table 14 Young's modulus for wet cancellous bone specimens from uniaxial compression tests in SI orientation of the human femoral head....   | 42 |
| Table 15 Empirical relationship between ash density of bone and density measured by a QCT scanner. ....  | 45 |
| Table 16 Empirical density relationship (ash fraction) for ash and apparent density of bone. ....  | 46 |
| Table 17 Mathematical description of failure criterions.....   | 53 |

|  |     |
|--|-----|
| Table 18 Comparison of the results of the paper and computational calculation .....  | 75  |
| Table 19 Density-modulus conversion material model to assign material properties to the model from CT-image data.....  | 76  |
| Table 20 Density-modulus relationship for porcine femur bone to convert CT-density to Young's modulus information .....  | 115 |
| Table 21 Demographics for the five patients selected for testing the fracture prediction method. Patient 02_003 showed subchondral fracture.....   | 133 |
| Table 22 Lesion volume and ARCO classification for each patient included in the study. Head volume was estimated by calculating the volume of a sphere with the same diameter, lesion volume was calculated by multiplying the number of voxels in the lesion mask by the voxel volume. The ARCO grade was assigned based on the presence (Grade III) or Absence (Grade II) of fracture – note that all lesions were visible on radiographs and were by definition grade II or higher. The volume classification was dictated by the percentage involvement (<15% = A; 15%-30%=B; >30% = C). Location in the A-P and M-L planes was established by assessing whether the lesion was present in the Medial (M), Central (C) and Lateral (L); Anterior (A), Central (C) and Posterior (P) quadrants respectively. <i>Reproduced from Anderson, 2015.</i> ..... | 134 |
| Table 23 The fracture prediction tool was used to rank the patients in ascending order. The EA-ratio described the relative stiffness difference of an AVN affected femoral head compared to a reference set of healthy femoral heads. A low EA-ratio indicated a high fracture risk. The ranking correlated with the ARCO classification and grade. ....  | 144 |
| Table 24 Demographics for additional three patients selected for comparing the fracture prediction methods. ....   | 148 |
| Table 25 Disease classification of three patients according to ARCO (Anderson, 2015). ....   | 148 |
| Table 26 Case by case results of the beam tool analysing patient-specific femoral head geometric volume models. The axial stiffness was calculated along the beam axis for a healthy femoral head (red line), a lesion affected sample (blue line) and a lesion affected sample with heel strike loading (green line). ....  | 152 |
| Table 27 Comparison of the individual risk scores of the finite element tool to the fracture risk results of the beam theory tool which were expressed through the relative reduction in axial stiffness. Both methods used the same geometric volume model. The EA-ratio limited to a minimum of 0.5 as a result of the assigned material properties. The order of risk of both methods was compared to the ARCO classification.....  | 155 |
| Table 28 Material model used for cancellous and cortical femoral bone..  | 177 |

## List of Figures

|   |    |
|---|----|
| Figure 1 A) Schematic of the anterior view of the right human femur including blood supply of the femur head. <i>Adapted from Openstax college, 2013.</i> B) The structure of bone as shown in the long bone. <i>Reproduced with permission of © Krebsinformationsdienst, Deutsches Krebsforschungszentrum.</i> .....   | 4  |
| Figure 2 Blood supply of right femur head. (A) Anterior view, (B) Posterior view. (1) Inferior, (2) superior and (3) anterior retinacular artery. (4) Arteries of the ligamentum teres from obturator artery. <i>Image from Zhao and Yu (2015) reproduced with permission from Elsevier.</i> .....  | 6  |
| Figure 3 Movements about the hip joint. <i>Adapted from wikimedia.</i> .....  | 7  |
| Figure 4 Progression of Avascular Necrosis .....  | 13 |
| Figure 5 X-ray of a crescent sign (arrow). The crescent sign is an early radiographic sign of AVN. <i>Image from Assouline-Dayan et al. (2002) reproduced with permission from Elsevier.</i> .....  | 17 |
| Figure 6 CT-image of a pelvis. The right femoral head on the left collapsed as a result of avascular necrosis. ....   | 18 |
| Figure 7 Double Line Sign in a T2 weighted MRI image of a proximal femur. Inner white rim represents oedema and outer dark rim sclerotic bone. <i>Image from Choi et al. (2015) reproduced with permission from Springer.</i> ..  | 20 |
| Figure 8 Schematic drawing showing an anterior-posterior view of the femoral head with two necrotic lesions of different size and location, but with the same angular measurements.....   | 27 |
| Figure 9 Schematic drawing of a core decompression (left), augmented with bone grafts (middle) and a multi hole core decompression (right). .....   | 31 |
| Figure 10 Percentage of hospitals that recommended a treatment for AVN for a respective disease stage. <i>Data taken from Tingart et al. (2004).</i> .....  | 37 |
| Figure 11 Percentage of surgeons that recommended a treatment for a hypothetical 24 year old patient for different disease stages. BG = bone grafting, THA = total hip arthroplasty. <i>Data taken from McGrory et al. (2007).</i> .....  | 37 |
| Figure 12 Modulus of elasticity as a function of apparent density as reported across the literature for femoral human bone (Snyder and Schneider, 1991; Keller, 1994; Morgan et al., 2003). *Pooled trabecular and cortical bone, #Cortical bone from the tibia. Apparent density was calculated from ash density using the relationship described by Schileo et al. (2008a). ..... | 47 |
| Figure 13 Schematic of the stress components acting on a femoral shaft segment. .....   | 50 |
| Figure 14 Dependency between Poisson's ratio and density for dry defatted trabecula bone samples. No relationship to the density was observed. <i>Data reproduced from Knauss et al. (1981).</i> .....  | 52 |

|  |    |
|--|----|
| Figure 15 Loading of the upper end of the femur during walking according to Pauwels (2012). The stress distribution within the femoral neck was calculated from compressive and bending load components of the resultant joint contact force (R) which acted towards the centre of the femoral head. R balances the bodyweight (BW) and the muscle force (M).....  | 55 |
| Figure 16 Pauwels (2012) explained the different types of stress that occur in the femur in form of a simplified column model. The femur is subject to compression, bending and shear stress. <i>Figure adapted from Pauwels et al. (2012)</i> .....   | 56 |
| Figure 17 Tool workflow (A-G) to assess the fracture risk of a femur based on a tomographic image. Structural parameters (E) or the calculated fracture load (F) can be used to predict the fracture risk.....   | 67 |
| Figure 18 (A) The proximal femur can be approximated as a beam structure in form of a stack of beam elements/cross-sections. Each of these cross-sections can be analysed in isolation of other cross-sections. (B) The structural parameters were calculated from the modulus map of a single selected cross-section. (C) The cross-section was characterised by these structural parameters $EA$ , $EI$ . (D) These were used to calculate the stress distribution within the homogenised cross-section as a result of the joint contact force $F$ . The stress distribution as a result of bending is shown in the y-z plane. The stress distribution was calculated in both x and y, but bending along the x-axis was significantly smaller for this load case. .... | 69 |
| Figure 19 Flowchart describing the steps of the developed MATLAB script. ....  | 72 |
| Figure 20 Cross-section with a simple geometry to verify structural tool calculations .....  | 75 |
| Figure 21 Occurrence rate (primary vertical axis) and density-modulus conversion model (secondary vertical axis) of each density of a CT cross-section of a human femoral head. ....   | 77 |
| Figure 22 Distal view of the same CT cross-sectional image of a porcine femoral head at different resolutions: (A) 82 $\mu\text{m}$ , (B) 123 $\mu\text{m}$ , (C) 246 $\mu\text{m}$ , (D) 492 $\mu\text{m}$ , (E) 984 $\mu\text{m}$ , (F) 1968 $\mu\text{m}$ .....   | 78 |
| Figure 23 Analysis of the sensitivity of the density and modulus to different CT resolutions. The area (A) was segmented manually. Density (B) and Young's modulus (C) were calculated for each pixel of a cross-sectional image after which the mean values were derived. The axial stiffness (D) is the product of mean density and Young's modulus.....   | 79 |
| Figure 24 Location where bone plug were extracted from the femoral heads. ....   | 80 |
| Figure 25 (A) Instron 3366 testing machine used to compression test bone plugs. (B) Bone plug prepared for platen compression testing.....   | 81 |
| Figure 26 Stress-strain curve of a compression test of a bone plug including the defined failure load and the slope of the steepest region. The stress-strain curve is characteristic of the material behaviour. ....  | 82 |

|   |    |
|---|----|
| Figure 27 Regression between the Young's moduli of cancellous bone plugs calculated from the developed material model based on CT density measurements and Young's moduli calculated from the slope of the stress-strain curve of the compression test (A), and computed Young's moduli from the fracture load of the compression test and beam theory (B).....                                       | 83 |
| Figure 28 Slope of regression between experimental failure loads of human femoral bone plugs and beam theory predicted failure loads based on the average density and the overall plug cross-sectional area (A) or beam theory predicted failure loads (FL) of the weakest slice of the bone plug (B).<br>.....   | 84 |
| Figure 29 The platen compression test of the cylindrical bone plugs created a constant error (A). If corrected, there is a good approximation between the density-modulus relationship described by Morgan et al. (2003) (blue line) and this test (B). .....   | 85 |
| Figure 30 Frequency of pixels with certain grey values in a CT cross-section of a femoral head. The Ridler threshold was calculated from equation 3.10. ....  | 86 |
| Figure 31 Three different masks were created for three CT cross-sectional images of the same porcine femoral head at the same position but with different resolutions. The first mask was based on a Ridler iterative threshold segmentation, the second on a was similar to the first but the threshold value was 0.5% greater and the last mask was a segmentation of the whole bone. ....          | 87 |
| Figure 32 Resolution dependency of the mean density and the axial stiffness for a Ridler-segmented cross-sections and segmentation of the whole bone.....   | 88 |
| Figure 33 Loading diagram for the hip while walking, where B is the body weight (minus the weight bearing leg), A is the abductor muscle force and F is the joint contact force. The load of the body weight does not go directly through the joint and the resulting moment is counterbalanced by the abductor force. The femoral head is therefore subjected with the joint contact force (F). .... | 90 |
| Figure 34 AP view of a segmented femoral head. The superior half of the head was modelled with a beam loaded with a single load pointing to the centre of the femoral head. The load was in direction of the mechanical axis. The thirty disc-like cross-sections (white lines) were perpendicular to the beam axis (black dashed line). ....   | 90 |
| Figure 35 Schematic illustrating the conical shape and location of the simulated lesion within the femoral head. The cone is angled at 45°.....   | 91 |

|   |     |
|---|-----|
| Figure 36 Axial (A) and bending (B) stiffness, and failure load (C) were calculated for each corresponding cross-section of four femoral heads with cone-shaped simulated lesions angled at -25° (1), 10° (2), 45° (3) and 80° (4) from the positive vertical axis. The plane of the cross-sections were perpendicular to the beam axis (white line) which was collinear with x-axis of the corresponding three line charts. The results of the four lesion affected femurs (blue lines) were compared to the results for an unaffected femoral head (red lines). The beam axis and loading was vertical which approximated a double-legged stance..... | 93  |
| Figure 37 Axial and bending stiffness, and failure load of cross-sections of four femoral heads with different cone-shaped simulated lesions (angled - 25° (1), 10° (2), 45° (3) and 80° (4)) compared to an unaffected femur. The beam axis (white line) had an angle of 10° about the vertical axis which approximated a single-legged stance.....  | 94  |
| Figure 38 Maximum difference between healthy and four lesion affected femoral heads for A) Axial stiffness, B) Bending stiffness, C) Fracture load. The cone-shaped lesions were angled at -25° (1), 10° (2), 45° (3) and 80° (4) from the vertical axis.....   | 95  |
| Figure 39 Stress distribution as a results of bending. Bending was not a result of a transverse load but the distance (a) between modulus weighted centroid and the load/beam axis. ....  | 96  |
| Figure 40 Schematic of hip model showing anterior posterior cross-section view of three 3D-printed proximal femur models including femoral head neck, greater and lesser trochanter. Two lesions were simulated with cone shaped voids at two different angles to the loading axis of the femur, 45° (B) and 80° (C). ....  | 102 |
| Figure 41 Schematic of the proximal femur including assumed straight beam axis. The analysed cross-sections are perpendicular to the beam axis. The axial stiffness of lesion affected cross-section was compared to the stiffness of the corresponding cross-section without lesion in order to predict fracture. ....   | 104 |
| Figure 42 A) Schematic of the process of selective laser sintering. The z-axis is in the direction of powder layers. Materials made with SLS are believed to be anisotropic depending on the build orientation. B) Tensile bars were made in different orientation to measure the effect of the build orientation on the material properties. ....  | 105 |
| Figure 43 The tensile bar was material tested to determine the ultimate tensile stress, tensile modulus and failure strain. ....  | 106 |
| Figure 44 Results of tensile tests of five DuraForm PA Nylon samples in each building direction: Young's modulus ( $1419\pm41$ MPa), ultimate tensile stress ( $42.4\pm2.4$ MPa) and failure strain ( $13.8\pm3.8\%$ ) vs build orientation of the test sample. ....  | 106 |
| Figure 45 PMMA cemented femoral head models from additive manufacture were compression tested. All mounted samples were loaded with a flat platen. ....   | 107 |

- Figure 46 Output from the developed tool, calculating the axial stiffness. Cross-sections were perpendicular to the beam axis. The stiffness of femur models with two different lesion types were compared against the stiffness of a control femur without lesion. Differently shaped voids in the head resulted in a lower stiffness. A low stiffness meant a higher fracture risk at the respective location..... 108
- Figure 47 Load-Displacement curve of a typical compression test on two femoral head samples. One sample had a lesion of type 1 and one sample had a lesion of type 2. Type 1 samples had a lower stiffness and a lower fracture load compared to samples with a lesion type 2..... 108
- Figure 48 (A) The typical observed fracture lines (red) from the *in-vitro* compression tests on the cemented additive manufacture femoral head models. (B) Photo of the fracture sample of lesion type 1. (C) Photo of a sample containing a lesion of type 2 post-fracture. ..... 109
- Figure 49: Schematic of the verification workflow. Two lesions were simulated by drilling a hole either lateral or medial to the fovea. Each sample was individually analysed by the fracture prediction tool and subsequently compression tested. ..... 112
- Figure 50 (A) Schematic of a porcine femur preparation. (B) The proximal femur was sectioned perpendicular to the loading axis. (C) The sample was fixated in a cement mould. (D) The greater trochanter was removed..... 113
- Figure 51 CT-scans showing holes were drilled into porcine femoral heads to mimic necrotic lesion. The hole were drilled either lateral (A) or medial (B) to the fovea and there was a control group with no lesion (C). ..... 113
- Figure 52 (A) Distal view of a CT cross-section of a femoral head. (B) A threshold filter was applied creating a binary image mask with bone being white. Noise was reduced with a 3x3pixel median filter. (C) A 10 pixel dilation followed by erosion closed cavities within the bone. The trochanter was removed..... 114
- Figure 53: Regression between Young's modulus and apparent density of porcine femoral head bone plugs ( $R^2=0.95$ ). Closed circles present porcine cancellous bone, open circles present tests results for porcine compact bone from \*Bonney *et al.* (2011). The regression line describes the density-modulus relationship for femoral porcine bone..... 115
- Figure 54: Box-whisker plot showing the experimental fracture loads of 18 porcine femoral heads. The porcine femoral heads were compression tested on an Instron. Porcine femoral head with a lesion lateral  $n=6$  (A) and medial  $n=6$  (B) to the fovea and control sample  $n=6$  (C). Samples with a lesion lateral had statistically a higher fracture risk. ..... 117

- Figure 55 Computational results of the fracture prediction tool: The developed tool calculated the axial stiffness of all cross-sections within the subchondral area of the femoral head. (A) The input of the tool is a tomographic image. (B) Cross-sections were reconstructed which were perpendicular to the loading axis (beam axis). The density of each pixel was estimated using a density calibration. (C) The axial stiffness (EA) of each cross-section was calculated by summing the stiffness of all pixels in that cross-section. (D) The cross-section of an analysed femoral head sample that showed the highest difference when compared to the mean stiffness of the control samples, was assumed to be the weakest. The ratio of the weakest cross-section was used to quantify the fracture risk..... 118
- Figure 56 The cross-section of a sample with the highest difference of the axial stiffness compared the control mean was assumed to be the weakest. This was the point where fracture was assumed to initiate. There was a low linear correlation between the difference of the axial stiffness of a porcine sample and its experimental fracture load..... 119
- Figure 57 Schematic of the verification workflow. A lesion was simulated by drilling a hole lateral to the fovea. Each sample was individually analysed by the fracture prediction tool and subsequently compression tested..... 122
- Figure 58 Human femoral head sample preparation steps: (A) Drilling lesion (B) sectioning stem (C) Potting of sample (D) All samples (E) Platen compression test..... 123
- Figure 59 CT-scan of a potted sample with a simulated drilled lesion in the subchondral region of the femoral head (white arrows) administered through the femoral neck..... 124
- Figure 60 Schematic of the proximal femur including assumed straight beam axis. The analysed cross-sections are perpendicular to the beam axis. The axial stiffness of lesion affected cross-section was compared to the mean stiffness of the corresponding cross-section without lesion in order to predict fracture..... 125
- Figure 61 Computational results of the fracture prediction tool: The developed tool calculated the axial stiffness of all cross-sections within the subchondral area of the femoral head. (A) The input of the tool is a tomographic image. (B) Cross-sections were reconstructed which were perpendicular to the loading axis (beam axis). The density of each pixel was estimated using a density calibration. (C) The axial stiffness (EA) of each cross-section was calculated by summing the stiffness of all pixels in that cross-section. (D) The cross-section of an analysed femoral head sample that showed the highest difference when compared to the mean stiffness of the reference set, was assumed to be the weakest. The ratio of the weakest cross-section was used to quantify the fracture risk..... 126
- Figure 62 The computationally predicted fracture risk based on how the axial stiffness of a sample compared to a reference set of healthy samples was directly correlated with the experimental fracture load of that respective sample. There was a good correlation between the difference of the axial stiffness of a femoral head sample and its experimental fracture load..... 127

|   |     |
|---|-----|
| Figure 63 (A) The axial stiffness of six femoral head samples was calculated for each respective cross-section along the beam axis. All samples were individually compared against the mean stiffness of the reference set (black dashed line). (B) Load displacement curve of six cemented femoral heads which were platen compression tested. The fracture load was defined as the first local load maximum of the load-displacement curve (circled).....   | 127 |
| Figure 64 Flowchart illustrating the study design. ....   | 132 |
| Figure 65 Diagram of the indirect density calibration method: The mean density of cortical bone of the mid shaft of every femur in a calibrated CT set was calculated ( $\rho_{\text{mean reference}}$ ). AVN affected mostly the femoral head and the mean density of cortical bone at the corresponding location ( $\rho_{\text{mean AVN}}$ ) was assumed to be similar to the reference group. The calibration function of the uncalibrated AVN CT-set was approximated by using the density of cortical bone of the shaft as a reference value. This allowed the conversion of Hounsfield grey values (HU) with bone density.....   | 136 |
| Figure 66 The tool compared each femoral head sample against a healthy benchmark to assess the fracture risk. Two approaches were tested in this study. Option 1: The axial stiffness (EA) of a sample was compared to the corresponding stiffness of the contralateral femoral head of the respective sample. Option 2: The axial stiffness of a sample was compared to the corresponding mean stiffness of each sample of the reference set. The reference set included all healthy contralateral femoral heads of the AVN CT-set. ....   | 139 |
| Figure 67 The developed tool calculated the axial stiffness of all cross-sections within the subchondral area of the femoral head for five AVN patients. The tool calculated the stiffness based on CT-scans. The axial stiffness of each sample and the mean stiffness of all healthy contralateral samples (black dashed line) was plotted along the beam axis. Samples from the same patient had the same colour and the stiffness of the AVN affected femur had a significantly lower stiffness than the contralateral femur. Patient P01_001 had a THA at the contralateral side and therefore no contralateral femoral head.....  | 140 |
| Figure 68 Comparison between the results from fracture prediction tool and the ranking of the ARCO classification. (A) The calculated axial stiffness of each cross-section was compared to the stiffness of the corresponding cross-section of the contralateral femoral head. The EA-ratio describes the reduction in stiffness between the healthy benchmark and the AVN affected femoral head. <sup>#</sup> P01_001 had a THA at the contralateral side and is therefore not listed. <sup>*</sup> The contralateral femoral head of P02_003 showed signs of necrotic lesions which led to an inaccurate EA ratio. (B) The calculated axial stiffness of each cross-section was compared to the mean stiffness of a reference set of unaffected femoral heads. The results were normalised against the body weight. .... | 142 |

Figure 69 CT cross-section with an AP view of the pelvis of P02\_003. (A) Femoral head was classified as ARCO IIIC and showed initial subchondral fracture. (B) The contralateral femoral head showed signs of necrotic lesions visible as local density reductions..... 143

Figure 70 The beam theory and the finite element tool analyse different cross-sections of the femoral head model (P01-003). The beam tool predicted the fracture risk of the same geometric volume femoral head models as the finite element tool in this study. Necrotic bone was assigned an elastic modulus of 150MPa and healthy bone 300MPa. Healthy bone is grey and necrotic bone is green. (A-B) The beam tool analysed the whole volume of the upper femoral head by calculating the fracture risk of each cross-section along the beam axis. (C) The FEA tool predicted the fracture risk based on six predetermined cross-sections by calculating the stress difference at the lesion interface. Two cross-sections were in anterior-posterior orientation, two in medial-lateral orientation and two were angled at 20° flexion to simulate a heel strike loading. (D) AP cross-section..... 150

Figure 71 Computational results of the fracture prediction tool based on beam theory for stance loading of sample P01\_003: The developed tool calculated the axial stiffness of all cross-sections within the subchondral area of the femoral head. (A) The input of the tool was a patient specific two-material geometric model. (B) Cross-sections were reconstructed which were perpendicular to the loading axis (beam axis). Necrotic bone was assigned an elastic modulus of 150MPa and healthy bone 300MPa. (C) The axial stiffness (EA) of each cross-section was calculated by summing the stiffness of all pixels in that cross-section. (D) The cross-section of an analysed femoral head sample that showed the highest difference when compared to the stiffness of the healthy bone, was assumed to be the weakest. The ratio of the weakest cross-section was used to quantify the fracture risk..... 152

Figure 72 The minimum EA-ratio quantified the fracture risk of each sample. The predicted fracture risk was calculated for two loading situations, stance and heel strike. A heel strike loading caused a slightly higher fracture risk compared to a stance loading simulation..... 156

Figure 73 The location of the centre of the femoral head was selected in three planes (A) AP, (B) Medial lateral and (C) distal. The interface showed a virtual X-ray image in all three planes. The tool helped selecting the centre of the femoral head by allowing the user to draw a circle around the spherical head (yellow line)..... 159

Figure 74 Comparison of virtual X-ray images from a CT image. (A) Clinical patient CT. (B) Threshold improved image which helped to identify anatomical landmarks..... 160

Figure 75 (A) A proximal femur and a full femur including the pelvis were segmented and arbitrarily orientated. (B) A proximal femur model was referenced against a full femur model in order to approximate the shaft axis for samples without shaft. Anterior posterior view of the proximal femur model (grey) referenced with the full femur model (green)..... 160

|   |     |
|---|-----|
| Figure 76 Biomechanical loading model of the hip according to Pauwels (2012). The lever arm b of the bodyweight B is approximately three times longer than the lever arm a of the muscular force A. The joint contact force F is about four times the force of the body weight B.....   | 169 |
| Figure 77 AP view of a proximal femur. The location and curvature of the final curved beam axis (black) was calculated based on the location of the modulus weighted centroid (yellow) of cross-sections which were perpendicular to the straight neck and shaft axis (blue). The location of the modulus weighted centroids of cross-sections perpendicular to the final curved beam axis (pink) mostly correlated with the beam axis except at the intertrochantic region where the mass of the trochanter shifted the centroids. The centre of curvature of the curved beam axis is green. ....  | 171 |
| Figure 78 Deflection of a curved beam element subjected to a moment (M). ..   | 173 |
| Figure 79 Analysis of the principal axis angle. The axis deviated slightly from the medial-lateral axis within the intertrochantic area. Pink asterisk indicates point of highest stress. ....  | 175 |
| Figure 80 Segmented femur mask. ....  | 176 |
| Figure 81 Density-modulus relationship for cortical (blue) and cancellous bone (orange).....  | 178 |
| Figure 82 Beam theory analysis of a femur. (A) AP image of a right femur from projected computed tomography. The fracture load of each cross-section was calculated. Beam cross-sections (white) were perpendicular to the beam axis (black) which was derived from the location of the centroidal axis (yellow). The femoral neck showed the highest fracture risk as its predicted fracture load was the lowest. (B) The femoral beam model consisted of a series of stacked beam cross-sections. The colour of each pixel correlates with the Young's modulus of that element. (C) Modulus map for a cross-section of a curved beam element. (D) Modulus map for a cross-section of a straight beam. The structural stiffness of each cross-section was calculated by summing the stiffness of all pixels in that cross-section..... | 179 |
| Figure 83 Comparison between a straight and curved beam theory approach and its effect on the predicted fracture load. Analysed cross-sections were perpendicular to the respective beam axis. Straight beam theory failed to identify the high fracture risk for the femoral neck. The x-axis of the line chart was collinear with the respective beam axis. ....  | 180 |
| Figure 84 Comparison between two different simulated loading situations: Joint reaction force parallel to the shaft axis and the simulation of a one leg stance. When simulating a one leg stance, the consideration of the abductor muscle force had no significant influence on the predicted fracture load. In general, the predicted fracture loads for the neck area were less affected by the loading direction. Ignoring shear stress components for fracture load calculations seem only to effect the ends of the femur.....   | 181 |

|  |     |
|--|-----|
| Figure 85 A typical picture of the neck fracture of a mechanically tested femur. <i>Image from Tanck et al. (2009) reproduced with permission from Elsevier.</i> .....   | 182 |
| Figure 86 Schematic of the proximal femur including assumed curved beam axis (dashed black line). The cross-sections are perpendicular to the beam axis. At the centre of the femoral head the curved beam axis starts at an angle 45° to the horizon. It is defined as an arc and it ends at the lower trochanter. (The number of cross-sections shown is not representative) ..... | 185 |
| Figure 87 (A) Uniaxial compression test of a proximal femur model. (B) A total of twelve femur models generated by additive manufacturing were tested. ....  | 186 |
| Figure 88 Comparing predicted and experimental results: The computational tool identified the femoral neck and the end of the stem to have the highest fracture risk. The red lines show the typical observed fracture lines from the invitro test which match the computational prediction. ....  | 187 |

## Abbreviations

|         |   |
|---------|---|
| ARCO    | Association of Research Circulation Osseous                 |
| AP      | Anterior-posterior  |
| AVN     | Avascular necrosis  |
| BMD     | Bone mineral density  |
| BV/TV   | Bone volume over total volume                               |
| CT      | Computed tomography   |
| DEXA    | Dual energy X-ray absorptiometry                            |
| E       | Young's (Elastic) modulus                                   |
| FEA     | Finite element analysis                                     |
| HRp-QCT | High resolution peripheral quantitative computed tomography |
| HU      | Hounsfield unit   |
| MRI     | Magnetic resonance imaging                                  |
| NJR     | National Joint Registry                                     |
| OA      | Osteoarthritis  |
| ON      | Osteonecrosis   |
| OP      | Osteoporosis  |
| PMMA    | Poly methyl methacrylate                                    |
| QCT     | Quantitative computed tomography                            |
| SARS    | Severe acute respiratory syndrome                           |
| S-I     | Superior-inferior   |
| THA     | Total hip arthroplasty                                      |

## Chapter 1 Introduction

Up to 60% of total hip arthroplasties in Asian populations are attributable to avascular necrosis (AVN) or osteonecrosis of the femoral head (Kim and Rubash, 2007). Patients with a diagnosis of AVN are quite young with a mean age around 38 years (Mont and Hungerford, 1995). If untreated, the bone collapses and the spherical femoral head surface gets deformed and flattened causing severe pain and immobility. As patients with AVN are generally younger and have higher functional demands, total hip replacement can be problematic. One major problem, even for experienced physicians, is the difficulty in predicting fracture risk associated with AVN in the clinical environment. Thus there is a need for a diagnostic tool to determine AVN in an early stage before the onset of the destruction of the joint articular surface. Not all lesions progress to failure and current classification methods have poor differentiation and reproducibility (Schmitt-Sody et al., 2008). If AVN is diagnosed at this earlier stage, there is a broad spectrum of different joint preserving treatments to halt or slow down the progress of the disease. There is a need to improve upon existing methods for identifying at-risk patients.

The aim of this study was to develop a diagnostic tool to non-invasively assess the fracture risk secondary to AVN. This project developed an image-based method for predicting fracture in patients' femoral heads before they occur. It has the potential to help identify patients whose disease is at risk of progressing, as well as helping to provide a target for surgical intervention.

The project used engineering methods such as structural mechanics and strength of material to analyse the hip which is a biological system. The hip is a complex structure consisting of bones, joints and muscles. A verified biomechanical model defining forces, bodies and constraints was vital in order to apply structural mechanics to those systems. The strength of bones, including the femur, can be calculated using beam theory with a view to ascertaining fracture risk. A fracture prediction tool based on structural mechanics and beam theory accounts for both material and for geometrical properties compared to current classifications that only assess the lesion volume and location. Previously, the strength of the femur has been predicted using beam theory: treating the bone as a structural member subjected to stresses and strains (Toridis, 1969; Rybicki et al., 1972; Huiskes et al., 1981; Raftopoulos and Qassem, 1987; Hipp et al., 1995; Mourtada and Beck, 1996). Material properties can be derived from tomographic images using empirical

relationships between density measurements and Young's modulus (Carter and Hayes, 1976).

The ability of the tool to predict the fracture risk of lesion affected femoral heads can be tested with *in-vitro* disease models created from additive manufacturing as well as explanted porcine and human disease models. The ability of the tool to identify necrotic lesions that were likely to progress to fracture can be validated by predicting the fracture risk of femoral heads from AVN patients. To highlight the advantages of the beam theory approach, the fracture prediction tool needs to be compared to current diagnostic methods and another fracture prediction method based on FEA in regards of objectivity, robustness and usability.

## Chapter 2 Literature review

### 2.1 Overview of the hip

#### 2.1.1 Bony anatomy of the proximal femur

The hip is a ball and socket joint. The femoral head being the ball portion of the joint and the acetabulum the socket. The acetabulum is a concave surface of the pelvic bone and is formed medially by the pubis, superiorly by the ilium, laterally and inferiorly by the ischium (Gray, 1919). The femoral head is approximately spherical with an average radius of around 25 mm (Figure 1A) (Gilroy et al., 2008).

The entire load of the body during daily activities is transmitted through the acetabula onto the femoral heads. The femur is the longest and strongest bone in the skeleton and is the only bone in the thigh.

The head of the femur has a non-articular depression (fovea) on its medial surface for the attachment of the *ligamentum teres* which connects it to the acetabulum (Drake et al., 2009). The head is connected to the shaft of the femur by the neck, a cylindrical strut of bone which projects from the shaft at an angle of around 135° (115°-142°) for both Caucasian and Asian populations (Hoaglund and Low, 1980). The upper part of the shaft bears the greater and lesser trochanter, which are attachment sites for muscles that allow for motion of the hip joint (Drake et al., 2009). The shaft is almost cylindrical in form (Gray, 1919).

Cortical bone is one of two types of bone tissue that form bones. The outer shell of the femur consists of cortical bone made up mostly of calcium and minerals. Up to 70% of its dry mass is hydroxyapatite,  $\text{Ca}_{10}(\text{PO}_4)_6(\text{OH})_2$  (Hall, 2015). The remaining organic part is mostly collagen. This dense layer of cortical bone supports the weight of the body and is hard, stiff and strong. Cortical bone tissue consists of osteons and Haversian systems, cylindrical structures that contain an inorganic matrix and also osteocytes in cavities between the concentric rings (Figure 1B). They are aligned parallel along lines of stress. The blood vessels inside the Haversian canal provide oxygen and nutrients and remove waste.

Especially at the end of femora, proximal to the articular surface, cancellous bone makes up the interior of the bone. Cancellous bone is less dense and hence has a higher surface area compared to compact cortical bone. Cancellous bone tissue does not contain osteons but consists of trabeculae.

Blood vessels within this tissue bring nutrients to osteocytes and remove waste. Trabeculae are a network of small needle-like or flat pieces of bone. It is a lightweight design that allows a reduction in material and weight while having highest rigidity. The structure is aligned with the load vectors that occur during daily activities such as standing and walking.

Bone is an anisotropic material which means that it has different Young's moduli depending upon the orientation. The porosity of cancellous bone is around 80% in contrast to cortical bone with only 3.5% (Renders et al., 2007). The higher porosity and the larger surface allow a quicker turnover of bone material. The open spaces in the network are filled with bone marrow where blood cells are produced.

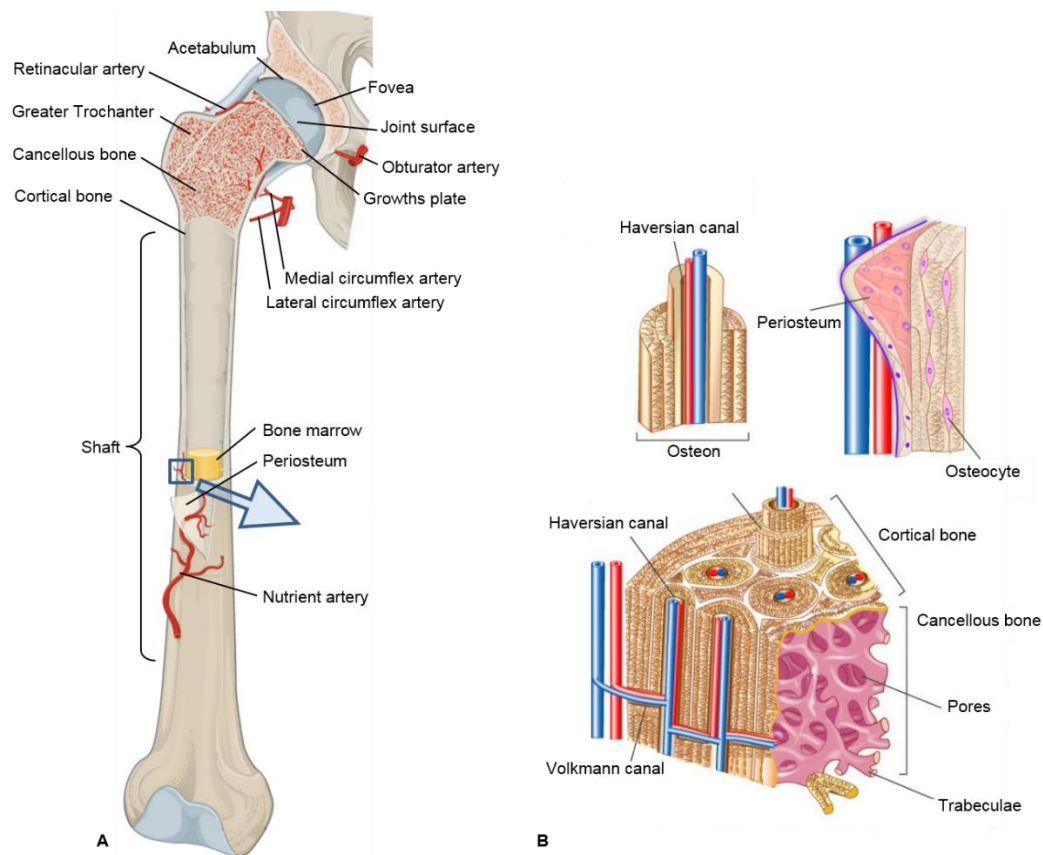


Figure 1 A) Schematic of the anterior view of the right human femur including blood supply of the femur head. Adapted from Openstax college, 2013. B) The structure of bone as shown in the long bone. Reproduced with permission of © Krebsinformationsdienst, Deutsches Krebsforschungszentrum.

### 2.1.2 Bone metabolism

In 1892, Wolff reported that the bone grows and remodels itself over time to respond to functional demands of the mechanical loading that is placed upon it (Wolff et al., 1986). This remodelling also controls the reshaping or replacement of bone following injuries like fractures but also tiny breaks, which

come as a result of normal loading. Vessels grow actively into the lesion and dead tissue is resorbed and replaced, in part, by living tissue (Steinberg et al., 1984). Functionally, new bone tissue is constantly replacing old bone.

Two types of bone cells are responsible for bone remodelling, osteoclasts and osteoblasts. In healthy bone, osteoclasts remove old bone tissue while osteoblasts form new bone in metabolic equilibrium (Rodan, 1992). Osteoclasts create an acidic environment that dissolves the bone's mineral content. The remaining collagenous organic part is removed by enzymes emitted by osteoclasts. Following the resorption of bone, osteoblasts start to produce an organic matrix called osteoid. Osteoid is mostly made out of collagen and forms a scaffold in which minerals including calcium phosphate begin to crystallise. Together with adjacent osteoblasts, this calcified matrix forms the surface of new bone tissue. Some osteoblast cells become trapped in the bone matrix they secrete and transform into osteocytes which are believed to sense high bone loads and respond with an increase of osteoblastic activities, whereas under low loading conditions, osteoclasts remove bone tissue, optimising its structure.

A negative imbalance in resorption and formation of bone results in a loss of strength of the affected bone.

### **2.1.3 Blood supply of the femoral head**

The blood supply to the femoral head that supplies oxygen and nutrients is via branches of the inferior gluteal artery and the lateral and medial circumflex femoral arteries (Figure 2). Branches from the lateral but mostly from the medial circumflex arteries pierce the capsular ligaments at the base of the neck and so become the retinacular arteries which extend towards the head and surround the neck of the femur. If the neck of the femur is fractured, the close proximity of these arteries to the neck put them at risk of being disrupted. The compact bone of the femur has tiny holes and passageways, through which these arteries enter the bone. Once within the cortex, these arteries run towards the femoral head forming a rich network inside the cancellous bone (Brodtetti, 1960). At the upper part of the femoral head, superior to the growth plate, these blood vessels meet and anastomose with the acetabulum branch coming from the obturator artery which enters the femoral head through the fovea adjacent to the ligament of the femoral head (Trueta and Harrison, 1953). However, the blood supply of the femoral head remains mainly through the retinacular arteries with only minimal supply from the obturator artery (Trueta and Harrison, 1953; Grose et al., 2008). Additionally the obturator

artery degrades over time. If the retinacular arteries are blocked, the blood supply to femoral head would be severely limited as other vessels cannot compensate for the loss.

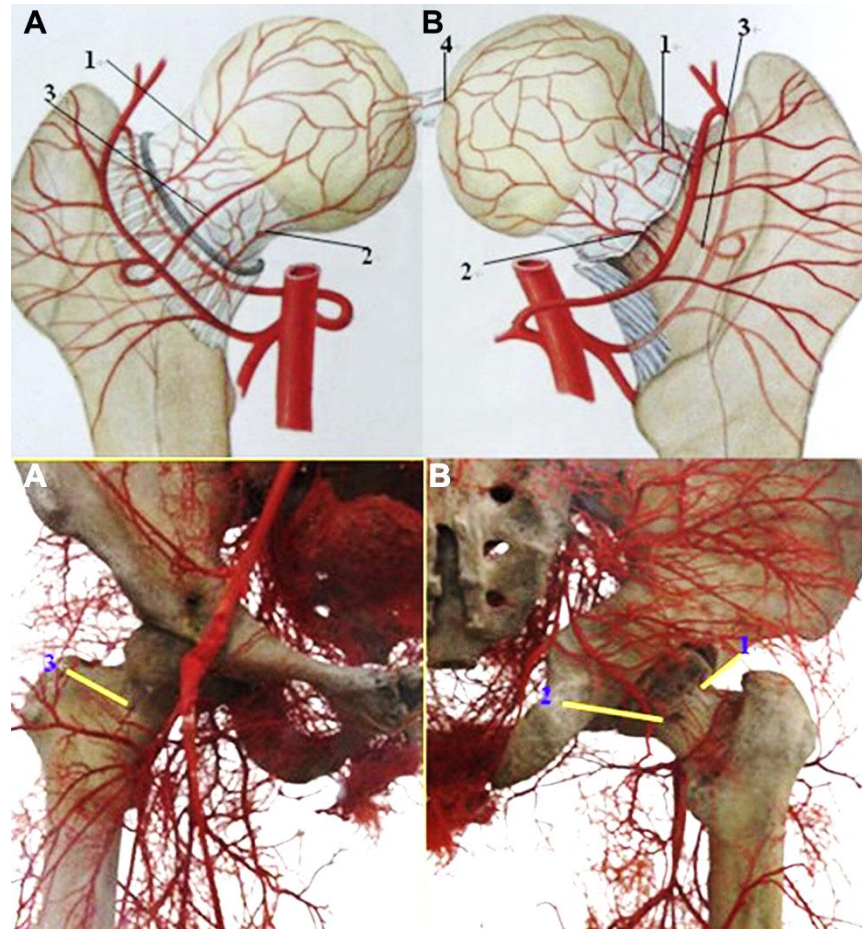


Figure 2 Blood supply of right femur head. (A) Anterior view, (B) Posterior view.  
(1) Inferior, (2) superior and (3) anterior retinacular artery. (4) Arteries of the ligamentum teres from obturator artery. *Image from Zhao and Yu (2015) reproduced with permission from Elsevier.*

#### 2.1.4 Joint loading and muscular anatomy

The femur is subjected to a spectrum of forces and moments which vary in magnitude and direction for different activities such as double-leg standing, single-leg standing gait. The magnitude of the acting forces is also influenced by factors like bodyweight and activities performed. Muscles attached to the bone surface and the joint contact force are acting upon the femur. Muscles play a substantial role in balancing the loads within the femur to assure that the bone is loaded axially, rather than in bending (Duda et al., 1997). They have also a significant influence on the joint contact force because an increased muscle force results in an increased hip contact force.

Body weight compresses the bone while muscles pull the bone at its surface area. The hip allows wide range of motion for which a large number of controlling muscles are necessary. In addition to providing motion for the hip these controlling muscles arise from a wide surface area not only contributing to stability but also preventing undue bending stresses on the femur (Byrne et al., 2010).

Seireg et al. (1975) reported the variation of the total joint force on the femoral head surface during walking. The joint forces can be up to 5.4 times the body weight. At heel strike the hip moves to 20° of flexion (Houglum, 2016). In general, the hip joint has the following ranges of movement: Extension (10°), flexion (125°), abduction (45°), adduction (45°), external rotation (45°) and internal rotation (45°) (Roach and Miles, 1991).

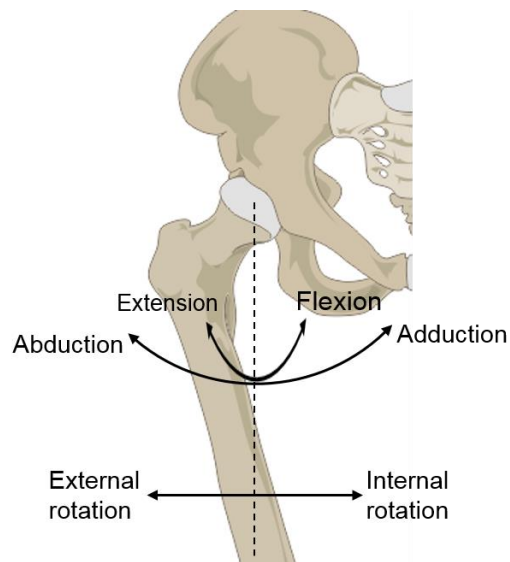


Figure 3 Movements about the hip joint. *Adapted from wikipedia.*

## 2.2 Biomechanical model of the proximal femur

A mechanical simulation of joint and muscle loading relies on a comprehensive musculoskeletal model which include all relevant forces on the hip. Muscles have complicated three-dimensional geometry and joints have sophisticated kinematics (Blemker et al., 2007).

A model reflecting all 22 muscles in the hip would be too complex, so the musculoskeletal model needs to be grossly simplified in order to reduce the number of muscle fibres. Paul (1967) combined the 22 hip muscles into six muscle groups. Heller et al. (2001) developed a musculoskeletal model for the hip by segmenting muscles groups on CT-scans. The model had 30 lines of muscles in action and was also used by Bergmann et al. (2001) for his gait

analysis studies. However in a later study, he was able to simplify the model even further by removing muscles that had only a small effect on hip joint loading (Heller et al., 2005). Like other studies, he merged the muscles attached to the proximal femur to a single abductor muscle (Simoes et al., 2000; Heller et al., 2005; Byrne et al., 2010). However, most studies that simulate fracture loading on the hip use a biomechanical model with a single joint contact load only and neglect all muscle forces (Cristofolini et al., 1996; Heller et al., 2005). This simplification is justified when the focus of a stress analysis lies on the femoral neck and head area.

Using a simplified biomechanical model allows estimation of the magnitude of the joint load and resultant contact stress that is distributed over the articular surface of the femoral head. In a study by Brown et al. (1983), the local distributions of articular contact stress were assembled from direct measurement in seventeen cadaveric hips by an array of several miniature transducers placed upon the cartilage. Due to the shape of the acetabulum, the load bearing surface does not fully cover the spherical femoral head. The stress distribution at the underlying joint surface respective to the gait cycle was not replicated in the study, though the loading was tested in various configurations. The study revealed that the stress acting on the femoral head is not static but highly dynamic (Brown and Shaw, 1983).

## **2.3 Avascular necrosis of the femoral head**

While it can affect any bone, common sites of avascular necrosis (AVN) are the joints at the shoulder, knee, ankle and especially the hip (Assouline-Dayan et al., 2002). AVN occurs predominantly in the femoral head where it ultimately leads to the destruction of the hip joint. A blockage of blood vessels (avascular) inside the bone leads to a shortage of oxygen and glucose which results in the cellular death (necrosis) of bone tissue.

In literature AVN is also known as osteonecrosis (ON), aseptic necrosis and ischemic necrosis. ON comprises all forms of necrotic lesions whereas AVN solely refers to a condition with ischemic lesions.

### **2.3.1 Epidemiology**

There are no centralised registers to report AVN. However, some data can be retrieved from literature and some national joint registries where AVN is listed as an indication for a total hip replacement.

AVN occurs more frequently in Asian populations than among Caucasian populations (Table 1). While in countries with a mainly Caucasian population hip replacement surgeries are mainly performed for osteoarthritis (OA), AVN is the main indication in Asian countries where 60% of the world's population lives indicating the socioeconomic impact of AVN. A nationwide survey in Japan in 2004 found that 11,400 (9 in 100,000) patients sought medical treatment for idiopathic osteonecrosis of the femoral head. In Korea, the number of patients treated for ON went up from 22,354 in 2007 (46 in 100,000) to a total of 25,993 patients in 2013 (Lee, 2014). In England, Wales and NI the number of hip replacements attributed to AVN grew from 1,705 (3 in 100,000) to 2,057 in the same time, despite having a slightly bigger population than Korea (National Joint Registry, 2007, 2013).

Table 1 Proportion of total hip replacements that are due to avascular necrosis. AVN is more prevalent among the Asian populations.

| <b>Country</b>   | <b>Percentage of THA</b> | <b>Source</b>                             |
|------------------|--------------------------|---|
| Taiwan           | 46.3%                    | Lai et al., 2008                          |
| Korea            | 50% - 60%                | Kim & Rubash, 2007                        |
| Hong Kong        | 41.2% - 45.6%            | Chiu et al., 1998; Chan et al., 2016      |
| India            | 49%                      | Pachore et al., 2013                      |
| USA              | 5% - 12%                 | Mankin, 1992                              |
|                  | 10%                      | Mont and Hungerford, 1995                 |
|                  | 2.9%                     | AJRR, 2016                                |
| England Wales NI | 3%                       | National Joint Registry, 2015             |
| Sweden           | 3.3% - 3.5%              | Swedish Hip Arthroplasty Register, 2014   |
| Germany          | 3.1%                     | Bitzer et al., 2010                       |
| Netherlands      | 3%                       | Nelissen and Schreurs, 2015               |
| Switzerland      | 4.1%                     | Schweizerisches Implantatregister, 2014   |
| Australia        | 3.4%                     | National joint replacement registry, 2016 |

Patients suffering from AVN are generally young adults aged 30 to 50 years, with the mean age being 38 years (Mont and Hungerford, 1995). Patients with a diagnosis of non-traumatic AVN are around 20-50 years old (Steinberg et al., 1984). The prevalence of AVN in younger age groups is demonstrated by data from the National Joint Registry for England, Wales and Northern Ireland (2015). Among the age group of under 30 year olds 22% of all annual THA are due to AVN. It is still 17% in the 30-39 year age group and is then gradually dropping to 2-3% between the ages of 40-89.

Males are three times more likely to be affected than women (Assouline-Dayan et al., 2002).

Perthes' disease is an idiopathic hip disorder in children. It represents a form of AVN which mostly affects Caucasian boys between 2 and 14 years from a lower social class background. In contrast to AVN, children of Asian descent are less affected which may be due to differences in bone maturation (Barker and Hall, 1986). As the disease is linked to the socioeconomic background, the occurrence of the Perthes' disease in the UK is dependent on the geographic region with London 4.6 and Scotland 10.39 per 100,000 0-14 year olds (Perry et al., 2012).

### **2.3.2 Aetiology (Cause)**

The disruption of the vascular supply may or may not be linked to trauma. Traumatic cases include femoral neck fractures, hip dislocations and vascular injuries that lead to a mechanical interruption of the blood supply to the femoral head, and is the most common cause of AVN with more than 50% of cases attributable to the cause (Jacobs, 1978; Assouline-Dayan et al., 2002). Defining the cause of bone death for non-traumatic induced AVN remains a diagnostic challenge because causal relationships are not always obvious (Assouline-Dayan et al., 2002). Therefore, non-traumatic AVN is sometimes referred to as idiopathic because it is still unknown what exactly 'causes' AVN. However it can be attributed to certain risk factors.

The two most common risk factors of non-traumatic AVN are corticosteroid therapy and alcohol abuse, which together account for as many as 90% of new non-traumatic cases (Hamilton et al., 2009). These two risk factors are described in this section followed by an overview of other ethologic factors.

Why AVN is more prevalent among Asian, men or young patients is not clear but steroid treatments are generally more common in Asian countries and

young men are more likely to have an alcohol habit. Genetic related lack of nitric oxide synthases among the Asian population (Cubbon et al., 2010) might be an explanation for the susceptibility to osteonecrosis as nitric oxide increases the blood flow and improves vascular repair (Glueck et al., 2007; Koo et al., 2006). However, the aetiology is still not entirely clear and is subject to research.

### **2.3.2.1 Corticosteroid therapy**

Corticosteroids are an anti-inflammatory medicine which suppress the immune system.

Several causal relationships between steroids administration and bone death have been suggested including mechanisms such as suppression of the bone metabolism or cell toxicity (Glimcher and Kenzora, 1979; Weinstein et al., 1998; Calder et al., 2004) and fat embolism (Jones and Engleman, 1966; Fisher et al., 1972). However, the exact mechanism that causes the necrotic lesion by corticosteroid remains still unclear.

In a nationwide survey in Japan in 2004, Fukushima et al. (2010) linked 51% of all AVN patients to steroid administration. Chan et al. (2016) linked about 28% of AVN patients that underwent a total hip replacement to steroid use. Additionally patients with a diagnosis of AVN secondary to steroids usually have a severe form of the disease (Mont, Carbone, & Fairbank, 1996).

During the outbreak of severe acute respiratory syndrome (SARS) in southern China in 2003, many patients received high dose corticosteroid therapy (Table 2). A number of studies analysed whether these patients developed AVN as a side effect of the treatment by screening tomographic scans. Griffith et al. (2005) strictly differentiated between osteonecrosis and nonspecific bone marrow abnormalities which were found in 30% of all analysed femurs. Therefore the reported number of SAR patients that developed AVN is significantly lower in their study.

Table 2 Likelihood of severe acute respiratory syndrome (SARS) patients receiving steroid treatment to develop AVN.

| Place of study | SAR patients that developed AVN | Source                |
|----------------|---------------------------------|-----------------------|
| Beijing        | 130 (24%) of 539                | Guo et al., 2014      |
| Beijing        | 101 (24%) of 420                | Cheng et al., 2006    |
| Beijing        | 31 (43.7%) of 71                | Lv et al., 2009       |
| Beijing        | 28 (43%) of 65                  | Hong and Du, 2004     |
| Hong Kong      | 12 (5%) of 254                  | Griffith et al., 2005 |

Osteonecrosis appears to develop soon after the initiation of steroid treatment (Lv et al., 2009). Lv et al. (2009) observed SARS patients with steroid treatment over a period of three years. They showed that 3-4 month after start of treatment 39.4% were diagnosed with AVN. Over a period of 36 month the number of patients which were diagnosed with AVN grew slightly from to 43.7% (Lv et al., 2009). Male SARS patients were more affected than women (Guo et al., 2014).

Metselaar et al. (1985) reported that 36% of patients with high dose steroid therapy following a kidney transplant developed osteonecrosis in a six years follow-up study in the US. They further suggested that there is an individual sensitivity to steroids (Metselaar et al., 1985).

AVN is also often linked to systemic lupus erythematosus (SLE) which is treated with high dosage steroid therapy. It is disputed whether AVN is caused by SLE (Dubois et al. 1960) or by the steroid treatment (Zizic et al., 1985; Felson and Anderson, 1987). Nakamura et al. (2010) reported that 238 (44%) out of 537 joints developed osteonecrosis after high dosage steroid treatment for SLE in Japan. Zizic et al. (1985) reported that 52% of patients developed necrosis in a study in the US.

### 2.3.2.2 Alcohol abuse

The link between alcohol abuse and AVN is not clear either. A possible mechanism related to alcohol is fat emboli (Jones and Engleman, 1966). Abusive alcohol consumption is further known for stimulating cortisol production in the body which increases the blood pressure and reduces the activity of the immune system (Rico et al., 1985). This alters the lipid

metabolism which may result in a fat embolism causing necrosis. The mechanism is therefore similar to corticosteroid induced AVN.

In Hong Kong the common cause of osteonecrosis in men getting a THA was alcohol abuse with 53% compared to 4% in female patients (Chan et al., 2016). Men are more susceptible to alcoholism which partially explains why there is a gender related difference in the number of AVN patients.

#### 2.3.2.3 Others causes/ associated factors

The remaining AVN patients are associated with diverse conditions like sickle-cell, Gaucher disease (diving disease), myeloproliferative disorders, coagulation deficiencies, pancreatitis, caisson disease and exposure to radiation (Mont and Hungerford, 1995). Lavernia et al. (1999) reported that 10-20% have no clearly identifiable risk factor and are classified as idiopathic.

#### 2.3.3 Pathophysiology

Although there are different or multiple origins that cause AVN, the pathological course is identical (Musso et al., 1986; Mankin, 1992; Lavernia et al., 1999) and is defined by degenerative process which eventually leads to the collapse of the femoral head (Figure 4).

The blood supply of the femoral head is supplied by 80% through branches of the medial circumflex arteries and thus a blockage of these vessels leads to interrupted transport of nutrients and metabolites resulting in the anatomic predisposition of AVN (Assouline-Dayan et al., 2002). The ischemia of non-traumatic AVN may be a result of avascular interruption, thrombotic occlusion or extravascular compression (Mankin, 1992; Chen, 2011). Cancellous bone is highly vascular and is therefore more affected by the ischemia than cortical bone.

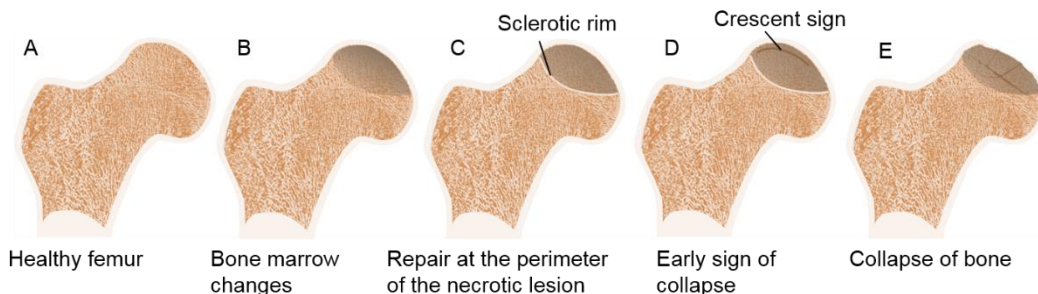


Figure 4 Progression of Avascular Necrosis

### **2.3.3.1 Cell death**

After an ischemic infarction, the oxygen- and nutrient-deprived bone cells die promptly. Studies show that death of bone marrow occurs generally after 6 to 12 hours, followed by bone cells like osteocytes, osteoclasts, and osteoblasts 12 to 48 hours after ischaemia (Hamilton et al., 2009). Bone marrow changes (Figure 4B) are an early manifestation of AVN (Turner et al., 1989).

### **2.3.3.2 Repair process**

Bone has the capability to repair itself by resorbing dead bone before replacement with new viable bone, a process which is called ‘creeping substitution’ (Jones and Engleman, 1966). The repair process begins about three days after the vascular disruption (Nakamura et al., 1997).

With most non-traumatic AVN, the vascular structures usually cannot penetrate deep inside the avascular lesion and repair is interrupted (Lavernia et al., 1999). Because of the lack of blood supply, osteocytes are resorbed leaving empty cavities, lacunae, in the bone. At the periphery of the lesion, osteoblasts lay new bone over the necrotic areas causing a thickening of bone (Figure 4C) (Hamilton et al., 2009).

This walling-off process of the necrotic lesion with sclerotic bone prevents the repair of the necrotic lesion and eventually leads to a loss of structural integrity of the femoral head (Mont et al., 1998). The healing process is therefore counter-productive as it ultimately prevents the complete revascularisation of the necrotic lesion (Assouline-Dayan et al., 2002). When there are insufficient nutrient minerals, trabeculae will become thinner due to osteoclastic activity and osteoid might not mineralise properly leading to an accumulation of decalcified fibrous cysts inside the femoral head (Ficat, 1985; Avadi, 2016). AVN shows a reduction in the BV/TV (Wang et al., 2014).

In a study analysing ten necrotic femoral heads from patients undergoing a total hip replacement, Wang et al. (2014) reported an increase of osteoclast and a decrease of osteoblasts activity in the necrotic and subchondral regions of the femoral head while osteoblast activity was high compared to healthy bone in the sclerotic region (Wang et al., 2014).

### **2.3.3.3 Bone fracture and collapse of femoral head**

As a direct result of the infarct, normal bone turnover comes to a halt. Hence the bone is no longer capable of repairing stress fractures and signs of fatigue induced by repetitive loads of weight bearing. This process weakens the cancellous bone in the load bearing region leading to bone fracture which

manifests as the ‘crescent sign’ on radiographs (Figure 4D and Figure 5) (Kaushik et al., 2012). Without the support of the cancellous bone in the subchondral region, the overlying cortical bone cannot bear the joint load and inevitably collapses.

The articular cartilage of the joint is not affected by the ischaemia until the collapse of the joint surface which leads to an articular degeneration, severe pain, and a loss of function in the joint (Figure 4E) (Patterson et al., 1964).

Atsumi et al. (1989) reported that lesions in the subchondral area, next to the joint surface, are particularly vulnerable to fracture as they are exposed to the highest stress.

Motomura et al. (2011) correlated the lesion position with the likelihood of fracture. If the lateral boundary of a necrotic lesion was within the load bearing area, then there was high chance that the femoral head surface fractured. The fracture originated at the lateral boundary of the necrotic lesion. When the whole femoral head was affected, fracture occurred deep in the necrotic lesion.

Nam et al. (2008) reported that from 105 asymptomatic AVN affected hips 62 became symptomatic within a mean period of 25 months. All of these 62 hips progressed to femoral head collapse with an average time between the onset of pain and surgery of 19 months. The occurrence of pain along with the lesion size appeared to be a major factor for femoral head collapse. Belmar et al. (2004), however, did not find any connection between pain and the progression to collapse. Collapse usually occurs within a timeframe of 1-3 years (Aubigné et al., 1965).

#### **2.3.3.4 Asymptomatic and self-repairing necrosis**

The pathology of asymptomatic AVN is usually quite different. If symptomatic AVN remains untreated, it usually becomes painful and leads to the collapse of the femoral head. AVN that remains asymptomatic can show self-healing of the necrotic lesion.

Spontaneous repair of asymptomatic osteonecrosis was observed in 51% of femoral heads in cohort of steroid treated patients whereas 35% of femoral heads collapsed but the lesion completely vanished in 9% after a mean follow-up period of 13.6 years (Nakamura et al., 2010).

Cheng et al. (2004) suggested that self-healing is dependent on an asymptomatic condition and the lesion size. Small lesions were likely to

resolve while larger lesions tend to become symptomatic and progress to subchondral collapse. Therefore, the lesion volume plays a significant role.

### 2.3.4 Diagnostic imaging

Invasive methods like core biopsy or functional exploration of bone, where the bone marrow pressure is measured by a cannula placed in the head of the femur, are hardly justified to diagnose AVN at the early stages as they pose a risk of infection (Steinberg et al., 1995). Imaging modalities, such as plain radiographs, nuclear imaging, magnetic resonance imaging (MRI), and computed tomography (CT) are relied upon to detect bony and cellular abnormalities which are caused by the pathologic changes of AVN. The earlier the disease is diagnosed, the broader is the spectrum of possible and effective treatments, especially at a disease stage before the occurrence of bone collapse. Because radionuclide imaging is considered to be too invasive for an early diagnosis of AVN, the most commonly used imaging modalities are in the following order: MRI, CT and plain radiographs which are described in this section.

A comparison of the described imaging modalities in terms of probability of detection is displayed in Table 3. MRI is the most sensitive modality by far and hence is widely used in the diagnosis of AVN.

Table 3 Comparison of sensitivity of different image modalities to detect changes resulting from AVN in an early stage

| Modality                   | Sensitivity | Disease stage | Reference                |
|----------------------------|-------------|---------------|--------------------------|
| <b>MRI</b>                 | 100%        | Pre collapse  | Saini & Saifuddin, 2004  |
| <b>SPECT*</b>              | 97%         | Pre collapse  | Lee et al., 1992         |
| <b>Planar scintigraphy</b> | 55%         | Pre collapse  | Collier et al., 1985     |
| <b>CT</b>                  | 55%         | Pre collapse  | Lee et al., 1990         |
| <b>Plain radiographs</b>   | 41%         | Post fracture | Resnick & Niwayama, 1995 |

\*Single-photon emission computed tomography

#### 2.3.4.1 Plain radiographs (X-ray)

Despite significant limitations, plain radiographs are widely used in the evaluation of AVN (Assouline-Dayan et al., 2002). Early changes are often not

observed because AVN only becomes visible after the development of a *crescent sign* (Figure 5), while the lack of radiographic findings does not necessarily mean that disease is not present (Stoica et al., 2009). Two-dimensional film does not detect early stage AVN, which means that a delay of 1-5 years may occur between the onset of symptoms and the appearance of radiographic abnormalities. Therefore, even for experienced physicians it is very hard to assess the fracture risk that is associated with AVN on radiographs, especially in a clinical environment (Anez-Bustillos et al., 2014).



Figure 5 X-ray of a crescent sign (arrow). The crescent sign is an early radiographic sign of AVN. *Image from Assouline-Dayan et al. (2002) reproduced with permission from Elsevier.*

#### 2.3.4.2 Computed tomography CT

The CT-scanner captures projections of a rotating X-ray beam which are then transformed into detailed three-dimensional images.

CT is also a radiographic imaging modality and therefore shares some of the disadvantages of plain radiographs. CT scans are insensitive for detecting early stage AVN (Stoica et al., 2009). Although CT may show subtle trabecular irregularity with bone necrosis when plain radiograph findings are normal, MRI and SPECT modalities are much more sensitive for evaluating early manifestations of the disease, such as bone marrow changes (Stoica et al., 2009). Clinically, CT is rarely used to diagnose AVN (Assouline-Dayan et al., 2002) however it is still part of current diagnostic classification (Gardeniers, 1993). CT also carries a high ionising radiation burden for the patient. Overall, CT scanning is considered as a complementary modality only.

The strength of radiographic imaging lies in visualising bone changes, as the X-rays, which pass through the body, are primarily absorbed by the mineral content of bone (Figure 6). Therefore, CT is superior to MRI in the detection of fractures (Lee et al., 1990). It allows identification of the sclerotic rim at the periphery of the necrotic lesion caused by AVN. However it is difficult to estimate the exact extent of the lesion size within the femoral head from CT imaging because the necrotic lesion may not be directly visible.

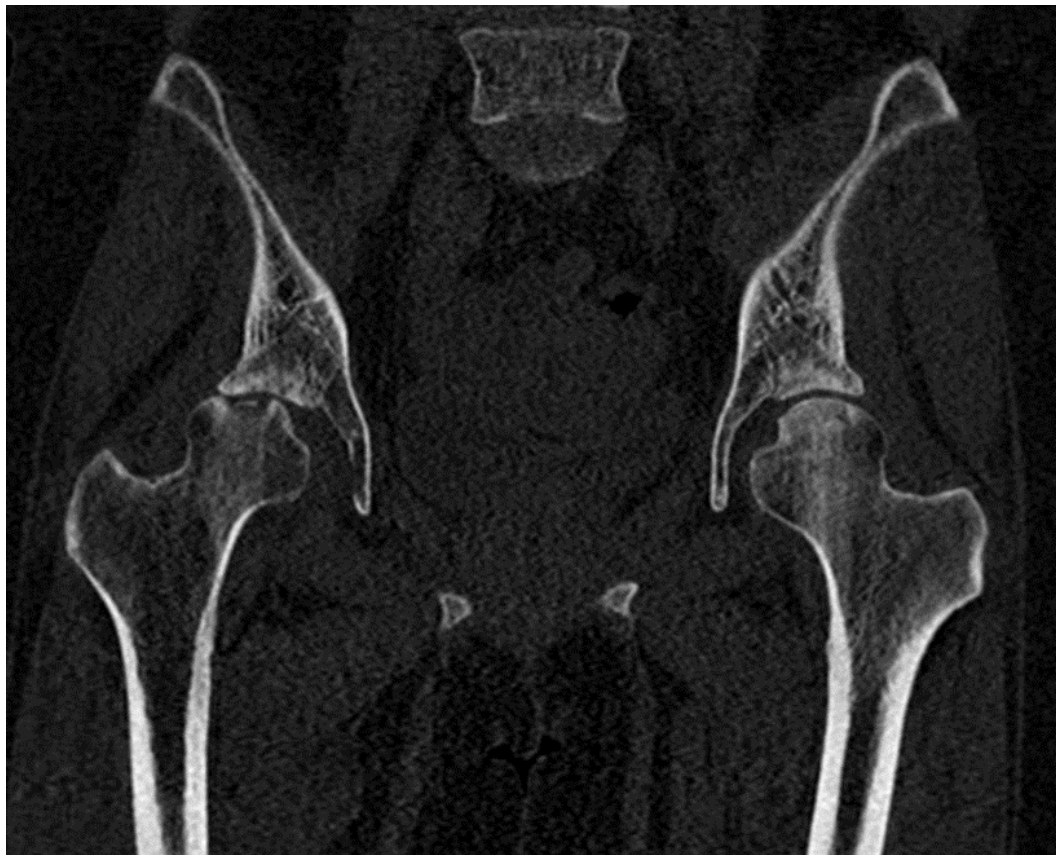


Figure 6 CT-image of a pelvis. The right femoral head on the left collapsed as a result of avascular necrosis.

CT imaging also allows visualisation of regions of decalcified necrotic bone tissue. However, for the naked eye these changes are mostly too subtle as the human eye cannot distinguish between the 65,535 grey values the scanner is able to produce, which makes CT less practical for the clinical practice to identify necrotic lesions. However, CT has potential to provide material property information for computational fracture simulations. The grey value is dependent on the measured density of the scanned material because the denser the tissue, the more X-rays are attenuated. Additionally, there is a clear density-Young's modulus relationship for bone (Currey, 1969), which allows correlation of X-ray attenuation to material properties of bone based on

established empirical density-modulus relationships. The density of bone can be measured from density calibrated CT (QCT) scans.

#### **2.3.4.3 Magnetic resonance imaging MRI**

MRI is very sensitive to changes in bone marrow composition and thus it can detect ischaemia even before the appearance of radiographic abnormalities and before it becomes symptomatic (Assouline-Dayan et al., 2002). The fat content in the affected femoral head changes as early as 5 days after vascular insult when adipocytes undergo necrosis (Hamilton et al., 2009).

MRI is probably the most common clinical imaging modality used to diagnose AVN as it can locate water and fat in the body. T1 and T2 are terms describing proton relaxation. Different tissues have different T1 and T2 values. Fat tissue appears bright on T1-weighted images while water appears dark. In contrast water appears bright on T2 images.

Dead and living tissue of the femoral head can be clearly distinguished on T1-weighted images as the MRI can highlight the fat content of viable bone marrow. The different intensities associated with living bone and necrotic lesions allows conclusions to be drawn about how advanced the disease is. If the intensities are relatively similar, this indicates an early stage of the disease.

On T2-weighted images, the boundary of the necrotic dead tissue and reparative interface of vascular reactive bone appears as a '*double-line sign*' which is characteristic of AVN and reported in up to 80% of cases though its absence does not exclude AVN (Figure 7) (Zurlo, 1999). The insufficient vascular reparative process appears as a high-intensity inner rim next to the dark rim of sclerotic bone (Zurlo, 1999).



Figure 7 Double Line Sign in a T2 weighted MRI image of a proximal femur. Inner white rim represents oedema and outer dark rim sclerotic bone. *Image from Choi et al. (2015) reproduced with permission from Springer.*

Additionally to the reparative tissue zones, MRI also shows cysts, marrow oedema and sometimes also bone fractures because fractured zones are usually filled with fluids (Mitchell et al., 1989). Bone marrow oedema may indicate an advanced stage of AVN (Meier et al., 2014).

MRI images present clear boundaries between viable and necrotic bone tissue so that the necrotic lesion can be clearly differentiated from the rest of the healthy femoral head. This is beneficial for the creation of computational segmentation models (Zoroofi et al., 2001).

However, MRI does not allow to describe the material properties of the scanned bone tissue, which is big disadvantage compared to CT. Therefore, CT is more suitable for computational model simulations as it provides material property information, despite MRI being superior for current clinical diagnosis.

### 2.3.5 Diagnostic Classification

A comprehensive classification system that classifies the exact stage of the disease has multiple benefits. It helps to quantify pathologic changes over a period of time. It helps to evaluate current treatments and compare the effectiveness of those methods. It helps research to develop and verify new

treatments. However most importantly, it helps the clinician to choose the best possible treatment by providing guidelines for any presented disease stage.

Current classification systems are based on the pathology and on quantifying the extent of involvement of the femoral head. There are several different classification systems described in the literature (Table 4):

Table 4 Evolution of classification systems used for AVN

| Classification System                                   | Year described | Reference              |
|---|----------------|------------------------|
| Ficat and Arlet   | 1970           | Ficat, 1985            |
| Marcus, Enneking and Massam                             | 1973           | Marcus et al., 1973    |
| Sugioka   | 1976           | Sugioka, 1978          |
| Steinberg   | 1980           | Steinberg et al., 1995 |
| Japanese Investigation Committee for Avascular necrosis | 1987           | Sugano et al., 2002    |
| ARCO  | 1993           | Gardeniers, 1993       |

All classification systems are based on identifiable changes of the pathology from imaging. They evolved with the imaging technology available at that time. The *grade* quantifies the extent of involvement within each stage, while the *stage* itself is classified by the type of radiographic change due to AVN according to specific diagnostic criteria. The most commonly used classification systems are Ficat and Arlet, Steinberg and the ARCO classification (Mont et al., 2006; Hamilton et al., 2009). These are described and compared in more detail in this section.

#### 2.3.5.1 Ficat Arlet

The first classification was developed by Ficat and Arlet in the 1960s. Initially it had three stages but a fourth stage was later added. It was further modified introducing a stage 0 and a transitional stage which however was never widely used clinically (Table 5).

As it was developed before the advent of MRI, the classification system is based on the identification of radiographic abnormalities in combination with

the findings from core biopsy, the occurrence of pain and clinical symptoms like limited range of movement.

Disadvantages of this classification system are that symptoms experienced by patients are highly subjective and biopsies are usually no longer used for the diagnosis of AVN. It also does not grade the disease stage based on the extent of femoral head involvement which has been reported to be an important factor for the likelihood of progression of AVN and the severity of the disease (Steinberg et al., 1999).

Table 5 Classification of AVN according to Ficat and Arlet (Ficat, 1985). Adopted from Steinberg and Steinberg (2004).

| Stage      |            | Clinical features  | Radiographic signs | Diagnosis without Core Biopsy  |
|------------|------------|--|--------------------|--|
| Early      | <b>0</b>   | Preclinical  | 0                  | 0<br>Impossible  |
|            | <b>I</b>   | Pre-radiographic   | +                  | 0<br>Impossible  |
|            | <b>II</b>  | Before flattening of head<br><br>Or sequestrum formation | +                  | Diffuse porosis,<br>sclerotic cysts<br><br>Flattening<br><br>Crescent sign |
| Transition | <b>III</b> | Collapse   | ++                 | Broken contour of head<br><br>Sequestrum<br><br>Joint space normal         |
|            | <b>IV</b>  | Osteoarthritis   | +++                | Flattened contour<br><br>Decreased joint space<br><br>Collapse of head     |

### 2.3.5.2 Steinberg

The classification system developed at the University of Pennsylvania outlined seven stages based on MRI beside plain radiographs and CT (Table 6). It is less ambiguous in distinguishing between stages compared to Ficat and Arlet. Steinberg also removed patient's symptoms and physical findings as a form of grading.

Table 6 Staging and Grading of AVN according to Steinberg et al. (1995) (University of Pennsylvania)

| Stage      | Grade       | Involvement  | Criteria   |
|------------|-------------|--|--|
| <b>0</b>   |             | Not quantified   | Normal or non-diagnostic radiograph, bone scan and MRI                     |
| <b>I</b>   | A, mild     | <15% of head involvement as seen   | Normal radiograph, abnormal bone scan and/or MRI                           |
| <b>II</b>  | B, moderate | 15% to 30% on radiograph or MRI  | Abnormal radiograph showing 'cystic' and sclerotic changes in femoral head |
|            | C, severe   | >30%   |  |
| <b>III</b> | A, mild     | subchondral collapse (crescent) beneath <15% of articular surface                                    | Subchondral collapse producing a crescent sign                             |
|            | B, moderate | crescent beneath 15% to 30%  |  |
|            | C, severe   | crescent beneath > 30%   |  |
| <b>IV</b>  | A, mild     | < 15% of surface has collapsed and depression is < 2mm   | Flattening of the femoral head   |
|            | B, moderate | 15% to 30% collapsed or 2 to 4mm depression  |  |
|            | C, severe   | > 30% collapsed or > 4mm depression  |  |
| <b>V</b>   | A, B, C     | Average of femoral head involvement, as determined in stage IV, and estimated acetabular involvement | Joint narrowing with or without acetabular involvement                     |
| <b>VI</b>  |             | Not quantified   | Advanced degenerative changes  |

Integral part of the Steinberg classification system is the quantification of the size of the necrotic lesion and the extent of collapse. Subchondral collapse is measured by the length of the crescent in respect of the entire articular surface. The extent of the femoral head collapse is measured by using concentric circles or planimetry. The size of the necrotic lesion can be measured by point counting with a grid to establish the percentage of head involvement. In 1995, Steinberg proposed a more comprehensive quantitative system to estimate the extent of lesion involvement which, however, was more intended for research and not for the clinical practise (Table 7).

Table 7 Methods to estimate the extent of lesion involvement in the femoral head as proposed by Steinberg et al. (1995).

| <b>Steinberg stage</b> | <b>Methods to estimate extent of involvement</b>  |
|------------------------|---|
| Stage I                | Lesion volume is approximated by using a computer program on serial MRI cuts.   |
| Stage II               | The visible necrotic area was added together on an antero-posterior and a lateral radiograph by using a point-counting with a grid. The lesion volume was approximated by multiplying both areas. |
| Stage III              | Extent of subchondral collapse is calculated by measuring the length of the crescent sign and expressing it as a percentage of the length of the entire subchondral surface                       |

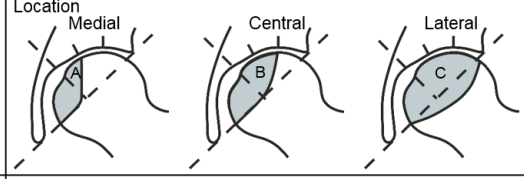
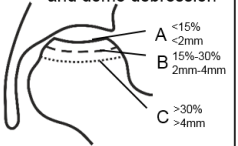
Steinberg's method of quantifying or grading the extent of head involvement mainly utilises plain radiographs instead of MRI and is far from being accurate nor is it suitable for the clinical application. Several studies suggested other ways to determine the percentage of femoral head involvement which can be used on top of the Steinberg and other quantitative classification systems (Kerboul et al., 1974; Koo and Kim, 1995; Cherian et al., 2003).

### **2.3.5.3 ARCO**

The Association Research Circulation Osseous (ARCO) was established after an International Symposium on Bone Circulation organised by Paul Ficat and Jacques Arlet in Toulouse in 1973. The ARCO classification system was established based on the Steinberg classification in 1991 and it was updated in 1992 and 1993. In its latest version, the ARCO system combines Steinberg's stages 4-6 eliminating the possibility to distinguish between different end stages of AVN (Steinberg and Steinberg, 2014) (Table 8).

The biggest alteration was adding the location of the lesion as a grading factor. Ohzono et al. found that collapse of the femoral head most often occurs when the lesion location is in the weight bearing area (Ohzono et al., 1991). However, other studies found that the lesion location was not an indicator for disease progression on its own (Nam et al., 2008).

Table 8 ARCO classification system for AVN (Gardeniers, 1993)

| Stage             | 0   | 1  | 2   | 3   | 4  |
|-------------------|---|--|---|---|--|
| Findings          | All presented techniques normal or non-diagnostic | X-ray, CT are normal; at least one of the below mentioned is positive                          | No crescent sign! X-ray abnormal: sclerosis, osteolysis focal porosis | Crescent sign! on X-ray and/or flattening of articular surface of femoral head  | Osteoarthritis! joint space narrowing, acetabular changes, joint destruction |
| Techniques        | X-ray, CT, Scintigraph, MRI<br>*Quantitate on MRI | Scintigraph, MRI<br>*Quantitate on MRI   | X-ray, CT<br>Scintigraph MRI<br>*Quantitate MRI and X-ray             | X-ray, CT only<br>*Quantitate on X-ray  | X-ray, only  |
| Subclassification | No  | Location<br> |   |   | No   |
| Quantitation      | No  | Quantitation<br>% area involvement<br>Minimal A<15%<br>Moderate B15%-30%<br>Extensive C>30%    | Length of crescent<br>A<15%<br>B 15%-30%<br>C>30%                     | %Surface collapse and dome depression<br> | No   |

#### 2.3.5.4 Quantifying lesion volume

Several studies have suggested ways of quantifying the lesion volume which might be used in addition to existing classification systems like Steinberg or ARCO. Real volumetric measurements are thought to be too demanding for clinical use and the volume of the necrotic lesion is therefore approximated by simpler methods as a proxy for the real lesion size (Steinberg et al., 2006).

Kerboul et al. (1974) developed an angular measurement method on two different tomographic planes to approximate the volume of the necrotic lesion. The angle is defined in the lateral and anterior-posterior radiographs by aligning the vertex to the head centre and the sides to the periphery of the necrotic lesion. The lesion volume was considered large when the sum of both angles was above 200 degrees, medium when between 160 and 200 and small when less than 160 degrees (Kerboul et al., 1974).

Koo and Kim (1995) developed angular measurements based on MRI instead of radiographs to quantify the volume of the necrotic lesion. Their 'index of necrotic extent' calculated the extent of the necrotic lesion in the weight-bearing portion of the femoral head (Eq.2.1). The angle is defined on the sagittal and coronal plane which show the largest lesion size. The angles were

divided by an angle of 180 degrees which was assumed to be the portion of the articular surface.

$$\text{index of necrotic extend} = \frac{A}{180^\circ} \cdot \frac{B}{180^\circ} \quad 2.1$$

$A$  is the arc of necrotic portion in mid-sagittal image and  $B$  is arc of necrotic portion in mid-coronal image. The lesion volume was considered large when the percentage was between 67 and 100, medium between 34 and 66 and small when less than 33 (Koo and Kim, 1995).

Cherian et al. (2003) modified the angular measurement method proposed by Koo & Kim and created a '*modified index of necrotic extend*'. They estimated the necrotic angle on MRI images that showed the maximal lesion size in the sagittal and coronal planes rather than on the mid-coronal and mid-sagittal images (Cherian et al., 2003).

Steinberg et al. (2006) compared the Kerboul and Koo and Kim methods against three-dimensional volumetric measurements of the necrotic lesion on 42 hips. They suggested a volumetric measurement was far more accurate but that angular measurements may provide a rough estimate of lesion size while being significantly easier to perform which is important for a clinical application (Steinberg et al., 2006). Hence angular methods are widely used clinically.

However, angular measurement methods do have an associated factor of uncertainty. Firstly, the true lesion size and the measured lesion size may vary considerably. A small lesion close to the centre of the femoral head has the same angular measurement as a much larger lesion occupying an area extending to the articular surface as long as both lesions have identical medial and latera borders (Figure 8). Secondly, the necrotic area of a single arbitrary cross-section is analysed, hence a lesion is only considered if it extends into that specific cross-section.

Kim et al. (1998) found poor repeatability and accuracy comparing seven different methods of measuring the extent of a necrotic lesion.

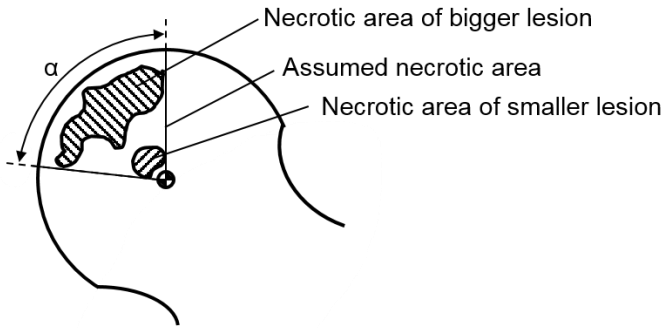


Figure 8 Schematic drawing showing an anterior-posterior view of the femoral head with two necrotic lesions of different size and location, but with the same angular measurements.

### 2.3.5.5 Reliability and reproducibility of current classification systems

Non-quantitative staging systems like Ficat and Arlet are still frequently being used. Newer systems like the ARCO classification take the occurrence of fracture, the lesion size and the lesion location into account which are known contributing factors for the progression of AVN to collapse.

Despite the evolution of classification systems for AVN with the advances of imaging technologies and a better understanding of the disease, the reliability and reproducibility of current systems to assess the status of AVN are still considered poor (Schmitt-Sody et al., 2008).

Several studies found poor inter-observer reliability and fair intra-observer reproducibility for the Ficat and Arlet (Kay et al., 1994), Steinberg (Plakseychuk et al., 2001) and the ARCO classification system (Smith et al., 1996; Schmitt-Sody et al., 2008).

A reliable comparison between different studies analysing the efficacy of different treatments is not possible because an unreliable categorisation of AVN patients may affect the interpretation of the respective results.

Current clinical treatment recommendations also rely on accurate classifications which otherwise may lead to the situation where unsuitable therapy options for patients being considered.

### 2.3.6 Treatment options for AVN

Treatment for AVN aims to relieve pain and maintain functionality of the joint. The most commonly used procedures are osteotomy, core decompression

and free vascularised fibular grafting (Malizos et al., 2007). Once the bone surface collapses total hip replacement (THA) is an effective treatment providing pain relief and restoration of functionality of the hip. However, THA may necessitate revision after around 10-15 years and hence a THA is usually delayed for as long as possible especially for young patients (Beaulé and Amstutz, 2004; Hamilton et al., 2009).

The effectiveness of a treatment option is dependent on the disease stage, the lesion size and location, the patient age and general health. The wrong treatment can cause unnecessary pain and suffering while still progressing to collapse. On the other hand, a prematurely chosen hip arthroplasty comes with consequential side effects where a joint preserving treatment would have been the better option. It is therefore important to know which lesion is likely to progress to collapse. The lack of understanding of AVN and the described uncertainty of current classification systems may lead to wrong treatment choices.

Early diagnosis is essential to get the best results especially for young patients (Ficat, 1985; Zizic et al., 1986; Assouline-Dayan et al., 2002). The earlier the disease is diagnosed, the broader is the spectrum of possible and effective treatments including joint sparing procedures.

The following section describes common treatment options for AVN in more detail and also highlights the effectiveness of these options at different disease stages based on currently used classification systems.

#### **2.3.6.1 Non-surgical / conservative treatments**

Beside restricting weight-bearing of the hip, non-surgical conservative treatments include lipid-reduction agents, bisphosphonates, and hyperbaric oxygen (Kaushik et al., 2012). Advantages for these modalities include lowering lipid levels in the blood because lipids have been associated with AVN as they can block the blood vessels. Bisphosphonates may improve bone osteoblastic activity. Treatments such as hyperbaric oxygen therapy may restore tissue oxygenation and reduce oedema which have been seen in patients (Reis et al., 2003). Non-operative treatments after the appearance of the crescent sign on x-ray, which is indicating subchondral collapse, are usually not successful (Hamilton et al., 2009). Therefore, non-operative treatment options are usually only suggested for patients with AVN of early pre-collapsed stages (Steinberg I,II; Ficat I,II). The respective outcomes of those treatments have been analysed in numerous studies.

Table 9 Literature review of outcomes of non-surgical treatments. Failure was assumed when a THA was necessary (clinical failure) or the femoral head collapsed.

| Initial disease Stage   | Failure rate   | Follow up   | Treatment   | Source                                   |
|---|--|---|---|--|
| Steinberg I (62 hips) + Steinberg II (43)<br>(<30%)*                            | 1 (5%) of 21   | Mean follow up 7 years 8 months (10 month – 22 years 8 month) | No treatment  | Nam et al., 2008                         |
| (30-50%)*   | 11 (46%) of 24   |   |   |  |
| (>50%)*   | 50 (83%) of 60   |   |   |  |
| Early stage, pre collapsed stage <sup>§</sup>                                   | 35 (35%) of 101  | >10 years   | Non-surgical  | Nakamura et al., 2010                    |
| Ficat I   | 65%  | Mean 34 months (20 months – 10 years)                         | Non-operative management (including restraining weight bearing) | Mont, Carbone, et al., 1996 <sup>#</sup> |
| Ficat II  | 69%  |   |   |  |
| Ficat III   | 87%  |   |   |  |
| Pooled  | 174 (80%) 219  |   |   |  |
| Large lesions and lesions located at the lateral end of the weight bearing area | 73 (95%) of 77   | Mean 15.5 month (2-36 month)                                  | Conservative treatment  | Ohzono et al., 1992                      |
| Lesions located elsewhere and small lesions                                     | 4 (10%) of 39  | 2-18 years  |   |  |
| Preventive measure for patients with high dosage steroid treatment              | Reduced the rate of patient who developed AVN to 1% from usually 3%-20%. | Mean 7.5 years  | Lipid lowering drug   | Pritchett, 2001                          |
| Ficat I   | 1 (7%) of 15   | 10 years  | Bisphosphonates   | Agarwala & Shah, 2011                    |
| Ficat II  | 1 (5%) of 19   |   |   |  |
| Ficat III   | 5 (26%) of 19  |   |   |  |
| Steinberg IIC + IIIC  | 2 (7%) of 29   | 24 months   | Bisphosphonates   | Lai et al., 2005                         |
| Steinberg IC  | 1 (8%) of 12   | 2 years   | Hyperbaric oxygen therapy                                       | Reis et al., 2003                        |
| Ficat II  | 0 (0%) of 17   | 7 years   | Hyperbaric oxygen therapy                                       | Camporesi et al., 2010                   |
| Steinberg I   | 1 (3%) of 29   | Mean 11 years (7 months – 16 years 7 months)                  | Hyperbaric oxygen therapy                                       | Koren et al., 2015                       |
| Steinberg II  | 3 (10%) of 29  |   |   |  |

\*Volume of lesion estimated based on (Beltran et al., 1990); <sup>#</sup>Eight out of ten were advanced Ficat stages III and IV. <sup>§</sup>Pooled results from review of 21 studies of a total of 819 hips. <sup>§</sup>Hips were classified according to (Sugano et al., 2002).

There is a correlation between clinical failure rates and the presented stage of AVN as well as the lesion size and location (Table 9). Patients treated

pharmacologically were more likely to require a surgical intervention when their disease stage was more advanced at the beginning of their treatment (M. Mont et al., 1996; Agarwala and Shah, 2011; Koren et al., 2015). It further showed that while a conservative treatment appears to be relatively successful for certain types of lesions, it had little effect on the progression to femoral head collapse for the others (Ohzono et al., 1992; Nam et al., 2008). That reiterates the importance of an accurate classification of the presented disease stage and the nature of the lesion in order to choose an appropriate treatment which achieves the best possible clinical outcome for the patient.

### **2.3.6.2 Surgical treatments: Core decompression**

Ficat and Arlet introduced core decompression in 1962 which involved drilling a cylindrical hole into the necrotic femoral head (Ficat, 1985). This technique has been used to preserve the joint in early AVN and to relieve pain (Koo et al., 1995). AVN causes an increase in bone marrow pressure within the femoral head (Assouline-Dayan et al., 2002) but it is debated whether increased intraosseous pressure is caused directly by AVN or is an ethologic factor (Hungerford and Zizic, 1978). Core decompression reduces this pressure and improves the osseous blood flow, by stimulating an angiogenic response in the drilled channels (Mont and Hungerford, 1995).

Modification of the technique uses multiple small diameter holes instead of one large tract (Figure 9). This treatment method gives similar long term clinical results compared to traditional core decompression but is less invasive and has fewer complications (Song et al., 2007; Al Omran, 2013; Bae et al., 2013).

Core decompression can also be augmented with grafting. Various types of bone-graft procedures have been used to provide mechanical support for the affected bone and delay the need for THA (Assouline-Dayan et al., 2002). The highest survival rates have been reached with vascularised fibular grafting although it is a more complex procedure (Assouline-Dayan et al., 2002). These grafts deter progression of pre-collapse lesions but can also delay the development of further stages of AVN after mild collapse has occurred (Kaushik et al., 2012). The vascularised bone grafts retain their intrinsic blood supply, speed up bone-healing and restore the bone's stability. The patient's own fibula is harvested including its fibular artery with its two veins and placed into the core tract and stabilised with a wire. The ascending branches of the lateral circumflex artery and vein are then anastomosed (reconnected) to the fibular vessels using microvascular surgical techniques (Hamilton et al.,

2009). This is a complex procedure and has the downside of donor site morbidity.

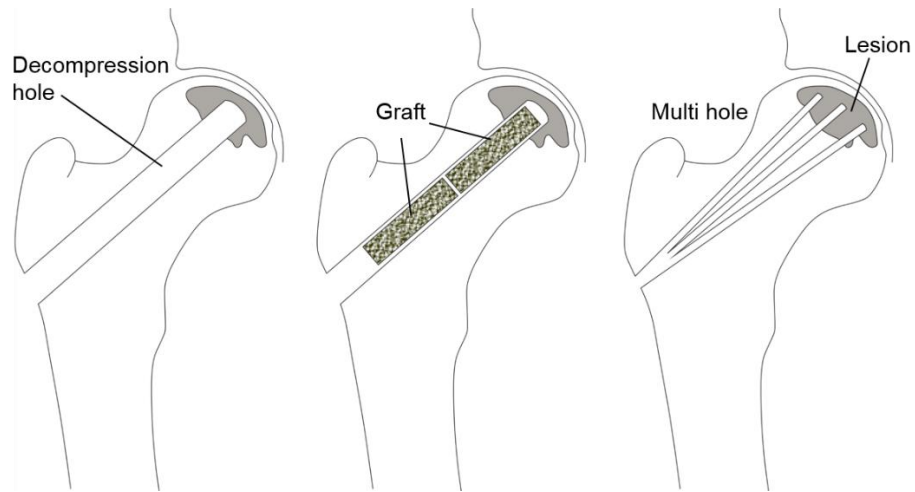


Figure 9 Schematic drawing of a core decompression (left), augmented with bone grafts (middle) and a multi hole core decompression (right).

The clinical success of plain core decompression generally declines with advancement of the necrotic lesion (Kaushik et al., 2012) however it can prevent fracture at early stages of osteonecrosis (M. Mont et al., 1996). It is notable that these therapies have minimal utility after subchondral collapse has happened in the femoral head. So core decompression is mostly used in pre-collapse AVN prior to Ficat and ARCO stage II and Steinberg stage III (Kaushik et al., 2012).

Table 10 Literature review of outcomes of core decompressions stratified by the disease stage at the beginning of the treatment. Failure was assumed when a patients required additional surgery (clinical failure) or the femoral head collapsed.

| Disease Stage      | Failure rate    | Follow up                            | Treatment                                       | Source                                   |
|--------------------|-----------------|--------------------------------------|---|--|
| Ficat I            | 37 (16%) of 227 | Mean 30 months (range, 6-114 months) | Core decompression (pre 1992)                   | Mont, Carbone, et al., 1996 <sup>#</sup> |
| Ficat II           | 84 (35%) of 239 |                                      |   |  |
| Ficat III          | 46 (53%) of 86  |                                      |   |  |
| Ficat I            | 20%             | Mean 63 months (1-176 months)        | Core decompression (1992-2007)                  | Marker et al., 2008 <sup>†</sup>         |
| Ficat II           | 35%             |                                      |   |  |
| Ficat III          | 66%             |                                      |   |  |
| Steinberg IA       | 0 (0%) of 3     | Mean 39 months (2-6 years)           | Core decompression and grafting                 | Steinberg et al., 1999                   |
| Steinberg IB       | 1 (25%) of 4    |                                      |   |  |
| Steinberg IC       | 2 (50%) of 4    |                                      |   |  |
| Steinberg IIA      | 1 (9%) of 11    |                                      |   |  |
| Steinberg IIB      | 3 (33%) of 9    |                                      |   |  |
| Steinberg IIC      | 13 (31%) of 42  |                                      |   |  |
| Steinberg I        | 19 (28%) of 69  | Mean 63 months (23-146 months)       | Core decompression                              | Steinberg et al., 2001                   |
| Steinberg II       | 45 (34%) of 133 |                                      |   |  |
| Pooled I+II A      | 14%             |                                      |   |  |
| B                  | 48%             |                                      |   |  |
| C                  | 42%             |                                      |   |  |
| Steinberg III      | 3 (23%) of 13   |                                      |   |  |
| Steinberg IV       | 45 (49%) of 92  | > 2 years                            | Multiple hole core decompression                | Al Omran, 2013                           |
| Modified Ficat I   | 0 (0%) 6        |                                      |   |  |
| Modified Ficat IIa | 55 (22%) 14     |                                      |   |  |
| Modified Ficat IIb | 6 (46%) of 13   |                                      |   |  |
| Modified Ficat I   | 8 (22%) of 39   | Mean 26 months (4-36 months)         | Multiple hole core decompression                | Song et al., 2007 <sup>§</sup>           |
| Modified Ficat IIa | 15 (23%) of 64  |                                      |   |  |
| Modified Ficat IIb | 4 (24%) of 17   |                                      |   |  |
| Modified Ficat III | 28 (65%) of 43  |                                      |   |  |
| A (<25%)*          | 0 (0%) of 15    |                                      |   |  |
| B (25-50%)*        | 7 (16%) of 44   |                                      |   |  |
| C (>50%)*          | 48 (46%) of 104 | >5 years (4.5-12.2 years)            | Free Vascularised Fibular Grafting <sup>^</sup> | Urbaniak et al., 1995                    |
| Marcus I           |                 |                                      |   |  |
| Marcus II          | 2 (11%) of 19   |                                      |   |  |
| Marcus III         | 5 (23%) of 22   |                                      |   |  |
| Marcus IV          | 17 (43%) of 40  |                                      |   |  |
| Marcus V           | 7 (32%) of 22   |                                      |   |  |

<sup>#</sup>Pooled results from review of 24 studies of a total of 819 hips. <sup>†</sup>Literature review of 2,605 hips from 47 studies. \*Lesion volume estimated with method 4 from (Kim et al., 1998). <sup>§</sup> Retrospective literature review of 163 hips. <sup>^</sup>Usually treatment category on its own.

An overview of the failure rates stratified by the disease stage are presented in Table 10 to illustrate how the stage and lesion extent affect the treatment outcome. Mont et al. (1996) analysed the treatment of 2,025 hips in 42 reports and have compared the failure rates of non-operative treatment and core decompression. While the success rate of non-operative treatment of the hip is about 22.7%, studies have shown a success rate of 63.5% for core decompression (M. Mont et al., 1996). Marker et al. (2008) analysed the clinical failure rates 2,605 hips of 47 studies between 1992 and 2007. The results correlated with Mont et al. (1996) and it was concluded core decompression is a safe and reliable treatment for early stage AVN (Marker et al., 2008).

The treatment success decreased abruptly for later stages of AVN. The high number of failures for Ficat II and Steinberg III hips as well as for hips with large necrotic lesions indicate the need for additional staging criteria to improve the patient selection for core decompression. The evaluation of the fracture risk is paramount to choose an appropriate treatment.

The Ficat stage and the lesion size were significant parameters for the success of the core decompression. Hips with large lesions (Kerboul angle >200°) were more likely to fail (59%) than hips with small lesions (25%) (Marker et al., 2008). Steinberg et al. (1999) came to the same conclusion in two studies (33% for large lesions versus 7% for small lesions (Steinberg et al., 1999); or 42% versus 14% (Steinberg et al., 2001)).

An unsuccessful core decompression required additional surgery after a mean of 29 months (range 3-155 months) (Steinberg et al., 2001). This unsuccessful treatment increases costs and causes avoidable patient suffering.

Concerns about the success of core decompression raised in some studies (Koo et al., 1995), may be a result of not optimally standardised surgical techniques and varying levels of clinical experience. Beside this, patients might have had a more severe form of AVN for example secondary to high doses of steroids and hence the results of these patient groups are not comparable to other studies (M. Mont et al., 1996). The extent of involvement of the head is usually higher in steroid induced AVN.

### **2.3.6.3 Osteotomy**

Osteotomies have been used to shift the collapsing segment of the femoral head away from the principal weight bearing area and to reduce mechanical stress (Hamilton et al., 2009). The femoral bone is cut to change its alignment.

It is used to treat AVN at Ficat stage III and IV (Beaulé and Amstutz, 2004) and to delay or avoid a hip arthroplasty (Sugioka, 1978).

The failure rates stratified by the presented disease stage, lesion extend or location are presented in Table 11.

Table 11 Literature review of outcomes of osteotomy stratified by the presented disease stage or lesion extend. Failure was assumed when a patients required additional surgery (clinical failure) or the femoral head collapsed.

| Disease Stage  | Failure rate  | Follow up                 | Treatment                  | Source                                    |
|--|---------------|---------------------------|----------------------------|---|
| Stage I*   | 0 (0%) of 13  | 30 months (18-50 months)  | Angular osteotomy          | Sugioka, 1978                             |
| Stage II*  | (11%) of 98   | 132 months (3-16 years)   | Angular osteotomy          | Sugioka et al., 1992                      |
| Stage III*   | (27%) of 134  |                           |                            |   |
| Stage IV*  | (70%) of 64   |                           |                            |   |
| Lesion extended to lateral part of the weight bearing surface <sup>‡</sup> | 3 (43%) of 7  | 10 years                  | Varus half-wedge osteotomy | Ito et al., 2012                          |
| Less extend <sup>‡</sup>   | 1 (4%) of 27  |                           |                            |   |
| Lesion extended to lateral part of the weight bearing surface <sup>‡</sup> | 4 (57%) of 7  | 20 years                  |                            |   |
| Less extend <sup>‡</sup>   | 3 (10%) of 27 |                           |                            |   |
| Ficat II   | 1 (33%) of 3  | 57 months (18-106 months) | Sugioka osteotomy          | Dean & Cabanela, 1993 <sup>†</sup>        |
| Ficat III  | 9 (75%) of 12 |                           |                            |   |
| Ficat IV   | 3 (100%) of 3 |                           |                            |   |
| Ficat II   | 1 (16%) of 6  | 11.5 years (5-18 years)   |                            | Mont, Fairbank, et al., 1996 <sup>§</sup> |
| Ficat III  | 8 (26%) of 31 |                           |                            |   |

\*Classification system according to (Sugioka, 1978). <sup>‡</sup>Post-operative lesion extend within the weight bearing area with less or more than 25%. <sup>†</sup>Race was proposed as reason for bad outcomes. <sup>§</sup>Patients were less than 45 years old.

Osteotomy delivers promising results for Ficat stage II and III with small and medium sized lesions (M. A. Mont et al., 1996). However, osteotomy is a technically complex intervention and it may hinder the outcome of a subsequent total hip arthroplasty. Patients with a conversion to a THA face a higher risk of infections and bone defects caused by previous screws and plates can lead to implant loosening (Ferguson et al., 1994).

Dean and Cabanela (1993) suggested that race-dependent differences in the anatomy of the hip capsule may explain why osteotomy is more successful with Japanese patients, as reported by Sugioka et al., than for Caucasian patients as reported by Dean et al.

Important factors for the success of the treatment are race, age, lesion extent but mostly the post-operative lesion location because the purpose of the surgery is to shift the necrotic area within the femur head away from the load-bearing area (Shannon and Trousdale, 2004; Ha et al., 2011; Ito et al., 2012).

#### 2.3.6.4 Joint reconstruction

When the degeneration is too far developed or other treatment options have failed, a hip reconstruction is unavoidable. It is an effective method to restore mobility and to relieve pain especially in an advanced stage where osteoarthritis is present and femoral head-preserving procedures cannot bring any sufficient improvement.

The procedure most often performed is a total hip replacement (THA), but others include bipolar arthroplasty and resurfacing arthroplasty depending on the stage and extent of the disease. A hip replacement is the most frequently performed treatment for AVN with 65% in Japan (Fukushima et al., 2010).

Table 12 Literature review of outcomes of hip replacements stratified by the presented disease stage or lesion extend. Failure was assumed when a patient required revision surgery.

| Disease Stage               | Failure rate     | Follow up                           | Treatment                   | Source                     |
|-----------------------------|------------------|-------------------------------------|-----------------------------|----------------------------|
| Steinberg IIIC<br>(18 hips) | 12 (25%) of 48   | Mean<br>years<br>years)             | Bipolar<br>Hemiarthroplasty | Ito et al., 2000*          |
| Steinberg IVC<br>(23)       |                  |                                     |                             |                            |
| Steinberg VC (7)            |                  |                                     |                             |                            |
| Ficat II, III, IV           | 2^ (2.3%) of 101 | Mean 7.5 years<br>(2.9-10 years)    | Resurfacing<br>arthroplasty | Aulakh et al.,<br>2010     |
| Ficat III, IV               | 0 (0%) of 73     | Mean 8.5 years<br>(7-9 years)       | THA                         | Kim et al., 2011‡          |
| Ficat III, IV<br>Age <50    | 9 (50%) of 18    | Mean<br>years<br>(10-25.4<br>years) | Cemented THA                | Ortiguera et al.,<br>1999† |
| Age >50                     | 8 (11%) 76       |                                     |                             |                            |

\*All hips were symptomatic. Three had a previous osteotomy. No difference between cemented and uncemented implants was found. Failure probability 70% after 15 years. ‡Patients younger than 50 years. Alumina-on-highly cross-linked polyethylene implant. Excluding infection. †Surgery performed between 1969 and 1973. ^Fractured 1 and 50 months after surgery. A Birmingham Hip Resurfacing implant (Smith & Nephew, Warwick, UK) was used.

The stage of AVN has no effect on a treatment with a THA and seems to play only a secondary role for resurfacing arthroplasty (Table 12). Bipolar hemiarthroplasty is not used anymore as a treatment option for AVN because the outcomes are not better than for THA and even resurfacing arthroplasty

shows suboptimal results in some studies (Ito et al., 2000; Mont et al., 2015). Very few hip resurfacings were done in recent years (National Joint Registry, 2015).

As patients with AVN are generally younger and have higher functional demands, THA can be problematic. The durability of THA is dependent on the lifestyle and is limited to around 10-15 years due to wear and osteolysis leading to aseptic loosening. Considering the life expectancy of young patients, they will inevitably face a revision and the results of a revision are generally worse than those of the primary THA (Beaulé and Amstutz, 2004).

Ortiguera et al. (1999) further reported that the mechanical failure rate in patients younger than 50 years receiving a THA have been 79% for AVN and 36% for osteoarthritis after a follow up of 20 years. Complications include infections mostly seen in systemic lupus erythematosus and sickle cell patients, high risk of dislocation, compromise in soft tissue healing and implant loosening, particularly in patients with alcohol abuse (Kaushik et al., 2012). However, more recent studies demonstrate that AVN does not lead to inferior outcomes of total hip arthroplasty with no difference in outcomes compared to patients that were diagnosed with OA (Johannson et al., 2011).

#### **2.3.6.5 Current clinical situation and management of AVN**

Tingart et al. (2004) conducted a survey of 115 German hospitals enquiring what treatment they would recommend for each respective disease stage of AVN (Figure 10). For early stage AVN, 33% of the participants recommended a conservative treatment whereas 53% favoured a core decompression (Tingart et al., 2004).

Another survey of 753 members of the American Association of Hip and Knee Surgeons reported that core decompression was the most common procedure for early stage AVN and total hip replacement was the most common treatment of post-collapse stages (Figure 11) (McGrory et al., 2007).

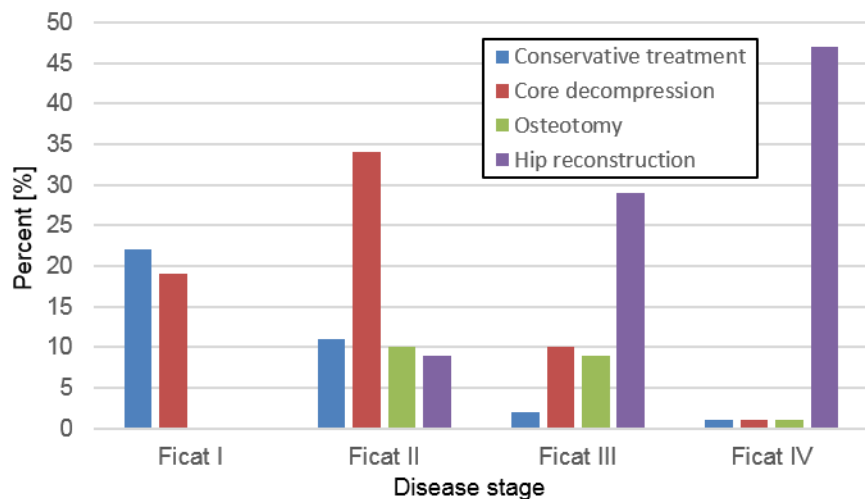


Figure 10 Percentage of hospitals that recommended a treatment for AVN for a respective disease stage. *Data taken from Tingart et al. (2004).*

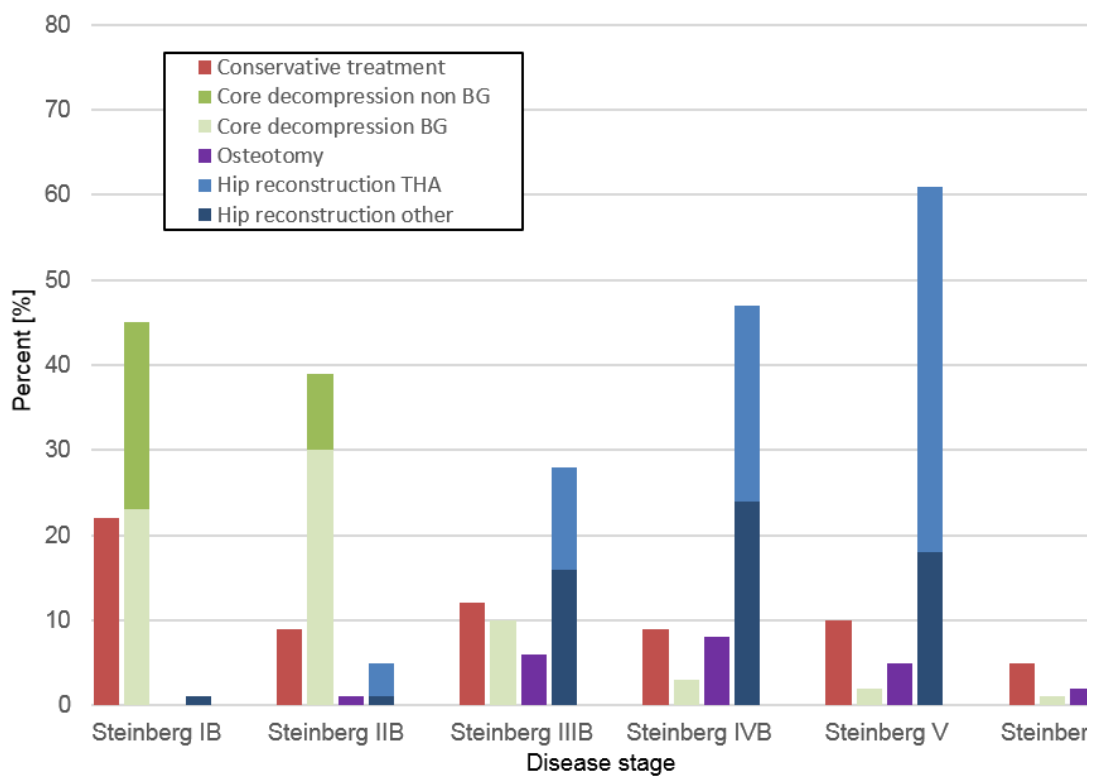


Figure 11 Percentage of surgeons that recommended a treatment for a hypothetical 24 year old patient for different disease stages. BG = bone grafting, THA = total hip arthroplasty. *Data taken from McGrory et al. (2007).*

The huge number of different treatment options for each disease stage indicates that there is a lack of consensus in how to treat AVN and that the current classification systems are not sensitive enough to appoint a potent treatment to a certain disease stage.

Treatment modalities are usually chosen depending on the age of the patient, the extent and location of the necrotic lesion, and whether the femoral head has collapsed (Lieberman et al., 2003). Several treatment recommendations have been reported in the literature (Table 13) however there is currently no standardised protocol for treating AVN.

Table 13 Treatment algorithm according to Ficat and Steinberg classification systems based on literature (M. A. Mont et al., 1996; Lieberman et al., 2003; Beaulé and Amstutz, 2004; Ha et al., 2011; Issa et al., 2013; Mont et al., 2015)

|          | Ficat I<br>Steinberg 0    | Ficat II<br>Steinberg I  | Ficat III<br>Steinberg II  | Ficat IV<br>Steinberg III                               | Steinberg<br>IV                                     | Stein<br>berg<br>V | Stein<br>berg<br>VI |
|----------|---------------------------|--|--|---|---|--------------------|---------------------|
| <b>A</b> | Conservative <sup>1</sup> | CD,<br>Conservative <sup>1</sup><br>Osteotomy <sup>2</sup>             | CD,<br>Osteotomy <sup>2</sup>  | CD,<br>Osteotomy <sup>2</sup> ,<br>THA, HR <sup>2</sup> | Osteotomy <sup>2</sup> ,<br>THA,<br>HR <sup>3</sup> | THA                | THA                 |
|          |                           | CD,<br>Osteotomy <sup>2</sup> ,  | CD,<br>Osteotomy <sup>2</sup>  | CD,<br>Osteotomy <sup>2</sup> ,<br>THA, HR <sup>2</sup> | THA, HR <sup>3</sup>                                | THA                | THA                 |
|          |                           | CD,<br>Osteotomy <sup>24</sup> ,<br>THA <sup>5</sup> , HR <sup>5</sup> | CD,<br>Osteotomy <sup>24</sup> ,<br>THA <sup>5</sup> , HR <sup>5</sup> | Osteotomy <sup>24</sup> ,<br>THA, HR <sup>3</sup>       | THA, HR <sup>3</sup>                                | THA                | THA                 |

<sup>1</sup> Asymptomatic condition, <sup>2</sup> Age < 45 years, <sup>3</sup> Age < 55, <sup>4</sup> Kerboul <200°, <sup>5</sup> Young patient and poor condition; CD = Core decompression, HR = Total hip resurfacing, THA = Total hip arthroplasty.

### 2.3.6.6 Conclusion on current management of AVN

Patient stratification is paramount for a successful treatment of AVN. Guidelines for treatments are based on classification systems but those have various limitations in their current form.

The femoral head usually progresses to collapse in less than 2 years, if the disease is treated ineffectively. The individual fracture risk of a presented femur is important to determine which treatment approach might be successful. Classification systems like ARCO provide an estimate of the given fracture risk based pathologic changes and extent of involvement in the femoral head. Signs of initial fracture on radiographs are a strong indicator for further imminent collapse. Large lesions and lesions located at the weight

bearing surface also point towards an increased fracture risk. However, small lesions can also progress to collapse and are more difficult to predict (Hernigou et al., 2004). Other factors, like the material properties of a necrotic lesion, the lesion shape or biological processes are not considered with current classification systems.

The lack of objectivity, accuracy and repeatability of current systems may also explain the aforementioned disparity of conflicting failure rates reported by different studies for the same treatments. Other reported explanations include age, race, technical factors means to determine the outcome (Steinberg et al., 2001). Pain as a diagnostic factor is also controversial as it is hugely subjective (Belmar et al., 2004; Nam et al., 2008). This “illuminates the need for a more reliable and reproducible classification system” (Smith et al., 1996). The latest classification system was updated in 1993.

Current classification systems appear not to be sensitive enough. Advances to add additional stages to the ARCO classification were deemed to over-complicate the staging system for the clinical environment and were later dropped (Steinberg and Steinberg, 2004). The failure rates of core decompression increase with stage II and III significantly which might be improved with a better patient selection.

## **2.4 Material model to replicate the mechanical response of bone tissue**

### **2.4.1 Measuring material properties of healthy and necrotic bone**

Fracture simulations rely on accurate material properties. Bone is a complex material and the acquisition of reliable material information is challenging.

Cortical bone can be mechanically tested with either three-point bending or tension and compression tests. The Young's modulus of human femoral cortical bone in loading direction is reported as  $18,600 \pm 1,900$  MPa (Cuppone et al., 2004) or  $17,000 \pm 1,700$  MPa (Reilly and Burstein, 1975). A significant difference between tension and compression was not found (Cuppone et al., 2004) and cortical bone has similar tensile and compressive moduli for small deformations (Reilly and Burstein, 1975; Keaveny et al., 1994b). Cortical bone is transverse isotropic which means that it has different moduli in the transverse and longitudinal direction. There is almost a linear decrease in the Young's modulus when changing from an axial to a transverse loading

direction with a reduction of about 55% for the transverse relative to the axial (Wirtz et al., 2000).

Bone is a composite material and can therefore be analysed at macro-, micro- or nano-level. While cortical bone has a relatively solid structure, trabecular bone fracture can be simulated at either continuum or micro-structural level.

A model that considers the micro-architecture of cancellous bone needs material property information of bone at tissue level such as the tissue Young's modulus. These can be measured by mechanically testing individual trabecular struts or by using nanoindentation.

At continuum level, the complex internal structures are not directly considered and the trabecular network is regarded as a solid material. The latter is more commonly used for fracture predictions as simulation of fracture in complex trabecular networks is challenging and requires significant resources. Material properties can be measured by mechanically testing trabecular bone cubes or plugs.

Cancellous bone at continuum level can be described as an inhomogeneous transverse isotropic viscoelastic material. The slope of the stress-strain curve at small strains from mechanical compression tests on bone samples is measured to obtain the Young's modulus. Cancellous bone has similar tensile and compressive moduli (Keaveny et al., 1994a, 1994b).

Reported apparent Young's moduli for cancellous bone are subject to variations among the different research groups, even for identical sites and orientations (Table 14). Reasons for this are multicausal but can include different factors related to the testing protocol used. Uncertainties surrounding mechanical testing of cancellous bone are described in the following section:

### External factors

- Misalignment can cause a Young's modulus reduction of up to 40% because of the anisotropic nature of bone (Öhman et al., 2007). Most studies report the orientation of the tested samples as tested in superior-inferior (S-I) orientation, in dominant trabecular orientation or in loading direction, which diminishes the inter study comparability and increases inaccuracy (Galante et al., 1970; J. Y. Rho et al., 1995; Morgan et al., 2003; Helgason et al., 2008).
- Drying bone tissue has a significant effect on the material properties and should be avoided. Dry bone specimen fracture in a more brittle manner than wet samples which indicates that they can absorb more

energy before failure (Evans and Lebow, 1951; Townsend et al., 1975).

- Platen compression tests are vulnerable to end effect artefacts. Damage at the ends of the specimen and friction at the interface lead to an additional error of about 18% and can be avoided by using cemented end caps (Keaveny et al., 1994b, 1997).
- Keaveny et al. (1993) reported that 5mm cubic bone plugs have a 36% lower modulus due to trabecular defects than cylindrical where the cutting surface is smaller (Keaveny et al., 1993).
- Bone samples stored in a freezer between tests have not been reported to have any changes of material properties. Freezing and repetitive thawing (5 cycles) does not change the Young's modulus of bone tissue significantly (Linde and Sørensen, 1993).

#### Internal factors

- Several load cycles in the assumed linear elastic region can decrease the Young's modulus because of the viscoplastic behaviour of cortical and also cancellous bone (Keaveny et al., 1994b).
- The Young's modulus of cancellous bone is different depending on the anatomical site and the species (Yamada and Evans, 1970; Goldstein, 1987; Morgan and Keaveny, 2001). Even within the proximal femur there are huge regional differences in the Young's modulus (Evans and Lebow, 1951; Nazarian et al., 2007).
- The gaps between the trabecular struts are filled with bone marrow. Bone marrow increases the Young's modulus of the bone only at strain rates above  $10\text{s}^{-1}$ . For low strains (quasi-static) cancellous bone has linear elastic behaviour (Carter and Hayes, 1977). If bone is loaded to failure, it exhibits first elastic behaviour and then plastic failure. While this assumption is widely used, the concept of hydraulic stiffening is however controversial (Kafka, 1983).

Several studies pointed out that the protocol of the mechanical testing of cancellous bone samples has an effect on the measured Young's modulus and a common standard is needed to assure inter-study comparability (Linde et al., 1992; Keaveny et al., 1993).

Table 14 Young's modulus for wet cancellous bone specimens from uniaxial compression tests in SI orientation of the human femoral head.

| Disease state     | Young's modulus   | Sample number | Source                 |
|-------------------|-------------------|---------------|------------------------|
| Healthy bone      | 329 (274–385) MPa | 7             | Nazarian et al., 2007  |
| Healthy bone      | 3230±936 MPa      | 13            | Morgan & Keaveny, 2001 |
| Healthy bone      | 3386 MPa          | 800           | Brown & Ferguson, 1980 |
| Healthy bone      | 445 MPa           | 267           | Brown et al., 1981     |
| Necrotic bone     | 334 MPa*          | 267           | Brown et al., 1981     |
| Osteoporotic bone | 232±130 MPa       | 22            | Haba et al., 2012      |

\*Brown only reported the stiffness of the healthy samples and the necrotic as a reduction of those value in percent. Brown used the terminology stiffness and Young's modulus interchangeably.

While the material properties of 'healthy' bone are widely reported, there is little data available on the material properties of necrotic bone tissue. Cancellous bone is more affected by AVN than cortical bone (Section 2.3.3). Brown et al. (1981) reported that early stage (pre-collapsed) necrotic cancellous bone showed a 59% reduction of the Young's modulus compared to healthy bone. The overall reduction of the Young's modulus of necrotic bone was 72%. The later included pre- and early post-collapse cases of AVN.

An animal study with piglets by Koob et al. (2007) found a reduction of the Young's modulus of 59%, 67% and 80% two, four and eight weeks respectively after ischemia.

Pringle et al. (2004) found a reduction in the stiffness of necrotic bone after two weeks post ischemia in pig femurs by using indentation on the whole femoral head. The stiffness was reduced by 52% compared to controls and 72% after eight weeks.

All three studies reported similar reductions of the Young's modulus for necrotic tissue. The Young's modulus for control cancellous bone samples reported by Brown et al. was significantly lower than values reported by other studies. This might be a result of the test protocol which included the use of cubic bone samples, extremely low strain rates and a compensation for end effect artefacts of the platen compression test.

While measurements of stiffness with indentation on a macro scale found reduced values, a nano-indentation study conducted by Aruwajoye et al. (2013) found increased stiffness for necrotic trabecular, indicating that necrotic bone becomes more brittle at a tissue level. Wang et al. (2014) did not find any difference in the Young's modulus between necrotic and healthy trabecular bone when using nano-indentation. The trabecular structure degrades in necrotic lesions (Wang et al., 2014), which indicates that necrotic bone tissue might be less anisotropic.

#### **2.4.2 Simulating material properties with density-modulus relationships**

When modelling bone, the density or the bone morphology can be used to describe how bone responds to external loads. Bone adapts to the loads under which it is placed by remodelling, a process described by Wolff's law. The trabecular structure has a profound effect on the strength. The morphological characteristics can be described through different parameters including trabecular spacing (Tb.Sp), trabecular thickness (Tb.Th), the density of connectivity (Conn.D), bone volume fraction (BV/TV) and the level of isotropy. A relationship between BV/TV and the Young's modulus has been found in several studies (Galante et al., 1970; Gibson, 1985; Hernandez et al., 2001; Nazarian et al., 2008b), but a reliable material model does not exist at this point of time. This would potentially allow the use of MRI in the future as the trabecular structure can be assessed with micro MRI (Wehrli, 2007) because AVN shows a reduction in the BV/TV (Wang et al., 2014). A characterisation of micro-structure of trabecular also requires high resolution imaging which is not necessarily available in the clinical setting. Therefore most material simulations of bone rely on the density to describe the material properties while acknowledging that other factors have a significant impact on the quality of the bone.

It is widely accepted that there is a density-modulus relationship for bone (Vose and Kubala, 1959; Currey, 1969; Carter and Hayes, 1976; J.Y. Rho et al., 1995; Helgason et al., 2008; Haba et al., 2012). Reported density based

models use empirical relationships between measured apparent densities of bone samples and the respective Young's modulus from mechanical compression tests as described in the previous section.

Apparent density of wet bone tissue is widely used for density-modulus conversion material models. The apparent density is defined as the mass of bone divided by the bulk volume. The 'real', 'true', 'tissue' or 'material' density is defined as the mass of the bone divided by the volume of the bone matrix usually determined by water displacement (Galante et al., 1970). While tissue densities of cortical bone and trabecular bone are quite similar, there can be significant differences between the apparent densities of those two because of the high porosity of trabecular bone.

The density of bone can also be measured from density calibrated CT (QCT) scans which can quantify the mineral content of the bone (Keyak et al., 1994; Kaneko et al., 2003, 2004; Schileo et al., 2008a). A calibration phantom with a known set of different densities is used to correlate linear attenuation or Hounsfield units with bone mineral density (BMD). This produces a linear calibration function.

A density calibration also mitigates differences between different CT scanners so that different studies are comparable. Two types of phantoms are currently used, liquid phantoms (e.g. Potassium phosphate) and solid phantoms (e.g. Hydroxyapatite) (Lindsey and Beaupre, 2009).

Bone density is measured in equivalence to the density of the phantom which cannot perfectly mimic bone attenuation (Schileo et al., 2008a). The conversion to density for two different phantoms can be affected by the tube voltage, the distance to the scanned specimen in the tube and the media that surrounds the specimen (Nazarian et al., 2008a). In four studies the apparent scanner density was correlated to ash density for hydroxyapatite and for potassium phosphate phantoms respectively (Table 15). Ash density is the most reproducible way to measure bone density (Keyak et al., 1994). The ash-density is calculated as ash weight/bulk volume.

Table 15 Empirical relationship between ash density of bone and density measured by a QCT scanner.

| Relationship                                    | Size | Phantom             | Source                |
|---|------|---------------------|-----------------------|
| $\rho_{ash} = 1.06\rho_{QCT} + 0.0389^\ddagger$ | n=36 | Potassium phosphate | Keyak et al., 1994    |
| $\rho_{ash} = 0.290\rho_{QCT} + 806^\dagger$    | n=8  | Hydroxyapatite      | Kaneko et al., 2003   |
| $\rho_{ash} = 0.792\rho_{QCT} + 79.8^\ddagger$  | n=22 | Hydroxyapatite      | Kaneko et al., 2004   |
| $\rho_{ash} = 0.887\rho_{QCT} + 0.079^*$        | n=30 | Hydroxyapatite      | Schileo et al., 2008a |

Densities are in mg/cm<sup>3</sup>. <sup>‡</sup>Trabecular bone, <sup>†</sup>cortical bone, \*pooled trabecular (n=15) and cortical bone (n=15).

Schileo et al. (2008) suggested that the calculated equation is fairly constant for other hydroxyapatite (HA) phantoms, for trabecular and cortical bone, for different anatomical sites and also for bone of different species. Bone diseases were found not to affect the equation (Kaneko et al., 2004). The linear relationship found by Kaneko et al. (2003) appears to be too low compared to the relationship for trabecular and the relationship described by Schileo (2008a). An explanation might be the low sample size of just eight.

As mentioned before, most density-modulus material models are based on the apparent density of wet bone tissue. Several relationships between ash and apparent density are reported in the literature (Table 16). Schileo et al. (2008) suggested that the variations are due to measurement inaccuracies and concluded that their estimated ratio of 0.6 was constant for human femoral bone.

Table 16 Empirical density relationship (ash fraction) for ash and apparent density of bone.

| Ash fraction                             | Deviation     | Bone                                      | Source                   |
|--|---------------|---|--------------------------|
| $\frac{\rho_{ash}}{\rho_{app}} = 0.55^*$ | $R^2 = 0.992$ | Trabecular bone                           | Keyak et al., 1994       |
| $\frac{\rho_{ash}}{\rho_{app}} = 0.658$  | SD = 0.015    | Cortical bone <sup>‡</sup>                | Snyder & Schneider, 1991 |
| $\frac{\rho_{ash}}{\rho_{app}} = 0.522$  | $R^2 = 0.992$ | Trabecular and cortical bone <sup>‡</sup> | Keller, 1994             |
| $\frac{\rho_{ash}}{\rho_{app}} = 0.60$   | $R^2 = 0.990$ | Trabecular and cortical bone              | Schileo et al., 2008a    |

\*Intercept ignored. <sup>‡</sup>Dry bone tissue.

Wirtz et al. (2000) and Helgason et al. (2008) reviewed and normalised several studies which proposed density-modulus relationships finding huge differences between those studies (Wirtz et al., 2000). The differences between the proposed relationships were mainly attributed to the different protocols that were used to test the bone samples (Helgason et al., 2008). The mathematical description of density-modulus relationship of trabecular bone can be postulated in the form of a power law (Carter and Hayes, 1977). The material relationship of cortical bone is mostly expressed as a linear relationship (Cuppone et al., 2004).

Cortical and trabecular bone can be described as two separate mathematical relationships. However, Helgason et al. (2008) proposed the use of a single relationship when modelling bones like the femur because trabecular bone is difficult to discriminate from cortical bone on CT data.

Several regularly cited density-modulus models are shown in Figure 12. Morgan et al. (2003) developed a density-modulus relationship from cancellous bone plugs of human femoral heads and tested those with a robust testing protocol which included cemented caps to avoid end effect artefacts, a strictly defined loading direction and a sufficient low strain rate as discussed in previous Section 2.4.1.

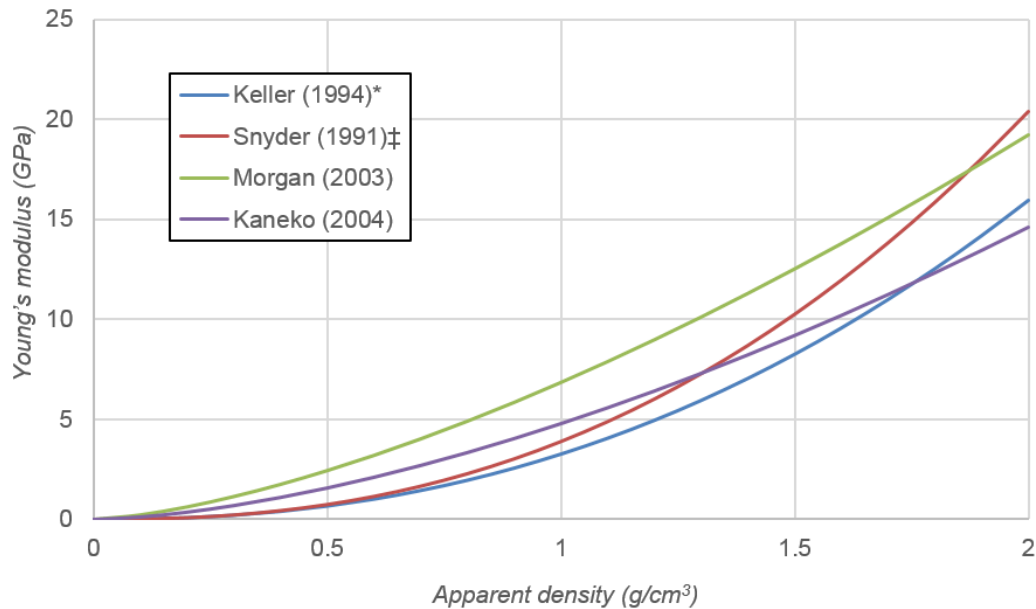


Figure 12 Modulus of elasticity as a function of apparent density as reported across the literature for femoral human bone (Snyder and Schneider, 1991; Keller, 1994; Morgan et al., 2003). \*Pooled trabecular and cortical bone, ‡Cortical bone from the tibia. Apparent density was calculated from ash density using the relationship described by Schileo et al. (2008a).

AVN most commonly affects Asian populations. Asian populations are believed to have a lower bone mineral density compared to Caucasians while having similar or even lower fracture risks. It has been suggested that Chinese have a more efficient microstructural skeletal organization (Liu et al., 2011). A density-modulus material model would have to account for such differences. On the other hand, smaller bone size and lower bone density might also be compensated by differences in hip geometry and lower body weight (Cong and Walker, 2014). The material model would be still valid for these.

The Young's modulus increases significantly with age while mechanical strength and bone density are reduced. This indicates bone fragility as bone becomes more brittle especially among the age group of over 70 years. AVN mostly affects patients between 20-50 years (Section 2.3.1). Density and Young's modulus are relatively stable among this age group (Havaldar et al., 2014).

To the authors knowledge there is only one study that presented a density-modulus model for porcine cortical femoral bone (Bonney et al., 2011) despite porcine bone being widely used as a substitute for human bone in research to validate fracture simulations.

The density-modulus relationship allows the mapping of the Young's modulus within the femur which can be used to calculate the stress in bone. Each voxel of the three-dimensional CT-data can be assigned to a Young's modulus value based on the grey value.

While most clinical CT scanners have a resolution of no higher than about 1mm<sup>3</sup> per voxel, micro computed tomography ( $\mu$ CT) and high resolution peripheral quantitative computed tomography (HRp-QCT) can accurately visualise the trabecular structure. The mean thickness of trabeculae in the proximal femur is 120 $\mu$ m (Fazzalari and Parkinson, 1996).

Continuum and trabecular level CT scans need to be distinguished. In high resolution scans, the density of a voxel containing a trabeculum is close to the density of cortical bone (Carter and Hayes, 1977) while in low resolution scans, a voxel contains a mixture between bone and air or soft tissue. There are two ways to solve this problem. The resolution of the scan can be reduced artificially or a single material relationship is needed that covers the entire spectrum of densities including the gap between trabecular and cortical bone.

The correlation of the shear modulus (G) with density was investigated by Knauss (1981) who concluded that the shear modulus was not dependent on the density and the value for the shear modulus was around 40MPa for a density range of 0.3-0.7 g/cm<sup>3</sup>. The values were however different from results found by Reilly and Burstein (1975) of about G=3,280MPa for compact bone. Ford et al. (1996) did not find a relationship between the shear modulus and the apparent density for trabecular bone in the bovine tibia.

The density-modulus material model can possibly be applied to osteonecrotic bone tissue. In an animal study, Bobechko & Harris (1960) reported an increase of the apparent density of the trabecular bone when affected by AVN. In an attempt to heal necrotic bone tissue, these areas are encased by a layer of sclerotic tissue which translates into an increased measured density. Hence necrotic areas would have significantly reduced material properties while having an increased bone mineral density which would make the application of a density-modulus relationship impossible. An increase of the bone density for necrotic bone was also reported by Brown et al. (1981). However, these two studies relied on plain radiographs where the distinction between the sclerotic rim and the necrotic lesion is difficult. As previously described, there is a formation of a sclerotic rim around the necrotic lesion but repair inside the lesion is interrupted because vascular structures cannot penetrate inside the lesion and the lesion contains fibrous tissue with a low mineral density. A density-modulus relationship can therefore be used despite a density increase

at the periphery of the necrotic lesion as the lesion itself is exposed to decalcification leading to a low mineral density (Ficat, 1985; Koob et al., 2007; Wang et al., 2013, 2014).

A density-modulus material model should only be used with extreme caution, once fracture in the femoral head occurred as collapse of bone leads to an increase of the apparent density because of compressed structures. Crushed trabecular have densities similar to that of cortical bone but have very low Young's moduli and strength. At a post-collapsed stage, the modelling of bone by using a density-modulus relationship is no longer valid and other methods need to be considered. The use of a segmented bone model consisting of two materials, healthy and necrotic bone, would be an alternative. The material properties of the necrotic bone tissue can be assigned based on a set of empirical modulus data which was described in this chapter. A limitation of such a model is that the creation of segmented models is time consuming and it would be impossible to differentiate femoral heads with necrotic lesions that occupy large parts of the femoral head.

#### **2.4.3 Comparing isotropic and transversely isotropic material assignments on fracture simulations**

Bone is an inhomogeneous material with material properties varying depending on the loading direction. Cortical bone is transversely isotropic (Reilly and Burstein, 1975). Turner and Cowin (1988) concluded based on material properties retrieved from literature that trabecular bone is truly orthotropic while cortical bone exhibits transversely isotropic behaviour. Orthotropy is a type of anisotropy in which the internal structure of the material creates unique elastic properties along each of the three orthogonal axes of the material (three elastic and three shear moduli and six Poisson's ratios) (Richmond et al., 2005). However several more recent studies have found transversely isotropic behaviour for trabecular bone (Ford et al., 1996; Öhman et al., 2007).

The overall consensus of several finite element analysis studies is that fracture simulations using an isotropic model produce sufficiently good results (Huiskes, 1982; Peng et al., 2006). Peng et al. (2006) analysed 72 finite element models and concluded that isotropic and orthotropic models do not differ significantly when simulating both double and single leg standing. Other critical loading scenarios such as heel strike have unfortunately not been considered in the study.

Huiskes (1982) found that a beam model based on linear elastic homogeneous and transversely isotropic material behaviour for long bones delivers an excellent agreement between results and theoretical predictions. However, he concluded that even an isotropic model delivers sufficient results when just analysing axial stresses.

The method by which strains can be calculated from stresses is dependent on whether bone is assumed to be isotropic or transverse isotropic. The relationship can be described in form of the elasticity tensor by using Hooke's law.

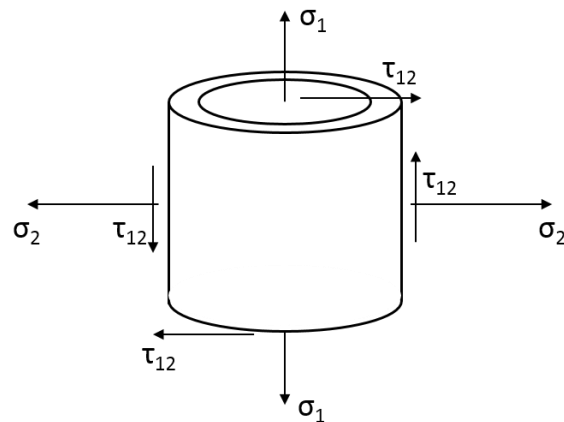


Figure 13 Schematic of the stress components acting on a femoral shaft segment.

If the bone segment in Figure 13 is of isotropic material, plane stress and strain can be correlated using the stiffness matrix (2.2):

$$\begin{bmatrix} \sigma_1 \\ \sigma_2 \\ \tau_{12} \end{bmatrix} = \begin{bmatrix} E & Ev & 0 \\ Ev & E & 0 \\ 0 & 0 & G \end{bmatrix} \begin{bmatrix} \varepsilon_1 \\ \varepsilon_2 \\ \gamma_{12} \end{bmatrix} \quad 2.2$$

$E$  is the Young's modulus,  $G$  is the shear modulus,  $\sigma$  is tensile stress,  $\tau$  is shear stress,  $\varepsilon$  is strain,  $\gamma$  is shear strain and  $v$  is the Poisson's ratio.

If bone is assumed to be transversely isotropic material, equation (2.3) needs to be used:

$$\begin{bmatrix} \sigma_1 \\ \sigma_2 \\ \tau_{12} \end{bmatrix} = \begin{bmatrix} \frac{E_{11}}{1 - v_{12}v_{21}} & \frac{E_{11}v_{21}}{1 - v_{12}v_{21}} & 0 \\ \frac{E_{11}v_{21}}{1 - v_{12}v_{21}} & \frac{E_{22}}{1 - v_{12}v_{21}} & 0 \\ 0 & 0 & G_{12} \end{bmatrix} \begin{bmatrix} \varepsilon_1 \\ \varepsilon_2 \\ \gamma_{12} \end{bmatrix} \quad 2.3$$

#### 2.4.4 Poisson's ratio

The Poisson's ratio is small for cancellous bone samples because it is plastic compressible material (Knauss, 1981). When compressing cancellous samples there is no bulging out laterally because trabecular material can expand into existing voids within the bone. Yielding of trabecular bone involves micro-structural damage of individual trabeculae (Keaveny et al., 1994a).

Knauss et al. (1981) found a Poisson's ratio between 0.26 and 0.38 for cortical bone and 0.01 and 0.34 for trabecular bone (Figure 14). No relationship to the density was observed. He further emphasised that a mathematical relationship between Young's modulus, shear modulus and Poisson's ratio based on Hook's law (Eq.2.4) for isotropic material are not valid for trabecular bone. They therefore oppose an assumption which is valid for homogeneous isotropic linear elastic materials.

$$E = 2G(1 + \nu) \quad 2.4$$

Reilly et al. (1975) found slight but insignificant anisotropy with a Poisson's ratio of 0.46 for the loading orientation and 0.58 for the transverse axis. Brown et al. (1981) did not find a significant difference between the Poisson's ratio of necrotic and healthy bone.

Turner et al. (1999) concluded that the Poisson's ratio hardly affects the calculated Young's modulus and that bone tissue can be therefore assumed to be isotropic with an Poisson's value of 0.3. This is in accordance to several studies which also assumed isotropic cortical and trabecular bone with a single Poisson's ration of close to 0.3 (Mourtada and Beck, 1996; Wirtz et al., 2000; Homminga et al., 2001; Schileo et al., 2008b; Szabó et al., 2011).

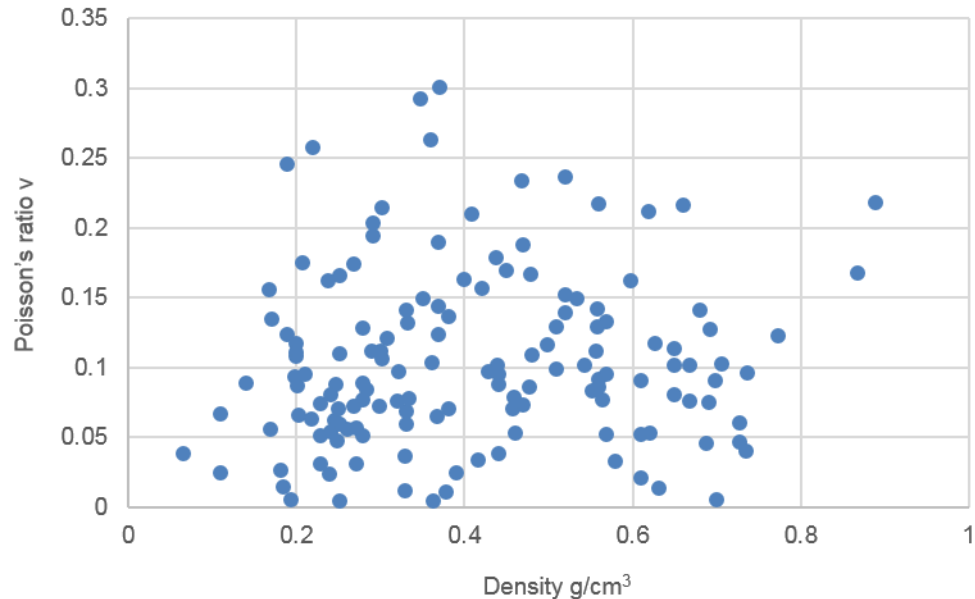


Figure 14 Dependency between Poisson's ratio and density for dry defatted trabecula bone samples. No relationship to the density was observed. *Data reproduced from Knauss et al. (1981).*

#### 2.4.5 Failure criterion for bone fracture simulations

An engineering failure criterion can be used when bone is modelled at a continuum level. Local fracture of bone can be modelled with a failure criterion based on either stress or strain. If the bone exceeds the previously defined critical value, failure can be assumed. As all previously described assumptions for simulating bone behaviour are only valid for the linear elastic part, failure can be assumed at the yield point (Whealan et al., 2000). For a fracture prediction tool this is a conservative approximation as it does not reach the ultimate fracture constraint.

All failure criteria allow the comparison of stress or strain from a complex three-dimensional loading scenario with the critical stress ( $\sigma_y$ ) or strain ( $\epsilon_y$ ) that can be obtained by a simple uniaxial mechanical tests.

The maximum principal stress criterion (Rankine criterion) compares the maximum principal stress of a multiaxial stressed material with the yield stress from a uniaxial tensile or compression test (Eq.2.5). The calculated stress is vulnerable to underestimation because only the maximum principal stress is compared and therefore, depending on the loading situation, this failure criterion is usually inferior to the von Mises yield criterion.

The von Mises yield criterion allows the comparison of stress from three-dimensional loading scenarios, which includes normal and shear stresses in

three dimensions, to the critical stress that can be obtained by uniaxial tensile tests (Eq.2.6). It is dependent on Hook's law. The von Mises criterion has the capability to account for anisotropic bone properties as its stress invariants can be used with any elastic material type (von Mises, 1928; Savvidis and Stabrey, 1997).

The maximum principal strain criterion (Saint-Venant) postulates that material under multiaxial straining yields when the principal strain of the greatest magnitudes equals the critical strain under uniaxial conditions (Eq.2.7).

Table 17 Mathematical description of failure criterions

| Failure criterion |  |     |
|-------------------|--|-----|
| Rankine           | $\sigma_y = \sup( \sigma_1 ,  \sigma_2 ,  \sigma_3 )$  | 2.5 |
| von Mises         | $\sigma_y = \sqrt{\frac{1}{2}[(\sigma_1 - \sigma_2)^2 + (\sigma_2 - \sigma_3)^2 + (\sigma_3 - \sigma_1)^2]}$                                       | 2.6 |
| St Venant         | $\varepsilon_y = \sup( \varepsilon_1 ,  \varepsilon_2 ,  \varepsilon_3 )$ with $\varepsilon_1 = \frac{1}{E}(\sigma_1 - \nu\sigma_2 - \nu\sigma_3)$ | 2.7 |

Keaveny et al. (1994) were one of the first to suggest that a strain based failure criterion might be more powerful to simulate bone fracture than a criterion based on stress (Keaveny et al., 1994b). Several FE studies suggested that a strain based failure criterion provides the best way to simulate bone fracture (Lotz and Hayes, 1991; Keaveny et al., 1994b; Yamashita, 1996; Schileo et al., 2008b). Yield strain is independent from apparent density, Young's modulus and trabecular orientation and therefore behaves isotopically (Ford et al., 1996; Keaveny et al., 2001; Schileo et al., 2008b; Pankaj, 2013).

Morgan et al. (2001) found that yield strain is dependent on the anatomical site however yield strain is similar for cancellous and cortical bone (Keaveny et al., 2001). Lotz et al. (1991) successfully used a strain based failure criterion based on von Mises whereas Keyak et al. (2000) found less favourable results. The discrepancy can be explained by limited strain prediction accuracy in the models used (Schileo et al., 2008b).

#### 2.4.6 Conclusion on material model

A density-modulus material model provides an appropriate method to retrieve Young's modulus information from femoral bone *in-situ*. BMD measurements from different types of calibration phantoms are not interchangeable, unless a

cross-calibration calculation is performed. An isotropic material model delivers sufficient results for models that are axially loaded. A strain based failure criterion can be used to predict bone fracture. Further investigations are needed to confirm if the material model is also valid for pre-collapsed necrotic trabecular bone despite denser bone tissue at the lesion interface from early repair.

## **2.5 Finite element analysis for avascular necrosis**

Finite element analysis (FEA) is an engineering tool to simulate the behaviour of structures. Some studies analysed the fracture risk of AVN affected femoral heads (Brown et al., 1981; Anderson, 2015) and also multiple studies compared the accuracy of FE with beam theory though not for AVN (Huiskes, 1982; Mourtada and Beck, 1996; Anez-Bustillos et al., 2014; Oftadeh et al., 2016). FEA and beam theory analysis are two methods in direct competition when simulating material behaviour. Each method has its advantages and disadvantages. While FEA is more accurate, beam theory is less complex and therefore has the potential to be used in the clinical environment (Whealan et al., 2000). While many key steps are similar such as image processing and loading directions, FEA would need to include more bone to avoid boundary constraint affects and partial volume effects. The generation of simplified loading conditions is non-trivial in FEA and requires greater user input. Patient-specific micro-FE models based on high resolution tomographic scans come with a significant computational expense (Van Rietbergen et al., 2003).

## **2.6 Beam theory approaches to simulate the mechanical behaviour of the femur**

### **2.6.1 Introduction**

Pauwels (2012) calculated the magnitude of the load acting on the proximal femur during the single leg stance phase of walking based on simple mechanical considerations. The bodyweight (BW) minus the weight of the bearing leg acted on the centre of gravity, the location which was described by Fischer (1900). The centre of the femoral head was assumed to be the centre of rotation of the joint. The abductor force (M) balanced the moment caused by the body weight creating an equilibrium around the hip. The resulting joint force (R), which acted on the centre of the femoral head, reacted against the bodyweight and the muscle force and formed an angle of 16°

medial to vertical. This biomechanical model based on the equilibrium approach is consistent with the aforementioned approaches.

After calculating the load acting on the femoral head, by regarding the human skeleton as system of cantilevers and joints, Pauwels analysed stress within the proximal femur with engineering means, namely strength of materials. When calculating the stress distribution within the femoral neck, the joint contact force can be divided into a bending (S) and a compressive (C) load component (Figure 15). Shear stress was neglected. Pauwels assumed a linear stress distribution within the neck and did not consider the inhomogeneous anisotropic nature of bone. The shear force remained constant for the length of the neck as it only depended on the inclination of the resultant force (Pauwels, 2012).

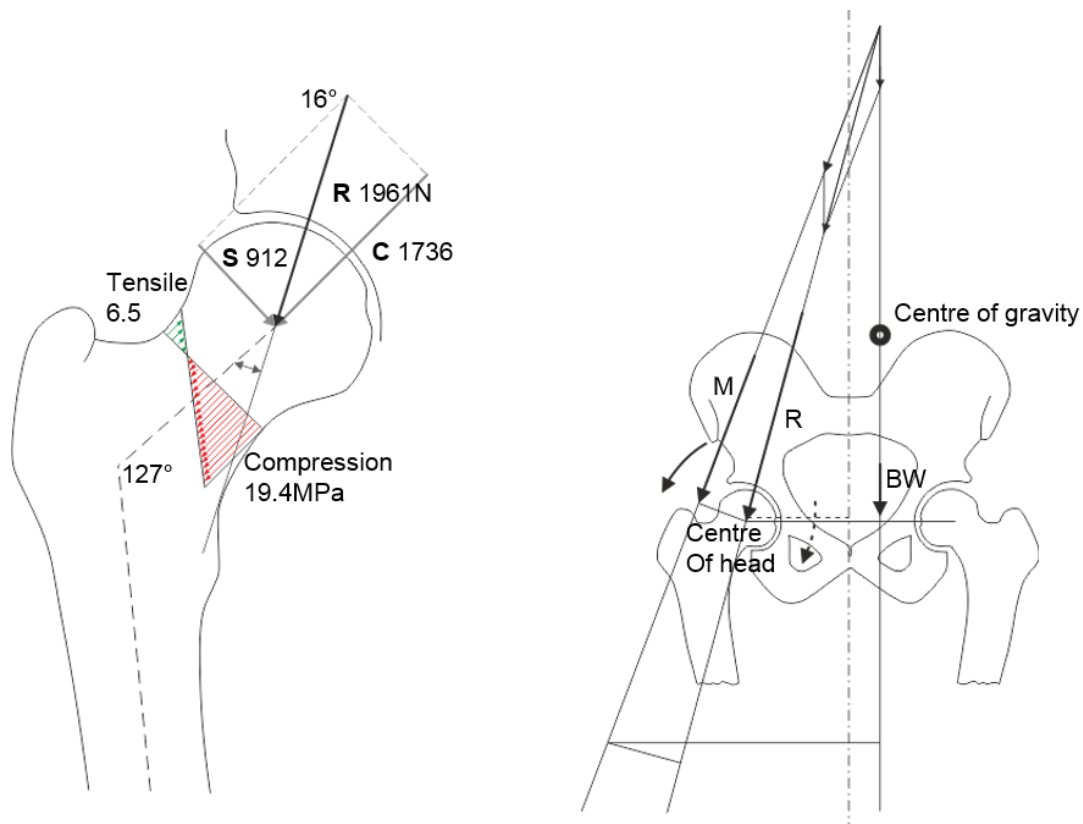


Figure 15 Loading of the upper end of the femur during walking according to Pauwels (2012). The stress distribution within the femoral neck was calculated from compressive and bending load components of the resultant joint contact force (**R**) which acted towards the centre of the femoral head. **R** balances the bodyweight (**BW**) and the muscle force (**M**).

Pauwels (1965) illustrated the different type of stresses within the proximal femur as well as the fracture risk of the bone with a simple model of beams (or columns) (Figure 16). If a beam is loaded with a force, stress occurs within

the beam. There is a correlation between the magnitude of the load, the cross-sectional area and the stress. When the load is increased to a level where the stress reaches its yield threshold, fracture starts to occur. The axial compression stress is equally distributed throughout an imaginary cross-section of the beam.

If the same load is eccentric, this induces bending stress in addition to the same amount of compression stress. Depending on the lever arm, bending causes additional compressive and tensile stresses. Bending stress is superimposed on the compression stress. The stress distribution of a beam cross-section is no longer equally distributed due to the bending stress. When estimating the fracture risk, the stress distribution within the beam is irrelevant because fracture at a single point of the beam leads to fracture of the entire structure. The highest magnitudes of stress are found at the periphery of the beam. Bending can cause high magnitudes of stress hence Pauwels concluded that the formation and construction of bone tries to avoid bending at macro scale (Pauwels, 1965).

Shear stress occurs when the beam is loaded with a transverse force (Pauwels, 1965). Stretching due to shear is 30% greater than through tension and therefore bone tries to avoid shear stress with a smart trabecular structure (Pauwels, 2012).

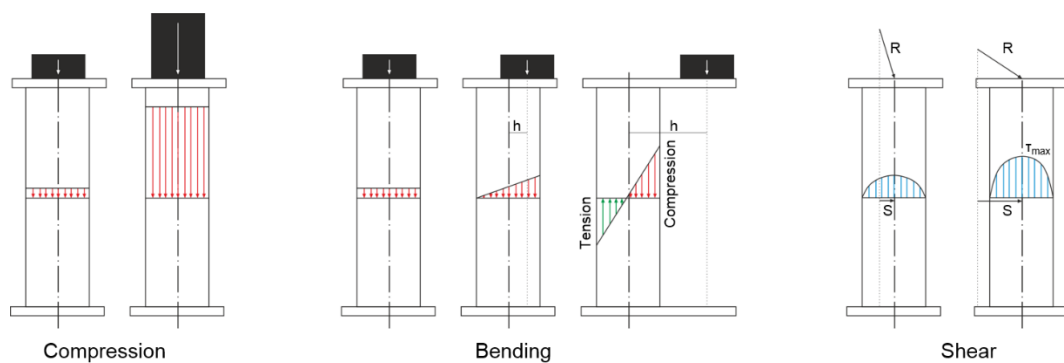


Figure 16 Pauwels (2012) explained the different types of stress that occur in the femur in form of a simplified column model. The femur is subject to compression, bending and shear stress. *Figure adapted from Pauwels et al. (2012).*

## 2.6.2 Formulated theories

Similar to beams having the mechanical function to support the structure of a building, bones provide structural support for the human body (Toridis, 1969).

Beam models have been used to describe of load bearing capacity and deformation of the femur. The stress and deflection of beams can be calculated using beam theory. Two beam theories are commonly used, Euler-Bernoulli (Euler, 1759) and Timoshenko (Timoshenko, 1922).

Euler-Bernoulli beam theory is a simplification of the linear theory of elasticity. Firstly, it is assumed that cross-sections perpendicular to the beam axis stay plane and perpendicular to the axis after deformation. Therefore it does not account for transverse shear strain, which is the major difference between Euler-Bernoulli and Timoshenko. Secondly, deformations are small and lastly, the material of the beam is assumed linear elastic and Poisson's ratio effects are ignored. The beam is straight slender and any taper must be slight.

Timoshenko beam theory is an alteration of Euler-Bernoulli accounting for shear deformations which makes it particularly suitable for short beams. A beam is often described as a prismatic slender body. In both theories, the material is assumed to exhibit linear elastic behaviour, it is either isotropic or orthotropic and the material is homogeneous across the cross sections.

The femur can be modelled as an Euler-Bernoulli beam loaded with a joint contact force. Shear stress is maximum along the neutral axis of the beam while bending stress reaches its maximum at the surface of the beam element. Fracture is usually observed to occur at the bone surface and therefore the bending influence is much larger than shear. Therefore, Huiskes (1984) argued that transverse shear stress is negligible.

The shear modulus would be required to analyse the influence of shear stress on the femur model. As described in the previous section, the shear modulus cannot be retrieved from CT-images as there is no density-modulus relationship and therefore the modulus would have to be approximated.

### **2.6.3 Studies using beam theory to analyse stress within the femur**

The following section gives an overview of different studies that estimate load transfer within the bone by using beam theory.

Koch (1912) used a beam theory similar to the theory described by Timoshenko to analyse the internal stresses of a femur. He assumed a two-dimensional curved beam axis for the proximal part and a straight beam axis for the rest of the femur. Because tomographic imaging was not available at that time, he sectioned a human cadaveric femur into 75 slices with slices perpendicular to the assumed beam axis in order to get geometric information

of the beam cross-sections. The beam axis was approximated so that it passed through the maximum number of centres of gravity of the cross-sections. A set of material properties for bone was assumed. The femur was loaded with a single joint contact force of 0.7 times body weight but muscle forces were not considered in the femur model (Koch, 1917). Koch's biomechanical model was not sufficient to represent the reality of femur loading. The assumed loading for a single leg stance was far too low because muscle forces were ignored. This also led to low stress magnitudes in the trochanter area and the shaft.

Toridis (1969) calculated internal stresses of the femur for different loading situations. He also neglected muscle forces but acknowledged them in his paper for certain loading conditions. Standard beam theory was adjusted to account for the curved shape of the femur. The femur was modelled as curved member in three dimensions subjected to compression, bending and shear forces (Toridis, 1969).

Rybicki et al. (1972) added muscle forces to Koch's beam model in order to analyse their effect on the resulting stresses and strain energy during a one-legged stance. They concluded that while beam theory is useful to calculate the stresses in the shaft, it gives inaccurate results in the regions of the greater trochanter and the femoral head because of the complexity of the shape. They questioned whether cross-sections remain plane when loaded and if shear deformation can be neglected as the cross-sectional shape is changing rapidly in the femoral head (Rybicki et al., 1972). Rybicki did not adjust the beam axis to account for the shape of the femoral head and its loading. The joint load was simplified with a single load that pointed towards the centre of the femoral head. The beam axis for the head followed the neck axis of the femur passing through the centre of the head up until the surface of the bone near the fovea. The part of the beam that modelled the apex of the femoral head was therefore not loaded and the predicted stress for half of femoral head was zero.

Huiskes et al. (1981) also reported that beam theory is mostly accurate for the femoral shaft. The results from beam theory were compared to measured results obtained by using strain gauges on an *in-vitro* loaded cadaveric femur. They concluded that the disparity between calculated and experimental results were due to simplifications in their model. They further concluded that bone can be assumed isotropic with good approximation when no torsion is considered, and it can be assumed transversely isotropic when torsion is considered. Geometric information was obtained by physically cutting the bone along the assumed beam cross-sections (Huiskes et al., 1981).

Raftopoulos et al. (1987) published a mathematical method to calculate stress and strain in a femur with a three-dimensional curved beam model. They considered that the cross-sectional shape is not axisymmetric which has an impact on how the bending stress is calculated (Raftopoulos and Qassem, 1987).

Salathe et al. (1989) also used a beam model curved in three dimensions but not for the femur. They analysed compression, bending, shear and torsion.

Beck and Ruff (1990) were one of the first research groups that deployed radiologic imaging techniques to retrieve sample specific material and structural properties for fracture simulations based on beam theory. Areal bone mineral density data from dual-energy X-ray absorptiometry (DEXA) scans in combination with a material conversion model where used to calculate the failure loads with a straight beam model in two dimensions. The stress within the femoral neck was analysed for a one legged stance with a single joint contact force.

Mourtada et al. (1996) improved this method based on DEXA and extended it to the whole proximal femur using a curved beam axis. An approximation of Timoshenko's beam theory was used in which in-plane distortions were ignored. The difference between the centroidal axis and the neutral axis for curved beam was considered. Beam curvature causes the neutral axis to shift away from the centroidal axis. It was concluded that torsion and shear can be neglected as they were small compared to principal stresses at the bone surface for compression and bending (Mourtada and Beck, 1996). The research group validated this method by successfully predicting the failure loads of 22 cadaveric femurs ( $R^2=0.91$ ) (Beck and Mourtada, 1998).

DEXA can only measure the profile of the beam cross-sections as it is a two dimensional imaging method. Therefore it cannot account for the cross-sectional geometry which is essential for an application of beam theory that correlates the measured material and structural properties with the failure load. Other limitations are that cortical and trabecular bone cannot be distinguished so that a single empirical density-modulus material model is necessary. Finally, the bending stiffness for the femur can only be calculated in the frontal plane because acetabular bone would compromise the calculation. In contrast, QCT scans can show the actual cross-sectional plane and adjacent bone structures and soft tissue can be segmented.

Snyder et al. (2004) used volumetric bone mineral density data from QCT scans to predict the fracture loads of ten cadaveric proximal femurs with

artificial defects *in-vitro*. They used experimental data from Tanck et al., (2009) for their validation. A single legged stance was simulated experimentally to compare experimental with computational results. Only bending and compression were considered. It was further assumed that bone fails at a constant strain independent of the density. The cross-sections were assumed to be axisymmetric. A strain based failure criterion was used to calculate the fracture load of each cross-section. The cross-section with the lowest fracture load was assumed to govern the failure of the entire bone. Their beam model was able to accurately predict sites of fracture. The beam axis was a two dimensional curved beam. The material in each cross-section was homogenised for the beam calculation (Snyder et al., 2004).

In an clinical study, Snyder et al. (2006) predicted the fracture risk of 20 patients with benign skeletal lesions in the femur based on axial, bending and torsional stiffness. Axial stiffness is a measure of resistance to uniaxial tensile or compression loads, bending stiffness is a measure of resistance to bending moments and torsional stiffness is a measure of resistance of the bone to torque. Hong et al. (2004) described a strong relationship between the reduction of experimental failure loads and the reduction of measured axial ( $R^2=0.95$ ), bending ( $R^2=0.91$ ) and torsional ( $R^2=0.91$ ) rigidities of whale trabecular bone. Based on these findings, the stiffness of the weakest cross-sections of the lesion affected femur was compared to the stiffness of the matching opposite healthy femur to identify whether that femur had an increased fracture risk. The bending and torsional stiffness had a higher predictive capability with 97% accuracy than established clinical diagnostic methods based on the relative size of the lesion measured on plain radiographs. This study used an indirect way of predicting the reduction of the failure load without explicitly calculating the fracture load using the beam equation. Together with the geometric information, the rigidities can be used to calculate the stresses, strains and also fracture loads for a given failure criterion.

Anez-Bustillos et al. (2014) compared the capacity of beam model analysis with FEA to predict fracture loads in femoral bone. Instead of using the beam equation based on Euler-Bernoulli to directly calculate the failure load of each femur, he used the underlying axial and bending stiffness to predict fracture. The beam axis was straight and collinear with the long axis of the bone even for the intertrochantic area of the femur. The cross-sections were perpendicular to the beam axis. The axial and bending stiffness of the weakest cross-section of a femur sample were calculated. A mathematical relationship

between the *in-vitro* fracture loads and the axial and bending stiffness was developed using the same experimental data as Snyder et al. (2004). Anez-Bustillos et al. finally concluded that axial and bending stiffness were similarly effective compared to FE in predicting fracture. However, there was no correlation between *in-vitro* and predicted loads if the fracture loads were directly calculated based on beam theory (Oftadeh et al., 2016). The loading of the femur and its shape is complex and therefore the proximal femur cannot be approximated with a straight beam axis. Therefore, the use of a straight beam axis and the lack of calculating specific fracture loads based on engineering principals must be seen as a step back compared to the method previously described by Snyder et al. (2004).

A recent study by Oftadeh et al. (2016) addressed the deficiencies of the study by Anez-Bustillos et al. (2014). Critical stresses within the proximal human femur were calculated by using curved beam theory in two flexural dimension. A total of 20 femurs were tested. The beam axis had no curvature except in the frontal plane. They reported that the curved beam outperformed the method proposed by Anez-Bustillos et al. (2014) and it further provided a magnitude of the failure load based on beam theory. They reported a high correlation between predicted and tested failure loads ( $R^2=0.87$ ). The mean difference was -385N with a standard deviation of 888N at a mean fracture load of the femur of  $5790\pm2685$ N. An iterative approach was used to determine the location of the beam axis by using the trajectory of all modulus weighted centroids. This reduced the disparity between the beam axis, which determines the slicing direction, and centroidal axis, which is the location where no bending stress occurs.

#### **2.6.4 Discussion**

Beam theory methods have been evaluated both clinically and against the results of cadaveric experiments. Oftadeh et al. (2016) reported excellent results for their approach using a curved beam. However, for a clinical application the biomechanical model needs to be amended to account for muscle forces. It remains to be determined, whether it is also successful in prediction of fracture *in-vivo*. A study by Yang et al. (2014) compared the effectiveness of beam theory and FE to predict hip fracture in a study of 204 postmenopausal women. While FE performed best, none of the models could predict the fracture risk during sideways fall (Yang et al., 2014).

Most studies report significant differences in magnitude of stress throughout the femur. This contradicts Wolff's hypothesis that bone adapts to the loads

under which it is placed. Bone would be a poor construction wasting material and weight. Pauwels described such a prospect as “ridiculous” (Pauwels, 2012). Not in all studies can this be explained with the negligence of muscle forces and only looking at certain load cases. When ignoring the abductor forces, the greater trochanter is still analysed for the hip contact force while not supporting the loaded structure at all. This might give an incorrect sense of safety where bone is already compromised.

Beam theory analysis is usually chosen because of its simplicity compared to more complex FEA (Whealan et al., 2000). This necessitates several simplifications for the loading, the material and the geometry of the femur. Most studies used static loading to simulate a single leg stance. Dynamic loading that occurs during a gait cycle is impossible to simulate with beam theory. However the loading situation can be replicated at different states of the cycle. Beam theory analysis assumes homogenous material properties within a beam cross-section and that the cross-sections remain in plane after bending. Shear deformation is neglected in an Euler-Bernoulli beam, an assumption of most beam theory models. Huiskes et al. (1981) found that an axisymmetric approximation of the shape of the femur cross-section in order to calculate bending stress is reasonable. It is tempting to simplify the complex loading of the femur down to a beam with joints at both ends. However this model is biomechanically not realistic considering that the femur has a complex shape with multiple muscle attachments. Therefore, the beam model can only be successful in predicting fracture for a certain pre-defined and verified setting.

There is currently no study that has looked at the use of beam theory to simulate AVN nor has used beam theory to analyse the strength of the subchondral region of the femoral head affected by lesions. The assessment of the fracture risk can be improved by using a combination of density-calibrated computed tomographic (QCT) imaging and engineering beam theory. The beam axis can be adjusted to better account for the shape of the femoral head and its loading which was a limitation of previous studies.

## 2.7 Summary

The literature has shown that AVN, if left untreated, follows a typical pathology by progressing to collapse of the articular surface which leads to osteoarthritis of the hip joint. The extent of involvement as well as the lesion shape and location have a huge influence on the fracture risk. Femoral heads with a low

fracture risk have shown a high chance of success when treated with a joint sparing treatment. On the other hand, femoral heads with an immediate fracture risk should be treated with a THA. A prolonged unsuccessful conservative treatment is costly and causes the patient suffering.

The literature showed that patient stratification is important for choosing the right treatment option with the best clinical outcome. Current classification systems are not sufficient for this task as they have poor differentiation and reproducibility. This becomes apparent when looking at the high failure rates of joint-sparing treatment options especially for pre-collapsed AVN. There is a currently unmet need for a robust method to determine fracture risk in AVN at a stage before the destruction of the articular surface.

Patient specific fracture simulations of the femoral head can be based on tomographic imaging. Although MRI is currently the gold standard to diagnose pre-collapsed AVN, CT allows analysis of the material properties of bone tissue *in-situ* by using an empirically derived density-modulus material model. Necrotic lesions show decalcification of trabecular bone and therefore the model possibly remains valid for pre-collapse AVN. Reported density-modulus conversion models show huge variations dependent on the anatomical site and the test protocol used. The relationship proposed by Morgan et al. (2003) appears to be reliable because they used robust testing protocols which aimed at reducing artefacts. It is also site-specific for the femoral neck. The proposed material model together with a strain based failure criterion can be used to simulate bone fracture.

Several FEA studies analysed the fracture risk of necrotic femoral heads to both better understand the disease progression and to improve clinical diagnosis. Beam theory represents an alternative to FEA. It is considered to be less complex which makes it suitable for the clinical environment (Whealan et al., 2000; Oftadeh et al., 2016). Several of the previously described studies showed promising results when validated against in-vitro tests. However it has not been used to predict the fracture risk of AVN affected femoral heads as yet.

The femur can be modelled as an Euler-Bernoulli beam loaded with a joint contact force. The femoral head has rapidly changing cross-sectional areas, a short length compared to its thickness and bone is neither linear elastic nor isotropic. These are attributes that are in conflict with the assumptions made for the application of beam theory. However, the literature has shown that even with numerous simplifications, beam theory remains sufficiently accurate to predict fracture loads. Euler-Bernoulli beam theory accounts for axial and

bending stiffness of its beam sections beside geometric information of the structure. These two basic properties can also be used to predict bone fracture of the femur (Snyder et al., 2004; Anez-Bustillos et al., 2014).

The loading of the beam is exclusively static and the contact stress respective to the gait cycle cannot be analysed. However it is possible to alter the direction of the loading vector to simulate different loading situations, such as heel strike or toe-off events, which can help to better understand failure mechanisms related to loading. This can help to identify physical activities that carry an increased fracture risk.

A fracture prediction based on beam theory analysis might help to stratify patients into well-defined risk groups, thus directing the surgeon towards appropriate surgical interventions and ease uncertainty, for example recommending a THA because another treatment would not stop or would not sufficiently delay collapse.

## 2.8 Aims and objectives

The overall aim of this thesis was to develop and validate a method based on engineering beam theory analysis and tomographic imaging to identify avascular-necrotic femoral heads which have a high risk of progression to fracture. The literature review revealed that there is a need for a non-invasive fracture prediction tool based on CT-images that has the potential to provide objective information in the clinical environment, at a low computational cost and minimal user input.

This was accomplished by the following objectives:

- 1. Define a beam theory model to simulate AVN pathology and verify it against a developed theoretical disease model.**

The first objective was to develop a fracture prediction tool based on beam theory analysis and to verify it against theoretical AVN pathology based findings from the literature. This included verifying the load calculations and parameters of the tool against simple geometries and CT-scans of femoral heads which were altered *in-silico* with AVN pathology.

- 2. Validate the beam model against a developed physical disease model *in-vitro* by utilising CT imaging.**

The second objective was an *in-vitro* validation of the beam tool against disease models generated by additive manufacturing with different simulated AVN lesions. The tool was also validated against explanted porcine and

human femurs with artificial necrotic lesions by using a density-modulus material model.

**3. Validate the beam model against clinical patient data and compare fracture risk predictions to classifications from current risk assessments and other novel methods.**

Thirdly, the fracture prediction tool was used to predict the fracture risk of AVN affected femoral heads from clinical CT scans. The results were compared against assessments using currently used classification systems. The tool was also compared against another novel fracture prediction method based on finite element analysis.

**4. Investigation of other applications for the beam theory tool.**

The broadening of the risk stratification method to other bone diseases would increase commercial interest in the developed tool. The operability of the tool was tested by utilising clinical CT-scans of human femurs and comparing the predicted fracture loads with fracture loads reported in the literature and by verifying the tool against femur models generated by additive manufacturing.

## Chapter 3 Development of a structural mechanics model for the proximal femur

### 3.1 Introduction to method development

This chapter describes the development of an *in-silico* fracture prediction tool based on structural mechanics and particularly beam theory to identify increased fracture risk within the femur based on density calibrated CT-scans. The femur was treated as a structural member subjected to stresses and strains. The fracture risk of the femur was estimated by analysing cross-sectional planes of this beam. The material and geometric properties of each cross-section were derived from computed tomography (QCT) scans of the analysed femur. A strain based failure criterion was used to identify the weakest cross-section of the femur and to predict its fracture risk.

Several studies demonstrated that there is a high correlation between calculated structural stiffness and *in-vitro* fracture loads of tested bone samples (Hong et al., 2004; Snyder et al., 2004; Anez-Bustillos et al., 2014). When using a Euler-Bernoulli beam approximation, structural and material properties can be correlated with stress and ultimately the failure load. A large number of studies have been published about the application of beam theory to analyse stress within the femur, most of which were published before the advent of easily accessible FEA (Toridis, 1969; Rybicki et al., 1972; Huiskes et al., 1981; Raftopoulos and Qassem, 1987; Salathe and Arangio, 1989; Hipp et al., 1995; Mourtada and Beck, 1996). The geometry of long bones such as the femur is suitable for beam modelling and therefore engineering beam theory is able to predict bone fracture. However, it has never been deployed to explicitly analyse the fracture risk of the subchondral area of the femoral head which is the region that is most commonly affected by AVN. Whether structural analysis or beam theory would allow for an accurate fracture risk prediction for structures with a geometry and loading regime such as the femoral head requires investigation.

The following section outlines the development of the general methodology of a fracture prediction based on structural mechanics and beam theory. Subsequent sections present the verification of the developed method against theoretical pathologies and simple geometries as part of the method development. The tool was also verified in respect of the material model and the sensitivity towards image resolution.

## 3.2 Fracture Prediction methodology development

### 3.2.1 Introduction

The fracture prediction tool described in this section was realised *in-silico* through a MATLAB (R2013b, MathWorks, MA) script which encompassed bone segmentation, density-modulus correlation, reconstruction of CT cross-sections, structural analysis and beam theory to identify fracture risk (Figure 17).

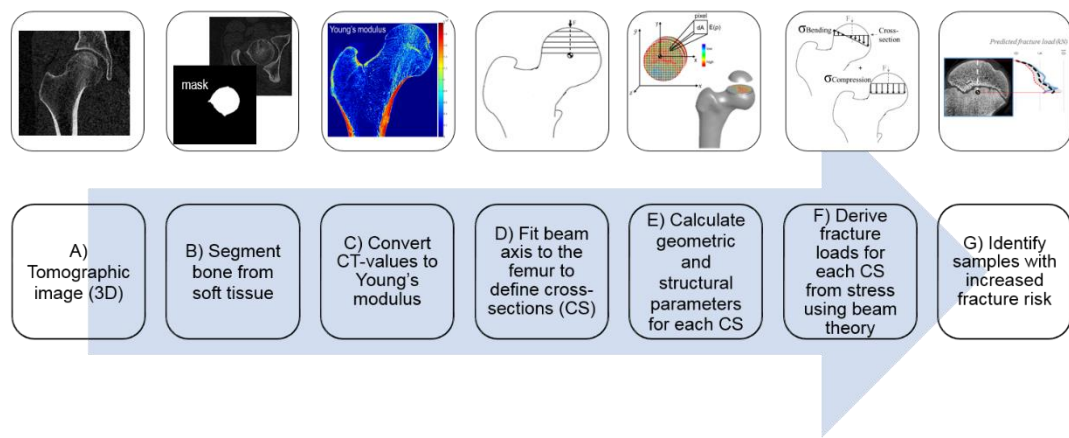


Figure 17 Tool workflow (A-G) to assess the fracture risk of a femur based on a tomographic image. Structural parameters (E) or the calculated fracture load (F) can be used to predict the fracture risk.

### 3.2.2 Bone segmentation

The CT-scan was segmented to isolate the femur from surrounding soft tissue and air which would compromise the beam calculation and hence needed to be excluded (Figure 17B). The segmentation of the bone also helped to identify boundary points such as the most distant fibre and the cross-sectional area which were important parameters for the beam calculation. An iterative selection method was used in this study to calculate a threshold grey value which in combination with other smoothing image filters was able to separate the femur from the image background (Ridler and Calvard, 1978). A single threshold value was calculated based on 10mm cube of trabecular bone at the centre of the femoral head. The filters included a median filter to reduce noise, a dilation filter followed by erosion to fill cavities to capture trabecular bone inside the cortical shell. By default the filter parameters for an image resolution of 82 $\mu$ m were 3x3 pixel for the medial filter and 10 pixel for dilation

and erosion but these parameters were amended proportionally to image resolution.

### **3.2.3 Density-modulus material model**

A density-modulus material conversion model based on empirical relationships was used to convert the X-ray attenuation of three dimensional CT images to the equivalent Young's modulus (Figure 17C). This was based on a power law ( $E = \alpha \cdot \rho^\beta + \gamma$ ) which has been found previously to describe the density-modulus relationship for bone (Carter and Hayes, 1977; Helgason *et al.*, 2008).

### **3.2.4 Beam axis and cross-sections**

The femur can be modelled as an Euler-Bernoulli beam loaded with a joint contact force ( $F$ ). A beam has a defined beam axis which is usually congruent with the neutral axis along which there are no longitudinal stresses. The neutral axis is the axis at which strain and stress is zero when the beam is subjected to bending only. The trajectory of all modulus weighted centroids represented the neutral axis. The selection of beam axis was influenced by the location of the centroids to achieve a close match. To analyse the subchondral area of the femoral head, a straight beam axis was established from the point of loading on the bone surface to the centre of the femoral head (Figure 18A).

Based on the defined beam axis, the CT-volume of the femur was divided into a stack of 2D cross-sections which were all perpendicular to the defined beam axis (Figure 17D + Figure 18A). The cross-sectional image planes were reconstructed from the three-dimensional CT-image. In the following each cross-section was analysed in isolation, without any influence from adjacent cross-sections, resulting in an independent failure load prediction for each slice.

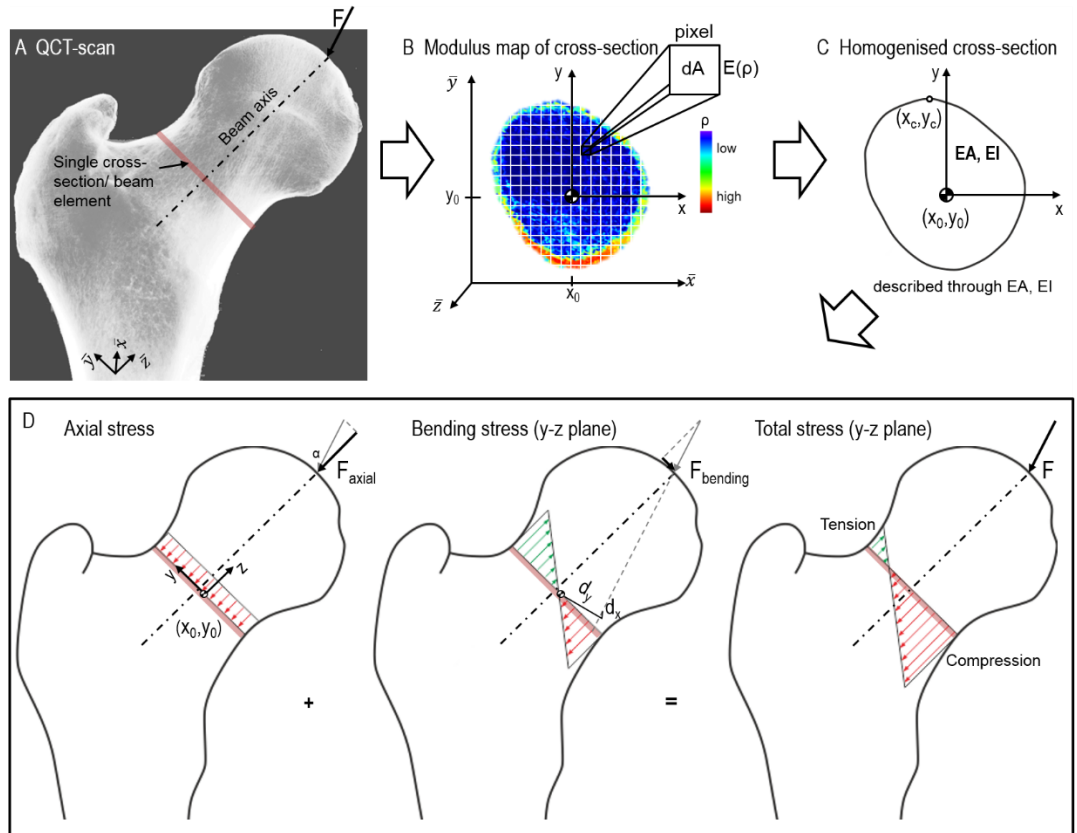


Figure 18 (A) The proximal femur can be approximated as a beam structure in form of a stack of beam elements/cross-sections. Each of these cross-sections can be analysed in isolation of other cross-sections. (B) The structural parameters were calculated from the modulus map of a single selected cross-section. (C) The cross-section was characterised by these structural parameters  $EA$ ,  $EI$ . (D) These were used to calculate the stress distribution within the homogenised cross-section as a result of the joint contact force  $F$ . The stress distribution as a result of bending is shown in the y-z plane. The stress distribution was calculated in both x and y, but bending along the x-axis was significantly smaller for this load case.

### 3.2.5 Structural analysis

Beam theory allowed the failure load in each transaxial cross-section to be calculated based on geometric and structural properties, namely the modulus weighted centroid (Eq.3.1) and the axial (Eq.3.2) and bending stiffness (Eqs.3.3 and 3.4). These properties were calculated for each cross-section based on the modulus map derived from the material model (Figure 17E and Figure 18B). The resolution of the modulus map was determined by the resolution of the CT-scan.

$$x_0 = \frac{\sum E_i \bar{x}_i dA}{\sum E_i dA} \quad y_0 = \frac{\sum E_i \bar{y}_i dA}{\sum E_i dA} \quad 3.1$$

$$EA = \sum E_i (\rho_{app}) dA \quad 3.2$$

$$EI_x = \sum E_i (\rho_{app}) y_i^2 dA \quad 3.3$$

$$EI_y = \sum E_i (\rho_{app}) x_i^2 dA \quad 3.4$$

$$EI_{xy} = \sum E_i (\rho_{app}) x_i y_i dA \quad 3.5$$

where,  $i$  represents the index of summation with an upper bound of the number of pixels of a analysed cross-section,  $x_0, y_0$  are the coordinates of the modulus weighted centroid as in Figure 18B,  $EA$  is the axial stiffness and  $EI$  is the bending stiffness of each cross-section.  $I_{xy}$  is the product moment of area.

### 3.2.6 Beam theory

Stress was assumed to be linearly distributed over the cross sections (Figure 17F + Figure 18D). Euler-Bernoulli beam theory further requires that cross-sections remain in-plane after bending and in-plane distortions were ignored (Mourtada and Beck, 1996) implying that there is no shear strain. Therefore, axial stresses through compression and bending are the most significant for failure (Huiskes, 1984). Deformations were assumed to be small and Poisson's effects were ignored.

The principle of superposition can be used to combine axial and bending stress components to a single resultant stress beam theory equation which is valid for linear-elastic material behaviour and for small deflections (Eq.3.6). The resultant stress for each location  $x, y$  within the cross-section was calculated using the axial and bending stiffness from equations 3.2 to 3.4.

$$\sigma = \frac{F_{axial}}{A} - \frac{M_x I_y + M_y I_{yx}}{I_y I_x - I_{yx}^2} y + \frac{M_y I_x + M_x I_{yx}}{I_y I_x - I_{yx}^2} x \quad 3.6$$

When applying Hooke's law the resultant stress can be rearranged for strain:

$$\varepsilon = \frac{F_{axial}}{EA} - \frac{M_x EI_y + M_y EI_{yx}}{EI_y EI_x - (EI_{yx})^2} y + \frac{M_y EI_x + M_x EI_{yx}}{EI_y EI_x - (EI_{yx})^2} x \quad 3.7$$

Where  $F_{axial}$  is the axial component of the joint contact load  $F$ ,  $A$  is the area of the cross-section,  $\sigma$  is stress,  $\varepsilon$  is strain,  $E$  is the Young's modulus and  $I$  is the second moment of area of the cross-section. The applied bending moment  $M$  is dependent on the location of the modulus weighted centroid and the joint contact force  $F$ .  $M_x$  is the product of the force component of  $F$  in  $y$  direction

and the distance  $d$  from the applied load to the centroid.  $M_y$  is the product of the force component of  $F$  in  $x$  direction and the distance from the applied load to the centroid. The beam theory equation 3.7 was finally rearranged for the joint contact load  $F$ :

$$F_{fracture} = \frac{\varepsilon_c}{\frac{\cos \alpha}{EA} - \frac{d_y EI_y + d_x EI_{yx}}{EI_y EI_x - (EI_{yx})^2} y_c + \frac{d_x EI_x + d_y EI_{yx}}{EI_y EI_x - (EI_{yx})^2} x_c} \quad 3.8$$

Where  $\varepsilon_c$  is the critical strain at which bone was assumed to fracture. Only the location  $x_c, y_c$  with the most critical fracture load was calculated. This location within the cross-section was the point where fracture was assumed to initiated. Therefore a direct correlation between the joint loading and the bone fracture in each cross-section was established.

The methodology described in this section was realised in MATLAB. The different steps of the developed script are shown in Figure 19.

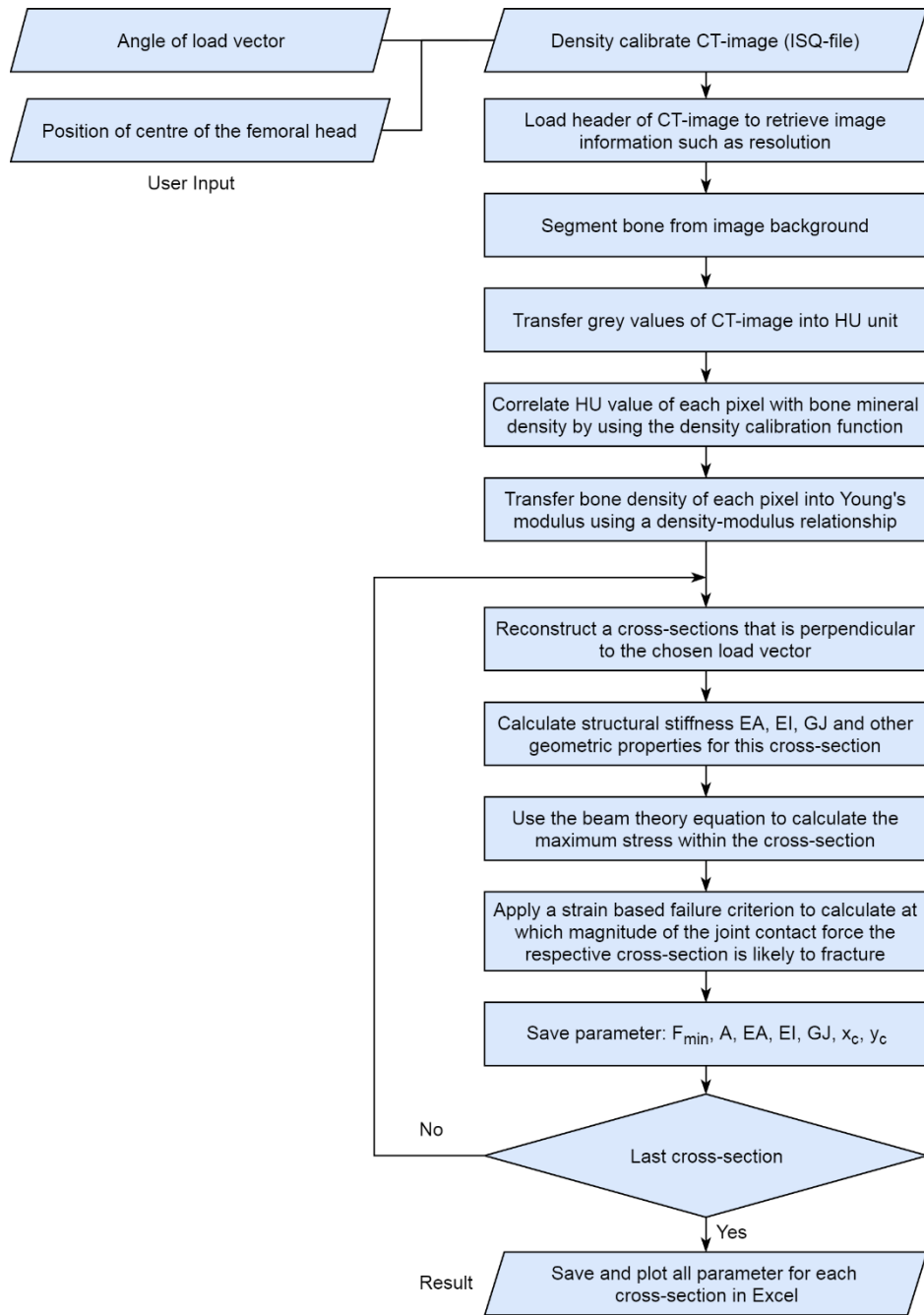


Figure 19 Flowchart describing the steps of the developed MATLAB script.

### 3.2.7 Tool output and quantification of the fracture risk

The output of this fracture prediction method was a plot of the magnitude of the joint contact force at which each corresponding cross-section was likely to fracture (Figure 17G). A low predicted fracture load indicated a high fracture risk for the respective cross-section. The weakest cross-section with the lowest predicted failure load was assumed to lead to failure of the entire femur.

The identification of a single weak cross-section was relatively straight forward for straight slender structures such as the femoral shaft or for the femoral neck which only has slight taper. However the subchondral area of the femoral head had rapidly increasing cross-sectional areas and a short length compared to its thickness. These attributes are also in conflict with the assumptions made for the application of beam theory. The predicted failure loads increased gradually with the expanding cross-sectional area of the head without any clearly identifiable minimum of the failure load curve. The direct use of the beam theory equation to calculate exact fracture loads for the femoral head beam model was therefore potentially unreliable.

Alternatively, the mechanical behaviour of the femoral head can be analysed by using the structural stiffness, which is an integral part of the beam equation, as it accounted for both material and for geometrical properties. Structural stiffness has been successfully used to predict bone fracture of the femoral shaft and neck (Snyder et al., 2004; Anez-Bustillos et al., 2014). The developed tool calculated the axial (Eq.3.2) and bending stiffness (Eqs.3.3, 3.4) for each cross-section. The calculated stiffness of a lesion affected femoral head can be compared to an unaffected ‘heathy’ femur to identify cross-sections with significant reductions. The magnitude of the reduction of the stiffness was an indicator of the fracture risk of the analysed femoral head sample. For this kind of comparative analysis, it was not strictly necessary to use a density-modulus conversion model to calculate the Young’s modulus but density could be used directly. However, calculating the Young’s modulus allowed better inter-study comparison of the structural stiffness and made it easier to further develop the tool so that it could predict fracture loads of more slender parts of the femur. A modulus conversions is also required when analysing bending in form of EI.

Beam theory has never been used to analyse the impact of necrotic lesions within the femoral head and it needed to be investigated which approach had the best predictive capability. Therefore both approaches were verified against a theoretical femoral head disease model in section 3.6.

### **3.2.8 Discussion of fracture prediction methodology development**

The fracture prediction tool developed in this section was based on beam theory analysis. Beam theory was chosen because of its simplicity. However, this necessitated approximations within the bone model and therefore the

fracture risk prediction method needed extensive verification and validation to demonstrate its diagnostic potential.

The developed method did not use a stiffness approach to predict failure of the femur but analysed cross-sections which were characterised by structural parameters. This homogenisation of the cross-section meant that stress was linearly distributed across the cross-section.

Euler-Bernoulli beam theory assumes that cross-sections remained in plane after bending. Maximum shear stresses are located at the centre of a beam element whereas bending stresses peak at the surface of the element. The bending influence was much larger than shear and fracture was assumed to occur at the bone surface. Therefore shear stresses were ignored although it would have been possible to calculate them based on bending force components. The shear modulus ( $G$ ) was needed to calculate shear stresses which can be approximated from empirical values from literature as elastic constants should not be linked using equation 2.4.

### **3.3 Analytical verification of the scripted structural analysis**

The modulus weighted centroid, the axial and bending stiffness were based on a pixel by pixel analysis of each cross-sectional image. The applicability of this calculation needed to be verified. The complex modulus map of a CT slice was simplified to a simple geometry of three different materials (Figure 20). The capability of the developed *in-silico* tool to calculate the axial and bending stiffness was verified against a hand-calculation outside the computational tool. A sample cross-section with a simple geometry was analysed with the developed tool and the structural and geometric parameters were calculated. The results of the comparison showed only a small difference in EI which demonstrated that the developed script functioned as was intended (Table 18).

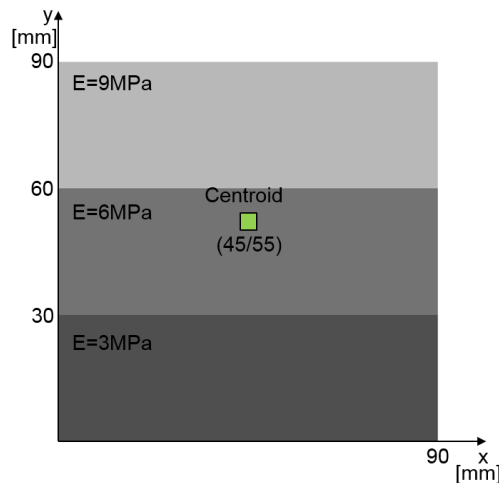


Figure 20 Cross-section with a simple geometry to verify structural tool calculations

Table 18 Comparison of the results of the paper and computational calculation

|                            | In-silico | Paper calculation | Percent error |
|----------------------------|-----------|-------------------|---------------|
| <b>Centroid [mm]</b>       | 45/55     | 45/55             | 0%            |
| <b>EA [N]</b>              | 48600     | 48600             | 0%            |
| <b>EI [Nm<sup>2</sup>]</b> | 2.7941e7  | 2.7945e7          | 0.014%        |

## 3.4 Material model

### 3.4.1 Material model from literature

The material distribution within a cross-section affects the structural properties used to determine the likelihood of fracture. The grey scale density of each pixel within a cross-section was converted to Young's modulus (E) using an empirical relationship. The modulus weighted pixels were then used to calculate the structural stiffness of that cross-section (Eqs.3.2-3.4). The patchwork of pixels with assigned modulus values is the modulus map of that cross-section as described in Figure 18.

The resolution of clinical CT-scans will not be able to image cancellous bone at trabecular level in the foreseeable future and a pixel within a cross-section contained a mixture of trabecular bone and gaps of bone marrow. Cancellous bone was therefore similar to a porous structure and the Young's modulus of

cancellous bone is approximately proportional to the square of the density (Gibson, 1985).

Both Morgan et al. (2003) and Lotz et al. (1990) developed a density-modulus power law relationship from cancellous bone plugs of human femoral heads. Compared to the latter, Morgan et al. (2003) had a more robust testing protocol which included cemented caps to avoid end effect artefacts, a strictly defined loading direction and a sufficient low strain rate. It was therefore used in this study. The standard error of the conversion model was 443MPa ( $R^2=0.85$ ) for measured empirical modulus values between 5440-8630MPa. The density range for the model was 0.26–0.75gHA/cm<sup>3</sup>. The relationship allowed correlation between wet apparent density and Young's modulus. The dimension of the tested bone plugs can be extrapolated to smaller volume elements defined by the voxel resolution of a CT-scan, if the density-modulus material model was resolution independent.

The beam tool estimated the structural stiffness of cancellous bone in direction of the beam axis. However, the density-modulus relationship was developed with cancellous bone specimens loaded along the principal trabecular orientation. The principal direction of trabeculae corresponded with the main load direction of the bone. As the beam axis mostly followed the main load direction of the femur, the difference was relatively small. However, this disparity was a limitation of this study because of the anisotropic nature of bone which needed to be investigated.

The density calibrated CT-scanner measured bone density in equivalence to the calibration phantom used. In order to use the described density-modulus relationship for densities measured by a CT-scanner, the CT-density must be converted to wet apparent density. Schileo et al. (2008) described a relationship to convert CT-density with wet apparent density for human trabecular and cortical bone and for hydroxyapatite (HA) phantoms (Table 19).

Table 19 Density-modulus conversion material model to assign material properties to the model from CT-image data

| Relationship  | Source               |
|---|----------------------|
| $\rho_{QCT} = 0.00034836 \cdot HU - 0.0062665$ [g/cm <sup>3</sup> ] | Density calibration  |
| $\rho_{ash} = 0.877 \rho_{QCT} + 0.0789$ [g/cm <sup>3</sup> ]       | Schileo et al., 2008 |
| $\rho_{app} = \rho_{ash} \div 0.6$ [g/cm <sup>3</sup> ]             | Schileo et al., 2008 |
| $E = 6850 \cdot \rho_{app}^{1.49}$ [MPa]                            | Morgan et al., 2003  |

Scanner density ( $\rho_{QCT}$ ) as measured by a density calibrated CT-scanner, ash density ( $\rho_{ash}$ ) as ash weight per original sample volume, apparent density ( $\rho_{app}$ ) as weight of hydrated bone tissue without bone marrow divided by sample volume, Young's modulus (E) in MPa.

The density range of a cross-section within the femoral head with an image resolution of  $82\mu\text{m}$  was between 0 and  $2 \text{ g/cm}^3$  (Figure 21) and a density-modulus correlation was established for pooled cortical and trabecular bone which seemed justified as trabecular bone is difficult to discriminate from cortical bone (Helgason et al., 2008). A lower resolution resulted in larger voxel elements which had an average density of the higher resolution voxels it encompassed. Therefore the density of low resolution voxels were usually lower compared to voxels that just contained bone. This observation confirmed that the material model was resolution dependent. Further investigation was needed to quantify the extend of this to determine the applicability of the density-modulus material model.

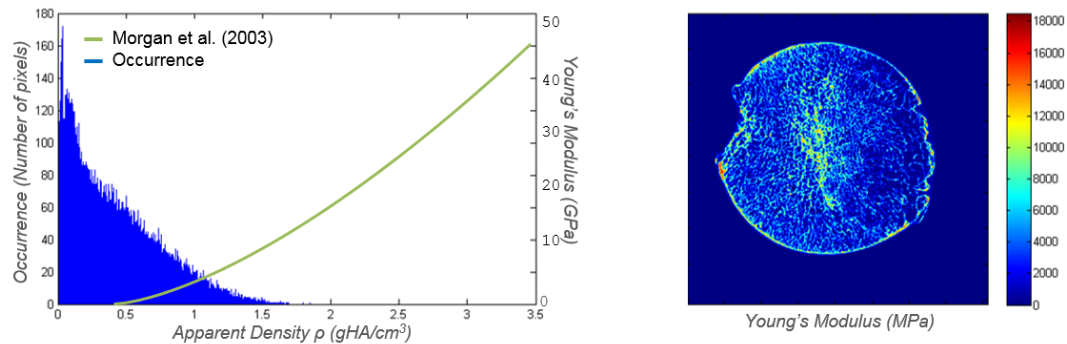


Figure 21 Occurrence rate (primary vertical axis) and density-modulus conversion model (secondary vertical axis) of each density of a CT cross-section of a human femoral head.

### 3.4.2 Resolution dependency of density-modulus material model

Verification was required as to whether the density and modulus of tested bone plugs could be extrapolated to smaller volume element defined by the voxel resolution of a CT-image. The sensitivity of the density and modulus to the CT resolution was analysed to verify whether the described material model was valid. A parameter sweep for various image resolutions was conducted.

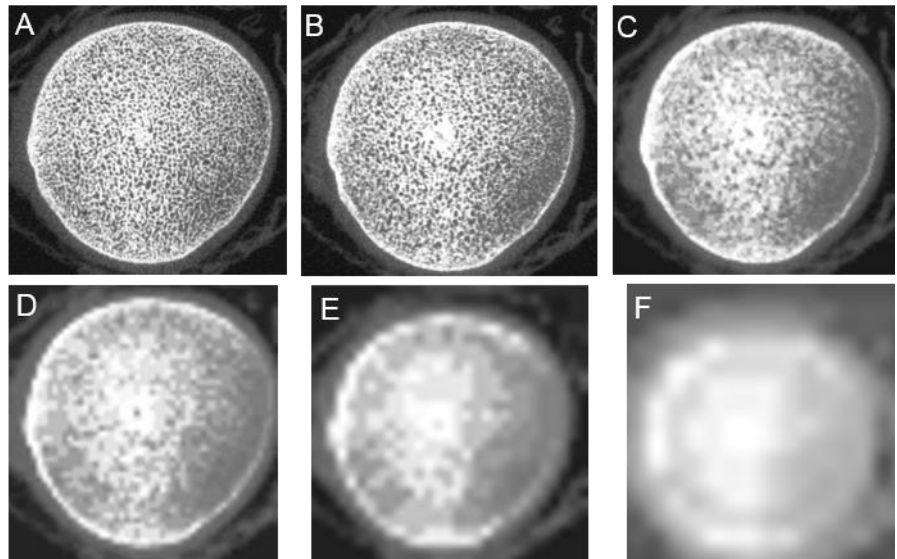


Figure 22 Distal view of the same CT cross-sectional image of a porcine femoral head at different resolutions: (A) 82 $\mu\text{m}$ , (B) 123 $\mu\text{m}$ , (C) 246 $\mu\text{m}$ , (D) 492 $\mu\text{m}$ , (E) 984 $\mu\text{m}$ , (F) 1968 $\mu\text{m}$ .

This study analysed a cross-section through the centre of the femoral head which was assumed to be more affected by a potential resolution dependency compared to a more homogenous structure such as the femoral shaft with only cortical bone. A porcine femoral head was CT-scanned at three different isotropic resolutions, 82 $\mu\text{m}$ , 123 $\mu\text{m}$  and 246 $\mu\text{m}$  (Figure 22), using a HRp-QCT-scanner (XtremeCT, Scanco Medical, Switzerland). The scanner was density calibrated using a hydroxyapatite phantom. The samples were scanned in air with 59kVp tube voltage and 300ms integration time. The bone itself was hydrated and did not show any traces of air. Additionally to the aforementioned resolutions, the CT-scan of 246 $\mu\text{m}$  resolution was further reduced to a resolution of 492 $\mu\text{m}$ , 984 $\mu\text{m}$  and 1968 $\mu\text{m}$  using the ‘imresize’ function in MATLAB. A single cross-section at the same location in each scan was analysed to compare the average density and Young’s modulus for each resolution. The bone was manually masked from the image background which created a small variation of the analysed area within the cross-section ( $446 \pm 5 \text{ mm}^2$ ).

The analysis of the cross-section was relatively stable with changing resolution despite partial volume effects on the boundaries of the bone (Figure 23). The average density of the cross-sections at each resolution was 0.3526 gHA/cm<sup>3</sup> with a low standard deviation of 0.0052 gHA/cm<sup>3</sup>. Using the described density-modulus material conversion model led to an average Young’s modulus of  $3631 \pm 85$  MPa. The average axial stiffness (EA) was

$1681 \pm 19\text{kN}$ . The standard deviation as a percentage of the mean density was 1.5% (Young's modulus 2.3%, Axial stiffness 1.1%).

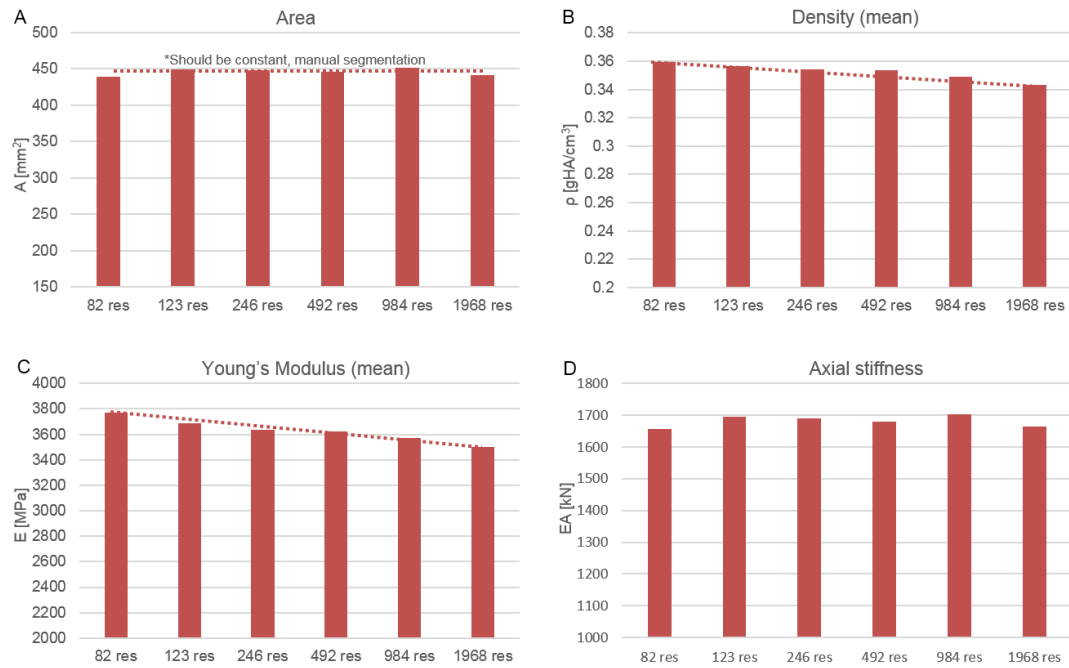


Figure 23 Analysis of the sensitivity of the density and modulus to different CT resolutions. The area (A) was segmented manually. Density (B) and Young's modulus (C) were calculated for each pixel of a cross-sectional image after which the mean values were derived. The axial stiffness (D) is the product of mean density and Young's modulus.

The errors resulting from different CT-resolutions are lower than the errors of the mechanical tests on which the model is based. Even a resolution of about 2mm led to reasonable results. Therefore it can be assumed that the density-modulus material model is relatively resolution stable for CT image resolutions between 0.082mm and 2mm.

### 3.4.3 Verification of the used density-modulus material model for beam simulations

In this section the material model proposed by Morgan et al. (2003) was verified against compression test on human femoral head bone plugs that were conducted as part of this study. It was also verified whether the calculated Young's modulus delivered reliable results in combination with beam theory.

A series of 13 bone plugs were tested to assess the Young's modulus of human femoral cancellous bone and compared with the calculated Young's modulus from CT measurements. The sample preparation and testing of the

bone plug was jointly conducted with Mahsa Avadi (Avadi, 2016). Samples in this study were obtained from a non-transplant human cadaveric tissue bank (Platinum Training, Phoenix, AZ) following approval of ethics application from University of Leeds Ethics Committee (Approval number: MEEC 13-002). Bone samples were obtained from subjects with an age range from 55-69 years with one male and two females. Three human femoral heads from the right side of the pelvis were dissected and bone plugs with a diameter of 9mm were extracted. The bone plugs were extracted from the load bearing area of the femoral head which was defined as halfway between the cartilage/femoral neck junction and *ligamentum teres* (Taylor et al., 2011). Bone plugs were also extracted from anterior, posterior and inferior locations of the head (Figure 24). One of the three femoral heads was large enough to extract two plugs from the load bearing area.

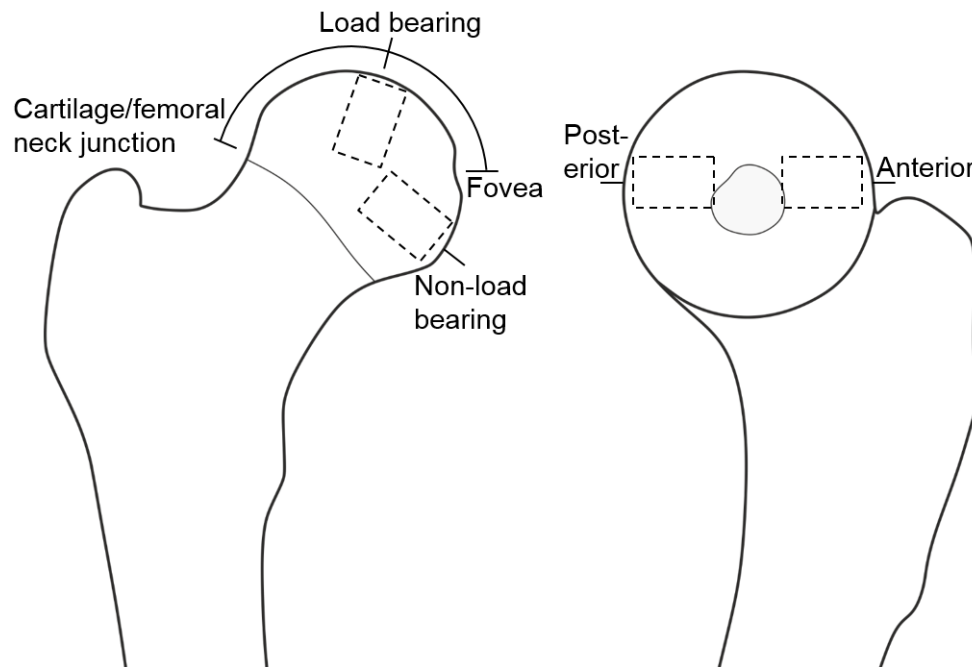


Figure 24 Location where bone plug were extracted from the femoral heads.

The cartilage was removed with a scalpel. All samples were kept hydrated with cloths soaked with phosphate-buffered saline solution and were frozen between dissecting, scanning and testing.

The bone plugs were CT-scanned at an isotropic resolution of 82 $\mu$ m using a HRp-QCT-scanner (XtremeCT, Scanco Medical, Switzerland). The scanner was density calibrated using a hydroxyapatite phantom. The samples were scanned in air with 59kVp tube voltage and 300ms integration time. The built-in Scanco software was used to measure the average apparent bone mineral

density of the bone plugs. The dimensions of the plugs were measured on the CT-scans using ImageJ (National Institute of Health, Bethesda, MD).

The bone plugs were compression tested between platen until failure using an Instron 3366 single axis tension-compression machine (Instron, Norwood, MA) (Figure 25). The displacement rate was  $0.01 \text{ mms}^{-1}$  to avoid a loading rate effect on the compressive strength of the tested bone (Carter and Hayes, 1976). In this study, failure was defined as the first local maximum of the load-displacement or stress-strain curve (Figure 26).

The Young's modulus was determined in three ways. Firstly the modulus was measured from the slope of the steepest region of the stress-strain curve of the compression test (Li and Aspden, 1997; Patel et al., 2008) (Figure 26). Secondly the modulus was calculated based on the density-modulus material model described by Morgan et al. (2003) (Table 19) using the average bone mineral apparent density of each bone plug. Finally the modulus was indirectly computed from the fracture load of the compression test and the beam theory equation. The Young's moduli from all three methods were compared.

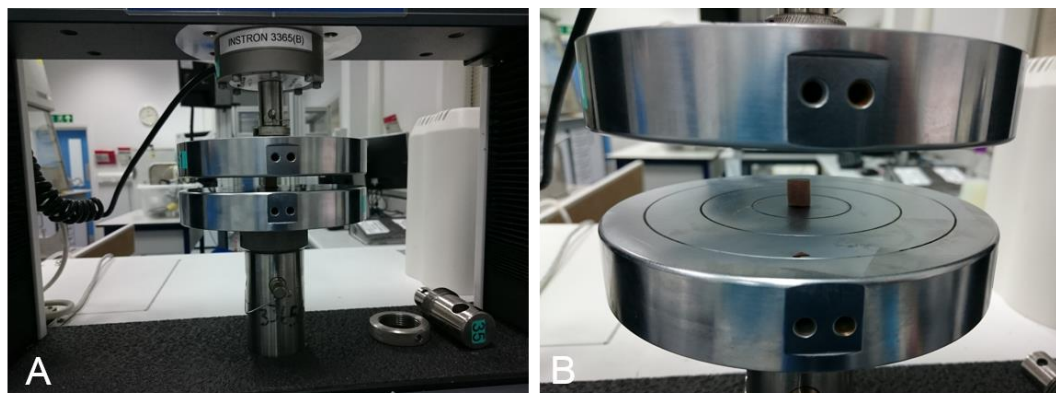


Figure 25 (A) Instron 3366 testing machine used to compression test bone plugs.  
(B) Bone plug prepared for platen compression testing.

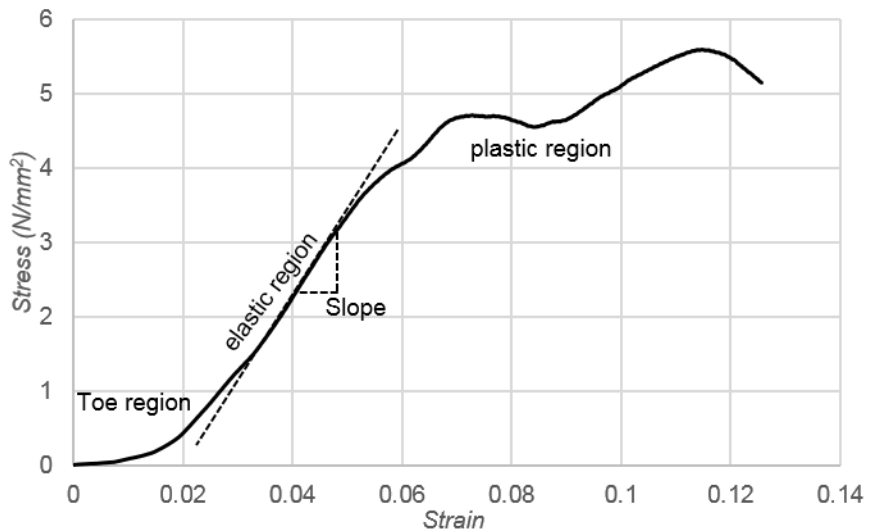


Figure 26 Stress-strain curve of a compression test of a bone plug including the defined failure load and the slope of the steepest region. The stress-strain curve is characteristic of the material behaviour.

No correlations were seen between the Young's modulus from the CT-measurements and the modulus based on the stress-strain curve of the compression test (Figure 27A). This indicated that one of these methods is not very accurate. The estimation of the modulus from the stress-strain curve is challenging for natural materials, as described in the literature review (Section 2.4.1). Therefore the Young's modulus was indirectly computed from the failure load of the compression test. The failure load was a parameter that was easy to identify. A failure strain of 0.85% was used for the beam theory calculation (Morgan et al., 2003). There was a good correlation between those two Young's moduli (Figure 27B).

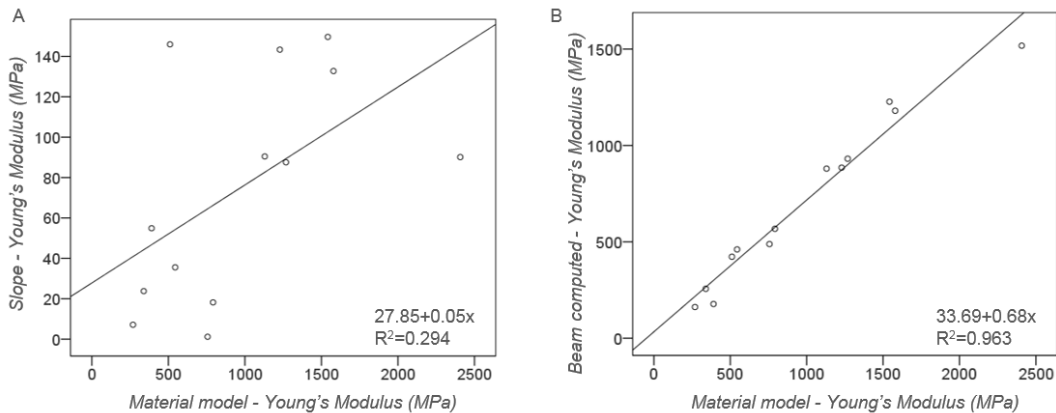


Figure 27 Regression between the Young's moduli of cancellous bone plugs calculated from the developed material model based on CT density measurements and Young's moduli calculated from the slope of the stress-strain curve of the compression test (A), and computed Young's moduli from the fracture load of the compression test and beam theory (B).

In a next step, the Young's modulus calculated from the density-modulus material model was used to predict the failure load of the bone plugs. The bone plugs were modelled as a beam loaded with a vertical load. Beam theory was used to predict fracture in two ways. The material of the beam was homogenised by using the average density of the bone plug (Figure 28A). Alternatively to reading the average bone density for the plug from the CT-scanner directly, the CT-density was converted pixel by pixel to apparent wet density using the relationship described in Table 19. The fracture load was predicted for each of the cross-sections along the beam axis. The weakest cross-section was assumed to govern failure of the bone plug and was therefore the predicted fracture load of that bone plug (Figure 28B). However, this method is very different to how density-modulus relationships were developed.

The predicted fracture loads of both methods correlated equally well with the fracture load seen experimentally. The fracture load was calculated using axial loading only with a yield strain of  $\varepsilon=0.85\%$ .

$$F_{failure} = \varepsilon EA$$

3.9

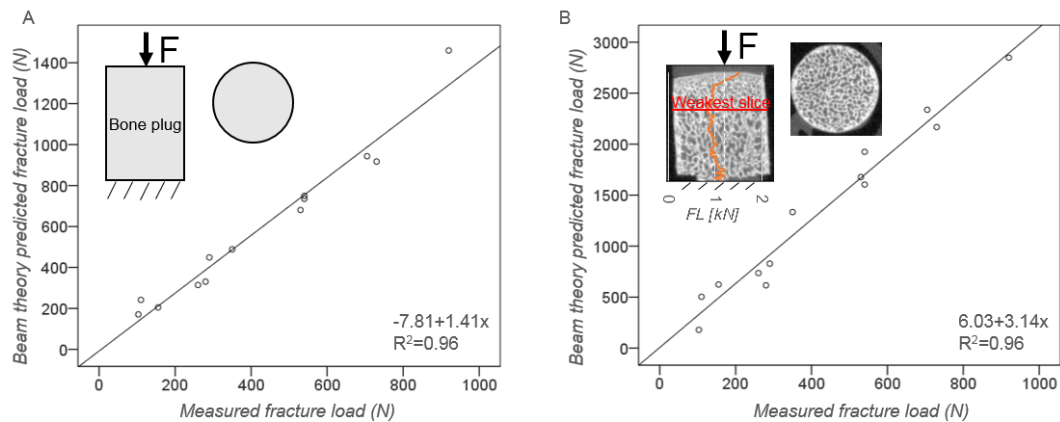


Figure 28 Slope of regression between experimental failure loads of human femoral bone plugs and beam theory predicted failure loads based on the average density and the overall plug cross-sectional area (A) or beam theory predicted failure loads (FL) of the weakest slice of the bone plug (B).

There was a high correlation ( $R^2=0.96$ ) between experimental fracture loads and predicted fracture loads when predicting fracture based on a density-modulus relationship and beam theory. However the computational fracture prediction underestimated the experimental fracture load by a constant error.

This could be explained by inevitable errors in the experimental testing procedures. Firstly, the process of cutting bone compressed mortised bone into the trabecular structure resulting in an increase in radiographic density without an increase in mechanical strength. Secondly, the extracting process caused trabecular defects at the periphery of the bone plugs which inevitably reduced their Young's modulus (Keyak et al., 1994). The fracture load correlated with the Young's modulus as area and failure strain are constant (Eq.3.9). The error in this study was 30%. When compensating this constant error in the modulus calculation, there was a good match between the density-modulus conversion material model described by Morgan et al. (2003) and the measured density-modulus distribution of individual bone plugs (Figure 29). Keaveny et al. (1993) reported modulus differences of 18% and 36% depending on how the bone samples were cut. The aim of this study was to analyse femoral heads which did not have any such defects and as a result were expected to have a higher modulus. Therefore, this study used the density-modulus material model developed by Morgan et al. with the described beam method for fracture simulations.

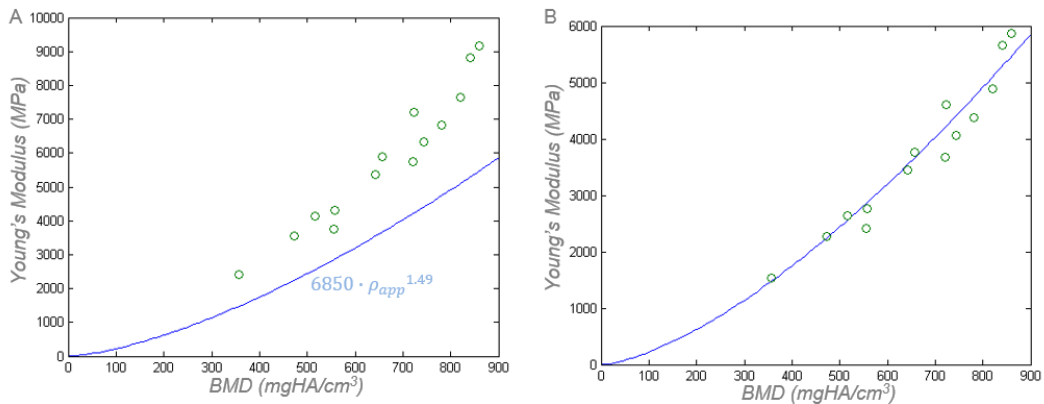


Figure 29 The platen compression test of the cylindrical bone plugs created a constant error (A). If corrected, there is a good approximation between the density-modulus relationship described by Morgan et al. (2003) (blue line) and this test (B).

### 3.5 Image segmentation of bone

#### 3.5.1 Introduction

The bone needed to be segmented as surrounding soft tissue and adjacent bone structures would compromise the beam calculation. When analysing bone within the femoral head, cancellous networks can be further segmented from the surrounding bone marrow which potentially would lead to an even better fracture simulation. However, this is only feasible when the CT resolution is sufficiently high and single trabeculae can clearly be visualised otherwise there would be partial volume effects which would falsify the assignment of material properties.

A threshold algorithm appeared to be a viable option to separate the brighter trabecular bone from the darker pixels of the image background, bone is a dense material and appears bright on radiographic images. Ridler et al. (1978) described a method to objectively estimate a threshold value which is capable of extracting an object from its background (Figure 30). The threshold value (*thresh*) was calculated using equation 3.10. The grey value (*GV*) was weighted by the frequency of occurrence.

$$\sum_{-1000}^{\text{thresh}} GV_i * count_i = \sum_{\text{thresh}}^{8000} GV_i * count_i \quad 3.10$$

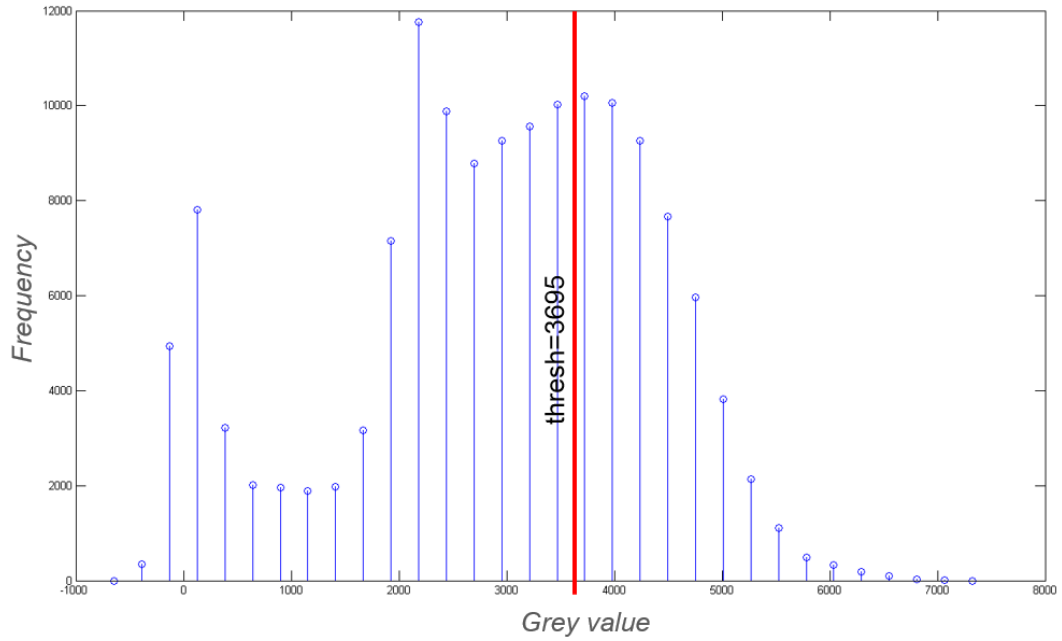


Figure 30 Frequency of pixels with certain grey values in a CT cross-section of a femoral head. The Ridler threshold was calculated from equation 3.10.

If the femur was segmented as a whole, cancellous bone was analysed at continuum level. If the trabecular network was segmented using a Ridler threshold, cancellous bone was analysed at trabecular level. The Ridler segmentation reduced the area of the bone within a cross-section but increased the density of the analysed bone. The calculated axial rigidity of that cross-section should be similar for both segmentation types if the density-modulus conversion model is valid for the relevant density range.

The aim of this study was to investigate if both methods produced similar values of the axial stiffness. The sensitivity of the Ridler segmentation method was analysed for different CT resolutions and how deviations of the threshold value affect the calculated axial stiffness.

### 3.5.2 Methods

A single CT cross-section of a porcine femoral head was analysed at different resolutions to see the effect of resolution.

Three image masks were created to segment bone from the image background. Firstly, a Ridler threshold was calculated for the cross-sectional image. Based on the threshold, a binary image mask (black and white) was created, where white represents bone and black represents the image background (Figure 31). A second mask was created using the same threshold which was 0.5% greater to investigate the effect a small alteration

of the threshold value might have. Finally the bone was masked as a whole. By multiplying the mask image with the original greyscale image, the background areas were multiplied with zero and thus erased from the original image. The resulting images were used to calculate the area and average density of the three segmented cross-sections. The density-modulus material model described in Table 19 was used to calculate the axial stiffness (EA) of the cross-section.

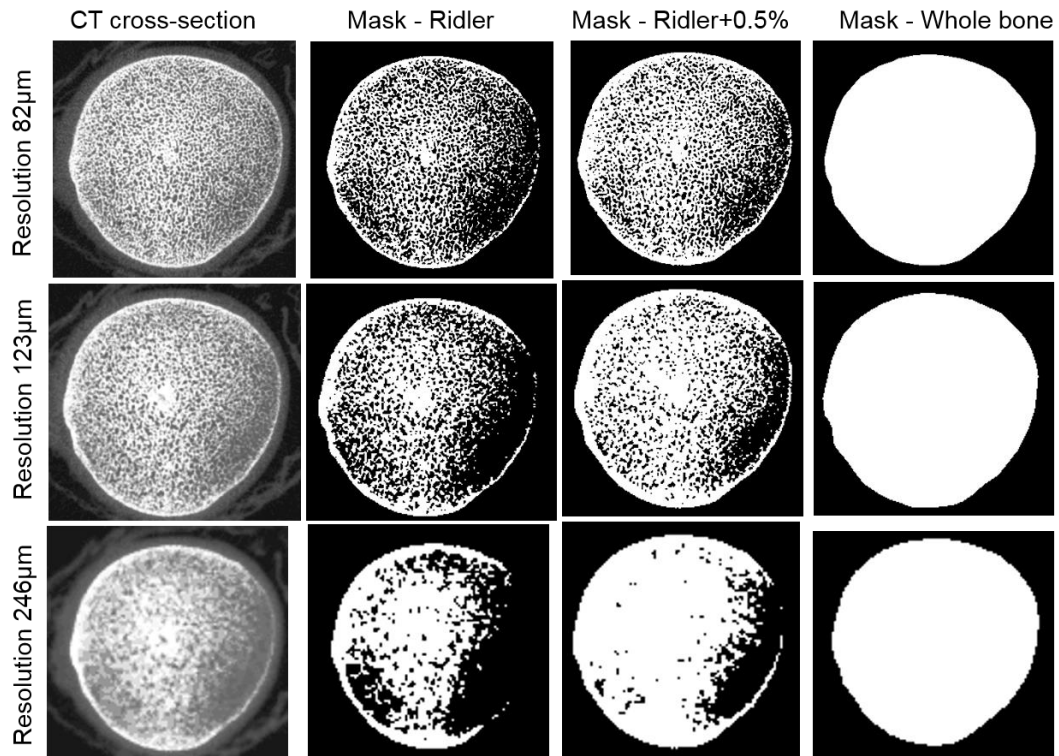


Figure 31 Three different masks were created for three CT cross-sectional images of the same porcine femoral head at the same position but with different resolutions. The first mask was based on a Ridler iterative threshold segmentation, the second on a was similar to the first but the threshold value was 0.5% greater and the last mask was a segmentation of the whole bone.

### 3.5.3 Results

While a resolution of 82 $\mu\text{m}$  was still sufficient to display single trabecular networks, resolutions of 123 $\mu\text{m}$  and 246 $\mu\text{m}$  were too low and a reliable segmentation of trabecular was not possible. The bone area of the Ridler segmentation increased by 5% with each reduction of the resolution. When increasing the Ridler threshold by 0.5% the area was up to 25% greater at a resolution of 246 $\mu\text{m}$  compared to 82 $\mu\text{m}$ .

In addition to the segmented area, the mean density and the axial stiffness of each segmented cross-section was calculated and compared (Figure 32). At

the highest resolution, the calculated axial stiffness of the Ridler segmented cross-section was 49% lower when compared to segmentation of the whole bone. The axial stiffness based on a segmentation from the altered Ridler threshold was also 20% higher compared to the unchanged Ridler segmentation, which indicated that an error in the threshold had a huge influence on the predicted stability of the cross-section.

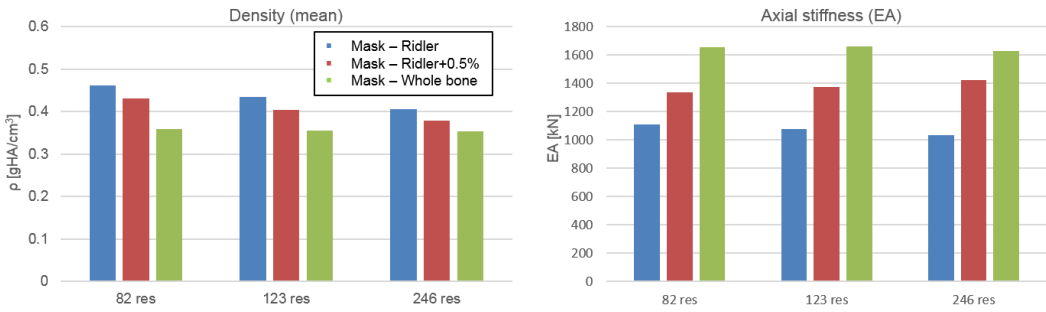


Figure 32 Resolution dependency of the mean density and the axial stiffness for a Ridler-segmented cross-sections and segmentation of the whole bone.

### 3.5.4 Discussion

Segmentation of the cancellous network did not lead to superior results in this study. The calculated structural properties of the Ridler-segmented cross-section were sensitive to the CT resolution which is problematic as clinical CT-scans usually have resolutions that cannot image single trabecular networks. Further, most material models for cancellous bone are based on apparent density which regards cancellous bone as a continuum. A bone segmentation of the whole femur appeared to deliver more reliable results when working with changing CT-resolutions and it was therefore used for the developed fracture prediction method.

## 3.6 Verification against theoretical pathology

### 3.6.1 Introduction

The aim of this study was to verify whether the developed fracture prediction method based on structural mechanics and beam theory was capable of identifying the increased fracture risk that comes with AVN pathology. Beam theory has never been used to analyse the fracture risk of the femoral head, the region most commonly affected by AVN. The impact of necrotic lesions

within the femoral head had to be analysed. The developed tool calculated structural parameters and predicted the fracture loads for a set of cross-sectional slices of the upper femoral head which were perpendicular to the defined beam axis. It was investigated whether these three parameters were sensitive enough to detect the structural impact of simulated AVN lesions within the femoral head. The predictive capability of all three parameters was analysed. It was also analysed how different lesion locations affected the calculated axial and bending stiffness.

### **3.6.2 Methods**

The fracture prediction tool was used to analyse the fracture risk of the subchondral area of the femoral head. The tool methodology was described in section 3.2.

In the model, the femoral head was assumed to be a beam subjected to a single load similar to the biomechanical hip model by Pauwels (1935). The load direction simulated a one leg stance and pointed towards the centre of rotation of the femoral head (Figure 33). This load case was a good starting point as AVN leads to gradual bone decay and it has not been reported that there are any high risk activities for AVN. The loading angle acting on the femoral head had an angle of 10° from the mechanical axis. A straight beam axis was established which followed the simplified loading vector from the point of loading on the bone surface to the centre of the femoral head. The developed method required only two manual inputs, the angle of the load vector and the position of the centre of the femoral head. The structural stiffness and the failure load were calculated for each slice of a stack of 30 cross-sectional slices which were reconstructed from the three-dimensional CT-image (Figure 34). In addition to the one leg stance load, a loading vector in direction of the mechanical axis of the femur was tested to analyse the effect of different slicing directions. The loading vector defined the beam axis and the correlation of the location of the modulus weighted centroids and the beam axis.

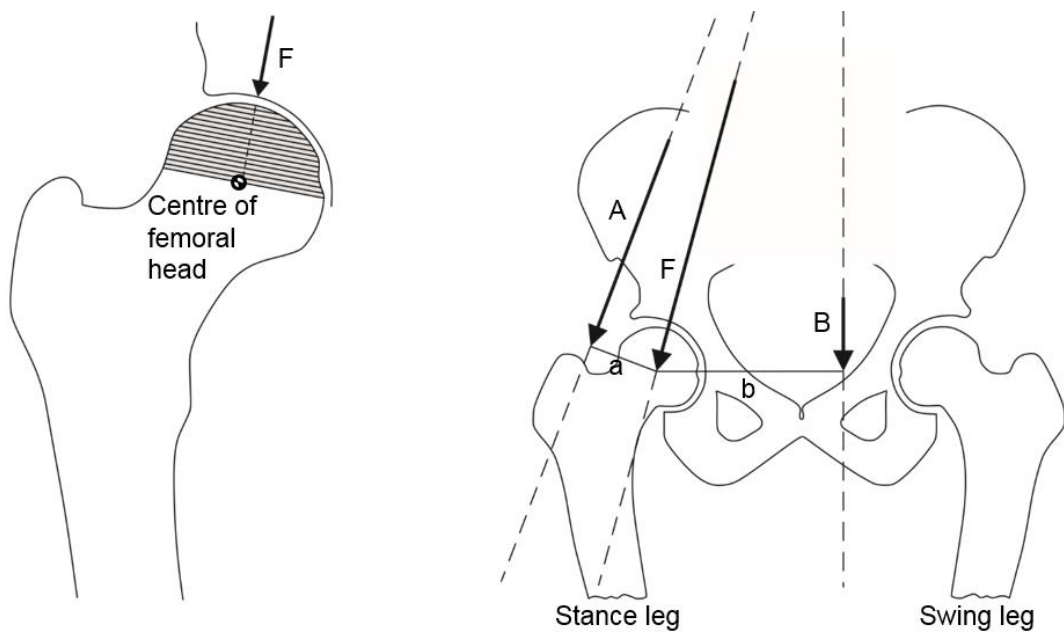


Figure 33 Loading diagram for the hip while walking, where B is the body weight (minus the weight bearing leg), A is the abductor muscle force and F is the joint contact force. The load of the body weight does not go directly through the joint and the resulting moment is counterbalanced by the abductor force. The femoral head is therefore subjected with the joint contact force (F).

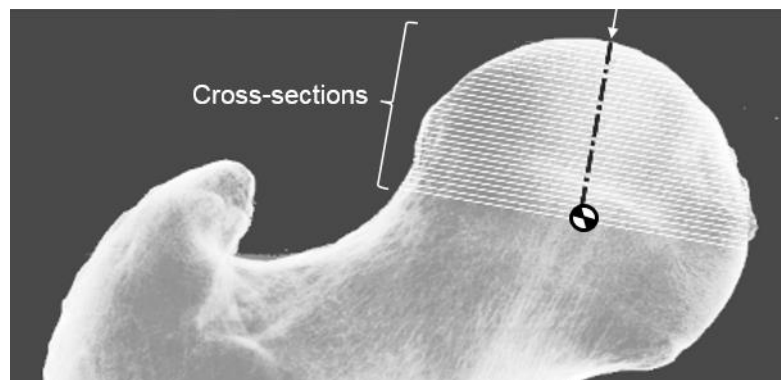


Figure 34 AP view of a segmented femoral head. The superior half of the head was modelled with a beam loaded with a single load pointing to the centre of the femoral head. The load was in direction of the mechanical axis. The thirty disc-like cross-sections (white lines) were perpendicular to the beam axis (black dashed line).

A single CT-scan of a 'healthy' femur was used for this study (University of Leeds ethics approval MEEC 13-002). The femoral head sample was CT-scanned at an isotropic resolution of  $82\mu\text{m}$  using a HRp-QCT-scanner (XtremeCT, Scanco Medical, Switzerland). The scanner was density calibrated using a hydroxyapatite phantom. The sample was scanned in air

with 59kVp tube voltage and 300ms integration time which was similar to the described settings in section 3.4.2.

The CT-scan was subsequently manipulated to simulate AVN pathology to mimic the appearance and behaviour of clinical lesions. Necrotic lesions have been described as having a conical shape with an apex pointing towards the centre of the femoral head (Jones and Engleman, 1966; Mont et al., 1998). Therefore lesions were approximated with a cone-shaped structure within the femoral head which allowed further parametrisation in terms of geometry and location (Figure 35). The Young's moduli of the cone-shaped necrotic area was reduced by 72% as reported by Brown et al. (1982). Finally the CT-scan was manipulated into four different CT-scans which contained a cone-shaped lesion of the same geometry at four different angles from the centre of the femoral head. The lesions were orientated at  $-25^\circ$ ,  $10^\circ$ ,  $45^\circ$  and  $80^\circ$  from the positive vertical axis. This covered the range of locations previously described by Ohzono et al. (1991) and Motomura et al. (2011). The cortical bone was left unaffected. The included angle of the cone was  $90^\circ$ .

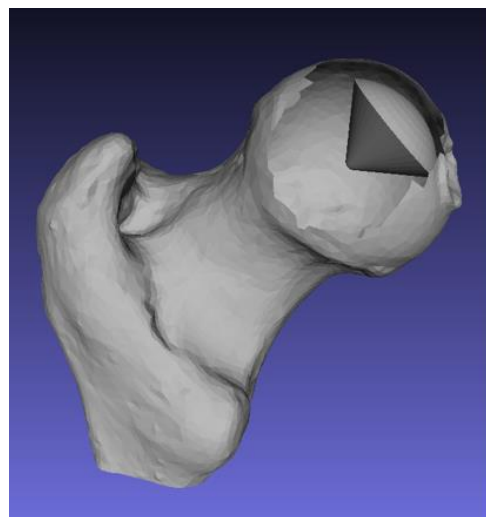


Figure 35 Schematic illustrating the conical shape and location of the simulated lesion within the femoral head. The cone is angled at  $45^\circ$ .

The tool calculated the axial and bending stiffness (EA, EI) for each cross-section of a sample (Eqs. 3.2, 3.3, 3.4). The beam theory equation (Eq. 3.8) was then used to predict the fracture load at which bone in each respective cross section was likely to fracture. The calculated structural parameter and failure loads of each lesion affected femur were compared against results from the CT-scan of the original unaffected femur to analyse the stiffness and

failure load differences that were caused by the lesions. The maximum differences were calculated and compared across all samples. A significant reduction of the structural stiffness may indicate a weak cross-section where fracture might initiate. The reduction in structural stiffness could potentially be used to quantify the fracture risk of the femoral head where the application of the beam theory equation was deemed unreliable because of the geometric shape of the bone.

The shape of the cross-section was approximately axisymmetric as the femoral head forms a sphere (Huiskes et al., 1981). The bending stiffness ( $EI$ ) needed to be calculated in two directions which led to two different values. Alternatively, the average bending stiffness can be measured as the torsional stiffness ( $GJ$ ) as the torsional constant ( $J$ ) was the sum of the second moment of area ( $I$ ) in both bending orientations,  $J=I_{xx}+I_{yy}$  (Lieberman et al., 2004). The shear modulus can be approximated with  $G=E/3$  (Salathe and Arangio, 1989). Linking both elastic constants can be justified in this context as  $GJ$  was used as a comparative value only.

### 3.6.3 Results

Failure load, axial and bending stiffness of cross-sections of the four femoral heads with cone-shaped simulated lesions were calculated for two loading scenarios (Figure 36 and Figure 37). The location of the modulus weighted centroids had a better fit with the beam axis angled at 10°.

There was a significant reduction of the axial stiffness in lesion affected areas of the femoral head (Figure 38A). The reduction of the bending stiffness was heavily influenced by the distance of the lesions to the centroid (Eqs.3.3,3.4). All lesions were symmetric about the coronal plane and therefore reduction of the bending stiffness ( $EI_y$ ), which was rotated around the medial-lateral axis of the femoral heads, was relatively constant and mostly lower than the bending stiffness about the anterior-posterior axis ( $EI_x$ ).  $EI_x$  was strongly influenced by the lesion type. The lesion angled at 10° was aligned to the beam axis and therefore both  $EI_x$  and  $EI_y$  were equally slightly reduced as the lesion was close to the centroid in both rotational axes (Figure 38, B2).

The predicted failure loads showed a reduction when the lesion was close to the point of loading (Figure 38C 1,2). However the femurs with lesions angled at 45° and 80° (Figure 37C 3,4) surprisingly showed an increased and less harmful predicted failure load compared to the healthy femur.

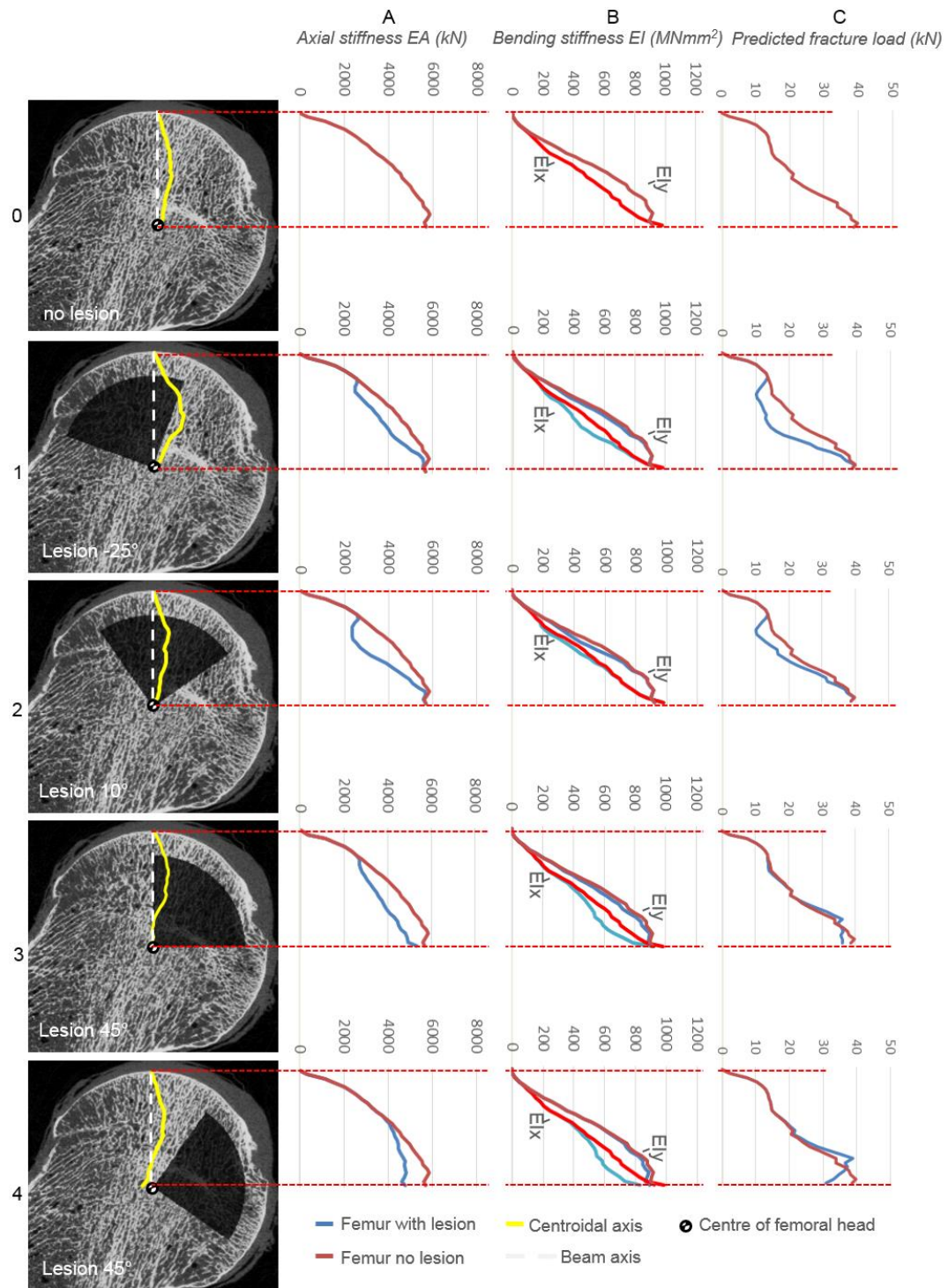


Figure 36 Axial (A) and bending (B) stiffness, and failure load (C) were calculated for each corresponding cross-section of four femoral heads with cone-shaped simulated lesions angled at  $-25^\circ$  (1),  $10^\circ$  (2),  $45^\circ$  (3) and  $80^\circ$  (4) from the positive vertical axis. The plane of the cross-sections were perpendicular to the beam axis (white line) which was collinear with x-axis of the corresponding three line charts. The results of the four lesion affected femurs (blue lines) were compared to the results for an unaffected femoral head (red lines). The beam axis and loading was vertical which approximated a double-legged stance.

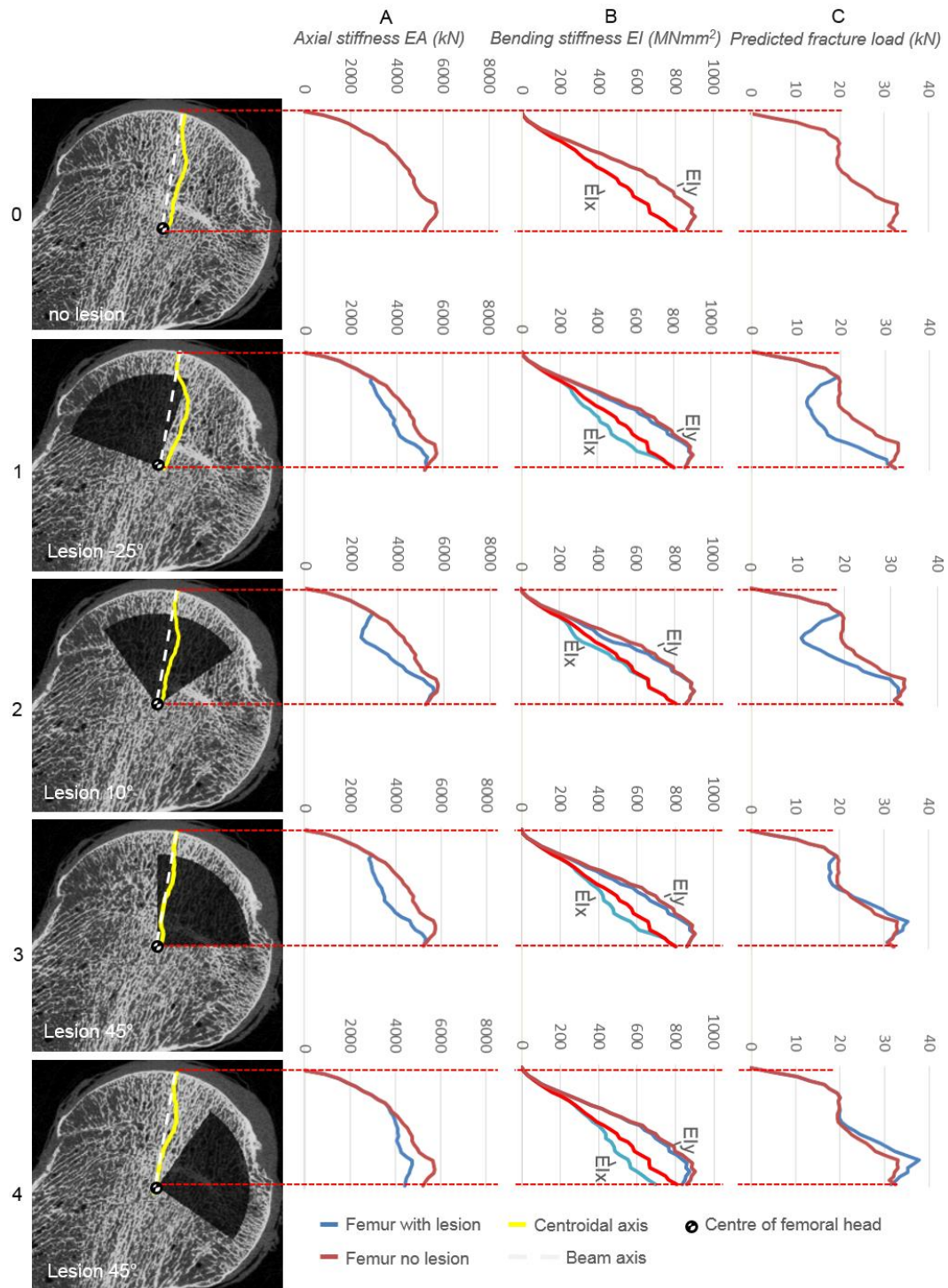


Figure 37 Axial and bending stiffness, and failure load of cross-sections of four femoral heads with different cone-shaped simulated lesions (angled -25° (1), 10° (2), 45° (3) and 80° (4)) compared to an unaffected femur. The beam axis (white line) had an angle of 10° about the vertical axis which approximated a single-legged stance.

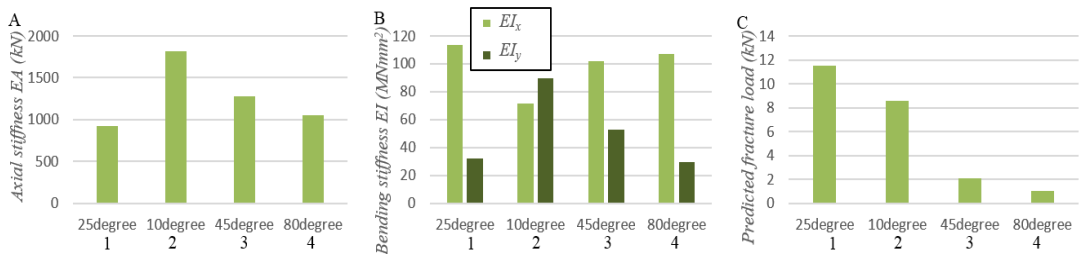


Figure 38 Maximum difference between healthy and four lesion affected femoral heads for A) Axial stiffness, B) Bending stiffness, C) Fracture load. The cone-shaped lesions were angled at  $-25^\circ$  (1),  $10^\circ$  (2),  $45^\circ$  (3) and  $80^\circ$  (4) from the vertical axis.

### 3.6.4 Discussion

This study, the beam tool was used to calculate the axial stiffness, the bending stiffness and the fracture load for each cross-section of a lesion affected femoral head and the results were compared against the same femoral head without lesion. The ability of all three parameters to predict the increase of the fracture risk as a result of a necrotic lesion was compared.

The direct use of the beam theory equation (Eq.3.8) to calculate exact fracture loads for the femoral head beam model was unreliable which had two reasons. Firstly, the cross-section with the lowest predicted fracture load was assumed to be the weakest and fracture was assumed to initiate here. However, the identification of a single weak cross-section was not possible for the femoral head. The predicted fracture load increased gradually with the expanding cross-sectional area of the head without any clearly identifiable minimum of the stiffness curve and therefore the identification of a single weak cross-section was not possible as it would be possible for a bone structure without taper. The assumed point load at the top of the femoral head created a high stress concentration.

Secondly, the predicted fracture load was strongly influenced by the location of the beam axis. The tool predicted that lesions angled at  $45^\circ$  and  $80^\circ$  were locally stronger than a lesion unaffected femoral head which was unrealistic (Figure 36C 3,4). The beam equation consisted of two stress components, bending and compression (Eq.3.11) (Figure 39). The medial side of the healthy femoral head had a denser structure than the lateral side. This inhomogeneity of the material distribution in the healthy femur shifted the modulus weighted centroid away from the beam axis which increased the bending moment. The bending moment is defined by the distance ( $a$ ) between the beam axis and the centroid multiplied by the joint contact force ( $F$ ).

$$\sigma = \left\{ \frac{F}{A} \right\}_{axial} + \left\{ \frac{F \cdot a}{I} \cdot c \right\}_{bending} \quad 3.11$$

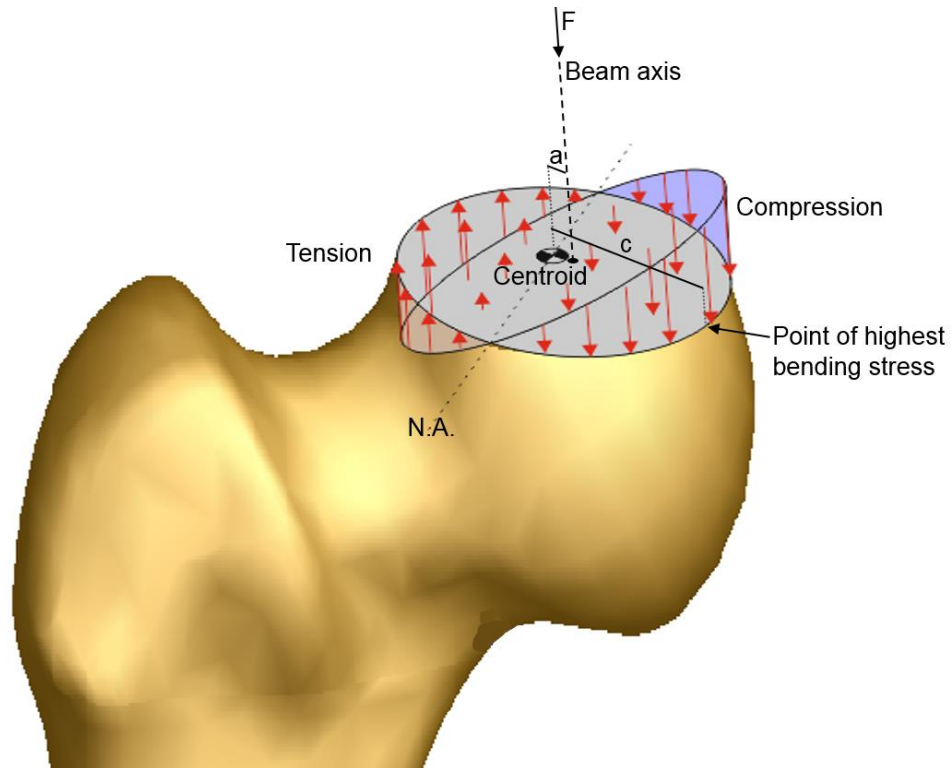


Figure 39 Stress distribution as a results of bending. Bending was not a result of a transverse load but the distance (a) between modulus weighted centroid and the load/beam axis.

The lesion angled at 45° and 80° counter balance this shift of the modulus weighted centroid and reduced the distance  $a$ . This reduced the stress component from bending leading to a higher predicted fracture load for the femur than the unaffected femur. In this test, the bending influence varied from being slightly greater than the axial compression to almost no influence at all which was caused by the discrepancy between the beam and centroidal axes. A close match between the centroidal and the beam axis is desirable to avoid compromising the calculation. There was generally a better fit between the beam axis (white line) and the centroid (yellow line) in Figure 37 than in Figure 36. However a beam axis in form of a higher parameter function which exactly followed the trajectory of the modulus weighted centroids was presumed inappropriate as it would not lead to better results. A beam axis with a winding appearance would lead to an unsuitable slicing direction because the analysed cross-sections are perpendicular to the beam axis. For structures

with inhomogeneous material distributions like the human femoral head, a precise estimation of the exact magnitude of the fracture load was not possible and the predicted loads were not very indicative.

The fracture risk can be assessed by comparing the structural stiffness of an lesion affected femoral head with the corresponding stiffness of an intact femoral head. The maximum relative difference quantified the fracture risk. Structural stiffness accounted for both material and for geometrical properties.

The preliminary test showed that simulated necrotic lesions significantly reduced the axial stiffness (EA). It was mainly influenced by the lesion volume and the reduction of the Young's modulus. The axial stiffness described the ability of a beam cross-section to withstand axial loading (Lieberman et al., 2004). Axial compression was assumed to be the main loading mode of the upper part of the femoral head (Keyak et al., 2005; Cristofolini et al., 2007). Therefore the axial stiffness appeared to be an excellent parameter to assess the fracture risk of the femoral head.

The bending stiffness (EI) described the ability of a cross-section to withstand a bending moment. The bending stiffness took the lesion position into account. Lesions close to the surface were more critical as they were further away from the centroid. However, the relative stiffness difference was not as distinctive as the axial stiffness which indicated that it had inferior predictive capability as fracture prediction tool for the femoral head.

Although all simulated lesions were of the same volume, some of them resulted in higher stress concentrations in some areas and hence were potentially more severe. Material influence appeared to be an important factor for the fracture risk.

In conclusion, the axial stiffness was capable of identifying necrotic lesions that might lead to fracture of the femoral head. In contrast, the predicted fracture load did not appear to be a reliable criterion to identify lesions that are at risk of fracturing. The choice of the beam axis should reflect the location of the trajectory of the modulus weighted centroid in each cross-section. The beam axis angled at 10° to the medial had a better fit than the vertical axis. It also better aligned with the principal trabecular orientation. Overall, the initial tests with the computational beam tool showed that a fracture prediction tool based on CT-images seemed practical as the axial stiffness had a good predictive abilities. The magnitude of the reduction of the stiffness was an indicator of the fracture risk of the analysed femoral head sample. Further

investigation is needed to verify the fracture prediction tool against *in-vitro* tests.

### 3.7 Summary

The first part of this chapter led to the following findings:

- A fracture prediction tool based on structural mechanics and beam theory was successfully developed which used density calibrated CT-scans.
- A density-modulus conversion material model was verified against trabecular bone plugs from human femoral heads showing that such a model is able to produce reliable material property inputs for fracture simulations based on beam theory.
- A sensitivity study showed that the material model was relatively resolution stable when calculating structural properties.
- A segmentation of the trabecular bone did not lead to more accurate results and also required high resolution CT-scans which were not necessarily available in the clinical setting.

The tool was finally used to predict the fracture risk from CT-scans of femoral heads with simulated necrotic lesion. While the predicted fracture loads and the bending stiffness had poor results, the axial stiffness appeared capable of identifying necrotic lesions that might lead to fracture of the femoral head. Further investigation is needed to verify the fracture prediction tool against experimental tests.

## Chapter 4 Verification of the fracture prediction tool against physical disease models

### 4.1 Introduction

This chapter describes the verification of the developed fracture prediction tool against physical disease models *in-vitro* following previous verification against simple theoretical disease models as described in section 3.6. It was demonstrated that the *in-silico* tool was sensitive enough to detect lesions however it needed to be verified whether the predicted increased fracture risk as a result of a lesion correlated with experimental tests. Therefore the tool was verified against *in-vitro* tests of human femoral head disease models generated by (1) additive manufacturing, (2) porcine and (3) human femoral head disease models.

The aim of these three studies was to find out if the tool had a predictive capability to identify femurs that have a high fracture risk. Data generated by compressing femoral head models *in-vitro* was used to demonstrate the efficacy of the prediction method in this application compared to a categorisation of the fracture risk based on the lesion type (Table 8). It also helped to better understand failure mechanisms and mechanical behaviour of lesion affected femoral heads.

In the first part of the study, the tool was verified against a solid femur model made via additive manufacturing. Compared to samples of natural tissue, femur models from additive manufacturing did not have variations in structure or material properties which allowed assessment of the effects of lesion geometry and location in isolation. It has been reported that the fracture risk depends on the location of the lesion within the femoral head. The effect of two different lesion positions was analysed for a femur model with otherwise similar geometric shape and material properties. The experimental fracture loads of both samples were compared to investigate whether the lesion position was indeed a significant driver for fracture and whether the *in-silico* tool was able to correctly predict this trend. The tool predicted fracture based on the material properties and the geometry of the femur.

The second part of the study investigated whether natural femoral head samples with similar lesions also had similar *in-vitro* fracture loads. A porcine model was chosen as it allowed to look at a great number of femur samples of similar size and age. It allowed to include effects of natural bone tissue variations and trabecular structure. The verification against porcine femoral

head models also assessed whether material and structural parameter could be retrieved from density calibrated CT-scans. A disadvantage of porcine samples was slippage of the epiphyseal plate at higher loads which the tool cannot detect. While epiphyseal plates were very poor in bearing shear stress, they can withstand axial loads (Heimkes et al., 1993), nevertheless they remained vulnerable to fracture at high axial loads. An accurate fracture prediction was therefore difficult.

In the last study, the tool was verified against human femoral head samples with simulated lesions. The computational tool characterised the fracture risk of each sample based on how its axial stiffness compared to a reference set of healthy samples. While a risk classification based on the lesion volume and location only took geometrical information into account, the fracture prediction method based on axial stiffness also considered material properties of bone which potentially increased its predictive capability.

In all three verification studies, simple voids were used to mimic the appearance and behaviour of avascular necrotic lesions, however the mechanical implications of AVN lesions are largely unknown. Despite not accurately resembling a necrotic lesion, the simulated lesions provided a method to verify the fracture prediction model in respect of AVN. Attempts to simulate necrotic bone tissue by substituting a drilled hole with bone plugs of reduced material properties was not successful as the interface between the femur and the bone plug was not able to provide support to the loaded femur (Anderson, 2015). Injections with acid to reduce the material properties were not successful either as the acid would not disperse within dense trabeculae of bone volume of the porcine heads (Avadi, 2016).

## **4.2 Verification against femoral head models with simulated lesions made by additive manufacturing**

### **4.2.1 Introduction**

In a first instance, solid proximal femur models were used to verify the developed fracture prediction tool. Two femoral head models with identical geometric shape but with two different lesion positions were created which allowed an isolated assessment of the lesion geometry and location in terms of fracture risk. In contrast to natural trabecular bone, additive manufactured models did not have material variations and all material properties were known. Ohzono et al. (1991) reported that collapse of the femoral head most often occurs when the lesion location is in the weight bearing area.

The first objective of this study was to analyse the effect different lesion locations had on the experimental fracture load of the femur. It was showed if a femoral head model with a lesion within the subchondral area had a higher fracture risk than a sample with a lesion elsewhere. A secondary objective was to investigate whether the *in-silico* fracture prediction tool could predict a similar trend or even have better predictive capabilities than the fracture risk prediction based on the lesion location. Whether the developed tool was able to identify points within the proximal femur models where fracture was likely to initiate was assessed finally.

#### **4.2.2 Methods**

##### **4.2.2.1 Femur model**

A solid three-dimensional model of a proximal femur was developed using SolidWorks2013 (Dassault Systèmes, France). The geometric shape of the bone model was based on a CT-scan from a cadaveric femur from a 55 year old male donor (supplied by Platinum Training, USA and use approved by University of Leeds Engineering research ethics committee, MEEC 13-002). The femur was segmented using ScanIP (Version 6.0, Simpleware Ltd., UK).

Using this initial femur model, two further models were created which incorporated two different types of cone-shaped voids that were intended to simulate AVN lesions in a similar way as described in Chapter 3.6.2. The apex direction of the lesions were fixed in the coronal plane and angled to the loading axis of the femur at 45° (*Lesion Type 1*) and at 80° (*Lesion Type 2*). Including the model with no lesion, three solid proximal femur models were tested and compared (Figure 40). The slant height of the cone-shaped lesion was 20mm (Appendix A). The shape of necrotic lesions is commonly described as a wedge shaped zone centred at the centre of the femoral head (Brown et al., 1982). Ohzono et al. (1991) reported that collapse of the femoral head most often occurs when the lesion location is in the weight bearing area therefore one lesion was positioned within the weight bearing area and the other lesion was angled more medial. Both cases had a similar lesion volumes.

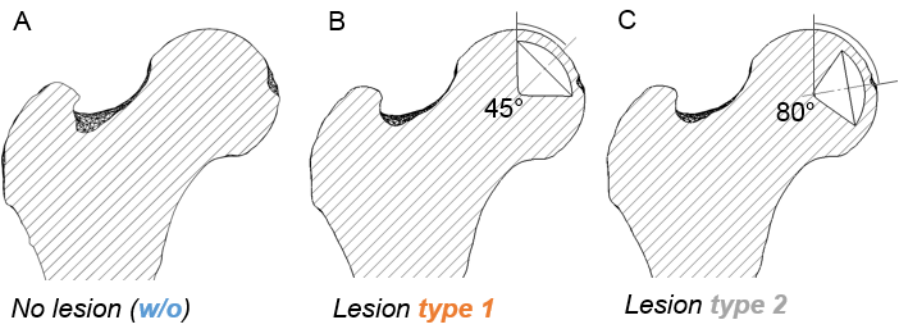


Figure 40 Schematic of hip model showing anterior posterior cross-section view of three 3D-printed proximal femur models including femoral head neck, greater and lesser trochanter. Two lesions were simulated with cone shaped voids at two different angles to the loading axis of the femur, 45° (B) and 80° (C).

#### 4.2.2.2 Femoral head beam model

The three femoral head cases were then modelled by a beam loaded with a single joint contact load. The loading approximated a single legged stance as described in chapter 3.6.2. A straight beam axis was established which followed the simplified loading vector from the point of loading on the bone surface to the centre of the femoral head. The beam axis defined the virtual slicing direction of the femur model as all cross-sections were perpendicular to the beam axis. The beam tool analysed a total of 30 cross-sections which were evenly distributed along the beam axis. The geometric shape of the proximal femur samples was known and a binary image matrix, which was derived from the STL-file, was imported directly into the fracture prediction tool.

The subchondral area of the femoral head has rapidly increasing cross-sectional areas and a short length compared to its thickness. These attributes were in conflict with the assumptions made for the application of beam theory that the beam is straight slender and any taper must be slight. The use of the beam theory equation to calculate exact fracture loads for the femoral head was therefore not possible. However, Euler-Bernoulli beam theory accounts for axial ( $EA$ ) and bending stiffness ( $EI$ ) of its beam sections beside geometric information of the structure. The structural stiffness was used as a predictor of bone fracture within the femoral head as it accounted for both material and for geometrical properties. The axial stiffness described the ability of a cross-section to withstand axial loading which was assumed to be the main loading mode of the upper part of the femoral head.

The beam tool calculated the axial stiffness of each cross section. As described in chapter 3.2.7, the calculated stiffness increased gradually with the expanding cross-sectional area of the head without any clearly identifiable minimum of the stiffness curve and therefore the identification of a single weak cross-section was not possible. For this reason, the axial stiffness could only be used in a way to compare relative differences to the intact sample. The fracture risk was computationally assessed by comparing the axial stiffness of all cross-sections of each lesion affected sample with the corresponding axial stiffness of the unaffected sample (Figure 41). The axial stiffness of the lesion affected femoral head sample was divided by the corresponding stiffness of the unaffected sample (Eq.4.1). The ratio gave an indication for the reduction in the structural stiffness of the lesion affected femoral head relative to the intact head.

$$\min [EA_{lesion\ i} / EA_{no\_lesion\ i}] \quad 4.1$$

The number of the analysed cross-sections was  $i$  ( $i=0\dots30$ ). The cross-section with the lowest percentage of the control stiffness was assumed to be the weakest and fracture was likely to initiate here. The lowest ratio of each sample was compared against the sample's experimental fracture load to see which of the two lesions was more critical for fracture. The reduction in the axial stiffness was assumed to lead to a decrease of the fracture load of that sample.

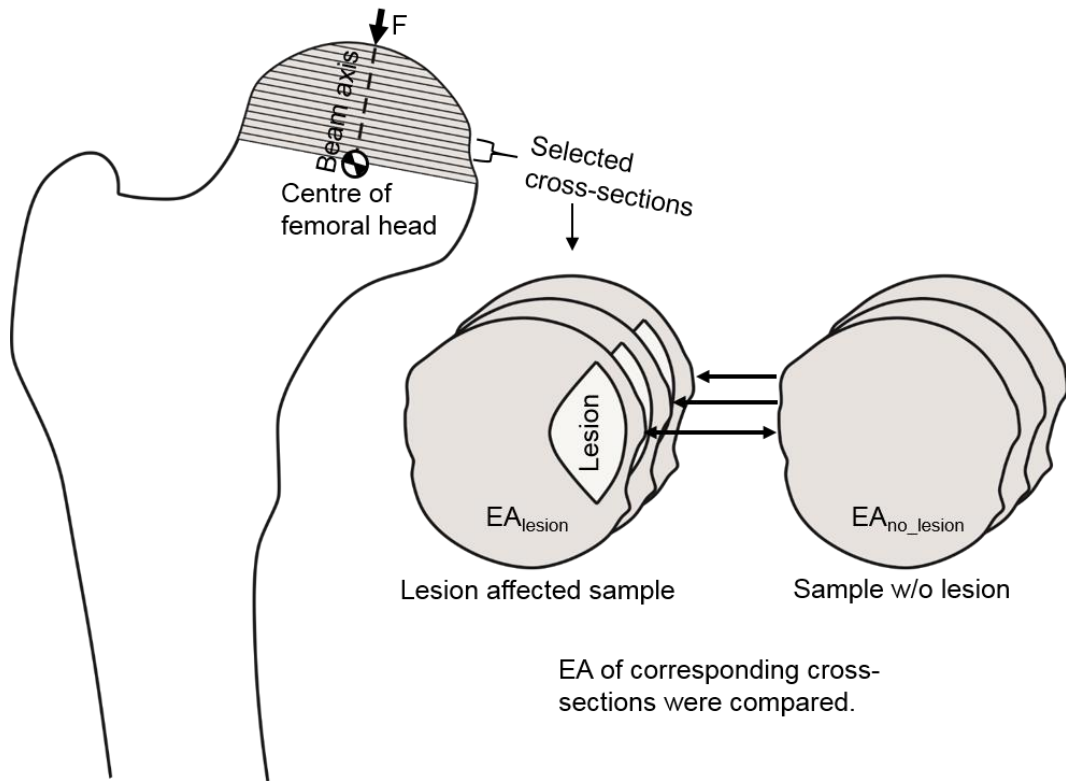


Figure 41 Schematic of the proximal femur including assumed straight beam axis. The analysed cross-sections are perpendicular to the beam axis. The axial stiffness of lesion affected cross-section was compared to the stiffness of the corresponding cross-section without lesion in order to predict fracture.

#### 4.2.2.3 Properties of Selective Laser Sintering material

A total of nine femur models (three of each type) were built on a Vanguard HS HiQ SLS (Selective Laser Sintering) Rapid Manufacturing machine (3D Systems Corporation, CA) and were manufactured from SLS DuraForm PA Nylon. SLS material tends to be anisotropic depending on the build direction. The specimens were printed with cross scan which means that the direction of scanning alternated from layer to layer making it as close to isotropic material as possible. However the building direction still had potentially reduced material properties.

A material test on tensile bars in accordance of ISO527-2 (BSI, 2012) was done to analyse the material properties in each building direction. The breadth of the sample was 4mm and the width was 10mm (Appendix B). All tests were completed at 26° temperature with strain rate of 1mm/min up until an extension of 2mm was reached and then at a strain rate of 5mm/min until fracture. Five samples for each of the three different build orientations were made (Figure 42) which helped to assess whether different building

orientations had an effect on the material properties. All 15 samples were tensile tested to measure the Young's modulus and the failure strain (Figure 43). While the Young's modulus and ultimate tensile strength were relatively unaffected by the build direction, the elongation at break differed significantly (Figure 44). Therefore, the building direction was set to be in the coronal plane of the femur model which was assumed to have the least effect on the overall integrity of the structure.

For the computational fracture simulation, the Young's modulus and the failure strain of the material of the model were required. Ajoku et al. (2006) analysed the material properties of the same material made from SLS and presented tensile, flexural, and compression tests according to ISO standards. Eventually, the Young's modulus was assumed to be 721.5MPa with a yield strain of 6% for compression and 2000MPa with 8.5% for tension.

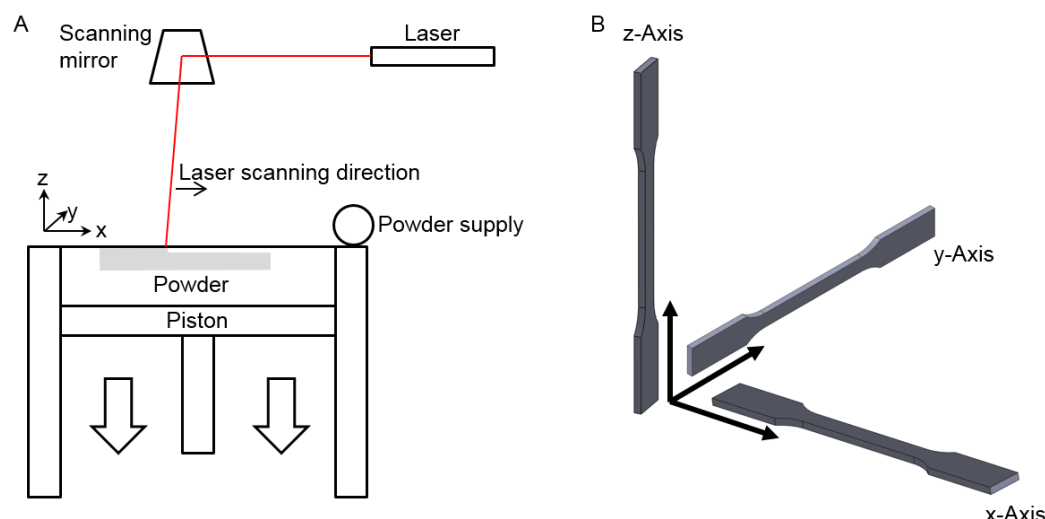


Figure 42 A) Schematic of the process of selective laser sintering. The z-axis is in the direction of powder layers. Materials made with SLS are believed to be anisotropic depending on the build orientation. B) Tensile bars were made in different orientation to measure the effect of the build orientation on the material properties.

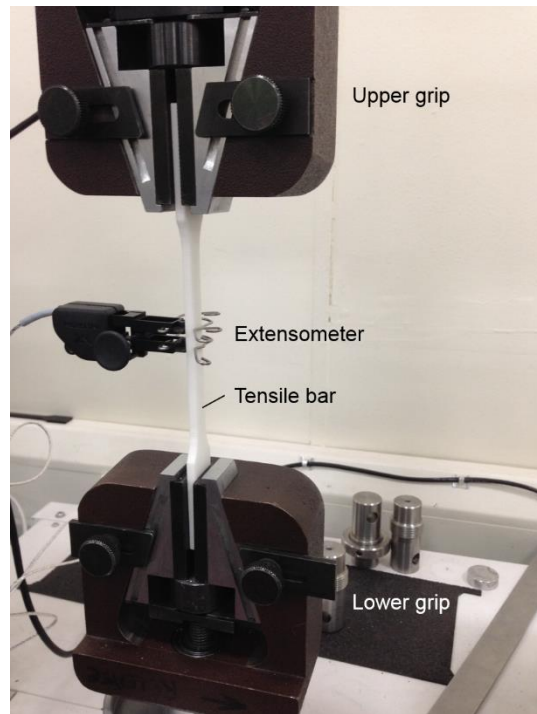


Figure 43 The tensile bar was material tested to determine the ultimate tensile stress, tensile modulus and failure strain.

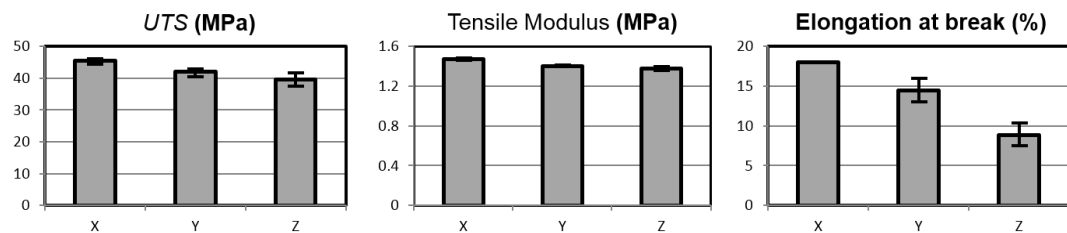


Figure 44 Results of tensile tests of five DuraForm PA Nylon samples in each building direction: Young's modulus ( $1419\pm41$  MPa), ultimate tensile stress ( $42.4\pm2.4$  MPa) and failure strain ( $13.8\pm3.8\%$ ) vs build orientation of the test sample.

#### 4.2.2.4 Experimental set-up

The 3D-printed femur models ( $n=9$ ) were compression tested until fracture or until a load of 35kN was reached using an Instron 3366 single axis tension-compression machine (Instron, Norwood, MA). The nine femoral head models were tested individually. The femoral heads (three of each lesion type) were fixed into a PMMA mould (Figure 45) (2 parts powder for 1 part liquid ,WHD plastics, Hull, UK) (Appendix C). The cement support just reached to the lower end of the head in order to avoid neck fracture. A cement fixture was used for these models to be able to compare the methodology to femur models from

natural tissue. The femur model was loaded with a flat platen. The direction of loading simulated the approximate loading position during a one legged-stand. The *in-vitro* loading correlated with the direction of the beam axis *in-silico*. The displacement rate was 0.2mm/min.

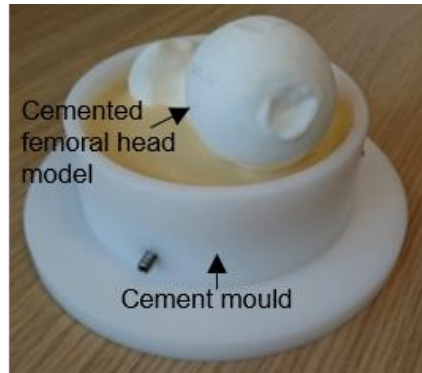


Figure 45 PMMA cemented femoral head models from additive manufacture were compression tested. All mounted samples were loaded with a flat platen.

#### 4.2.3 Results

For the computational analysis, the reduction in the structural stiffness of the lesion affected femoral head samples relative to the unaffected sample was quantified by the lowest ratio of its axial stiffness to the axial stiffness of corresponding unaffected sample (Figure 46). The sample with a lesion angled at 45° (type 1) showed a greater reduction in stiffness with a ratio of 0.78 compared to the sample with a lesion angled at 80° (type 2) which had a ratio of  $\min\{EA_{lesion\_type2} / EA_{no\_lesion}\} = 0.84$ .

This correlated with the experimental results. Three of each 3D-printed head samples of lesion type 1, type 2 and control samples were compression tested *in-vitro* ( $n=9$ ). The results for the three repeats were almost identical. The femoral heads fracture at  $24.50\text{kN} \pm 1.5$  for lesion types 1 and at  $27.50\text{kN} \pm 0.50$  for lesion type 2. Samples with a lesion type 1 had a lower experimental stiffness and fracture load than a sample containing a lesion of type 2 (Figure 47). Most samples showed fracture around the lesion (Figure 48). One sample of lesion type 1 was just compressed without detectable fracture. The three control samples (solid head without lesion) did not fracture up to a load of 35kN. It was not possible to identify the exact location within the post-fractured femur model where fracture initiated.

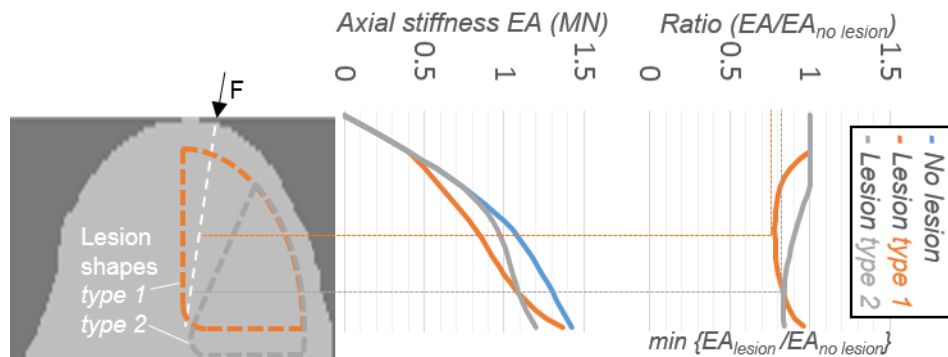


Figure 46 Output from the developed tool, calculating the axial stiffness. Cross-sections were perpendicular to the beam axis. The stiffness of femur models with two different lesion types were compared against the stiffness of a control femur without lesion. Differently shaped voids in the head resulted in a lower stiffness. A low stiffness meant a higher fracture risk at the respective location.

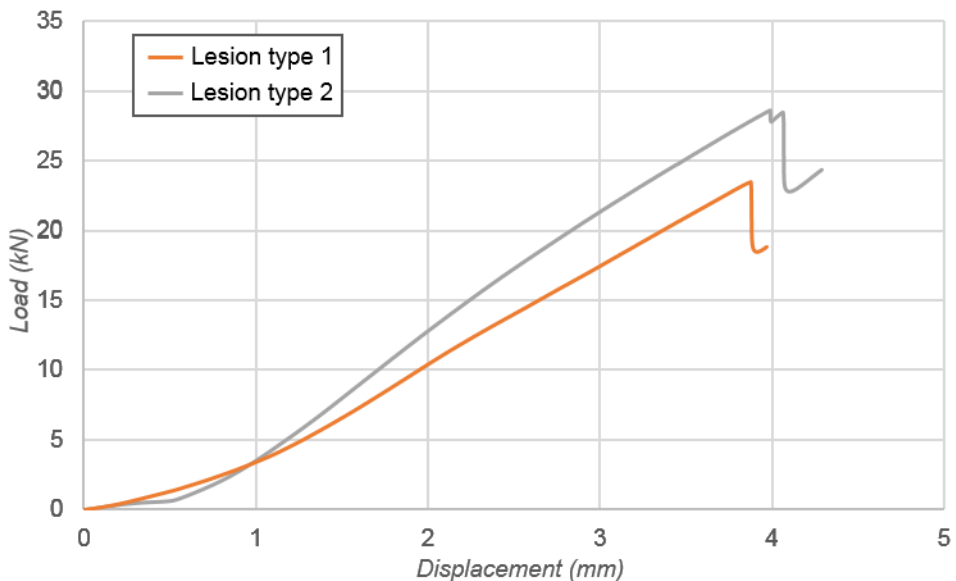


Figure 47 Load-Displacement curve of a typical compression test on two femoral head samples. One sample had a lesion of type 1 and one sample had a lesion of type 2. Type 1 samples had a lower stiffness and a lower fracture load compared to samples with a lesion type 2.

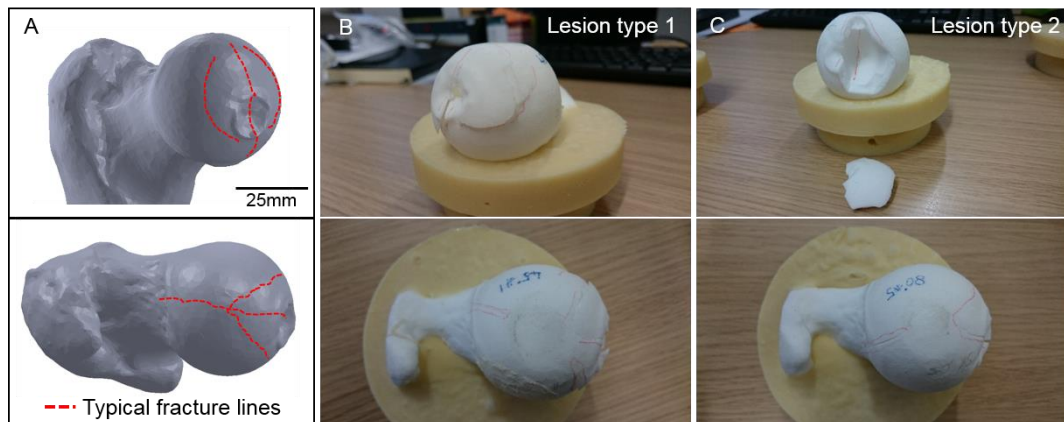


Figure 48 (A) The typical observed fracture lines (red) from the *in-vitro* compression tests on the cemented additive manufacture femoral head models. (B) Photo of the fracture sample of lesion type 1. (C) Photo of a sample containing a lesion of type 2 post-fracture.

#### 4.2.4 Discussion

The loading situation and the special geometry of the superior part of the femoral head with its rapidly increasing cross-sectional area were not suitable for the application of the beam equation. Rather than predicting an exact fracture load for the femoral head, the fracture risk was defined by how much the axial stiffness of a sample differed from a healthy unaffected femoral head sample.

The cross-section with the highest reduction in stiffness was assumed to be the location where fracture of the entire model initiated. Therefore, the highest reduction in axial stiffness within a sample was used to assess the overall increase of the fracture risk as a result of the simulated AVN lesions. However, it was not possible to identify the exact location within the post-fracture femoral head models where fracture initiated in order to correlate it with the location of the cross-section that was predicted to be the weakest.

Nevertheless, the tool correctly predicted that the femoral head model with a lesion in the weight bearing area had a higher fracture risk than the femur model with a lesion medial to the fovea as reported by Ohzono et al. (1991). This preliminary study indicated that the axial stiffness might have a good predictive capability to predict fracture risk within the subchondral area of the femoral head.

The experimental tests showed that the lesion location influenced both the stiffness and the fracture load of the femoral head model. A lesion lateral to

the fovea had a greater affect than a lesion which was located medial which supported findings from Ohzono *et al.* (1991) and Motomura *et al.* (2011).

Solid femoral head models made from rapid prototyping offered a way to structurally assess the geometry without the influence of inhomogeneous trabecular distribution. It was therefore more consistent compared to real bone tissue and the material properties were known. However, a solid femur model hardly resembles a natural femur which has a complex internal trabecular structure and therefore further verification was needed.

## 4.3 Verification against porcine femoral heads

### 4.3.1 Introduction

The fracture prediction tool was verified against porcine femoral heads. Additive manufacturing allowed to compare lesion affected femoral head models with unaffected models with otherwise identical geometric shape. A porcine model was chosen because it also allowed to look at a great number of femur samples of similar size and age. Porcine femoral heads had also a similar shape to human femoral heads (Raab *et al.*, 1991), however they had a denser trabecular network (Mosekilde *et al.*, 1993). To enable accurate predictions, the beam tool require geometric and material property inputs. Material properties can be derived from tomographic images using empirical relationships between density measurements and Young's modulus (Carter and Hayes, 1976; Keaveny *et al.*, 1994; Helgason *et al.*, 2008; Schileo *et al.*, 2008).

The aim of this study was to verify the image based fracture prediction tool which non-invasively assessed the fracture risk of porcine femoral heads affected by simulated lesions. The first objective of this study was to investigate whether the axial stiffness, which comprehends material and geometric properties, had better predictive capabilities in terms of fracture risk than a categorisation of the fracture risk based on the lesion type which was an assessment of the geometry alone. Data generated by compressing porcine femoral head models *in-vitro* was used to demonstrate the efficacy of this application by comparing the fracture loads with the calculated stiffness reduction. A predicted decrease in the structural stiffness would ideally be reflected by a low experimental fracture load. The second objective was to analyse whether femoral head samples with similar lesions also had similar *in-vitro* fracture loads. Because of the similar geometric size, femoral head samples with a similar lesion type in terms of location and volume should show

the same experimental fracture loads, if the lesion was really the most significant driver for fracture.

### 4.3.2 Methods

#### 4.3.2.1 Sample preparation

A series of eighteen porcine femoral head models were tested to assess the effect of lesions within the head (Figure 49). Fresh whole porcine legs were obtained from a local abattoir where the age of slaughter was between 24 to 26 weeks (mean weight at point slaughter  $76.6 \pm 7.3\text{kg}$ ). The mean head diameter of all porcine femoral heads was 37.1mm with a low standard deviation of 1.6mm. All samples were prepared within 24 hours of sacrifice and were kept hydrated with cloths soaked with phosphate-buffered saline solution.

After removing soft tissue, the porcine femoral heads were cemented into a mould. The femur sample was mounted along loading axis which was angled at  $10^\circ$  to the physiologic biomechanical axis in the coronal plane. The greater trochanter was removed as it would have interfered with the loading of the femoral head (Figure 50). The cement supported the lower end of the femoral head to avoid neck fractures as AVN mainly affects the subchondral area of the femoral head.

Two lesion groups were created with two different lesion characteristics. Samples were prepared with a hole (mimicking a lesion) lateral to the fovea ( $n=6$ ) (Figure 51A), with a hole medial ( $n=6$ ) (Figure 51B) and control samples with no lesion ( $n=6$ ) (Figure 51C). A hole with a diameter of 11mm was drilled into the porcine femoral head through the femoral neck without damaging the cortex of the head to mimic the lesions. It has been reported that the fracture risk depends on the location of the lesion within the femoral head (Ohzono *et al.*, 1991). Care was taken to create lesions that were equivalent in location and position within each lesion group. The edges of the drill bit were rounded in order to reduce the impact of stress concentrations caused by sharp changes in geometry. University of Leeds standard operating procedure (SOP.07.17, Appendix D) was followed to create the drilled lesions.

A limitation of using a porcine model was that the lesion could not be contained as it was with the additive manufactured femur model. The lesion was drilled through the neck to avoid damaging the cortex of the femoral head which inevitably weakened the neck. The samples were therefore supported to the lower end of the head in order to avoid neck fracture. In preliminary tests,

lesions were created through the femoral head surface from the inferior, medial and anterior side. When these femoral heads were compression tested, the opening just widened without measurable fracture.

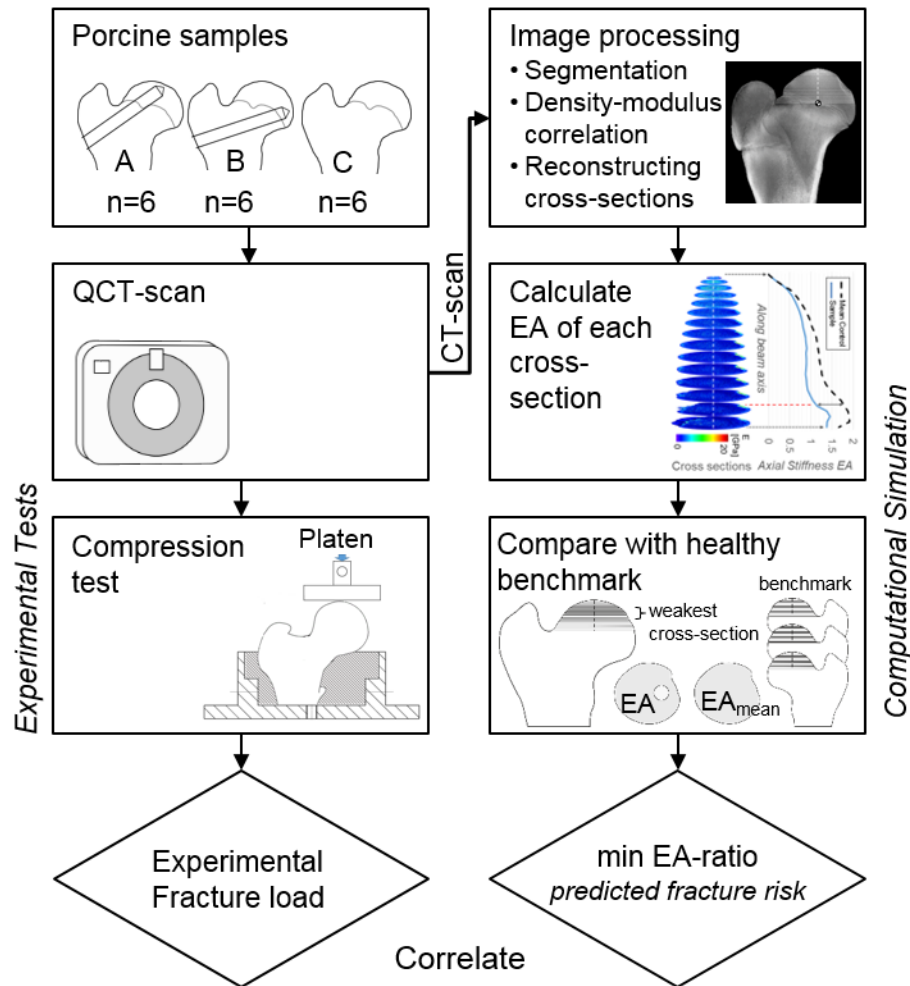


Figure 49: Schematic of the verification workflow. Two lesions were simulated by drilling a hole either lateral or medial to the fovea. Each sample was individually analysed by the fracture prediction tool and subsequently compression tested.

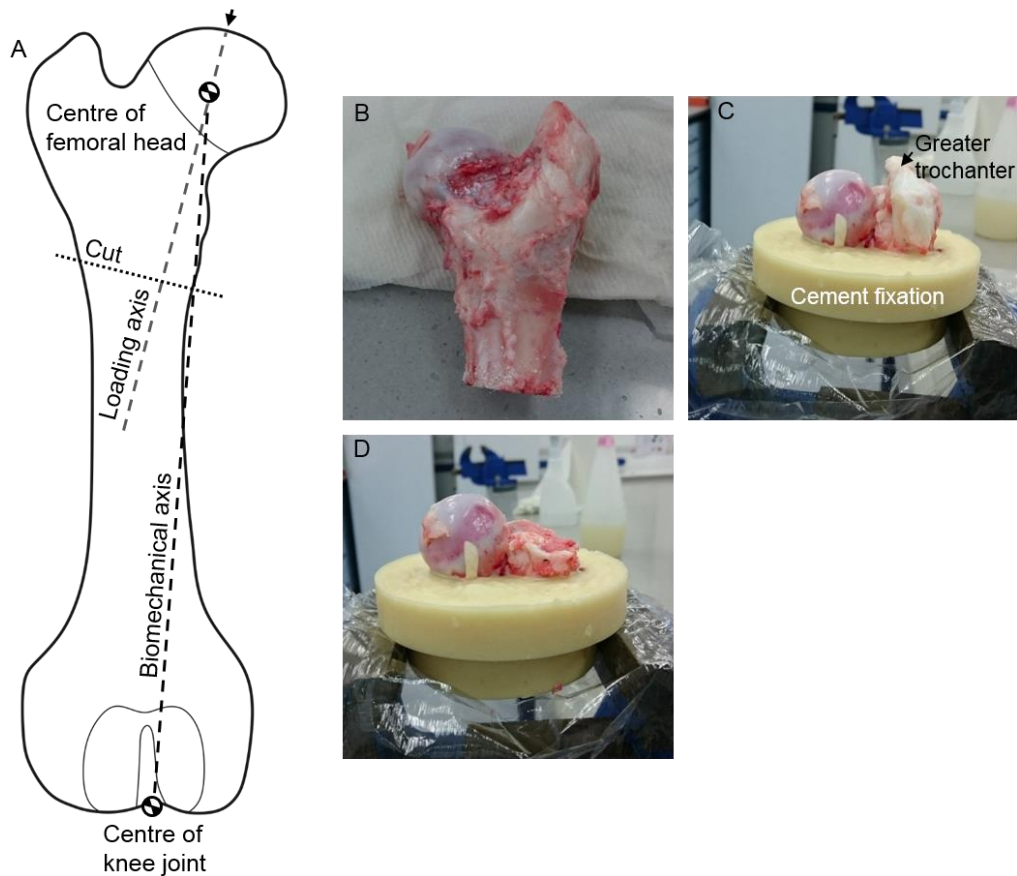


Figure 50 (A) Schematic of a porcine femur preparation. (B) The proximal femur was sectioned perpendicular to the loading axis. (C) The sample was fixated in a cement mould. (D) The greater trochanter was removed.

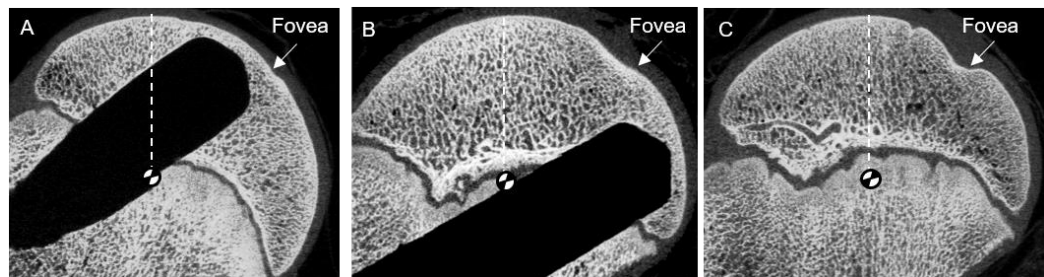


Figure 51 CT-scans showing holes were drilled into porcine femoral heads to mimic necrotic lesion. The hole were drilled either lateral (A) or medial (B) to the fovea and there was a control group with no lesion (C).

#### 4.3.2.2 Femoral head beam model

The femoral heads were then modelled by a beam loaded with a single joint contact load. Like in the previous study, a straight beam axis was established which followed the simplified loading vector from the point of loading on the bone surface to the centre of the femoral head.

#### 4.3.2.3 Image processing

Image planes were reconstructed from the three-dimensional CT-images (generated using HRp-QCT, Scanco Medical, Switzerland). The same scanner settings were used as described in 3.6.2. The femur samples were scanned in air with a voxel size of  $82 \times 82 \times 82 \mu\text{m}^3$ .

To calculate the stiffness of cross-sections of the femur, the bone needed to be segmented on the CT-scan from surrounding soft tissue and air which would compromise the calculation and hence needed to be excluded. An iterative selection method was used in this study to calculate a threshold grey value which in combination with other smoothening image filters was able to separate the femur from the image background (Ridler and Calvard, 1978). The filters included a 3x3pixel median filter to reduce noise, a 10 pixel dilation followed by erosion to fill cavities to capture trabecular bone inside the cortical shell (Figure 52).

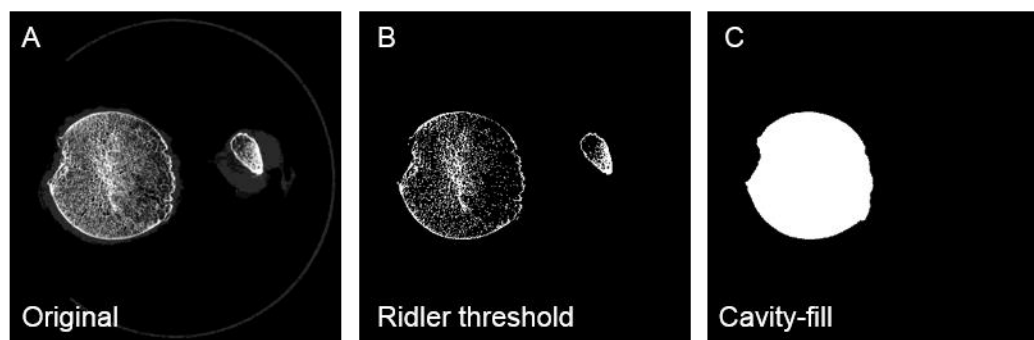


Figure 52 (A) Distal view of a CT cross-section of a femoral head. (B) A threshold filter was applied creating a binary image mask with bone being white. Noise was reduced with a 3x3pixel median filter. (C) A 10 pixel dilation followed by erosion closed cavities within the bone. The trochanter was removed.

#### 4.3.2.4 Material model

A material conversion model based on empirical relationships was used to convert the X-ray attenuation of three dimensional CT images to the equivalent Young's modulus ( $E$ ) (Table 20). The ash content of porcine femur cortical bone is similar to human bone (Aerssens, 1998) and therefore the relationship between scanner density ( $\rho_{\text{QCT}}$ ), ash density ( $\rho_{\text{ash}}$ ) and apparent density ( $\rho_{\text{app}}$ ) for human bone tissue was used as described in (2.4.2).

No density-modulus material model for cancellous porcine bone was reported in the literature and therefore had to be developed. A power law ( $E = \alpha \cdot \rho^\beta$ ) has been found to describe the density-modulus relationship for bone (Carter and Hayes, 1977; Helgason *et al.*, 2008). Therefore, a power law was

approximated from platen compression tests of porcine cancellous bone plugs and data from literature for cortical bone (Figure 53) (Bonney et al., 2011; Avadi, 2016). The sample preparation and testing of the bone plugs followed the methodology described in Chapter 3.4.3. This density-modulus correlation was established for pooled cortical and trabecular bone to account for the whole density range between 0 and 2 g/cm<sup>3</sup> as trabecular is difficult to discriminate from cortical bone on CT-images of the femoral head (Helgason et al., 2008).

Table 20 Density-modulus relationship for porcine femur bone to convert CT-density to Young's modulus information.

| Relationship  | Source                |
|---|-----------------------|
| $\rho_{ash} = 0.877 \rho_{QCT} + 0.0789$ [g/cm <sup>3</sup> ] | Schileo et al., 2008a |
| $\rho_{app} = \rho_{ash} \div 0.6$ [g/cm <sup>3</sup> ]       | Schileo et al., 2008a |
| $E = 5610 \cdot \rho_{app}^{2.13}$ [MPa]                      | Figure 53             |

Ash density  $\rho_{ash}$ , scanner density  $\rho_{QCT}$ , apparent wet density  $\rho_{app}$ , Young's modulus E;

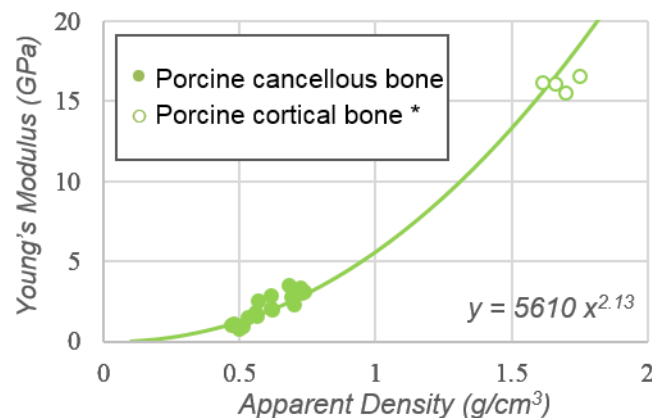


Figure 53: Regression between Young's modulus and apparent density of porcine femoral head bone plugs ( $R^2=0.95$ ). Closed circles present porcine cancellous bone, open circles present tests results for porcine compact bone from \*Bonney et al. (2011). The regression line describes the density-modulus relationship for femoral porcine bone.

#### 4.3.2.5 Experimental set-up

After CT-scanning, the porcine femoral head models were compression tested until fracture using an Instron 3366 single axis tension-compression machine

(Instron, Norwood, MA). The femur was loaded with a flat platen in the experimental set-up. The alignment simulated the approximate loading position during a one legged stand. The *in-vitro* loading correlated with the assumed simplified point loading *in-silico*. The displacement rate was 0.2mm/s which was low enough to avoid a loading rate effect on the compressive strength of the tested bone (Carter and Hayes, 1976). The mounted samples were compression tested until the fracture load was reached. The fracture load of the femur sample was defined as the first local maximum of the load-displacement curve (Figure 26).

#### **4.3.2.6 Post processing of computational output**

In the previous study on additive manufactured femoral head models, the predicted stiffness reduction as a result of a lesion was estimated by dividing the stiffness of each cross-section of the lesion affected femoral head sample by the stiffness of the corresponding cross-section of the control sample without lesion. The relative difference in stiffness of the lesion affected femoral head model to the same femoral head model without lesion was then compared to the experimental fracture load.

Similarly, the reduction in stiffness as a result of a simulated lesion in porcine femoral head samples could be estimated by comparing the stiffness before and after the lesion was administered. This approach, however, had two downsides. Firstly, the predicted reduction in stiffness could not be replicated experimentally as the femoral head samples were destructively compression tested which did not allow a direct experimental comparison of the same femoral head with and without lesion. Secondly, this approach would not translate into a clinical application. Therefore, the calculated stiffness of the porcine femoral head samples was compared against a benchmark stiffness which was defined by the mean stiffness of all control samples. In this study, the axial stiffness of each cross-section of a porcine femoral head sample was divided by the mean stiffness of the corresponding cross-section of a reference set of 'healthy' femoral head samples ( $n=6$  control samples). The cross-section of a sample with the lowest  $EA_{sample}/EA_{mean\_control}$  ratio was the one with the greatest reduction of stiffness compared to the reference set and therefore it was assumed to be the weakest cross-section. As fracture was likely to initiate at the weakest cross-section, the lowest  $EA_{sample}/EA_{mean\_control}$  ratio of each sample was used to quantify its fracture risk.

#### 4.3.3 Results

All 18 porcine femoral head samples were mechanically tested. A statistical analysis (SPSS version 21; IBM Corporation, Armonk, NY) of the experimental data confirmed that a sample with a lesion lateral to the fovea was more likely to fracture at a low load (Figure 54). A lesion medial to the fovea was less critical from a statistical point of view. However a reliable categorisation of the fracture risk based on the lesion type was not possible. Despite a similar lesion volume and location within each lesion group, there was a larger amount of variation in regards of the fracture load for lesion affected femoral heads.

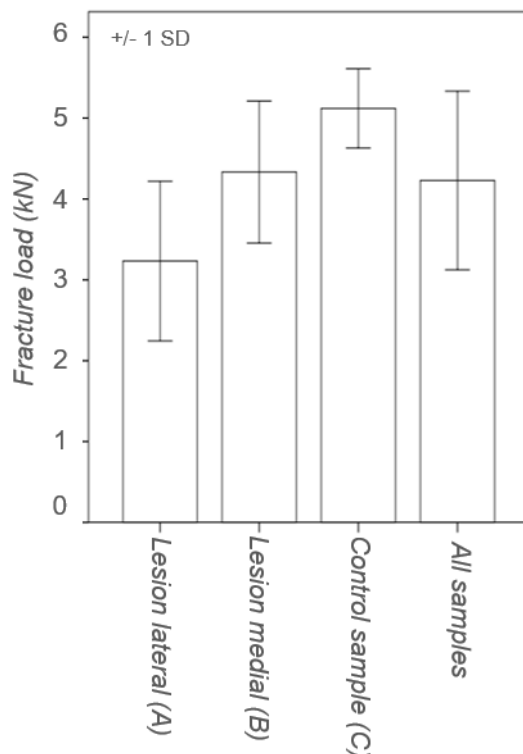


Figure 54: Box-whisker plot showing the experimental fracture loads of 18 porcine femoral heads. The porcine femoral heads were compression tested on an Instron. Porcine femoral head with a lesion lateral  $n=6$  (A) and medial  $n=6$  (B) to the fovea and control sample  $n=6$  (C). Samples with a lesion lateral had statistically a higher fracture risk.

The fracture prediction tool calculated the axial stiffness for each cross-section of all 18 porcine femoral heads and compared their results to the corresponding mean stiffness of a reference set of six control samples (Figure 55). The lowest  $EA_{\text{sample}}/EA_{\text{mean\_control}}$  ratio of each femoral head sample, which quantified the fracture risk, was compared to its experimental fracture load

(Figure 56). However, there was only a low linear correlation as the experimental fracture load was limited by slippage of the epiphyseal plate at about 5kN. The coefficient of determination was 0.29.

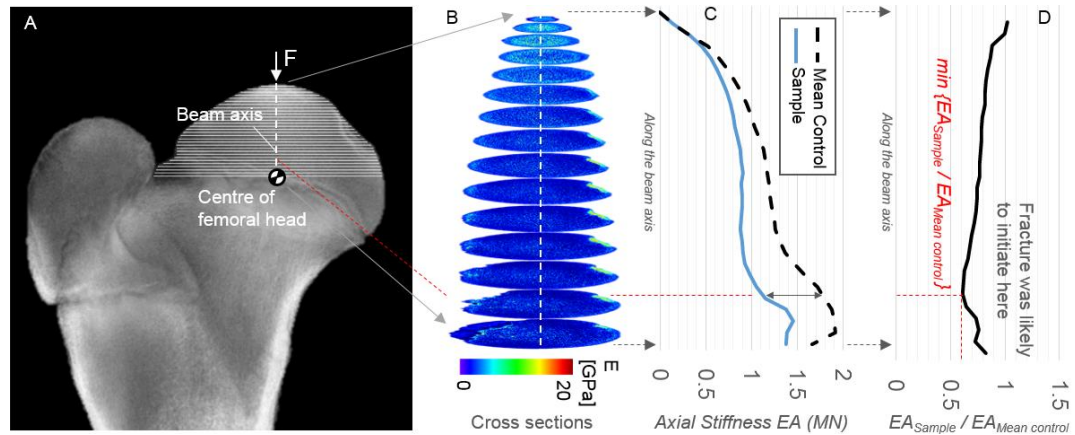


Figure 55 Computational results of the fracture prediction tool: The developed tool calculated the axial stiffness of all cross-sections within the subchondral area of the femoral head. (A) The input of the tool is a tomographic image. (B) Cross-sections were reconstructed which were perpendicular to the loading axis (beam axis). The density of each pixel was estimated using a density calibration. (C) The axial stiffness ( $EA$ ) of each cross-section was calculated by summing the stiffness of all pixels in that cross-section. (D) The cross-section of an analysed femoral head sample that showed the highest difference when compared to the mean stiffness of the control samples, was assumed to be the weakest. The ratio of the weakest cross-section was used to quantify the fracture risk.

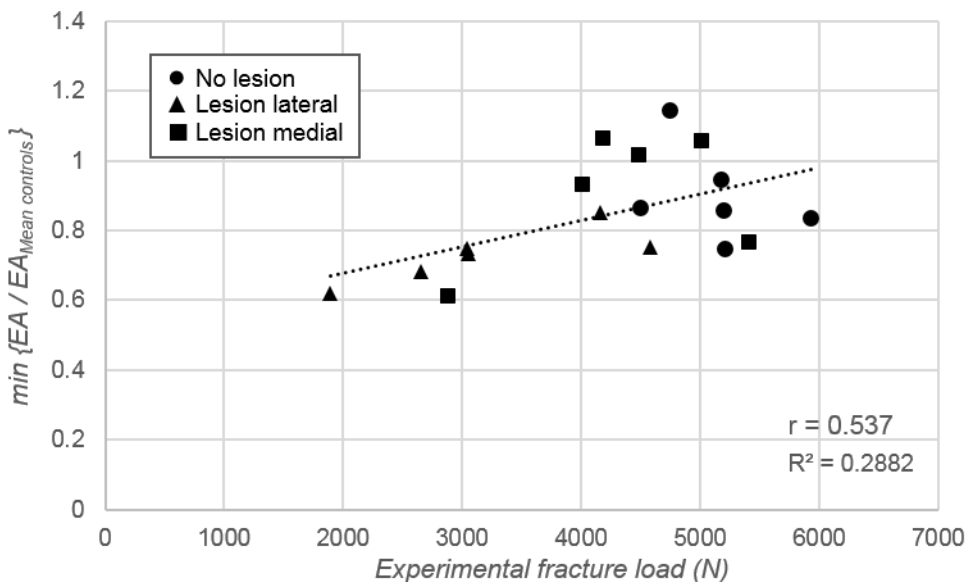


Figure 56 The cross-section of a sample with the highest difference of the axial stiffness compared the control mean was assumed to be the weakest. This was the point where fracture was assumed to initiate. There was a low linear correlation between the difference of the axial stiffness of a porcine sample and its experimental fracture load.

#### 4.3.4 Discussion

The current classification practice would classify all femoral heads with a lesion in the subchondral area as having a significant higher fracture risk compared to heads with a lesion elsewhere or with no lesion. The experimental results showed, however, a different picture.

Current classification methods rely on the identification of the lesion volume and location, an approach that is purely based on geometrical information. Ohzono et al. (1991) reported that collapse of the femoral head most often occurs when the lesion location is in the weight bearing area. The experimental data confirmed that a lesion within the subchondral area was statistically more critical for the stability of the femoral head than a lesion located elsewhere. However this study also showed that there was a large variation in measured failure loads among femoral heads with the same lesion type, despite identical cross-sectional areas of the defect. Therefore, the lesion volume and location did not account for the variation in failure loads and were unsuitable as a good predictor of fracture risk alone.

The fracture prediction based on axial stiffness took both material and geometrical properties into account. The predictive capabilities of the developed method were verified with *in-vitro* tests on porcine femoral head

models. However there was only a low linear correlation between computational results and the failure loads obtained from mechanical testing. While there was a stronger linear relationship for samples with lower experimental failure loads, this relationship ceased as the fracture loads of porcine femoral heads were limited by slippage of the epiphyseal plate, which was due to skeletal immaturity. It decreased the stability of the porcine femoral head and limited the fracture load to a maximum of about 5kN. Juvenile porcine femurs are commonly used across the literature to analyse the effects of AVN on the bone material properties (Pringle et al., 2004; Koob et al., 2007; Aruwajoye et al., 2013). When analysing the effects of structural properties, porcine samples should only be used with caution. While there was some indication for a correlation between experimental fracture loads and the predicted fracture risk, the relationship was not conclusive and confounded by the growth plate. A verification study on a human femoral head disease model would eliminate the growth plate as a limiting factor and would bring clarity if the addition of material properties derived from tomographic imaging can increase predictive power.

AVN lesions were modelled with drilled holes to mimic the appearance and behaviour of clinical lesions, however the mechanical implications of AVN lesions are largely unknown. Necrotic bone tissue shows a vast reduction in the Young's modulus (Brown et al., 1981; Koob et al., 2007). A density-modulus relationship can be used despite a density increase at the periphery of the necrotic lesion as the lesion itself is exposed to decalcification leading to a low mineral density (Ficat, 1985; Wang et al., 2013, 2014). A drilled lesion does not accurately resemble a necrotic lesion, however the simulated lesions provided a method to validate the fracture prediction model in respect of AVN.

## 4.4 Verification against human femoral heads

### 4.4.1 Introduction

In this study the fracture prediction tool was verified against a human femoral head disease model. The verification study on porcine femoral heads clearly demonstrated that a fracture prediction based on the lesion geometry and location had a poor predictive capability. A fracture risk prediction based on the lesion volume and location had also poor differentiation and reproducibility because they rely on the clinician to identify necrotic lesions from tomographic images or plain radiographs (Smith et al., 1996; Schmitt-Sody et al., 2008). The fracture prediction tool was largely automated and had the potential to

objectively assess the fracture risk based on density-calibrated CT imaging. However, the verification of the predictive capability of the tool with porcine models was not conclusive because the experimental fracture load of porcine femoral heads was limited by slippage of the epiphyseal plate.

The aim of this study was to verify the fracture prediction tool against *in-vitro* compression tests on a human disease model. AVN affected human femoral head samples from surgery to implant a total hip replacement were too degenerated for a meaningful verification study. Therefore AVN lesions were simulated similar to the porcine study by drilling a single hole into the subchondral area of the femoral head through the femoral neck. The computational tool characterised the fracture risk of each sample based on how its axial stiffness compared to a reference set of healthy samples. The stiffness reduction quantified the fracture risk of a sample. The calculated stiffness difference of each sample was compared to its experimental fracture load to demonstrate correlation.

#### **4.4.2 Methods**

##### **4.4.2.1 Sample preparation**

A series of six human femoral head models were tested to assess the effect of lesions within the head in respect of verifying the developed fracture prediction tool (Figure 57). Twelve dissected human femurs from six subjects were obtained from a non-transplant human cadaveric tissue bank (Platinum Training, Phoenix, AZ) following approval of ethics application from University of Leeds Faculty of MAPS and Engineering Ethics Committee (Approval number: MEEC 13-002). The age range of the subjects was between 55-70 years with three male and three female. The mean head diameter as its maximum in AP direction was 50.5mm with a low standard deviation of 3.4mm. The mean weight was  $77.7 \pm 27.6$ kg.

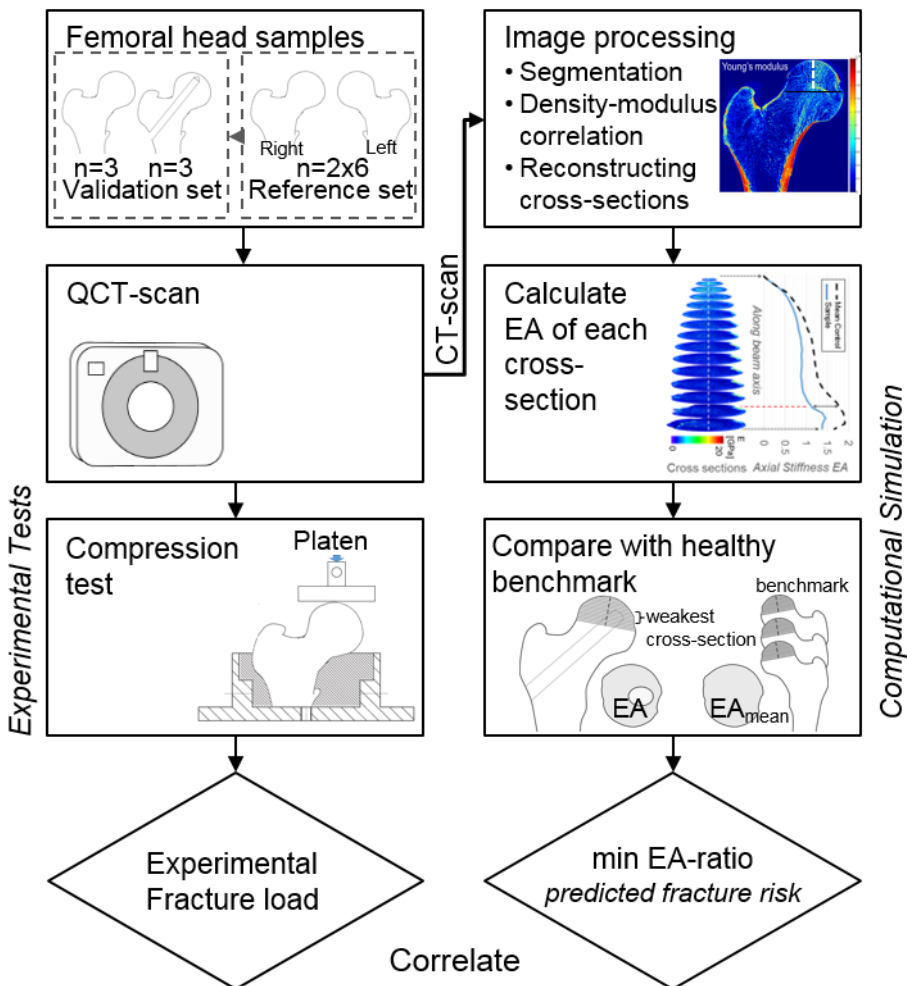


Figure 57 Schematic of the verification workflow. A lesion was simulated by drilling a hole lateral to the fovea. Each sample was individually analysed by the fracture prediction tool and subsequently compression tested.

Six femoral heads of the left femurs were cemented into moulds, a subset ( $n=3$ ) included a hole drilled into the subchondral area of the femoral head via the femoral neck (Figure 58). The simulated lesions provided a method to validate the fracture prediction model with respect to AVN. The hole had a diameter of 11mm and the edges of the drill bit were rounded to avoid sharp corners in the created lesion. The lesion was placed in the subchondral area of the femoral head and the lesion volume and location was similar between all cases. A University of Leeds standard operating procedure (SOP.07.17) was created to administer the drilled lesion.

All samples were kept hydrated with cloths soaked with phosphate-buffered saline solution and samples were frozen between dissecting, scanning and testing. All samples did not undergo more than five freeze thaw cycles to

prevent any changes to the Young's modulus of bone tissue (Linde and Sørensen, 1993).

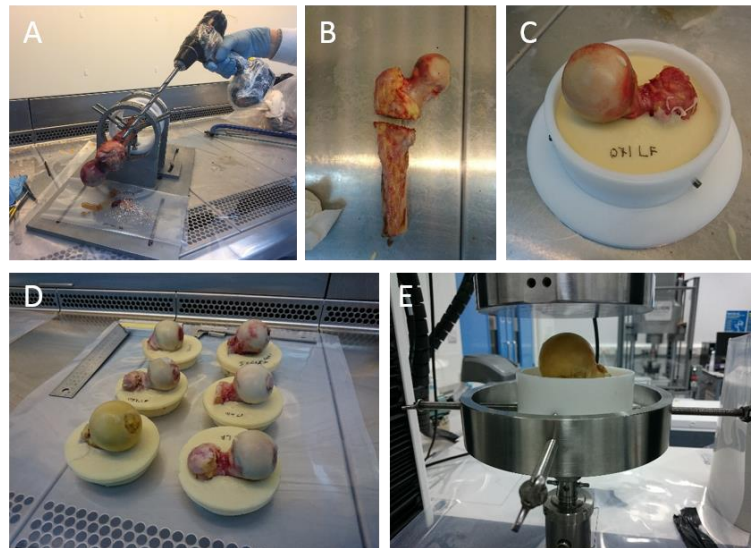


Figure 58 Human femoral head sample preparation steps: (A) Drilling lesion (B) sectioning stem (C) Potting of sample (D) All samples (E) Platen compression test.

#### 4.4.2.2 Image capture

The fracture prediction method used tomographic images to estimate material and geometric properties. Prior to the potting of the six left femur samples, all twelve femoral heads were CT-scanned. The same scanner settings were used as in the previous porcine verification study (4.3.2.3). The femur samples were scanned with an isotropic resolution of 82 $\mu$ m. These twelve samples formed the reference set.

Six of these samples were then further sectioned and potted. Before being compression tested, these six samples were scanned again with the same CT settings and orientation (Figure 59). These six samples formed the verification set.



Figure 59 CT-scan of a potted sample with a simulated drilled lesion in the subchondral region of the femoral head (white arrows) administered through the femoral neck.

#### 4.4.2.3 Material model

Material properties were assigned to the beam model from density calibrated CT-scans by using a density-modulus relationship using a material model proposed by Morgan *et al.* (2003) and a density relationship described by Schileo *et al.* (2008). The validity of these two relationships was verified against human femoral head bone plugs in Chapter 3.4.3.

#### 4.4.2.4 Beam model and fracture risk prediction

The developed fracture prediction tool calculated the structural stiffness based on the calibrated CT-scans of the femoral heads as described in Chapter 3.2. A straight beam axis was established which followed the simplified loading vector from the point of loading on the bone surface to the centre of the femoral head.

The increasing cross-sectional area of the femoral head did not allow to directly identify weak cross-sections as it would be possible for a bone structure without taper. Therefore, the structural stiffness of each of the six femoral heads was compared to the mean stiffness from twelve previously analysed human femoral heads (reference set) without lesions. The tool quantified the fracture risk as the relative reduction in axial stiffness (EA) compared to a healthy benchmark (Figure 60). The minimum  $EA_{\text{sample}}/EA_{\text{mean\_control}}$  ratio was calculated for each femoral head sample.

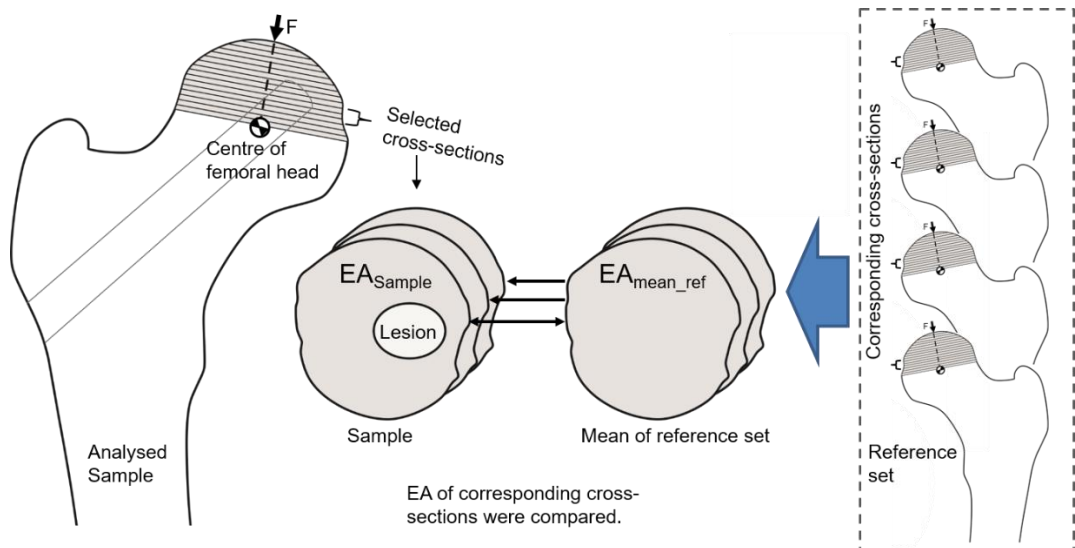


Figure 60 Schematic of the proximal femur including assumed straight beam axis. The analysed cross-sections are perpendicular to the beam axis. The axial stiffness of lesion affected cross-section was compared to the mean stiffness of the corresponding cross-section without lesion in order to predict fracture.

#### 4.4.2.5 Experimental set-up of compression test

The six cemented femurs from the verification set were compression tested until failure using an Instron 3366 single axis tension-compression machine (Instron, Norwood, MA). Failure was defined as the first local maximum of the load-displacement or stress-strain curve. The femoral heads were loaded with a flat platen approximating the loading orientation of a one-leg stand. The displacement rate was 5mm/min which was low enough to avoid loading rate effects (Carter and Hayes, 1977).

#### 4.4.3 Results

The tool calculated the axial stiffness for each cross-section of six human femoral heads and compared their results to the corresponding mean stiffness of a reference set of twelve pre-tested reference samples (Figure 61). The minimum  $EA_{sample}/EA_{mean\_control}$  ratio correlated with in-vitro fracture loads significantly better with a coefficient of determination of 0.83 than for the porcine samples (Figure 62). This demonstrated the predictive capability of the developed method to identify weak femoral head samples. The relationship between the calculated ratio and fracture load was:

$$F_{Fracture} = 12,500 EA_{ratio} - 6635N$$

The calculated overall axial stiffness through all cross-section correlated with the experimentally measured stiffness seen in the load-displacement curve of the compression test (Figure 63). There was a great amount of variation in regards of the experimental fracture load for all tested samples.

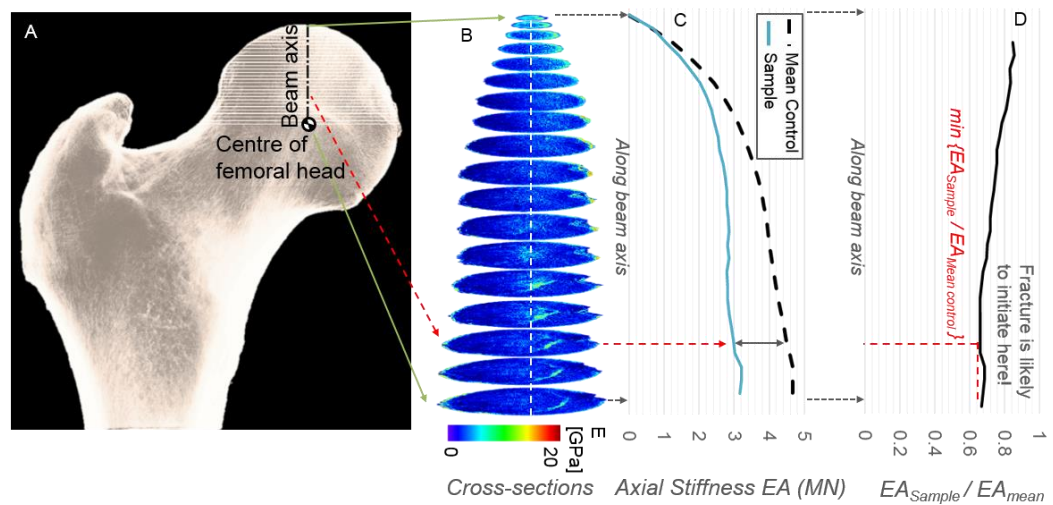


Figure 61 Computational results of the fracture prediction tool: The developed tool calculated the axial stiffness of all cross-sections within the subchondral area of the femoral head. (A) The input of the tool is a tomographic image. (B) Cross-sections were reconstructed which were perpendicular to the loading axis (beam axis). The density of each pixel was estimated using a density calibration. (C) The axial stiffness (EA) of each cross-section was calculated by summing the stiffness of all pixels in that cross-section. (D) The cross-section of an analysed femoral head sample that showed the highest difference when compared to the mean stiffness of the reference set, was assumed to be the weakest. The ratio of the weakest cross-section was used to quantify the fracture risk.

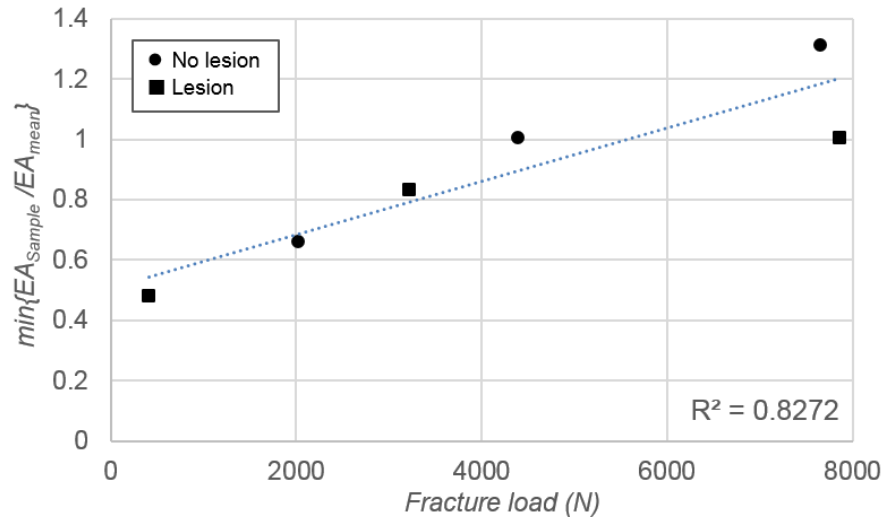


Figure 62 The computationally predicted fracture risk based on how the axial stiffness of a sample compared to a reference set of healthy samples was directly correlated with the experimental fracture load of that respective sample. There was a good correlation between the difference of the axial stiffness of a femoral head sample and its experimental fracture load.

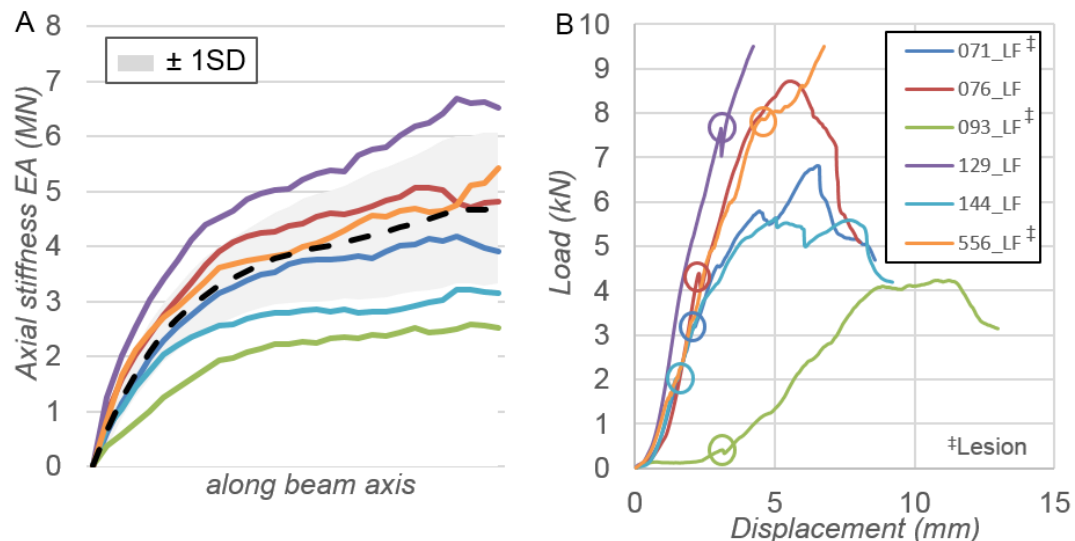


Figure 63 (A) The axial stiffness of six femoral head samples was calculated for each respective cross-section along the beam axis. All samples were individually compared against the mean stiffness of the reference set (black dashed line). (B) Load displacement curve of six cemented femoral heads which were platen compression tested. The fracture load was defined as the first local load maximum of the load-displacement curve (circled).

#### 4.4.4 Discussion

The developed method predicted the fracture risk of femoral heads based on both structural and material properties derived from non-invasive tomographic

imaging and it had the added advantage of being largely automated and therefore removing the majority of user bias. Each femoral head sample was given a minimum  $EA_{sample}/EA_{mean\_control}$  ratio which quantified how the respective sample compared against a reference set in a worst case. This value allowed ranking the samples in regards to their fracture risk.

There was a large amount of variation in experimental fracture loads among femoral heads with the same lesion type. The predicted fracture risk correlated reasonably well with the experimental fracture loads which indicated that a fracture prediction based on structural mechanics was a viable tool to predict fracture. While a risk classification based on the lesion volume and location only took geometrical information into account, the fracture prediction method based on axial stiffness also considered material properties of bone which increased its predictive capabilities. A limitation of this study was the low sample number ( $n=6$ ).

#### **4.5 Summary**

The three verification studies assessed different aspects of the fracture prediction tool. The tests with additive manufactured femoral head samples allowed analysis of the fracture prediction in respect of the lesion location as samples with otherwise similar geometric shape could be created. This study demonstrated that a lesion in the subchondral area was more critical than a lesion elsewhere. This trend was also predicted by the fracture prediction tool which compared the axial stiffness of the weakest cross-section of a lesion affected femur model to the stiffness of the corresponding cross-section of a femoral head model without lesion.

The second study showed that there was a large variation in measured failure loads among porcine femoral heads with the same lesion type, despite identical cross-sectional areas of the defect. Therefore, the lesion volume and location did not account for the variation in failure loads and were unsuitable as a good predictor of fracture risk alone. While a risk classification based on the lesion volume and location only took geometrical information into account, the fracture prediction method based on axial stiffness also considered material properties of bone which potentially increased its predictive capabilities. However, a conclusive verification of the fracture prediction tool was not possible as the experimental fracture loads of porcine femoral heads were limited by slippage of the epiphyseal plate.

The last study, therefore, used a disease model from human femoral heads to verify the developed tool to eliminate the effect of the growth plate. The axial stiffness was compared against the corresponding mean stiffness of a reference set of intact femoral heads. The minimum  $EA_{sample}/EA_{mean\_control}$  ratio quantified how the respective sample compared against a reference set in a worst case. Using natural tissue also allowed analysis of the influence of trabecular structure and variations of material properties which appeared to have a great influence of the fracture risk. The human verification study showed that it is possible to objectively analyse the fracture risk of the femoral head based on both structural and material properties derived from non-invasive tomographic imaging and it had the added advantage of being largely automated and therefore removing the majority of user bias.

All lesions were modelled as voids. While those voids did not replicate the true appearance of clinical lesions, the simulated lesions provided a method to validate the fracture prediction model in respect of AVN in terms of mechanical behaviour although mechanical implications of AVN lesions are largely unknown. As a next step the developed fracture prediction tool should be validated against clinical CT-scans of AVN affected femoral heads.

## Chapter 5 Feasibility of the fracture prediction tool in assessing clinical cases of avascular necrosis

### 5.1 Introduction

In this chapter, the feasibility of the image based fracture prediction tool to identify the fracture risk of patient-specific data was analysed. This was achieved by analysing whether the tool's ability to stratify patients in terms of their fracture risk correlated with the predicted risk of disease progression established by the ARCO classification. A second objective was a comparison on how the developed tool based on beam theory analysis performed against another novel fracture prediction tool based on finite element analysis (FEA) in terms of delivering an accurate risk score for the same set of patient scans. Finally, further requirements such as user-input and CT settings were assessed which are necessary for a future clinical diagnostic application of the tool.

These objectives were achieved by using a set of CT-scans of femoral heads from patients suffering from AVN. It was demonstrated in Chapter 4 that the developed image-based fracture prediction tool, which took both material and geometric properties into account, was able to give an indication about the fracture risk of physical disease models generated by additive manufacturing, as well as porcine and human tissue. However the disease models used simple voids to mimic the appearance and behaviour of avascular necrotic lesions which provided a method to verify the fracture prediction model in respect of AVN. In this study, the fracture prediction tool was used to calculate the fracture risk of AVN affected femurs. Based on the estimated fracture risk, all AVN affected femurs were ranked. This was compared to the ranking based on the ARCO classification which is the current gold standard for the clinical classification of femoral head AVN. A direct experimental validation of the predicted fracture risk was not possible because altering the standard treatment with a THA would be unethical. However by comparing the *in-silico* fracture risk predictions to the ARCO standard, the tool's sensitivity and ability to analyse the fracture risk can be estimated.

In the second part of the study the results of the fracture prediction tool were then compared against the results of another fracture prediction method based on FEA using the same patient set. The fracture prediction tool based on FEA was developed as part of another PhD thesis (Anderson, 2015). It required a two-material geometric model for which the femur and the necrotic

lesion had to be segmented. Material properties were assigned to the femoral head disease model with 300MPa for healthy bone and 150MPa for necrotic bone which was based on previous material tests. In contrast, the fracture prediction tool based on beam theory assigned material properties from CT-scans by using a density-modulus relationship. Each model had a risk score which was compared to the results of the tool of this study.

## **5.2 A comparison of the developed tool's ability to stratify patients for fracture risk and the ARCO classification system**

### **5.2.1 Introduction**

Current clinical methods to diagnose avascular necrosis (AVN) are subjective and a reliable assessment of the fracture risk is not available. The ARCO classification has poor differentiation and reproducibility because it relies on the clinician to identify necrotic lesions from tomographic images or plain radiographs (Schmitt-Sody et al., 2008). There is an unmet need for an objective and robust method to determine fracture risk in AVN and support clinicians in selecting appropriate treatments for optimum outcomes.

The fracture prediction tool based on beam theory can objectively calculate the fracture risk of lesion affected femoral heads based on density calibrated CT-scans. The aim of this study was to demonstrate the feasibility of the developed tool for clinical cases by predicting the fracture risk of femoral heads from patients suffering from AVN.

In a first step, it was analysed whether the tool was sensitive enough to detect necrotic lesions within the femoral head. The tool quantified the fracture risk as the relative reduction in axial stiffness (EA) compared to a healthy benchmark. In this study two different approaches were tested to identify which was more sensitive: The stiffness of each lesion affected femoral head was compared against the stiffness of its own contralateral femur and against a mean stiffness of a reference set of healthy femurs.

Finally, the predicted fracture risk of each sample was used to rank the samples according to their fracture risk. It was analysed whether the tool's predictive capability to stratify patients according to their fracture risk offered a similar good prediction compared to the currently used ARCO classification (Figure 64).

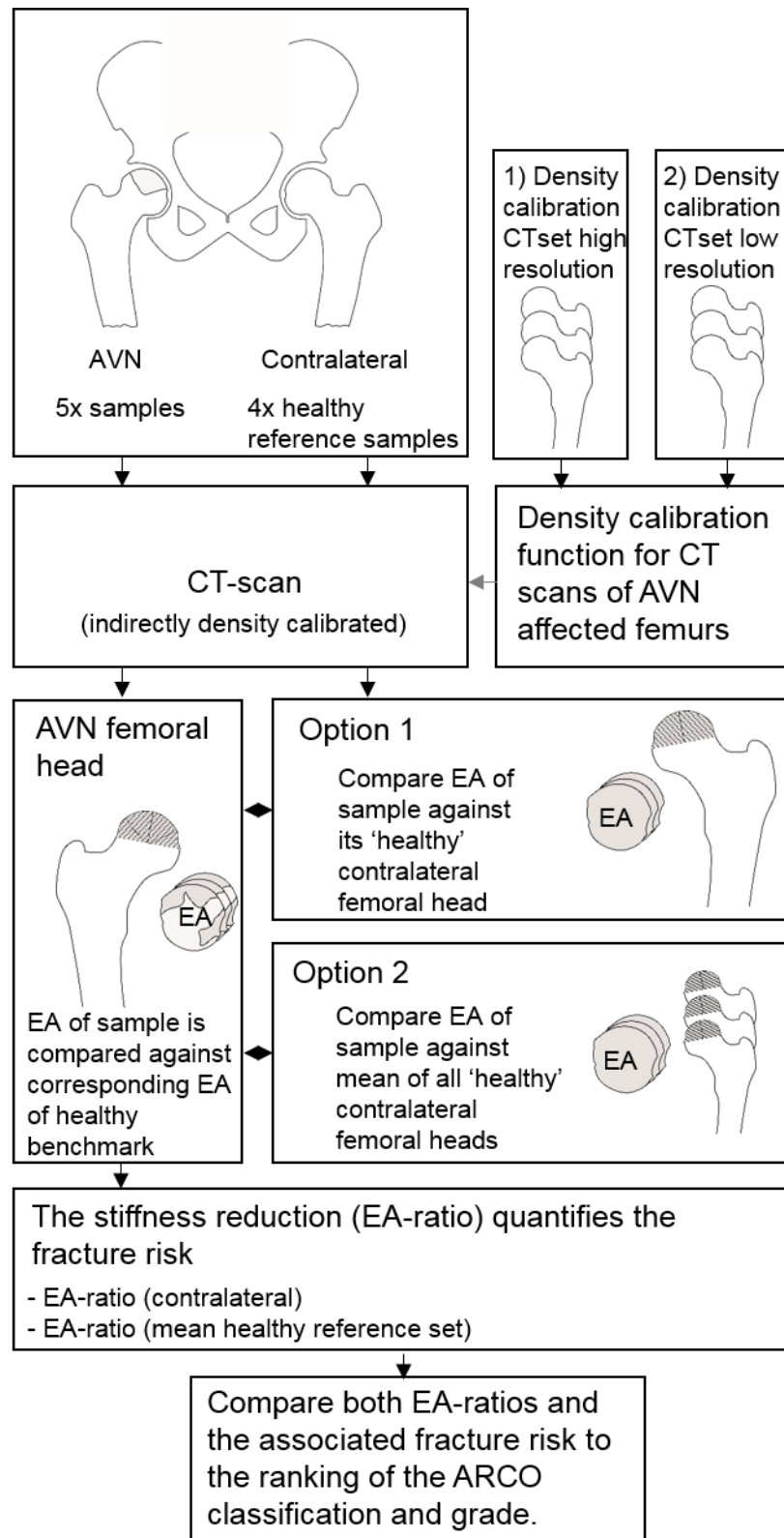


Figure 64 Flowchart illustrating the study design.

## 5.2.2 Methods

### 5.2.2.1 Patients and disease stage

Demographic data and CT-scans of five patients with avascular necrosis were used for this study which originated from a clinical trial initiated by DePuy Synthes Joint Reconstruction (Leeds, UK). The use of the patient data was approved by the University of Leeds Faculty of MAPS and Engineering Ethics Committee (Approval number: MEEC 10-011).

Patient demographics are shown in Table 21. One patient (P01\_002) was excluded because of advanced subchondral fracture with compressed bone tissue. Patient P01\_001 had a contralateral THA prior to image acquisition. Patient 02\_003 showed initial signs of subchondral fracture.

All patients were classified according to ARCO and their lesion involvement and location were clinically assessed as part of another PhD thesis (Anderson, 2015) (Table 22). The classification was done by a surgeon.

Table 21 Demographics for the five patients selected for testing the fracture prediction method. Patient 02\_003 showed subchondral fracture.

| Patient ID | Sex    | Height (cm) | Weight (kg) | Ethnicity | Age |
|------------|--------|-------------|-------------|-----------|-----|
| P01_001    | Female | 162         | 52          | Asian     | 44  |
| P01_003    | Male   | 172         | 72          | Asian     | 27  |
| P01_004    | Male   | 173         | 80          | Asian     | 41  |
| P02_001    | Male   | 171         | 66          | Asian     | 66  |
| P02_003    | Female | 160         | 70          | Asian     | 20  |

Table 22 Lesion volume and ARCO classification for each patient included in the study. Head volume was estimated by calculating the volume of a sphere with the same diameter, lesion volume was calculated by multiplying the number of voxels in the lesion mask by the voxel volume. The ARCO grade was assigned based on the presence (Grade III) or Absence (Grade II) of fracture – note that all lesions were visible on radiographs and were by definition grade II or higher. The volume classification was dictated by the percentage involvement (<15% = A; 15%-30% = B; >30% = C). Location in the A-P and M-L planes was established by assessing whether the lesion was present in the Medial (M), Central (C) and Lateral (L); Anterior (A), Central (C) and Posterior (P) quadrants respectively. *Reproduced from Anderson, 2015.*

| Patient ID | Head diameter (mm) | Lesion involvement (%) | ARCO Classification | ARCO grade | ARCO Location |       |
|------------|--------------------|------------------------|---------------------|------------|---------------|-------|
| P01_001    | 43                 | 9                      | II                  | A          | C,L           | A     |
| P01_003    | 46                 | 27                     | II                  | B          | M,C           | A,C,P |
| P01_004    | 49                 | 32                     | II                  | C          | M,C           | A,C,P |
| P02_001    | 44                 | 44                     | II                  | C          | M,C,L         | A,C,P |
| P02_003    | 43                 | 33                     | III                 | C          | M,C,L         | A,C   |

### 5.2.2.2 Image capture and processing

The fracture prediction method used tomographic images to estimate material and geometric properties. CT-scans of both femurs of the patients described in Table 22 were acquired using a 64-row CT scanner Brilliance64 (Phillips, Amsterdam, Netherlands) with 120kVp tube voltage. The slice thickness was 1mm and the in slice resolution was 0.68mmx0.68mm. The scan covered the pelvis to the mid shaft of the femur.

The femoral bone was segmented as surrounding soft tissue and adjacent bone would have compromised the fracture calculation. The close proximity of the acetabulum and the low resolution of the scans made the segmentation of the femoral head difficult. Low density necrotic lesions close to the bone surface were further challenging for the automated masking process used previously. The femur was therefore manually threshold segmented using ScanIP (Simpleware Ltd., Exeter, UK). Other functions used to segment the femur were un-painting adjacent bone structures, a morphological close filter and a flood fill filter. An interface was created to allow the import of the stl-file of the created bone mask into the developed fracture prediction tool in MATLAB.

### 5.2.2.3 Material model

The material properties of bone were assigned to the beam model using density calibrated tomographic images and a density-modulus relationship. However, the clinical CT-scans of the AVN patients in Table 22 were not density calibrated and no other density calibrated CT-scans of AVN affected femurs were available for this study. This was a major limitation because density calibrated CT-scans were essential for the tool's ability to predict the fracture risk.

Therefore, a calibration function had to be approximated by comparing the uncalibrated set of CT-scans to a second set of calibrated CT-scans. The density of unaffected parts of the AVN affected femur were compared with corresponding parts of femurs in calibrated CT-scans. A linear calibration function was established by using cortical bone of the mid shaft of the femur and air as density reference values. The average density of cortical bone in the shaft was assumed to be the similar among different individuals when averaged over a large number. The average density of cortical bone over a length of 10mm at the same anatomical position of the femur was compared (Figure 65). The other reference value was air.

The aim of the described retrospective and indirect density calibration was to get a rough approximation of the density calibration function for the AVN CT-set in order to apply the density-modulus relationship. It needs to be emphasised that this approach was prone to inaccuracies and it only allowed comparisons of material properties of bone amongst the same uncalibrated CT-set.

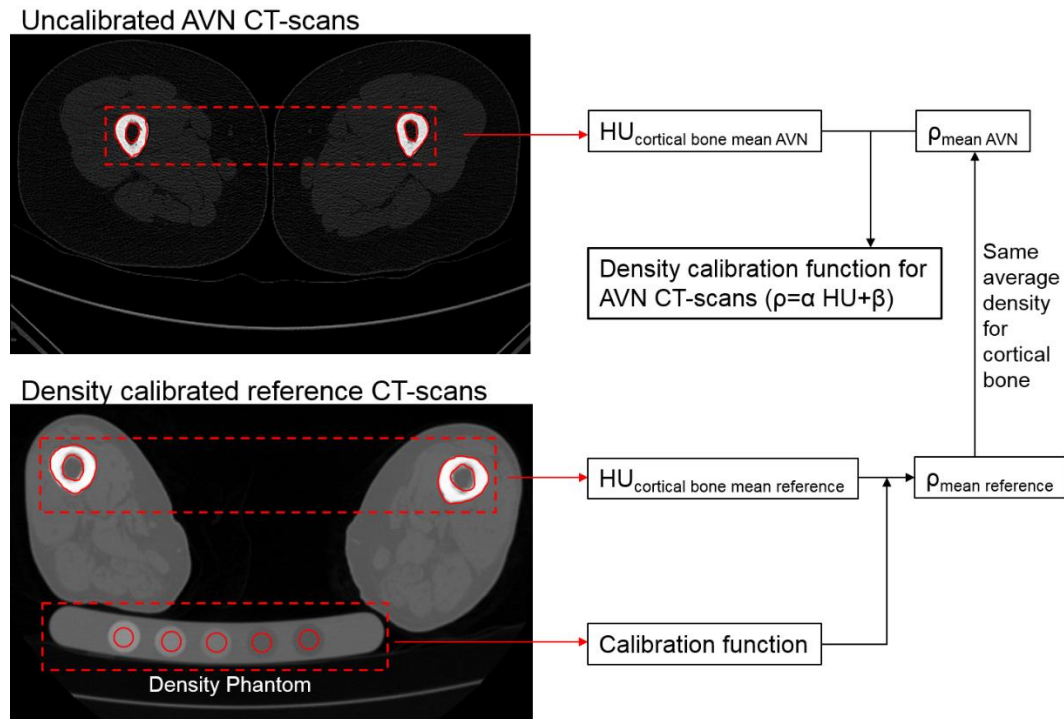


Figure 65 Diagram of the indirect density calibration method: The mean density of cortical bone of the mid shaft of every femur in a calibrated CT set was calculated ( $\rho_{\text{mean reference}}$ ). AVN affected mostly the femoral head and the mean density of cortical bone at the corresponding location ( $\rho_{\text{mean AVN}}$ ) was assumed to be similar to the reference group. The calibration function of the uncalibrated AVN CT-set was approximated by using the density of cortical bone of the shaft as a reference value. This allowed the conversion of Hounsfield grey values (HU) with bone density.

The calculation of the calibration functions was repeated for two different sets of calibrated CT-scans of disease unaffected femurs. The two calibration functions were compared to assess the accuracy of the indirect calibration approach. The two sets of density calibrated CT-scans of femurs were only used for the purpose of establishing a density calibration function and they were not used as baseline cases for the fracture prediction.

The first set were CT-scans of eight human femurs from four patients. The four white male subjects had an average bodyweight of  $64 \pm 7\text{kg}$  and were  $70 \pm 14$  years old. The CT-scans were generated using a Toshiba Aquilion (Toshiba, Japan) and had a resolution between 0.5 – 1 mm. Both legs were scanned at the same time and the scans were density calibrated using a potassium phosphate phantom. The CT-scans were provided by DePuy Synthes Joint Reconstruction (Leeds, UK) following approval of ethics application from University of Leeds Faculty of MAPS and Engineering Ethics Committee (Approval number: MEEC 11-044).

The second CT set included twelve dissected human femurs from six subjects which were obtained from a non-transplant human cadaveric tissue bank (Platinum Training, Phoenix, AZ) following approval of ethics application from University of Leeds Faculty of MAPS and Engineering Ethics Committee (Approval number: MEEC 13-002). The femur samples were scanned with an isotropic resolution of 82 $\mu$ m using a HRp-QCT scanner (Scanco Medical, Switzerland). The resolution of these CT-scans were significantly higher than the AVN CT-set but it was demonstrated in section 3.4.2 that the material model was resolution independent. They were scanned in air with 59kVp tube voltage and 300ms integration time. The scanner was density calibrated using a hydroxyapatite phantom. The age range of the subjects was between 55-70 years with three male and three female. The mean body weight was 77.7 $\pm$ 27.6kg.

The first CT set led to the calibration equation 5.1.

$$\rho_{QCT} = 0.67 \cdot HU - 707 \quad 5.1$$

The second HA calibrated CT-set with a much higher resolution compared to the CT-scans used in this study produced equation 5.2.

$$\rho_{QCT} = 0.65 \cdot HU - 644 \quad 5.2$$

While this indirect calibration method gave an indication how a real calibration might have looked like, the disparity between equation 5.1 and 5.2 showed that this was not a very accurate method. This limitation meant that the results of this study could not be compared against other data set as they were not universally valid. However the approximated calibration function was sufficient for comparing samples against samples of the same set by calculating their stiffness using a density-modulus conversion material model. For the following calculations equation 5.1 was used because the calibration function was based on clinical CT-scans.

Material properties were assigned to the beam model by using a density-modulus relationship using a material model proposed by Morgan et al. (2003) and a density relationship described by Keyak et al. (1994) as described in section 2.4.2.

#### 5.2.2.4 Beam model and fracture prediction

The developed fracture prediction tool calculated the structural stiffness based on clinical CT-scans of the femoral heads as described in section 3.2. A straight beam axis was established which followed the simplified loading

vector from the point of loading on the bone surface to the centre of the femoral head. The tool calculated the fracture risk of all femoral heads listed in Table 22.

In order to identify the weakest cross-section of an analysed sample, the structural stiffness was compared to the stiffness of a 'healthy' reference. This was done in two ways (Figure 66). Firstly, the stiffness of each cross-section of a sample was compared against the stiffness of the corresponding cross-section of the healthy contralateral femur. This allowed direct analysis of the stiffness reduction as a result of AVN. This was however only feasible when a healthy contralateral femur was available. One patient had a THA and another patient showed first signs of AVN at the contralateral femur.

Alternatively, the calculated stiffness of each cross-section was compared against the mean stiffness of all healthy contralateral femurs of the AVN CT-set (reference set). The CT-sets used for the density calibration in section 5.2.2.3 were not part of this reference set. The advantage of this method is that it creates a reference against which all affected femurs of this CT-set could be compared. The results were normalised against the body weight to account for different femur geometries and weight bearing.

In both cases, if the calculated stiffness was at any point significantly lower than the reference set, that respective sample was assumed to have a high fracture risk. How the respective sample compared against a reference set in a worst case was quantified with the minimum  $EA_{sample}/EA_{mean\_ref}$  or  $EA_{sample}/EA_{contralateral\_sample}$  ratio for axial stiffness.

The EA-ratio of the weakest cross-section quantified the fracture risk of each sample and its magnitude formed a risk score to compare different samples. All patients were ranked according to their predicted fracture risk and it was analysed whether the tool had a similar good predictive power compared to the ARCO classification as there was no experimental data available.

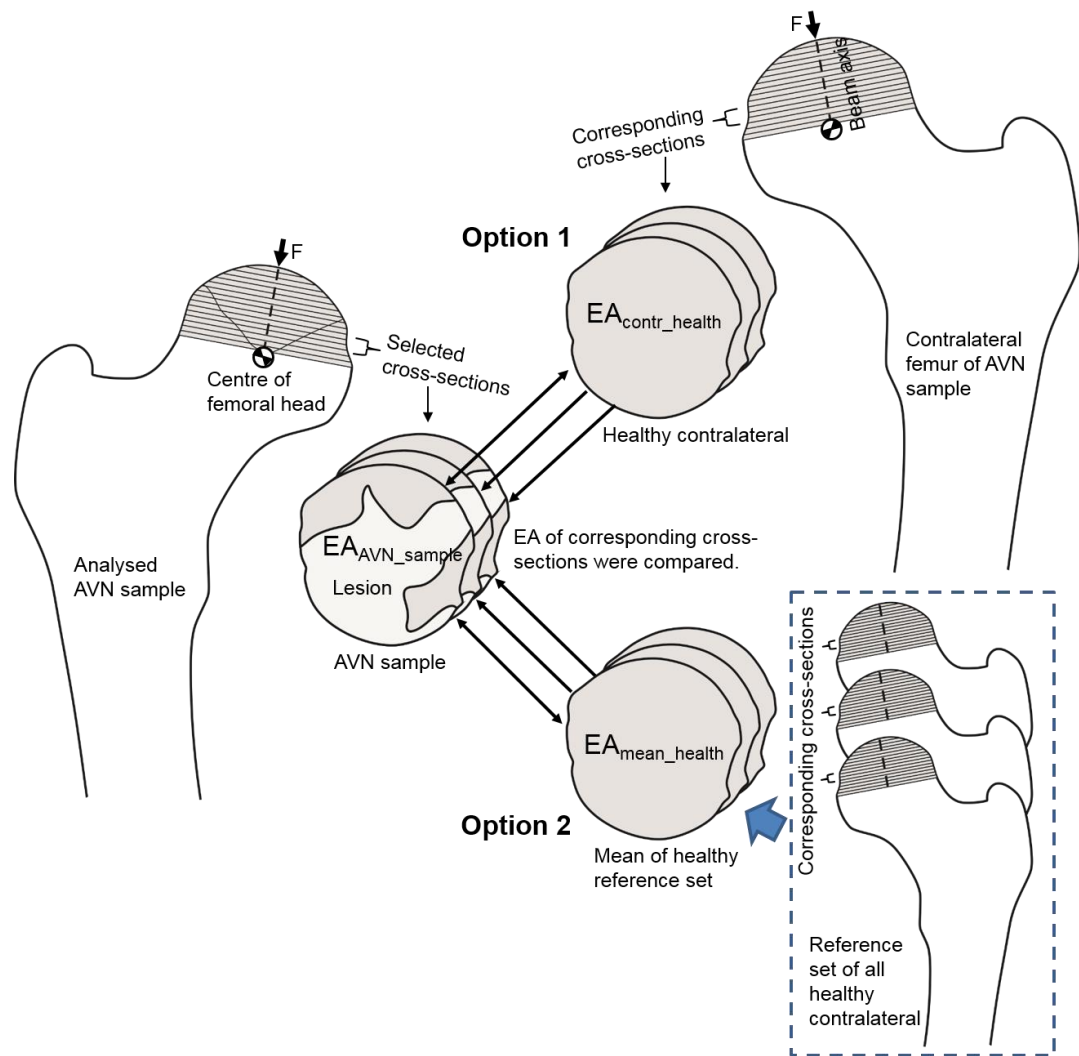


Figure 66 The tool compared each femoral head sample against a healthy benchmark to assess the fracture risk. Two approaches were tested in this study. Option 1: The axial stiffness (EA) of a sample was compared to the corresponding stiffness of the contralateral femoral head of the respective sample. Option 2: The axial stiffness of a sample was compared to the corresponding mean stiffness of each sample of the reference set. The reference set included all healthy contralateral femoral heads of the AVN CT-set.

### 5.2.3 Results

The fracture prediction tool calculated the axial stiffness (EA) for each cross-section of every femoral head described in Table 22 as well as their contralateral femoral head (Figure 67). The axial stiffness increased gradually with the increasing cross-sectional area of the femoral head. The axial stiffness of the unaffected contralateral head was higher than the AVN femoral head. Only the axial stiffness of the AVN affected femoral head of P01\_001

was plotted as the patient had a THA at the contralateral side. The mean stiffness of all healthy contralateral femoral heads were plotted in Figure 67.

The fracture risk of each femoral head was quantified by the greatest relative reduction in stiffness compared to a healthy benchmark which was expressed as the EA-ratio. Two different approaches to create such a benchmark were tested in this study. The axial stiffness of each sample was compared either to the corresponding mean stiffness of each sample of the reference set (Figure 68A) or to the corresponding stiffness of the contralateral femoral head of the respective sample (Figure 68B).

The resulting minimum  $EA_{sample}/EA_{mean\_ref}$  or  $EA_{sample}/EA_{contralateral\_sample}$  ratio stratified all patients according to their predicted fracture risk. This stratification was compared to the ARCO classification of each AVN affected femoral head.

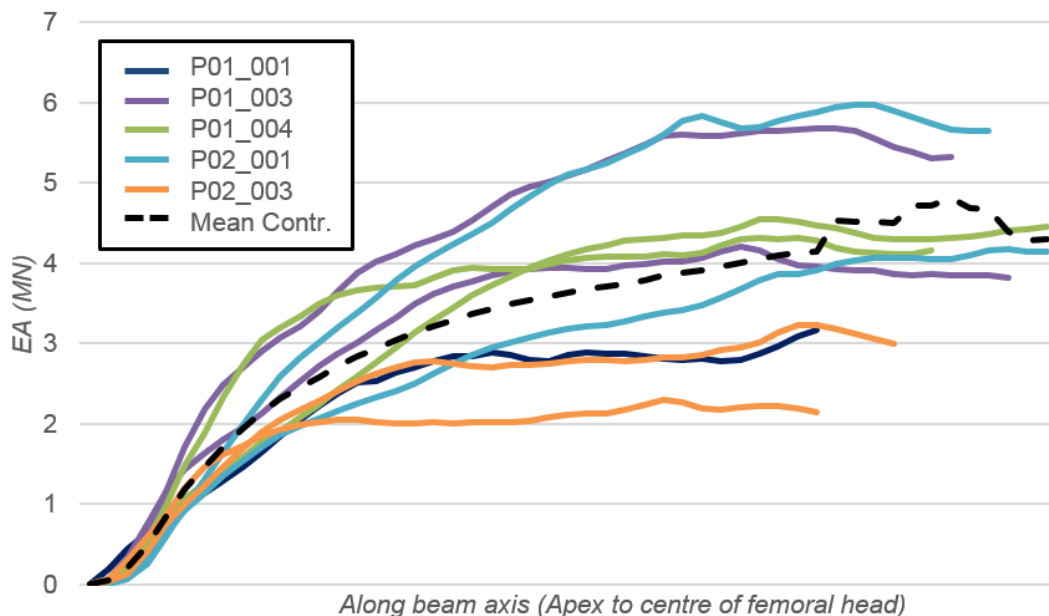


Figure 67 The developed tool calculated the axial stiffness of all cross-sections within the subchondral area of the femoral head for five AVN patients. The tool calculated the stiffness based on CT-scans. The axial stiffness of each sample and the mean stiffness of all healthy contralateral samples (black dashed line) was plotted along the beam axis. Samples from the same patient had the same colour and the stiffness of the AVN affected femur had a significantly lower stiffness than the contralateral femur. Patient P01\_001 had a THA at the contralateral side and therefore no contralateral femoral head.

The patient specific discrete grading of the ARCO classification was compared to the analytic fracture risk score of the fracture prediction tool in Figure 68. While there was a general trend that a low ARCO classification also had a low

EA ratio and vice versa, there was no strong correlation with the number of samples assessed.

The fracture risk of each sample was quantified by the highest relative difference in structural stiffness when compared to a 'healthy' reference. The study used two different approaches in terms of reference sets which led to different estimated fracture risks. Individual cases had to be scrutinised to shed light on the underlying reasons for that discrepancy:

Patients P01\_004 and P02\_001 were both classified as IIC according to the ARCO standard. When compared to the respective contralateral femoral head, the fracture prediction tool also characterised them to have a similar fracture risk. When compared against the corresponding mean stiffness of healthy femoral heads, the fracture prediction tool calculated two very different fracture risks for both. The reason for this was that the data of the later was normalised over the body weight. While there was no difference in the calculated stiffness, patient P01\_004 had a weight of 80kg compared to patient P02\_001 with 66kg. Therefore the femoral head with a similar stiffness had to bear a larger load which increased the fracture risk. The second question here was why did the tool estimate a similar fracture risk when comparing the femoral heads to their contralateral counterpart. The contralateral healthy femoral head of P01\_004 had a very low structural stiffness compared to the other samples (Figure 67), despite the increased body weight. When comparing the stiffness of an AVN affected sample to its contralateral femoral head, it was assumed that the opposite side represented a femoral head prior to AVN. However, patients with AVN often are affected bilaterally or patients may have a general low bone quality even though pathologic signs are not yet visible. Comparing the affected femoral head to a reference that also has an increased fracture risk, means an accurate fracture prediction was not possible. Comparing samples against a mean stiffness of a sample set may lead to more reliable results. Differences resulting from weight bearing of the femur were considered by normalising the body weight.

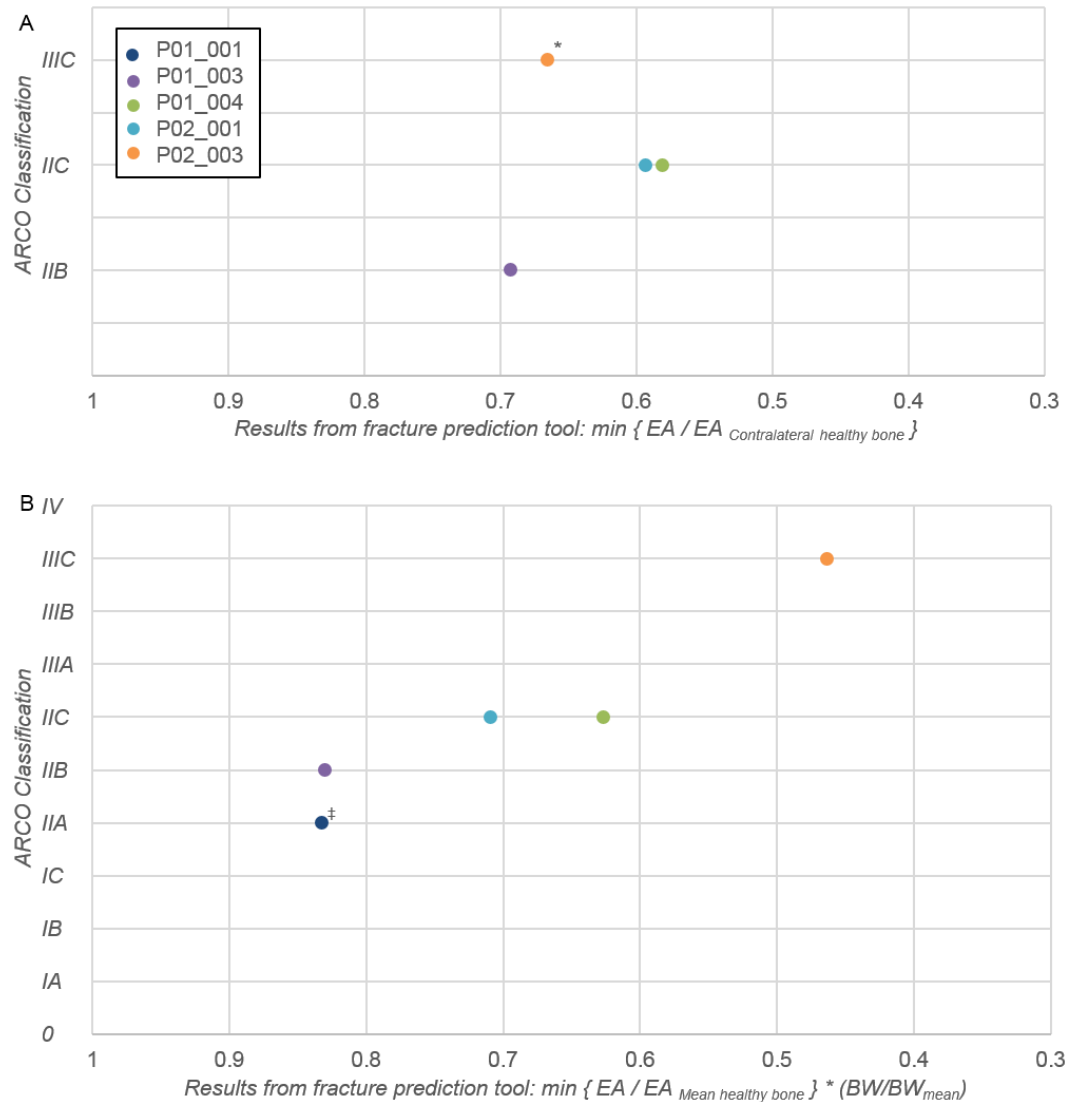


Figure 68 Comparison between the results from fracture prediction tool and the ranking of the ARCO classification. (A) The calculated axial stiffness of each cross-section was compared to the stiffness of the corresponding cross-section of the contralateral femoral head. The EA-ratio describes the reduction in stiffness between the healthy benchmark and the AVN affected femoral head. <sup>‡</sup>P01\_001 had a THA at the contralateral side and is therefore not listed. \*The contralateral femoral head of P02\_003 showed signs of necrotic lesions which led to an inaccurate EA ratio. (B) The calculated axial stiffness of each cross-section was compared to the mean stiffness of a reference set of unaffected femoral heads. The results were normalised against the body weight.

Similar to P01\_004, patient P02\_003 also had a contralateral femoral head that showed a low axial stiffness (Figure 67). In this case, the contralateral femoral head showed signs of necrotic lesions (Figure 69) and had a low structural stiffness. Therefore it could not be used to accurately predict the fracture risk of the AVN affected femoral head and led to an underestimation of the predicted fracture risk (Figure 68A). Using a benchmark in form of the

mean stiffness of a reference set of healthy femoral heads, produced more reliable results because it was not dependent on the soundness of a contralateral femoral head. In the following this approach was used.

The fracture prediction tool was used to rank all patients according to their predicted EA ratio. The EA-ratio was calculated by comparing the stiffness of each sample to the corresponding mean stiffness of the reference set. A low EA-ratio indicated a high fracture risk. The patients were ranked in ascending order in terms of fracture risk which correlated with the risk stratification of the clinical ARCO classification (Table 23).



Figure 69 CT cross-section with an AP view of the pelvis of P02\_003. (A) Femoral head was classified as ARCO IIIC and showed initial subchondral fracture. (B) The contralateral femoral head showed signs of necrotic lesions visible as local density reductions.

Table 23 The fracture prediction tool was used to rank the patients in ascending order. The EA-ratio described the relative stiffness difference of an AVN affected femoral head compared to a reference set of healthy femoral heads. A low EA-ratio indicated a high fracture risk. The ranking correlated with the ARCO classification and grade.

| Patient ID | EA ratio (BW normalised) | Rank | ARCO |
|------------|--------------------------|------|------|
| P01_001    | 0.833                    | 1    | IIA  |
| P01_003    | 0.830                    | 2    | IIB  |
| P02_001    | 0.709                    | 3    | IIC  |
| P01_004    | 0.627                    | 4    | IIC  |
| P02_003    | 0.464                    | 5    | IIIC |

#### 5.2.4 Discussion

The developed fracture prediction tool was compared against the current diagnostic gold standard for AVN of the hip, the ARCO classification. While the ARCO classification was purely based on geometrical information such as the lesion volume and location, the fracture prediction method also considered material properties of bone which potentially added predictive capability in terms of the fracture risk.

Fracture was predicted by analysing the axial stiffness of a femoral head and by comparing it to a healthy reference. This study demonstrated that a comparison against the mean stiffness of a reference set of multiple healthy femurs is potentially more accurate than a comparison against the contralateral femoral head. Firstly, the fracture prediction was independent from a contralateral femoral head. Some patients may have a THA or bilateral AVN. A general low bone quality also reduces the accuracy of the results. Secondly, using a global reference may lead to a clinical application where patients are compared against an established fracture risk score based on demographics.

The ARCO classification relied on the clinician to identify necrotic lesions from tomographic images or plain radiographs. The volume of necrotic lesions is typically approximated using an angular measurement method on two different tomographic planes. The angle is defined in the medio-lateral and anterior-posterior planes by aligning the vertex to the head centre and the sides to the periphery of the necrotic lesion (Kim et al., 1998). This approximation has poor differentiation (Schmitt-Sody et al., 2008). In contrast,

the fracture prediction tool was largely automated and therefore removed the majority of user bias.

The tool was based on material properties retrieved from density calibrated CT scans using a density-modulus conversion model. The material model limits the feasibility of the fracture prediction tool to a certain disease stage. Very early necrotic lesions don't show any bone and density changes and post-fractured bone is accompanied by compressed bone structure which appear dense and therefore strong on CT images. However the tool has an application for ARCO II and early III cases to identify patients for whom a conservative treatment is not a viable solution and who would be better served by a hip replacement. This study demonstrated that material properties can be derived from tomographic images using empirical relationships between density measurements and Young's modulus and necrotic lesions show an overall decalcification.

The CT-scans of this study were not density calibrated and an indirect calibration method was used to retrospectively calibrate the scans. This was a limitation of this study and future work should not be quantitatively compared to the results of this study. However, the used approximated calibration function gave a rough indication how the real calibration function might have looked like and the calculated structural stiffness was only compared against stiffness values of the same CT set. This mitigated effects of the inaccurate calibration function. In general terms, the calibration function is essential especially if the tool is further developed into a clinical diagnostic tool.

Another limitation of this study was the low number of clinical cases that were investigated. A clinical validation study with more cases is needed to confirm these promising initial findings. A follow-up study would also show how much the clinical outcome improved compared to current methods when the treatment was selected based on the calculated fracture risk of the affected femur.

### **5.3 Comparison of the efficiency and accuracy of developed beam tool with a novel fracture prediction tool based on finite element analysis**

#### **5.3.1 Introduction**

In this study the fracture prediction tool based on beam theory was compared against another novel fracture prediction method based on finite element

analysis (FEA) which was developed as part of a PhD thesis at the University of Leeds (Anderson, 2015). The fracture prediction method based on FEA focused on the lesion geometry, especially the interface between healthy bone and necrotic lesion. The lesion boundary was identified as the point where fracture was most likely to occur (Motomura et al. 2011). Therefore the stress difference between necrotic and healthy bone at the interface surface was calculated. A full three-dimensional femoral head model was deemed to be too complex for a tool in the clinical environment and would not translate into a clinical guideline in terms of lesion shapes. Hence, six cross-sectional slices of different orientations throughout the femoral head were individually analysed. The two-dimensional cross-sections were in AP, ML direction and at 20° flexion which simulated a heel strike loading condition. Cross-sectional images were also easier to segment. The relative difference in stress at the lesion interface was calculated with a patient-specific 2D FEA model with two different material properties for necrotic and healthy bone. A risk score was estimated based on the difference in stress which calculated the fracture risk as a result of lesion shape and size (lesion geometry). By including cross-sections at 20° flexion, the effect of other loading conditions were also included in the risk assessment. The risk score was finally normalised with the lesion volume to mitigate effects from masking and slice selection. All patients were ranked according to their predicted risk score.

The aim of this study was to compare the individual risk score of each patient to the fracture risk results of the beam theory tool which were expressed through the relative reduction in axial stiffness. Both fracture prediction methods had fundamental differences in their methodology. A second objective was therefore to analyse the effects of those different approaches such as (1) the analysed cross-sections, (2) the loading situation and (3) how material properties were assigned to the femoral head model:

While the fracture prediction of the FEA tool was mainly influenced by the lesion geometry as it assessed the stress differences at the lesion interface, the beam theory tool analysed the fracture risk by quantifying the fracture risk as the relative reduction in axial stiffness (EA) and ranking all femoral heads according to their EA ratio. The beam tool analysed each cross-section of the three-dimensional femoral head model while the FEA tool was limited to analysing a selection of six different two-dimensional cross-sections. In this study, the predicted risk score of each patient of both methods were directly compared.

A fracture prediction tool should simulate a loading situation that is most critical to fracture. Anderson (2015) hypothesised that a heel strike loading was more likely to cause fracture than a one legged stance loading. However, the results of the FEA study were not conclusive in this regard as the fracture risk was mainly influenced by the relative orientation of the load vector to the lesion boundary geometry. Therefore the beam theory tool was used predict the fracture risk of the patient specific geometric models at heel strike loading to demonstrate whether the overall predicted fracture risk would increase.

In this study, the beam theory tool predicted the fracture risk of the same patient-specific geometric volume models as the FEA study which allowed a direct comparison of both methods. However, using the developed beam theory tool to calculate the fracture risk of a geometric volume model that consisted of two materials had a couple of disadvantages. The tool calculated the percentage reduction of the axial stiffness of an AVN affected compared to a healthy femoral head. The axial stiffness (EA) described the cross-sectional area (A) and the mean Young's modulus (E) of the cross-section. In this study the geometry of the healthy and AVN affected femur model was the same and hence only the Young's modulus was compared. The Young's modulus of necrotic bone was assumed to be half of the value of healthy bone. Therefore the minimum EA ratio was limited to a minimum of 0.5 which reduced the differentiation of femoral heads with large lesion volumes significantly. As a result, the predicted fracture risk of the FEA tool was additionally compared against the fracture risk using beam theory and material properties based on density calibrated CT-scans where those CT-scans were available as described in Figure 68 in the previous section. This directly compared the usefulness of segmented patient specific geometric models to models with material properties retrieved from CT-scans.

### **5.3.2 Methods**

#### **5.3.2.1 Patients and disease stage**

In addition to the clinical patient data that was used in section 5.2.2.1, demographic data and segmented femur models of three further patients with avascular necrosis were used for this study. The use of the patient data was approved by the University of Leeds Faculty of MAPS and Engineering Ethics Committee (Approval number: MEEC 10-011). Patient demographics of the three additional patients are shown in Table 24. Their AVN disease classification is shown in Table 25.

Table 24 Demographics for additional three patients selected for comparing the fracture prediction methods.

| Patient ID | Sex    | Height (cm) | Weight (kg) | Ethnicity | Age |
|------------|--------|-------------|-------------|-----------|-----|
| P01_002    | Male   | 173         | 63          | Asian     | 62  |
| P01_005    | Female | 156         | 70          | Asian     | 60  |
| P01_006    | Male   | 157         | 60          | Asian     | 59  |

Table 25 Disease classification of three patients according to ARCO (Anderson, 2015).

| Patient ID | Head diameter (mm) | Lesion involvement (%) | ARCO Classification | ARCO grade | ARCO Location |       |
|------------|--------------------|------------------------|---------------------|------------|---------------|-------|
| P01_002    | 49                 | 47                     | III                 | C          | M,C,L         | A,C,P |
| P01_005    | 38                 | 21                     | II                  | B          | M,C           | C,A   |
| P01_006    | 44                 | 10                     | II                  | A          | M,C           | C,A   |

### 5.3.2.2 Development of patient specific disease model

The fracture prediction tool based on beam theory usually assigned material properties from CT-scans by using a density-modulus relationship. In this study, however, the beam theory tool additionally predicted the fracture risk of segmented volume models developed by Anderson et al. in order to allow a direct comparison between the tool based on beam theory and FEA by using the same AVN disease model. CT-scans for patients P01\_005 and P01\_006 were not available.

Anderson (2015) created three-dimensional patient-specific geometric femoral head models. The proximal femur and the necrotic lesion were segmented using ScanIP (Simpleware Ltd., Exeter, UK) by co-registering the CT and MR scans. CT allowed identification bone structures while MRI clearly defined the lesion boundary. Cancellous and cortical bone were not distinguished. While the fracture prediction tool based on FEA only used several 2D cross-sections extracted from that 3D femur model, the fracture prediction tool developed in this study used the femoral head model as a whole (Figure 70).

A method was developed to import the segmented volume models into MATLAB for the beam calculations. The ScanIP masks of the necrotic lesion and the healthy femur were exported as two separate surface stl-files. The surface model was transformed into a volume model by using a MATLAB script developed by Adam H. Aitkenhead, The Christie NHS Foundation Trust. The volume models of healthy and necrotic bone were then superimposed creating a three-dimensional matrix grid where air had the value 0, healthy bone the value 1 and necrotic bone the value 2. The same material properties as in the FEA study were assigned to the beam femur model with 300MPa for healthy bone and 150MPa for necrotic bone which was based on previous material tests.

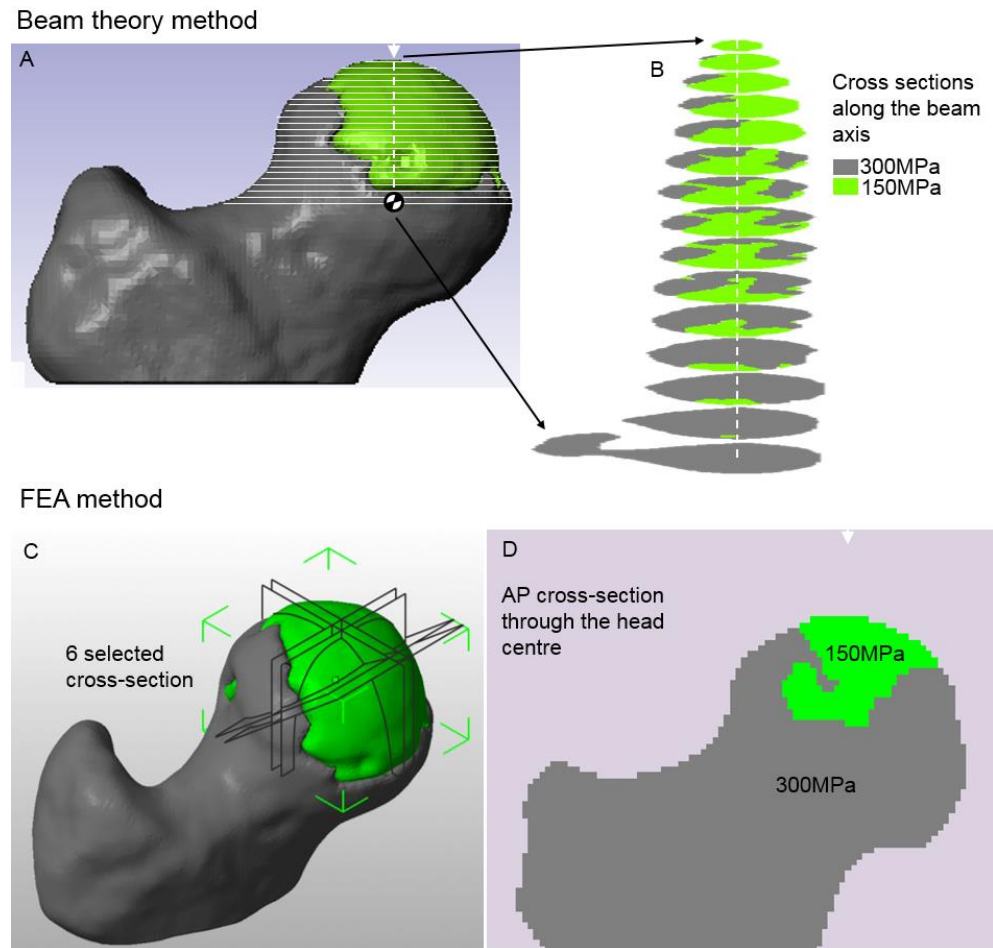


Figure 70 The beam theory and the finite element tool analyse different cross-sections of the femoral head model (P01-003). The beam tool predicted the fracture risk of the same geometric volume femoral head models as the finite element tool in this study. Necrotic bone was assigned an elastic modulus of 150MPa and healthy bone 300MPa. Healthy bone is grey and necrotic bone is green. (A-B) The beam tool analysed the whole volume of the upper femoral head by calculating the fracture risk of each cross-section along the beam axis. (C) The FEA tool predicted the fracture risk based on six predetermined cross-sections by calculating the stress difference at the lesion interface. Two cross-sections were in anterior-posterior orientation, two in medial-lateral orientation and two were angled at 20° flexion to simulate a heel strike loading. (D) AP cross-section.

The beam theory tool predicted the fracture risk based on the reduction of axial stiffness compared to a healthy unaffected reference femur. The healthy reference femur was simulated using the segmented femur model with the same material properties for both healthy and necrotic bone segments of 300MPa.

### 5.3.2.3 Beam model and fracture prediction

In this study, the beam theory tool predicted the fracture risk of the same patient-specific geometric volume models as the FEA study which allowed a sensible comparison of both methods. Additionally, the predicted fracture risk calculated by the FEA tool was compared against the fracture risk using beam theory and material properties based on density calibrated CT-scans where those CT-scans were available.

The fracture prediction tool based on FEA also simulated heel strike loading to assess the overall fracture risk. Heel strike loading represented an activity that potentially led to a higher fracture risk. The fracture risk at heel strike was also predicted using the beam theory tool by shifting the loading and beam axis to 20° flexion. The analysed cross-sections were perpendicular to the beam axis.

In summary, the beam theory tool was used to predict the fracture risk based on patient-specific two-material volume models at stance and heel strike loading. The fracture risk was also calculated from models with material properties retrieved from CT-scans using a density-modulus relationship. The  $EA_{sample}/EA_{healthy\_sample}$  ratio of the weakest cross-section quantified the fracture risk of each sample and its magnitude formed a risk score. The results of all three methods were then compared against the fracture predictions based on FEA as described by Anderson (2015).

### 5.3.3 Results

The beam tool calculated the axial stiffness for each cross-section of all femoral heads and compared their results to the corresponding stiffness of healthy femoral head (Figure 71). Each analysed femoral head geometric volume disease model alongside a case by case calculation of the axial stiffness similar to Figure 71C is shown in Table 26. The axial stiffness was calculated for a healthy femoral head (red line), a lesion affected sample (blue line) and a lesion affected sample with heel strike loading (green line).

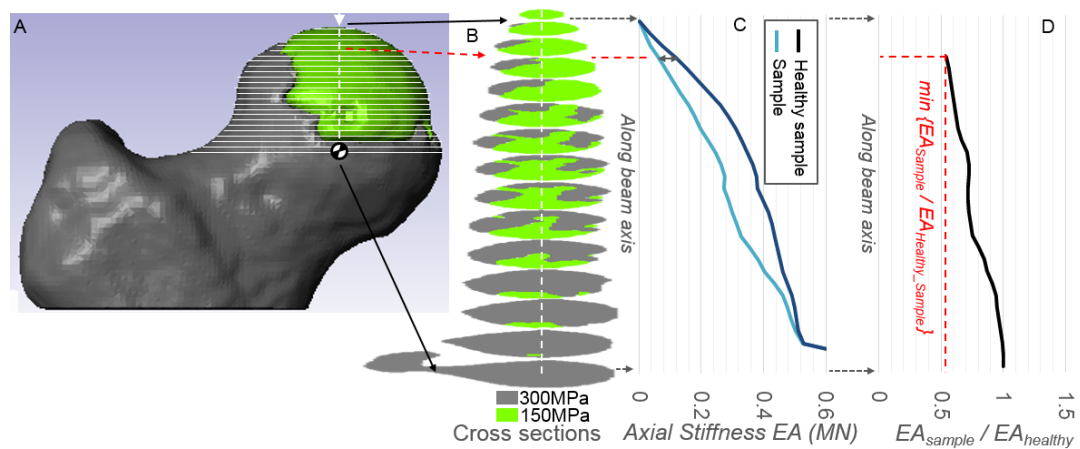
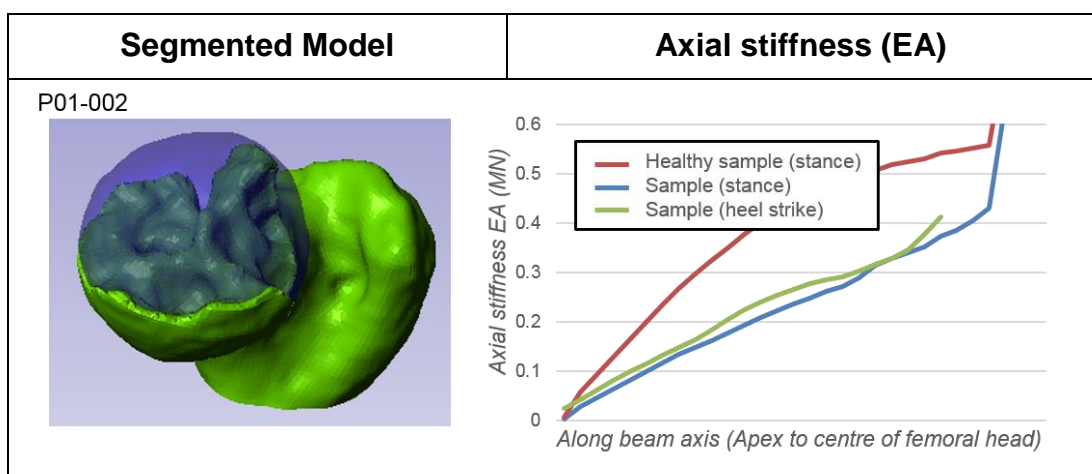
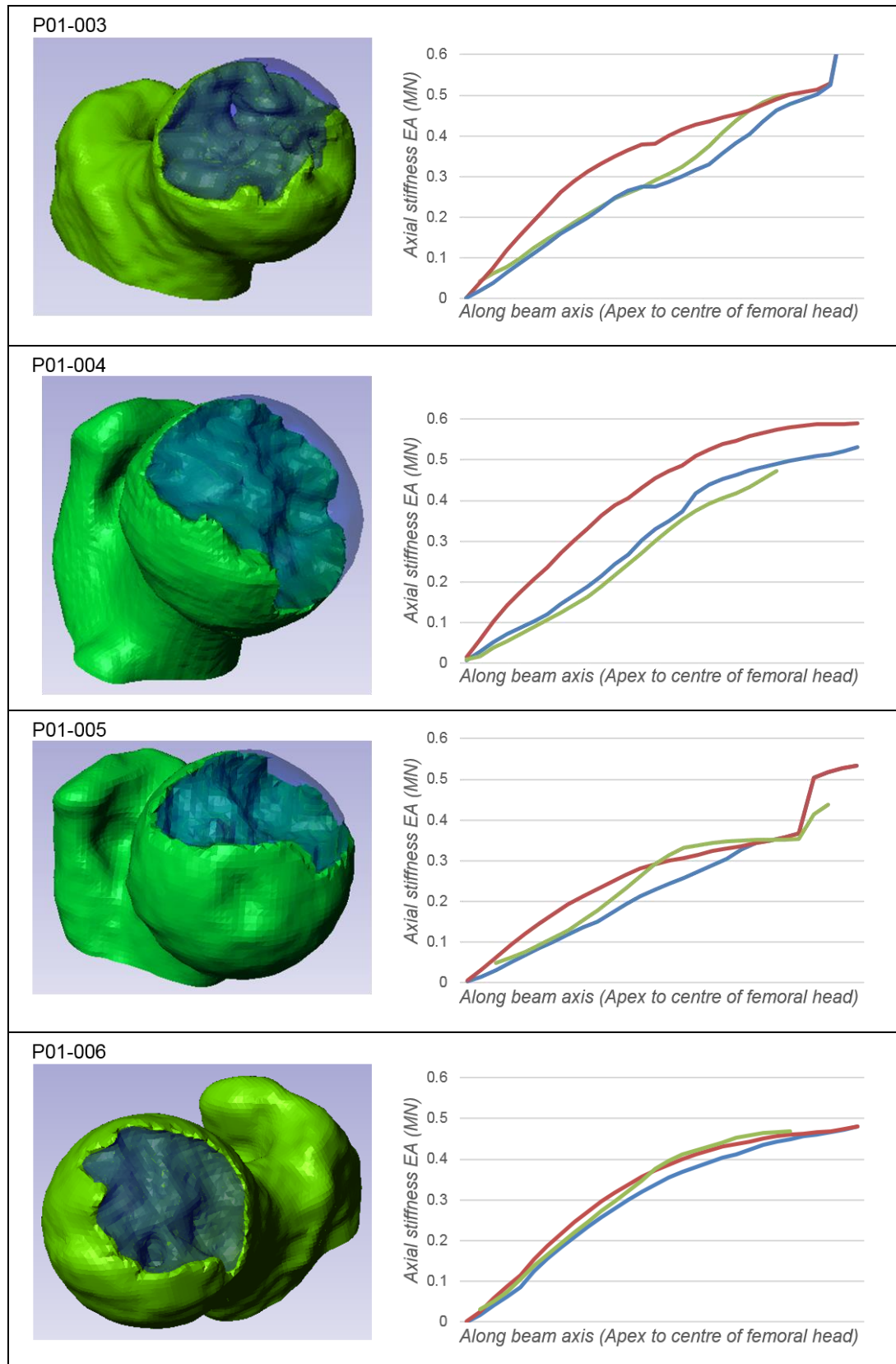
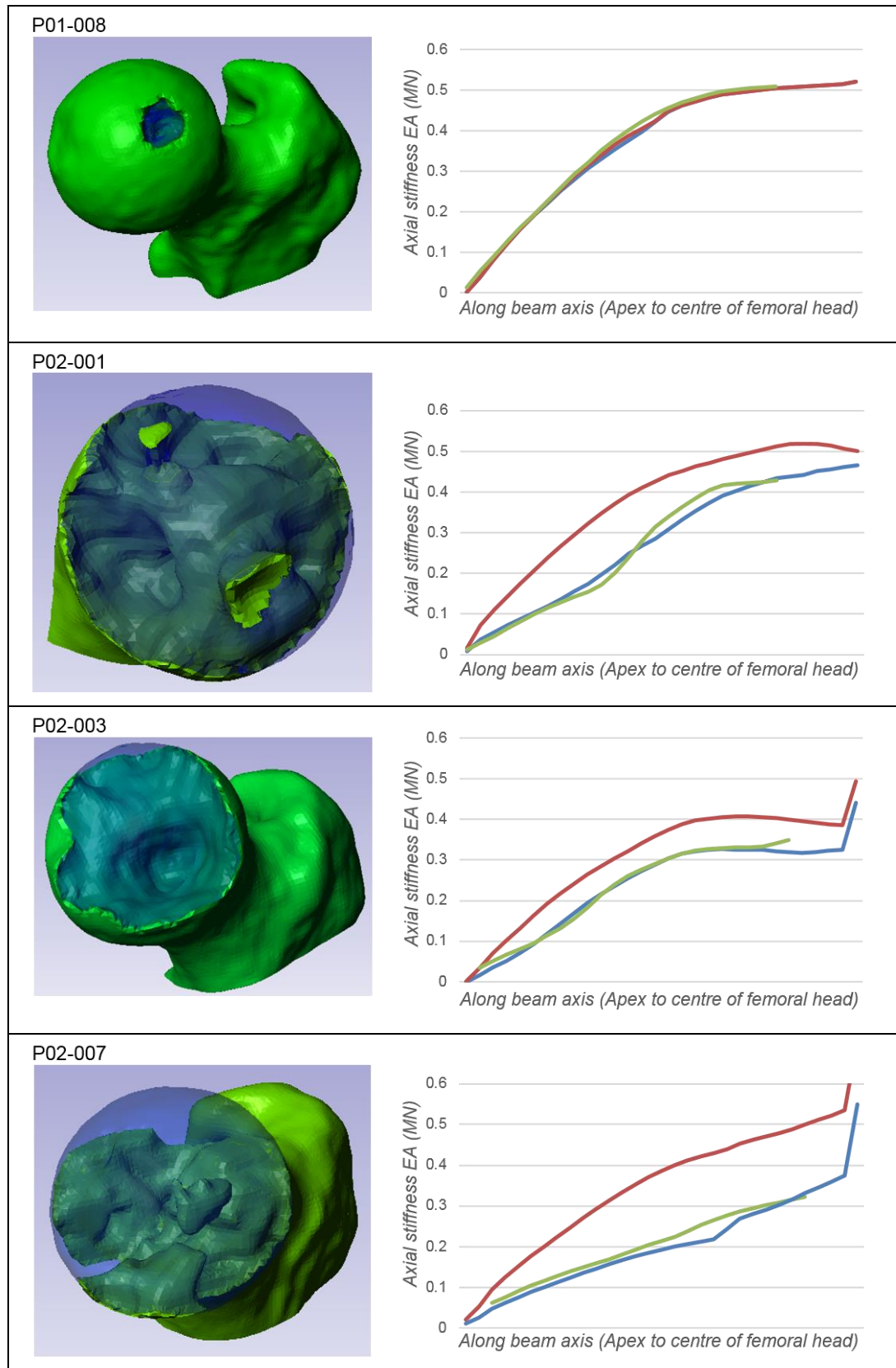


Figure 71 Computational results of the fracture prediction tool based on beam theory for stance loading of sample P01\_003: The developed tool calculated the axial stiffness of all cross-sections within the subchondral area of the femoral head. (A) The input of the tool was a patient specific two-material geometric model. (B) Cross-sections were reconstructed which were perpendicular to the loading axis (beam axis). Necrotic bone was assigned an elastic modulus of 150MPa and healthy bone 300MPa. (C) The axial stiffness (EA) of each cross-section was calculated by summing the stiffness of all pixels in that cross-section. (D) The cross-section of an analysed femoral head sample that showed the highest difference when compared to the stiffness of the healthy bone, was assumed to be the weakest. The ratio of the weakest cross-section was used to quantify the fracture risk.

Table 26 Case by case results of the beam tool analysing patient-specific femoral head geometric volume models. The axial stiffness was calculated along the beam axis for a healthy femoral head (red line), a lesion affected sample (blue line) and a lesion affected sample with heel strike loading (green line).







The beam tool estimated fracture risk based on the EA-ratio. The minimum  $EA_{\text{sample}}/EA_{\text{healthy\_sample}}$  ratio (red line / blue line) of each sample was calculated which quantified the fracture risk (Figure 71D). The revised risk score of the

FEA study was based on the difference in stress at the lesion interface for selected two-dimensional cross-sections and was then normalised with the lesion volume.

It was challenging to compare both methods as they rested on different inputs and mechanisms to predict fracture. For large lesions, the beam tool was not sufficiently granular. It was not able to differentiate the fracture risk because the EA-ratio was limited to 0.5. However, the EA-ratio moderately correlated with the revised risk score in terms of ranking and both methods did not contradict each other in their predictions (Table 27).

While there was a modest correlation when comparing the EA-ratio of the beam tool with the revised risk score of the FEA study, there was no correlation when comparing the revised risk score to the calculated EA-ratio based on the original CT-scans using a density-modulus relationship instead of a geometric volume model with homogenous material properties.

Table 27 Comparison of the individual risk scores of the finite element tool to the fracture risk results of the beam theory tool which were expressed through the relative reduction in axial stiffness. Both methods used the same geometric volume model. The EA-ratio limited to a minimum of 0.5 as a result of the assigned material properties. The order of risk of both methods was compared to the ARCO classification.

| Patient ID     | Rank EA ratio | Rank FEA risk score | Rank ARCO |
|----------------|---------------|---------------------|-----------|
| <b>P01_001</b> |               | 5 (762)             | 1 (IIA)   |
| <b>P01_002</b> | 5 (0.50)      | 7 (1133)            | 4 (IIIC)  |
| <b>P01_003</b> | 3 (0.565)     | 3 (416)             | 2 (IIB)   |
| <b>P01_004</b> | 5 (0.50)      | 4 (547)             | 3 (IIC)   |
| <b>P01_005</b> | 2 (0.567)     | 2 (328)             | 2 (IIB)   |
| <b>P01_006</b> | 1 (0.740)     | 1 (101)             | 1 (IIA)   |
| <b>P02_001</b> | 5 (0.5)       | 5 (762)             | 3 (IIC)   |
| <b>P02_003</b> | 4 (0.532)     | 6 (955)             | 4 (IIIC)  |

Anderson (2015) was not able to demonstrate that a heel strike loading led to an increase fracture risk. In this study the beam tool was used to predict the fracture risk at stance and at heel strike loading. The loading direction defined the beam axis of the beam model and therefore the slicing direction of the

analysed cross-sections. A trend emerged that simulating a heel strike loading increased the predicted fracture risk slightly compared a stance loading (Figure 72). However, looking at the calculated axial stiffness graphs of both heel strike and stance loading, the predicted axial stiffness was similar. There was no general increase or decrease in stiffness. Therefore it could not be demonstrated that heel strike loading increased the fracture risk significantly.

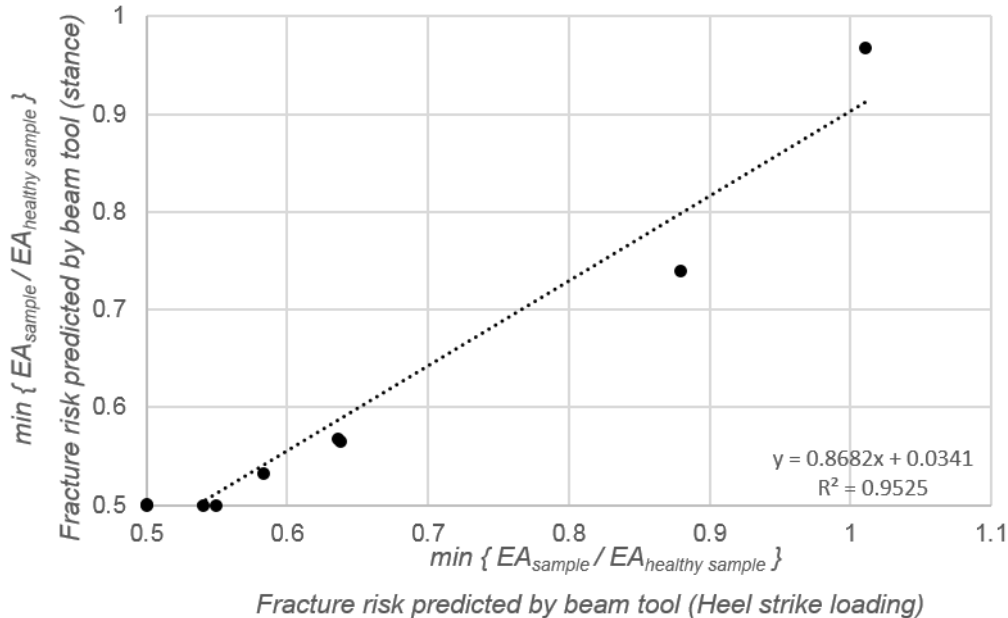


Figure 72 The minimum EA-ratio quantified the fracture risk of each sample. The predicted fracture risk was calculated for two loading situations, stance and heel strike. A heel strike loading caused a slightly higher fracture risk compared to a stance loading simulation.

### 5.3.4 Discussion

The fracture prediction tool based on beam theory was compared against another novel fracture prediction method based on FEA. A correlation or trend did not emerge when directly comparing the predicted fracture risks of both methods (Table 27) which was however limited by a low sample size of just five patients. Every fracture prediction method relies on their inputs and both methods had fundamental differences in loading directions and how material properties were assigned.

The beam theory tool analysed each cross-section of the three-dimensional femoral head model compared to the FEA tool that only used a set of six two-dimensional cross-sections. Therefore the FEA tool was affected by slice selection as each slice would have a different lesion geometry.

The fracture prediction based on FEA used patient-specific geometric models of the femoral head. Predetermined homogenous material properties were assigned to healthy bone and the necrotic lesion segments. In contrast, the beam tool assigned material properties to the femoral head model based on CT-scans by using a density-modulus relationship. When comparing the results of the FEA tool to the results of the beam theory tool when using the same geometric models, there was a better correlation. However the beam tool was inferior in calculating a differentiable fracture risk for large lesions because the EA-ratio was limited to 0.5. The beam theory tool was less effective in combination with a segmented patient-specific model. A geometric model where material properties are kept constant was verified in chapter 4.2. A disadvantage of patient-specific geometric models was that they did not quantify the decay of the necrotic lesion and its load bearing ability. In some cases necrotic lesions were encased by sclerotic bone which appeared to stabilise the weakened necrotic bone tissue. Homogenous material properties were assigned to necrotic and healthy bone but bone tissue is a non-homogeneous material. It remains questionable whether such a model was a relevant representation of a disease affected femur. The complex segmentation process was also a source for error. The developed beam tool used a model based on CT-scans which captured these material variations. Assigning material properties to the femoral head model based on CT-scans by using a density-modulus relationship appeared to be superior but only worked for bone that was not already fractured or compressed. Geometric models however still worked for post-fractured AVN stages, beyond ARCO stage III.

The risk score of the FEA tool included a heel strike loading orientation in its risk assessment. Analysing the fracture risk at a heel strike loading orientation did not add predictive power to the beam theory tool. These confirmed findings of Anderson (2015) that a heel strike loading did not generally increase the fracture risk.

The beam tool analysed the fracture risk of a sample by analysing each cross-section individually and in isolation to each other. Therefore it did not simulate the complex stress patterns that occurred within the model. This is a significant limitation of the application of beam theory. However, the tool appeared to have a good predictive capability despite not analysing the actual complex stress flow within a structure.

In general, FEA is a more comprehensive method compared to beam theory analysis but it also requires more input and computational capacity. Beam

theory is a simpler method to implement in comparison. FEA is an alternative method that can also be used to simulate fracture based on tomographic imaging. FEA would allow potential identification of failure locations, but the ability of FEA to provide an overall risk of fracture is sensitive to inputs and must be done relative to calibrated baseline cases, as in this case. While many key steps are similar such as image processing and loading directions, FEA would need to include more bone to avoid boundary constraint affects and the generation of simplified loading conditions is non-trivial in FEA and requires greater user input. In a future study the results of the beam tool for the AVN patients could be compared with the fracture load prediction of a continuum FEA model with assigned material properties based on CT-scans. However, a FEA method will always be more complex than a fracture prediction method using a beam theory approach.

## **5.4 Requirements for clinical application of developed tool**

The small degree of user input and low computational costs as a result of the simplicity of beam theory make the developed method a good option for a clinical application. If CT-scans are available, a surgeon could use this method to quickly assess the fracture risk of an AVN affected femoral head which aids the selection of a successful treatment at the point of care. This section outlines further requirements for advancing the tool into a clinical diagnostic tool.

### **5.4.1 User interface and input**

The fracture prediction tool was objective because it removed the majority of user bias by being largely automated. Once the femur is masked from surrounding soft tissue, only two anatomical positions needed be manually selected, the apex and the centre of the femoral head. These two points defined the beam axis. The centre of the spherical femoral head was easy to identify by drawing a circle around the head in three dimensions (Figure 73). The apex or starting point of the beam axis was identified as relative to the stem axis in order to simulate a one legged stance loading.

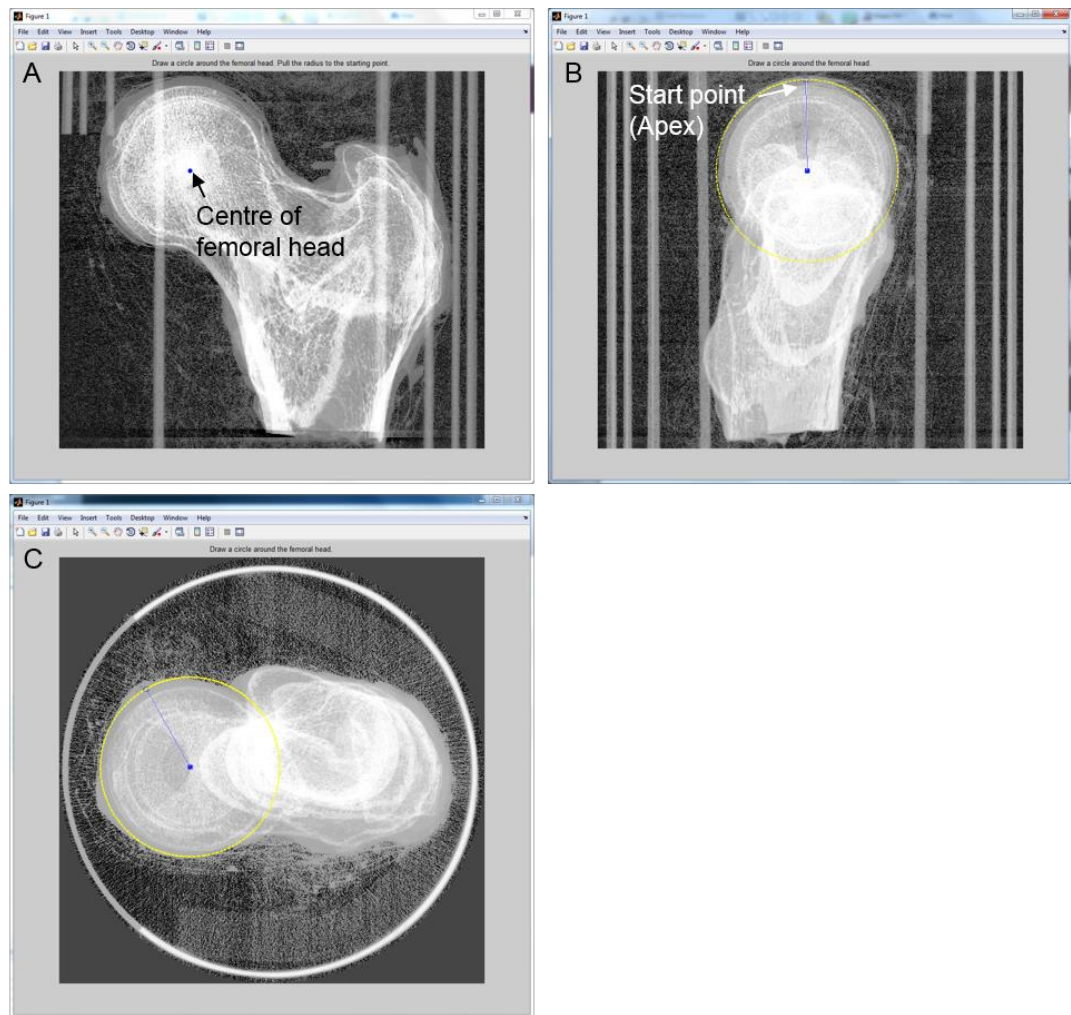


Figure 73 The location of the centre of the femoral head was selected in three planes (A) AP, (B) Medial lateral and (C) distal. The interface showed a virtual X-ray image in all three planes. The tool helped selecting the centre of the femoral head by allowing the user to draw a circle around the spherical head (yellow line).

Virtual X-ray images from the CT-scans were created to allow the selection of the centre of the femoral head. Clinical CT-scans needed to be threshold segmented to reduce noise from surrounding soft tissue (Figure 74). However, adjacent bone structures such as the acetabulum obscure the view on the femoral head which makes a selection difficult especially in a clinical setting.

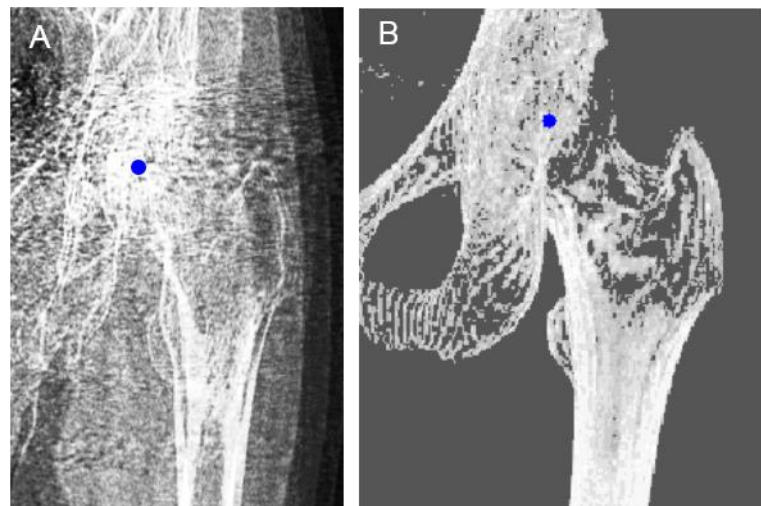


Figure 74 Comparison of virtual X-ray images from a CT image. (A) Clinical patient CT. (B) Threshold improved image which helped to identify anatomical landmarks.

Clinical CT-scans sometimes only cover the proximal femur to minimise X-ray exposure. In this case the femoral shaft axis can still be approximated by fitting the proximal femur to a geometric model of a full femur (Figure 75). This process can be complex within the clinical environment but it is not specific to beam theory simulations alone. Further automation could potentially eliminate the required user input. The anatomical orientation of the femur as well as the manual selection of anatomical points can be automatically determined based on available landmarks which can be referenced against a full femur model (Wright et al., 2011).

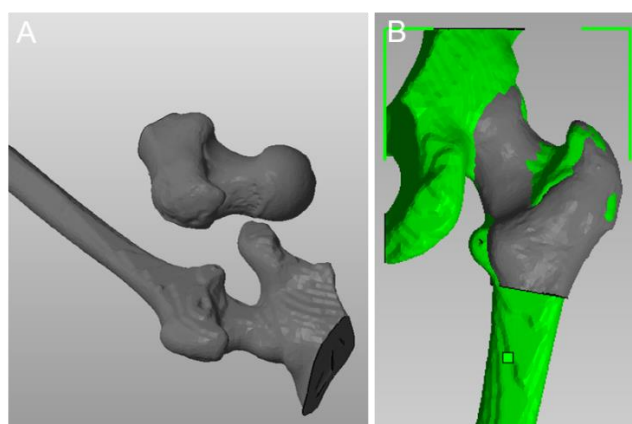


Figure 75 (A) A proximal femur and a full femur including the pelvis were segmented and arbitrarily orientated. (B) A proximal femur model was referenced against a full femur model in order to approximate the shaft axis for samples without shaft. Anterior posterior view of the proximal femur model (grey) referenced with the full femur model (green).

#### 5.4.2 Density calibrated CT-scanner differences

The fracture risk of was estimated by comparing an affected femoral head against calibrated baseline cases. This chapter demonstrated that the comparison to a reference set of healthy femurs was successful in identifying samples with a high fracture risk. The material properties of bone were retrieved from density-calibrated computed tomographic (QCT) imaging. In order to establish a universal target for surgical interventions, the scanner settings and the density calibration should be similar to produce reliable results. Large inter-scanner differences would affect the reliability of the results (Carpenter et al., 2014).

### 5.5 Summary

The image based beam theory tool was used to predict the fracture risk of AVN affected femoral heads. The tool was able to detect the increased fracture risk which was a result of the disease. All patients were stratified in terms of their fracture risk and subsequently ranked. The rank corresponded to the rank of the current diagnostic gold standard ARCO. This study also showed that the calculation of the fracture risk can be done relative to a reference set of healthy femurs. A feasible benchmark is important when developing the tool into a clinical application in the future.

In second part of this study the developed beam tool was compared against another novel fracture prediction tool based on FEA. The tools were used to calculate the fracture risk for the same set of AVN patients, however there was no direct correlation between both risk assessments. As both methods had fundamental differences in their methodology, the effects of those different approaches were analysed. The FEA tool used patient-specific segmented geometric models with homogenous material properties from previous material tests while the beam tool assigned material properties to the femoral head model based on CT-scans by using a density-modulus relationship. Only when both methods were used in the patient-specific geometric femoral head models to calculate the fracture risk did a correlation between the results emerge. Geometric models were advantageous as a density-modulus relationship was not practical for post-fractured AVN however those models could not incorporate the complexity of inhomogeneous bone tissue. The beam tool was also not able to calculate a differentiable fracture risk for femoral heads with large lesions for geometric

models. Simulating a heels strike loading did not improve the predictive capability of the tool compared to a one legged stance loading.

## 5.6 Conclusion

The fracture prediction tool used structural mechanics and density calibrated CT-scans to stratify AVN patients. The fracture risk was quantified by the reduction in stiffness.

This study showed that AVN affected femoral heads showed a reduction in axial stiffness which the tool was able to detect. This contradicted findings by Brown et al. (1981) who described a reduction in Young's modulus together with an general increase in bone mineral density of AVN affected femoral heads. The overall density of AVN affected femoral heads decreases and therefore it was possible to predict the fracture risk based on structural stiffness and the material properties retrieved from a density-modulus relationship.

The tool stratified patients according to their predicted fracture risk and the patients were ranked in ascending order. The ranking correlated with the classification and grade of the ARCO standard which indicated that the developed tool had similar good predictive capabilities.

Overall, beam theory was successful in calculating the fracture risk of AVN affected femoral heads and these findings were an important step for translating this method into a clinical application. Beam theory was mostly user independent removing the majority of user bias which is a key problem of current diagnostic classification systems. Further work in form of a larger follow-up study is needed to create a clinical benchmark with density calibrated CT-scans using controlled settings.

The tool was not able to predict the fracture risk of a femoral head once initial fracture occurred. Patients with initial fractures are at an advanced stage of the disease and are therefore easy to diagnose. The tool can help clinician to stratify patients with an pre-collapsed femoral head which is harder to diagnose.

The comparison of the fracture prediction tool based on beam theory and the fracture prediction method based on finite element analysis (FEA) was difficult as both tools had very different methods to predict fracture. A main difference was that the beam tool assigned material properties to the femoral head model based on CT-scans by using a density-modulus relationship while the FEA

tool used segmented geometric models with material properties based on empirical tests. The segmentation of lesion models required great user input. The beam tool was a simpler method compared to FEA and required less computational expense which is important in the clinical setting.

The developed tool can be further developed to assess the fracture risk of AVN affected femoral heads *in-vivo* by comparing the results with pre-calculated results of a reference set of healthy femoral heads, serving as a guideline to give a target for surgical interventions.

## Chapter 6 Other applications for the developed beam theory tool

### 6.1 Introduction

The need for an objective clinical tool to assess the fracture risk of bone goes well beyond AVN and the femoral head. The developed analytical beam theory method can potentially be used for a wide range of other bone diseases. Risk stratification can help to identify patients whom require immediate surgical treatment. The broadening of the developed method to other bone diseases might possibly also increase commercial interest. In Europe and the United States only approximately 3% of all THA are attributed to AVN or osteonecrosis of the femoral head (Bitzer et al., 2010; Swedish Hip Arthroplasty Register, 2014; National Joint Registry, 2015; AJRR, 2016). Therefore this chapter describes how the developed fracture prediction tool based on beam theory can be used for other applications beyond AVN in the future.

The developed fracture prediction method can be used for a wide range of other conditions that lead to bone fracture as long as the decrease of structural integrity of the bone is a result of material and/or geometric changes. The predictive capability of the developed method was based on the analysis of material and geometrical properties which were derived from density calibrated CT-scans.

This chapter discusses the potential universal nature of the developed fracture prediction method and how it can be used for other diseases. While AVN most commonly affects the femoral head, other conditions such as osteoporosis or skeletal metastasis can also affect other parts of the femur. In order to widen the application of the fracture prediction method, the whole femur including shaft and neck needed to be analysed. Therefore the developed fracture prediction was extended to the rest of the femur. Curved beam theory was used to account for the curved geometry of the intertrochanteric area of the femur. Beam theory allowed prediction of the failure load of femurs based on their geometric and material properties. The operability of the tool was tested by utilising clinical QCT-scans of human femurs and comparing the predicted fracture loads with fracture loads reported in the literature. The fracture prediction tool was further verified against twelve proximal femur models made from segmented CT-scans and additive manufacturing.

## 6.2 Possibilities for use of tool outside AVN

### 6.2.1 Osteoporosis

Osteoporosis (OP) is a progressive chronic bone disease which is characterised as a reduction in bone mass which may increase sensitivity to fracture (Melton, 1996). If not altered by drug treatment, there is a relationship between micro architectural deterioration and bone mass. The decrease in material properties of bone can be measured as a reduction in the bone density and therefore the described aetiology fits into the scope of the developed fracture prediction method which is sensitive to these kind of changes.

According to the NHS, around 3 million people have osteoporosis in the UK (National Osteoporosis Society, 2015). Osteoporosis most commonly affects the wrist, humerus, ribs, vertebral body, pelvis and hip. OP may be considered an almost universal phenomenon of aging. The imbalance between bone resorption (osteoclasts) and bone formation (osteoblasts) results in a constant reduction of the bone mineral density which weakens the bone structure. Until the mid-20's bone mass increases rapidly and loss begin after that (Cummings and Kelsey, 1985). The bone structure gets weaker which increases the risk that even minor accidents can cause bone fracture.

Osteoporosis is often first diagnosed when bone fracture occurs however it can be attributed to several risk factors such as age, hormone changes, low body weight, physical inactivity, prior steroid treatments, family history and race. The identification of these risk factors is a key element of the current diagnosis to identify those patients that need further assessment. If a patient belongs to a high risk group, a DEXA scan is currently the gold standard to quantify the fracture risk (Brown and Josse, 2002). The density of the femur is measured in the coronal plane and the density at the site is then compared to the density of a reference set of healthy patients. The analysed patient is then categorised depending on the number of standard deviations above or below the mean of the healthy reference set. This widely used classification system is called T-score (World Health Organisation, 2003). Osteoporosis is linked to a T-score lower than -2.5.

The developed fracture prediction method of this study also uses bone density as one predictor for fracture and is therefore similar to the current diagnostic approach for osteoporosis. An advantage of DEXA-scans is the low radiation exposure. However DEXA scans only take a two-dimensional density measurement and are affected by overlying thickness of tissue. Geometric

changes that increase the fracture risk further cannot be assessed with DEXA scans. This is not problematic when osteoporosis occurs in isolation but might be important when it occurs in conjunction with other bone diseases such as AVN. If multiple diseases are suspected the developed fracture prediction tool can be used to assess if a surgical intervention is necessary.

### **6.2.2 Skeletal metastasis**

Cancer may spread to bones like the femur where it develops osteolytic lesions that affect the strength of the affected bone. Skeletal metastases lead to a general decay of bone matter and they also alter the bone geometry. This reduces both material and geometrical properties of the affected bone such as the Young's modulus, the cross-sectional area and the second moment of area which were used by the developed tool to predict fracture. The density-modulus material model remains valid for bone with metastases (Kaneko et al., 2004).

The femur is a common place for metastatic lesions. Besides pain, these lesions pose a risk of pathologic fracture. A surgical intervention may be necessary depending on presented fracture risk. However, current diagnostic methods are not reliable in assessing the fracture risk. They rely on the lesion volume and a lesion is considered critical if it affects more than 50% of the bone diameter, or if it is bigger than 25 mm (Bast et al., 2017). Snyder et al. (2006) analysed femurs affected by benign bone lesions and demonstrated that bending and torsional stiffness were better parameters for predicting pathologic fracture than the current radiographic criteria. The structural stiffness takes both material and geometrical properties into account and can therefore reveal whether a smaller lesion at a specific location is more critical for fracture than a larger lesion elsewhere.

### **6.2.3 Discussion**

Structural properties such as axial, bending and torsional stiffness are highly significant predictors of bone fracture as they account for both material and for geometrical properties. Bone diseases usually lead to a reduction in the bone material or density which is linked to the Young's modulus. Lesions can further change the load optimised structure of bone which can lead to an increase of stress under an applied load. This geometry change is linked to the cross-sectional area and the second moment of area.

By accounting for changes in both bone material and bone geometry, the developed fracture prediction based on structural mechanics and beam theory

has the potential to be developed into a universal diagnostic bone tool that can be used for an array of different bone diseases. The increase of the fracture risk can be quantified by comparing the estimated structural stiffness (EA, EI, GJ) of an affected bone with either the corresponding healthy contralateral bone of the patient or the mean stiffness of a reference set of corresponding healthy bones. In cases where the analysed bone is slender, any taper is slight and the load can be assumed to be evenly distributed over the cross-sectional area, a precise estimation of the exact magnitude of the fracture load is possible by using the beam theory equation. The beam theory equation uses the aforementioned structural properties to calculate deflection. In combination with a strain based failure criterion, it can be used to predict at which load each of the cross-sections is likely to fracture. The cross-section with the lowest fracture load is assumed to be the point where fracture of the entire bone is likely to initiate.

Depending on the anatomical site, bone fracture can be predicted by comparing structural stiffness to a reference bone or by calculating the fracture load directly based on a beam theory equation. There is potential to improve the current assessment of the fracture risk by using a combination of density-calibrated computed tomographic imaging and structural mechanics.

## **6.3 Curved beam theory for fracture prediction of long bones**

### **6.3.1 Introduction**

The femur as a long bone was ideal for the application of beam theory analysis. The femur can be modelled as a structural member subjected to load. Beam theory analysis allowed prediction of the fracture load at each bone cross-section to assess which was likely to fracture. While the shaft of the femur can be modelled as a straight beam, the intertrochanteric area of the femoral head had a curved geometry which needed to be accounted for. Using straight beam theory for a curved structure would lead to an underestimation of the fracture risk (Bach and Baumann 1924).

An accurate loading model of the femur that represented the true *in-vivo* loading condition was another challenge. Multiple complex muscles are attached to the femur which sometimes interact with each other. Therefore, the loading of the femur with joint contact and muscle forces needed to be simplified to develop a simple and quick tool that can be used in the clinical setting. The main function of attached muscles beside creating motion is to

reduce bending moments (Pauwels, 2012). Ignoring muscles subject the femur to increased bending moments. Bones are designed to mainly support compressive loads at both macro and micro scale.

Pauwels et al. (2012) suggested a simple loading model based on the assumption that there is an equilibrium of moments around the centre of the femoral head which is the centre of the ball and socket joint (Figure 76). The lever arm  $b$  of the bodyweight  $B$  is approximately three times longer than the lever arm  $a$  of the muscular force  $A$ . Hence, the muscular force is about three times larger than the body weight. The joint contact force  $F$  is therefore about four times the force of the body weight  $B$  and acts on the femoral head to the greater trochanter. Bergmann et al. (1993, 2001) measured joint reaction forces which were slightly lower between 2-4 times the body weight. Heller et al. (2005) simulated abductor forces of max 104% BW for walking.

Because of the complexity of muscle forces and lack of ways to validate models, most studies simply ignored muscle forces (Yamada and Evans, 1970; Huiskes, 1984). Taylor et al. (1996) demonstrated that stress within the femur is influenced more by the direction of the joint contact force than the muscle forces and Rohlmann et al. (1983) suggested that physiological loading of the femur can be adequately simulated with a single joint load in direction of the longitudinal axis of the femoral shaft.

Currently, there is no diagnostic tool based on QCT and structural mechanics that would help clinicians assess the fracture risk. The aim of this study was to assess the potential of a three-dimensional analytical bone tool based on beam theory to predict fracture within the femur which may be developed to a universal bone tool in the future.

### **6.3.2 Method**

#### **6.3.2.1 Biomechanical loading model**

Stress simulations within the femur were dependent on the chosen biomechanical loading model. For fracture predictions, the loading situation with the highest fracture risk should be analysed (Keyak et al., 2001). In this study a one legged stance was analysed in which the whole body weight minus the weight bearing leg was channelled through the hip. The *in-vivo* loading conditions were too complex so that simplifications were inevitable (Figure 76). The effects of different loading conditions on the fracture prediction were therefore verified and compared in this study.

Initially the femur was loaded with a single joint contact force. Three different loading orientations were compared: (1) the loading vector was in alignment with the mechanical axis of the femur, (2) the loading vector was parallel to the femoral shaft axis and (3) a one legged stance was simulated.

In a next step, the effect of including the abductor muscles was analysed. The abductor muscles were merged to a single force that acted at the posterior surface of the greater trochanter. The abductor force was assumed to be 75% of the joint reaction force.

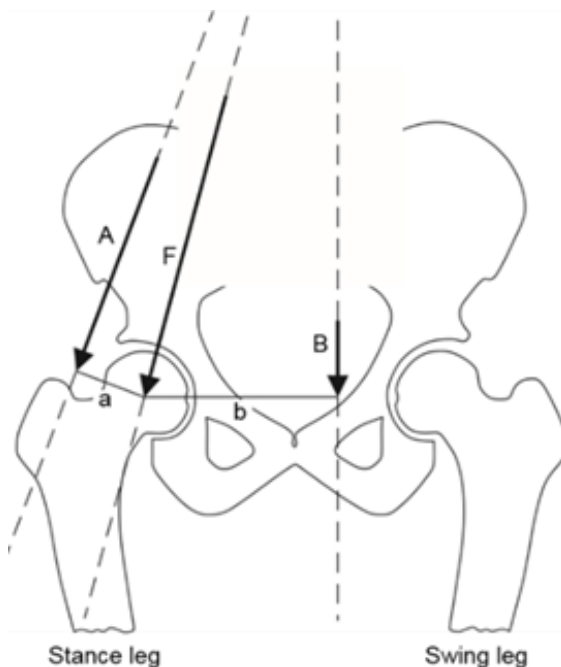


Figure 76 Biomechanical loading model of the hip according to Pauwels (2012).

The lever arm  $b$  of the bodyweight  $B$  is approximately three times longer than the lever arm  $a$  of the muscular force  $A$ . The joint contact force  $F$  is about four times the force of the body weight  $B$ .

### 6.3.2.2 Curved beam theory and fracture risk prediction

The location of the beam axis within the femur played an important role as the CT-volume of the femur was divided into a stack of 2D cross-sections which were perpendicular to the defined beam axis. These cross-sections were then individually analysed for the fracture prediction. The beam femur model and the fracture load prediction were realised in MATLAB (R2013b, MathWorks, MA).

A simple straight beam axis following the mechanical loading axis of the femur was not able to accurately predict fracture within the proximal part of the femur

as it did not account for the curved geometry of the intertrochanteric area. Fracture, however, was likely to occur at the proximal part of the femur.

The location of the chosen beam axis and the modulus weighted centroids should concur as the centroid was the point in a cross-section where no bending stress occurred which defined the neutral axis. The linear neck and shaft axis of the femur were a good fit. For a smooth transition and to account for the curved geometry of the intertrochanteric area, a hyperbolic function was used between those two axes.

In order to have a close as possible agreement between the location of the hyperbolic function and the modulus weighted centroids of that region, the hyperbolic function was defined in two steps. In a first step the location of the modulus weighted centroids was calculated for cross-sections perpendicular to the straight neck and shaft axis (Figure 77). Then, curve fitting was used to calculate a value for parameter  $c$  of the hyperbolic function (Eq.6.1) so that it closely matched the location of those centroids. This hyperbolic function linked the neck and shaft axes and therefore formed the final beam axis of that femur model.

$$\frac{y^2}{a^2} - \frac{x^2}{b^2} = c \quad 6.1$$

where,  $a$  and  $b$  describe semi-axes and  $c$  the linear eccentricity of the hyperbolic function in a Cartesian x-y coordinate system.

Despite this fitting process, the mass of the greater trochanter still caused the modulus weighted centroids to shift away from the assumed beam axis leading to an unwanted disparity between the beam and the neutral axis. Taking this into account through a higher parameter function would lead to unstable slicing direction of the femur model and the beam axis would also not follow the continuity of the stress flow. Therefore, the centroid-derived hyperbolic curve, which connected the neck and shaft axis, showed the best compromise for modelling the intertrochanteric area.

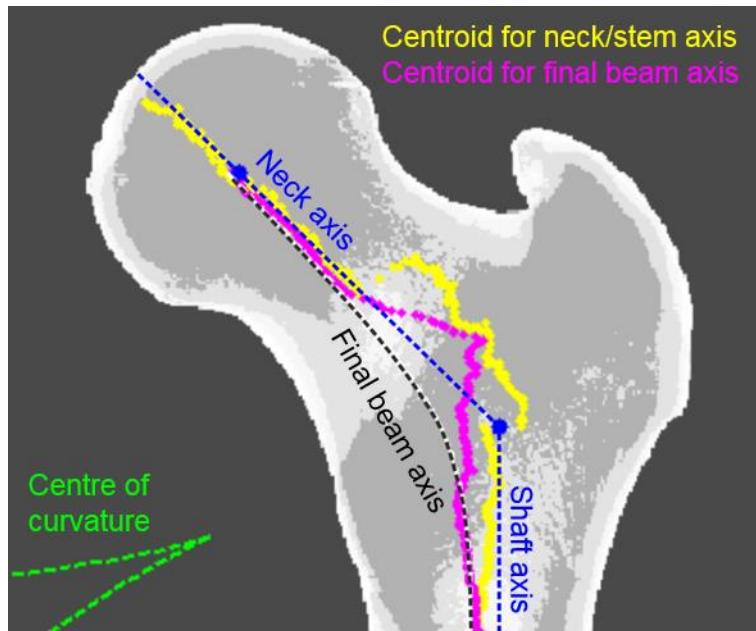


Figure 77 AP view of a proximal femur. The location and curvature of the final curved beam axis (black) was calculated based on the location of the modulus weighted centroid (yellow) of cross-sections which were perpendicular to the straight neck and shaft axis (blue). The location of the modulus weighted centroids of cross-sections perpendicular to the final curved beam axis (pink) mostly correlated with the beam axis except at the intertrochanteric region where the mass of the trochanter shifted the centroids. The centre of curvature of the curved beam axis is green.

There are differences in predicted and measured loads when using straight beam theory for beams with curvature. The fracture prediction method needed to account for this. Bach and Baumann (1924) demonstrated that predicted loads for curved beams were too small compared to experimental loads when using the beam equations for a Bernoulli straight beam. Beam curvature causes the neutral axis to shift away from the centroidal axis to the centre of curvature which leads to a stress concentration and a non-linear distribution of stress. Ignoring the stress concentration would lead to an underestimation of the predicted stress. If the ratio of the radius of curvature to depth for the beam is less than five, the beam equation used for straight beams is inadequate (Boresi et al., 1993). Winkler (1867) postulated how to calculate stresses within curved beams.

If a curved beam element as in Figure 78 is subjected with a moment the strain can be described as Eq.6.2. The constant  $k$  represents the curvature.

$$\varepsilon = \frac{(r_{na} - r) \delta\theta}{r d\theta} = k \frac{r_{na} - r}{r} \quad 6.2$$

The strain can then be substituted with Hook's law equation (Eq.6.2)

$$\sigma = \epsilon E = E k \frac{r_{na} - r}{r} \quad 6.3$$

For the curved beam element, the equilibrium dictates that if there is no axial force.

$$F = \int \sigma dA = 0 \quad 6.4$$

By using Eq.6.3, Eq.6.4 can be rearranged to

$$(=) E k \frac{r_{na} - r}{r} = 0 \quad 6.5$$

$$(=) E k \left( \int \frac{r_{na}}{r} dA - \int \frac{r}{r} dA \right) = 0 \quad 6.6$$

$$(=) r_{na} = \frac{dA}{\frac{dA}{r}} = \frac{A}{\int \frac{dA}{r}} \quad 6.7$$

The equilibrium function for the Moment is

$$M = \int y \sigma dA \quad 6.8$$

By using Eq.1.2 with  $y = r_{na} - r$ , Eq.6.8 can be rearranged to

$$= \int (r_{na} - r) E k \frac{r_{na} - r}{r} dA \quad 6.9$$

$$= E k (r_{na}^2 \int \frac{dA}{r} - 2r_{na} \int dA + \int r dA) \quad 6.10$$

By using Eq.1.6, Eq.6.10 can be rearranged to

$$= E k A (r_c - r_{na}) \quad 6.11$$

Ultimately, equations 6.3, 6.7 and 6.11 allow bending stress to be calculated. The difference between the radius of the modulus weighted centroid and the radius of the neutral axis is  $e$ .

$$\sigma_b = \frac{M}{A (r_c - r_{na})} \frac{r_{na} - r}{r} = \frac{M(r_{na} - r)}{A r (r_c - r_{na})} = \frac{M y}{A e (r_{na} - y)} \quad 6.12$$

This beam equation for bending can be superimposed with an axial stress component (Mourtada and Beck, 1996) which leads to the following equation for a curved beam:

$$\sigma = \frac{F}{A} - \frac{M y}{A e (r_{na} - y)} \quad 6.13$$

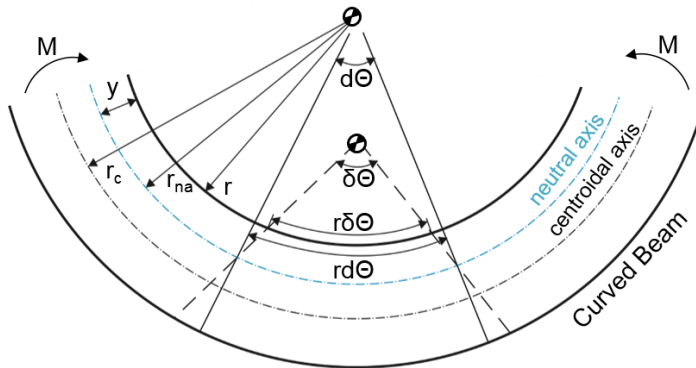


Figure 78 Deflection of a curved beam element subjected to a moment (M).

The curved beam equation (Eq.6.16) was used for the stress simulations as a result of forces and moments in the coronal plane and the straight beam equation (Eq.6.17) was used for forces and moments in the sagittal plane. If the ratio of radius of the curvature to the depth of the beam was less than ten, only straight beam theory was used in all planes. Cross-sections of the shaft were assumed to be axis symmetric and were assumed to remain in-plane after bending. Linear-elastic material behaviour and small deflections were assumed.

The highest von Mises stress was calculated for each cross-section along the beam axis. When applying Hooke's law the resultant stress can be rearranged for strain (Eq.6.14).

$$\varepsilon = \frac{\sqrt{(\sigma_{axial} + \sigma_{bending})^2 + 3(\tau_{torsion}^2 + \tau_{shear}^2)}}{E} \quad 6.14$$

$$\sigma_{axial} = \frac{L(F)}{A} \quad 6.15$$

$$\sigma_{bending (coronal)} = -\frac{M(F) y}{A e (r_{na} - y)} \quad 6.16$$

$$\sigma_{bending (sagittal)} = \frac{M(F)}{I} \cdot c \quad 6.17$$

$$\tau_{torsion} = \frac{T(F)}{J} \cdot c \quad 6.18$$

$$\tau_{shear} = \frac{Q(F)}{A} \quad 6.19$$

Where L is the axial load, M is the applied bending moment, T is the applied torque and Q is the transverse load. L, M, T, Q are dependent on the location of the cross-section and the joint contact force F. A is the area of the cross-

section,  $\epsilon$  is strain, E is Young's modulus, I is the second moment of area of the cross-section, J is the polar moment and c is the distance to the most distant fibre. The most distant fibre is the point of material in the cross-section which has the furthest distance from the modulus weighted centroid. The shear modulus was effectively simplified to  $E=3G$  (Salathe and Arangio, 1989). While the cross-sections were not axis symmetric, the principal axis only deviated slightly and therefore an assumed medial-lateral bending axis was sufficient (Figure 79). It was therefore justified to omit the use of the principal axes for the curved beam part.

When applying a strain based failure criterion, equations 6.4 can finally be rearranged for the joint contact load F at which the analysed bone will fracture. Therefore a direct correlation between the joint loading and the bone fracture in each cross-section was established. It was assumed that fracture is imminent for human trabecular at a yield strain of greater than 0.85% for compression and 0.61% for tension (Morgan et al., 2003).

Huiskes (1984) argued that shear stress can be neglected as it is insignificant compared to bending or compression stress. This can be supported by the fact that bone is designed to bear compressive stress. If shear stress is ignored, equation 6.14 leads to a much simpler equation. The effect of shear stress was analysed and compared in this study.

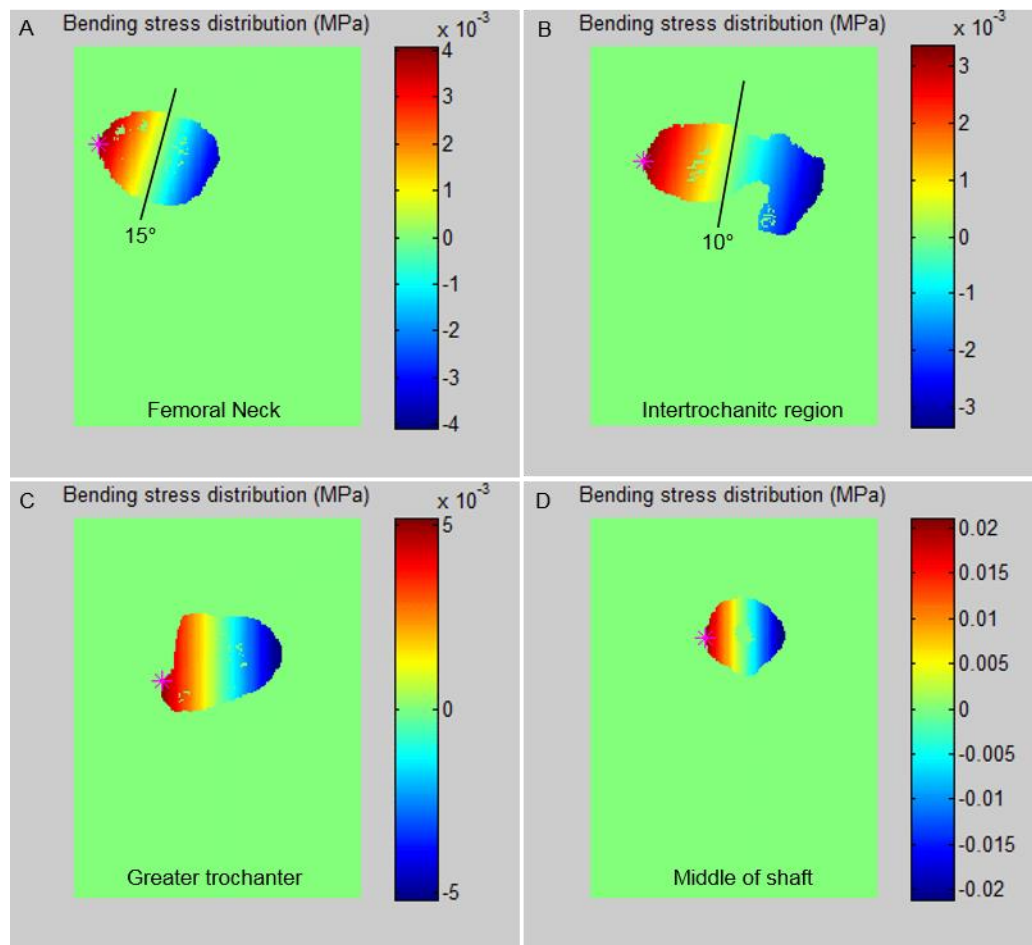


Figure 79 Analysis of the principal axis angle. The axis deviated slightly from the medial-lateral axis within the intertrochanthic area. Pink asterisk indicates point of highest stress.

### 6.3.2.3 Image processing

Clinical CT-scans of eight healthy femurs were used to test the developed beam tool. The four white male subjects had an average bodyweight of  $64 \pm 7\text{kg}$  and were  $70 \pm 14$  years old. The CT-scans were generated using a Toshiba Aquilion (Toshiba, Japan) and had a resolution between 0.5 – 1 mm. Both legs were scanned at the same time and the scans were density calibrated using a potassium phosphate phantom. The CT-scans were provided by DePuy Synthes Joint Reconstruction (Leeds, UK) following approval of ethics application from University of Leeds Faculty of MAPS and Engineering Ethics Committee (Approval number: MEEC 11-044).

The clinical CT-scans had a DICOM file format. The DICOM standard stores the three dimensional CT-image as a stack of separate cross-sectional images files. The axial slice orientation of those cross-sectional images corresponded to the scanning direction of the CT-scanner. The tool analysed

cross-sectional images that were perpendicular to the assumed beam axis and the orientation of those cross-sectional images was therefore different.

The stack of two-dimensional DICOM images was converted into a single three-dimensional image file. Reconstructing cross-sectional images from a single raw image file was computationally more efficient as only information which were required for the actual image reconstruction could be loaded without loading the entire CT-image onto the computer's random-access memory (RAM) which was computationally much more expensive.

The femoral bone was segmented as surrounding soft tissue and adjacent bone would have compromised the fracture calculation. The previously described automatic segmentation was unsuccessful for the tested samples. The CT-scans had a low resolution and the femoral head was indistinguishable from the acetabulum. Therefore the images were manually threshold segmented by using ScanIP (Simpleware Ltd., Exeter, UK) (Figure 80). Other functions used to segment the femur were un-painting adjacent bone structures, a morphological close filter and a flood fill filter. An interface was created to allow the import of the stl-file of the created bone mask into the developed fracture prediction tool in MATLAB.

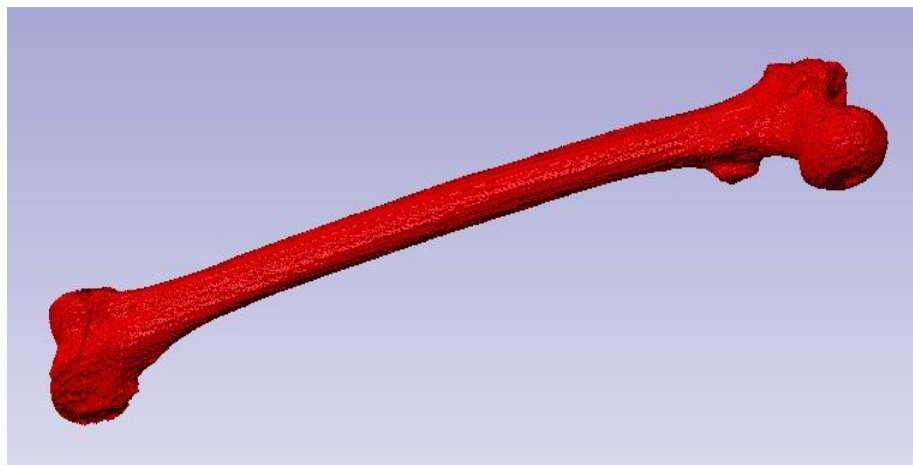


Figure 80 Segmented femur mask.

#### 6.3.2.4 Material model

Material properties were assigned to the beam model from density calibrated CT-scans by using a density-modulus relationship (Table 28). The QCT-density of each pixel in the CT-scan was estimated using a density calibration. Keyak et al. (1994) described a relationship for potassium phosphate

calibrated CT-scans to convert QCT-density to ash-density. Ash-density can then be converted to wet apparent density as discussed in section 2.4.2. Pixels below HU=0 were ignored.

In the literature there are different density-modulus relationships proposed for cortical and cancellous bone. While cancellous bone is usually described by a power law, cortical bone has a linear density-modulus relationship. A density threshold can be used to distinguish between cortical and cancellous bone.

Morgan et al. (2003) found a density range of 0.26-0.75 g/cm<sup>3</sup> for cancellous bone whereas Snyder et al. (1991) found a density range of 1.748-1.952 g/cm<sup>3</sup> for cortical bone. Most pixels however had an assigned density value which lay between those two density ranges, as described in chapter 3.4. An abrupt discontinuity which was caused by the use of two different material models was avoided in this study by using the material model proposed by Morgan et al. (2003) for cortical bone also. This assumption was supported by the fact that the Young's modulus of the cortical samples tested by Snyder et al. (1991) aligned with the power relationship for cancellous bone described by Morgan et al. (2003) (Figure 81) which led to an overall R-square value of 0.98.

Table 28 Material model used for cancellous and cortical femoral bone.

| Relationship   | Source                     |
|--|----------------------------|
| $\rho_{ash} = 1.06 \rho_{QCT} + 0.0389$ [g/cm <sup>3</sup> ]     | Keyak et al., 1994         |
| $\rho_{app} = \rho_{ash} \div 0.6$ [g/cm <sup>3</sup> ]          | Schileo et al., 2008       |
| $E_{canc} = 6850 \cdot \rho_{app}^{1.49}$ [MPa] <sup>#</sup>     | Morgan et al., 2003        |
| $E_{cort} = 21,910 \cdot \rho_{app} - 23,500$ [MPa] <sup>*</sup> | Snyder and Schneider, 1991 |

#Femoral head cancellous bone. \*Tibia cortical bone.

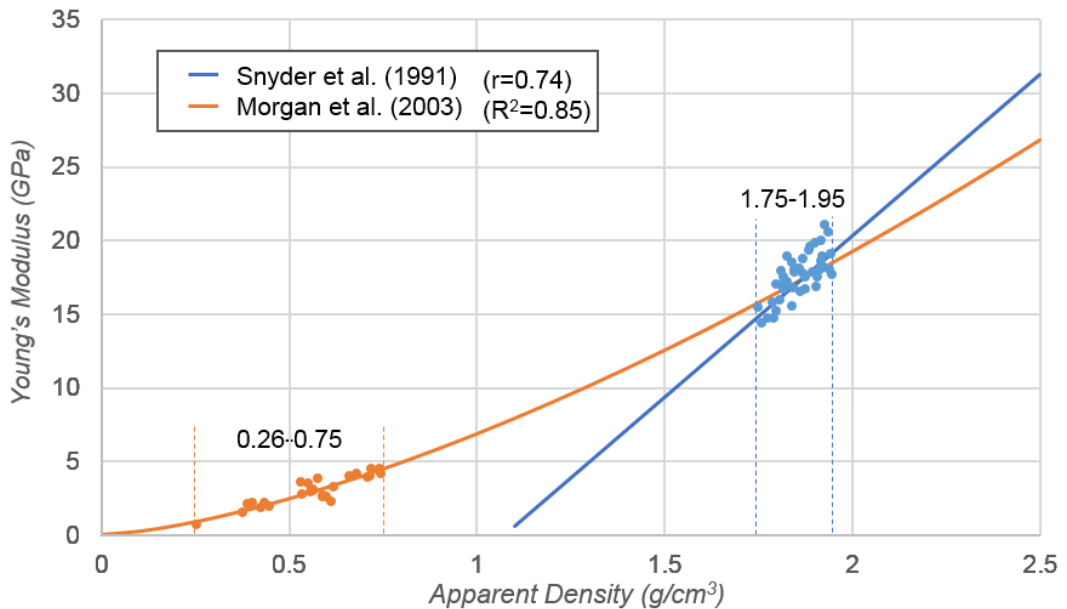


Figure 81 Density-modulus relationship for cortical (blue) and cancellous bone (orange).

### 6.3.3 Results

#### 6.3.3.1 Computational results

The results of a single right sided femur were presented in this section, as all tested femur led to very similar predicted fracture loads. The human femur was modelled with a beam (Figure 82A). The intertrochanteric area was modelled with a curved beam. The beam axis was closely aligned with the location of the modulus weighted centroids. Cross-sectional planes were reconstructed from the CT-data and were perpendicular to the chosen beam axis. A density-modulus material model was used to convert CT grey scale values to Young's modulus information (Figure 82B). The cross-sections were individually analysed to predict at which joint contact force they are likely to fracture. Depending of the grade of curvature either curved (Figure 82C) or straight beam theory (Figure 82D) was used.

The output of the fracture prediction tool was a plot of the estimated load magnitude at which each corresponding cross-section was likely to fracture. A *low predicted fracture load* indicated a *high fracture risk* for the respective cross-section. The cross-section with the lowest predicted fracture load was assumed to be the weakest and fracture was likely to initiate at this point.

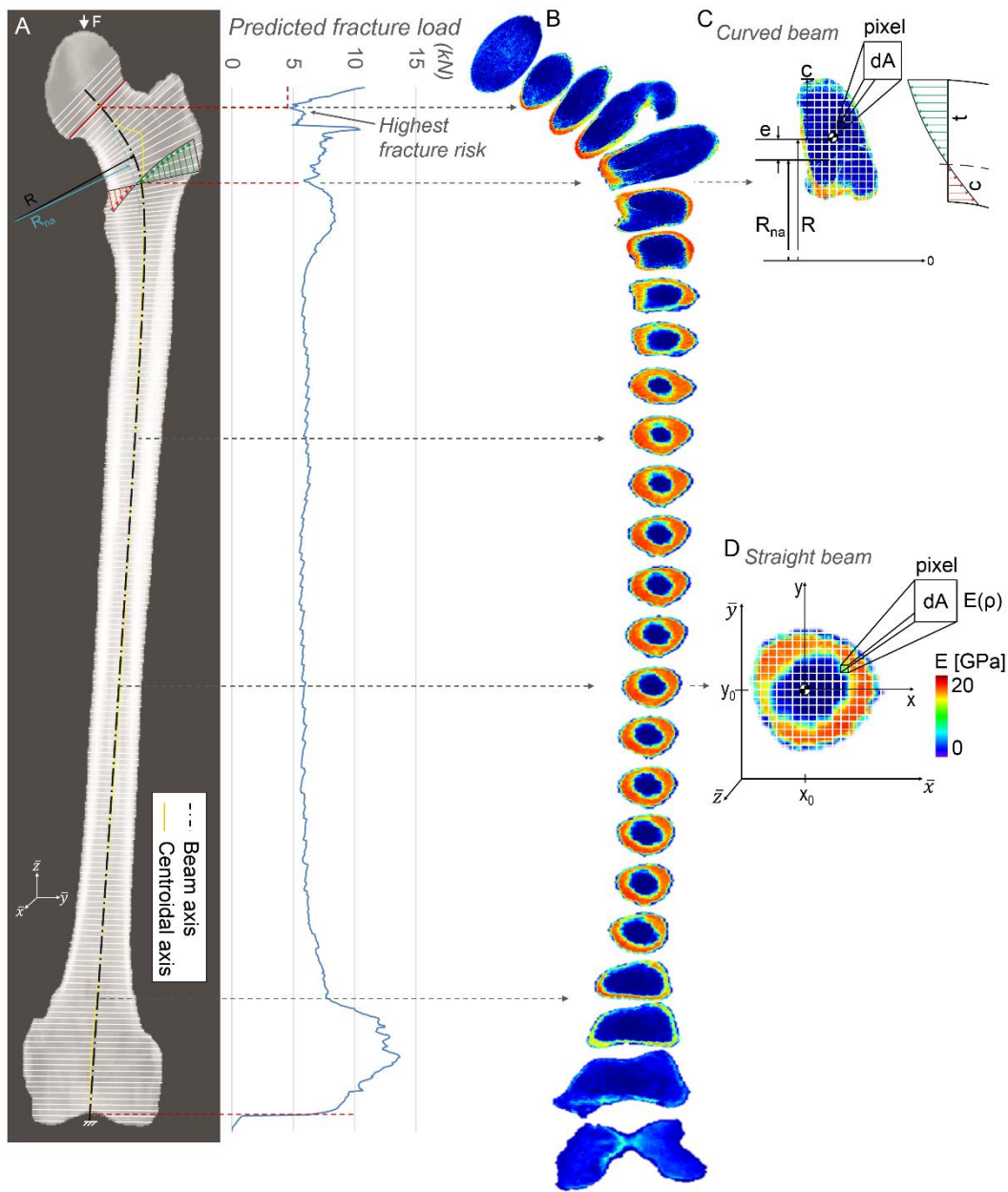


Figure 82 Beam theory analysis of a femur. (A) AP image of a right femur from projected computed tomography. The fracture load of each cross-section was calculated. Beam cross-sections (white) were perpendicular to the beam axis (black) which was derived from the location of the centroidal axis (yellow). The femoral neck showed the highest fracture risk as its predicted fracture load was the lowest. (B) The femoral beam model consisted of a series of stacked beam cross-sections. The colour of each pixel correlates with the Young's modulus of that element. (C) Modulus map for a cross-section of a curved beam element. (D) Modulus map for a cross-section of a straight beam. The structural stiffness of each cross-section was calculated by summing the stiffness of all pixels in that cross-section.

The results showed that a straight beam was not able to take the specific geometry between head, neck and shaft into account (Figure 83). The fracture prediction using a curved beam model identified the femoral neck as the area

where fracture was likely to start. The straight beam model failed to identify a high fracture risk for this area.

The shaft region was, as expected, very sensitive to the loading vector orientation (Figure 84). Loading the femur with a single joint contact force, which was parallel to the shaft axis, led to a high predicted fracture risk in the femoral shaft. The predicted fracture load was relatively constant throughout the shaft as the lever arm between shaft and force vector remained also unchanged. If the femur was loaded with a force vector in alignment of the hip-knee axis, the loading axis and the shaft axis converged which decreased the bending moment within the bone and increased the predicted fracture load slightly. When simulating a one legged stance loading, the shaft and loading axis crossed each other at which point the bending moment dropped to zero but increased again after that.

The effect of considering the abductor muscle in the model was insignificant as the reduction in compression stress within the bone was compensated by a higher bending stress component (Figure 84).

Ignoring shear stress components led to a reduced fracture risk at the ends of the femur. No change was observed for areas that were considered to have a high fracture risk such as the neck area.

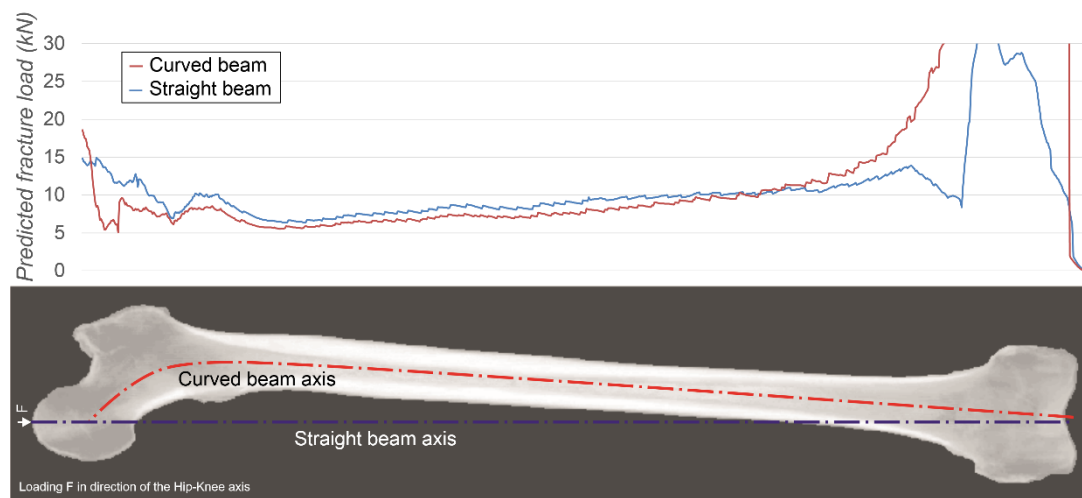


Figure 83 Comparison between a straight and curved beam theory approach and its effect on the predicted fracture load. Analysed cross-sections were perpendicular to the respective beam axis. Straight beam theory failed to identify the high fracture risk for the femoral neck. The x-axis of the line chart was collinear with the respective beam axis.

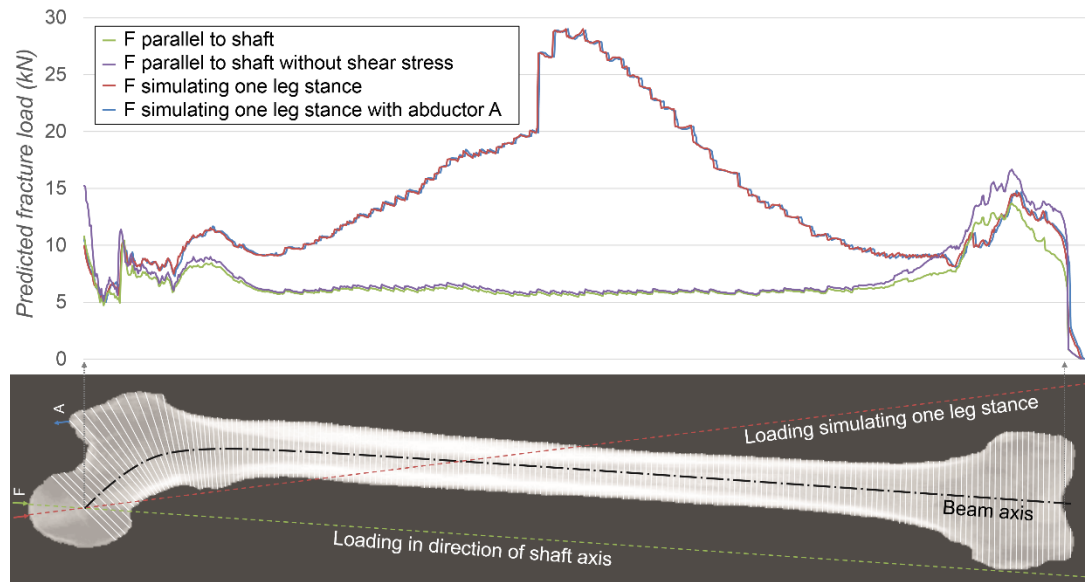


Figure 84 Comparison between two different simulated loading situations: Joint reaction force parallel to the shaft axis and the simulation of a one leg stance. When simulating a one leg stance, the consideration of the abductor muscle force had no significant influence on the predicted fracture load. In general, the predicted fracture loads for the neck area were less affected by the loading direction. Ignoring shear stress components for fracture load calculations seem only to effect the ends of the femur.

### 6.3.4 Discussion

The developed fracture prediction tool was able to estimate the fracture risk of an analysed femur based on CT-images. The use of curved beam theory accounted for the special geometry of the proximal part of the femur and it identified the femoral neck to be a point where bone fracture is likely to initiate within a healthy femur. The hyperbolic function used to link the axis between neck and shaft was a good compromise between matching the location of the modulus weighted centroids and having a reasonable slicing direction for cross-sections and the flow of stress. A straight beam axis was not able to identify the femoral neck to have a high fracture risk which is in contrast to favourable findings of Anez-Bustillos et al. (2014). The predicted fracture load for the neck was calculated to be  $4213 \pm 673$  N for the eight femurs.

The results of the fracture prediction of the analysed femurs in this study were not validated against *in-vitro* tests by the author. However the predicted fracture location correlated with experimental tests on human femurs reported in the literature. Tanck et al. (2009) mechanically tested the proximal part of five human femurs to failure simulating a one leg stance. The femurs fractured in the intra-capsular region at the neck with fracture loads between 4141N to

7970N ( $6249 \pm 1693$  N) (Figure 85). Cristofolini et al. (2007) also mechanically tested nine human femurs and reported intra-capsular fracture with failure loads ranging from 6319N to 11370N ( $8600N \pm 2080N$ ). These fracture values were slightly higher than the predicted loads of the beam tool despite using similar cadaveric femurs from subjects of similar age. However, there was also variation between both experimental studies which indicates that there was significant intra-subject variation. Cristofolini et al. reported a significantly higher body weight with  $81 \pm 15$  kg which might explain higher experimental fracture loads.



Figure 85 A typical picture of the neck fracture of a mechanically tested femur.  
*Image from Tanck et al. (2009) reproduced with permission from Elsevier.*

When loading the femur model along the mechanical axis, the highest predicted stress within the femur was almost exclusively at the lateral side of the femur in form of tension. The proximal part of the femur was subjected to high compression stress at the medial end of the femur cross-section.

While predicted fracture loads for the proximal femur were relatively unaffected by slight variations of loading orientations, the predicted fracture load for the shaft and distal part of the femur were highly sensitive to changes of the vector of the joint reaction force. The analytical fracture risk prediction in this study calculated fracture loads for a femur that was loaded according to the simulated loading situation rather than *in-vivo* loading. It remains difficult to answer which biomechanical loading model represents a high risk *in-vivo* loading situation as different studies in the literature use different models. This study supported findings from Rohlmann et al. (1983) that a femur model loaded with a single joint reaction force in parallel to the shaft axis can give a general indication for the fracture risk *in-vivo*. The predicted fracture load was

relatively constant along the entire shaft because the moment and compressive force did not change significantly. Wolff's law assumed that bone is a load optimised structure which should not allow huge variations in the fracture risk for different parts of the femur.

The simulated loading on the femur was exclusively static. The contact stress respective to the gait cycle was not analysed. Repetitive over loading which leads to buckling and fracturing of trabeculae cannot be analysed with this method. However it is possible to alter the direction of the loading vector to simulate different loading situations, such as heel strike or toe-off events, which can help to better understand failure mechanisms related to loading that result in pathological fracture. It also may help to identify high risk physical activities for an individual patient in order restrict those. The study showed that the force direction had an influence on the predicted fracture loads but a one legged stance loading during walking should give a sufficient indication for other atraumatic loading conditions such as stumping or stair climbing.

The abductor muscles had negligible influence on the predicted fracture load for the analysed loading models which was in agreement with findings of Keyak et al. (2005) and Cristofolini et al. (2007) who found no significant change for the intertrochanteric area. However, muscles can be critical for fracture if they are attached to a bone surface that is affected by a lesion. A computational fracture prediction tool based on beam theory is not necessarily able to assess this risk which is an disadvantage compared to fracture simulations using a continuum approach.

The ends of the femur, the superior part of the femoral head and the knee, were difficult to model with a beam as they had rapidly changing cross-sectional areas and were subjected to a point load. Therefore its questionable how reliable the predicted fracture loads for these areas were. As demonstrated in previous chapters, the fracture risk of the subchondral area of the femur was successfully analysed by comparing the structural stiffness to a reference set of healthy bone.

Bone is an anisotropic viscoelastic material meaning that its mechanical properties are not the same in different directions. However, several studies suggest that for axial stress calculations an isotropic linear elastic material model leads to similar good results (Huiskes, 1982; Lotz et al., 1991; Peng et al., 2006). The alignment of trabecular bone in the femoral head discourages shear of the structure under typical loading. The trabecular orientation is generally aligned with the principal stress flow. Further to this, yield strain is relatively isotropic and independent of density (Keaveny et al., 1994b; Ford et

al., 1996; Schileo et al., 2008c). Shear stress appeared to be insignificant when analysing the proximal part of the femur but led to a lower predicted fracture load for the knee area. Ignoring shear stress components as proposed by Huiskes (1984) seemed therefore justified for the analysed loading models. That would avoid using the von Mises stress (Eq.6.14) and the attached stark simplifications regarding the shear modulus and principal stresses. However shear stress may be an important factor for the stress analysis of femurs where a disease condition such as an unusual ante-version angle is present. Certain activities can also cause higher shear moments.

This study showed that it is possible to objectively analyse the fracture risk of the femur based on both geometrical and material properties derived from non-invasive tomographic imaging. The developed tool can potentially serve as a guideline to give a target for surgical interventions in the future.

## **6.4 Verification against additive manufactured femur models**

### **6.4.1 Introduction**

Curved beam theory was able to identify fracture at the neck and the intertrochantic area which was prone to fracture as discussed in section 6.3. Therefore the curved beam approach was verified against a proximal human femur model made from additive manufacturing. Additive manufacturing allowed to produce a large number of identical femur samples. The aim of this verification study was to investigate whether the tool was able to correctly predict not only the fracture location but also the fracture load.

### **6.4.2 Method**

#### **6.4.2.1 Beam model**

The proximal femur was modelled with a curved beam with an axis running from the centre of the femoral head to the shaft forming an arc which acknowledged the curved shape of the intertrochantic region (Figure 86). The beam axis defined the virtual slicing direction of the femur model as all cross-sections were perpendicular to the beam axis. The developed tool analysed a total of 30 cross-sections which were evenly distributed along each of the two beam axes. The geometric shape of the proximal femur samples was known and a binary image matrix, which was derived from the STL-file, was imported directly into the developed fracture prediction tool. Properties of the additive

manufacturing material were verified in section 4.2.2.3. The Young's modulus was assumed to be 721.5MPa with a yield strain of 6% for compression and 2000MPa with 8.5% for tension.

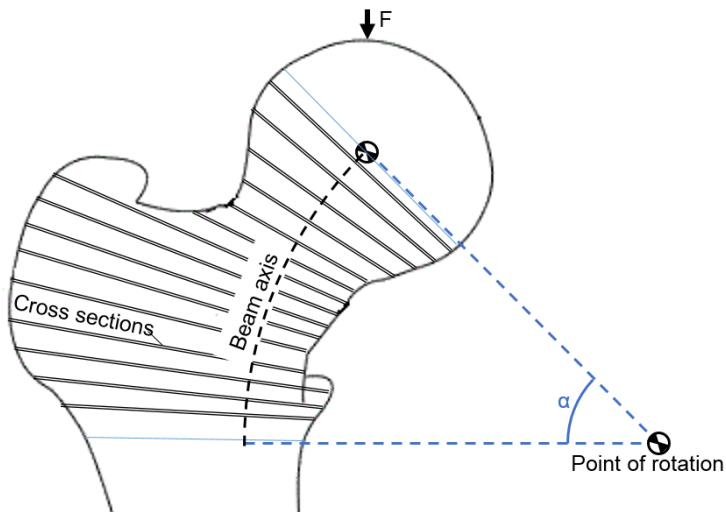


Figure 86 Schematic of the proximal femur including assumed curved beam axis (dashed black line). The cross-sections are perpendicular to the beam axis. At the centre of the femoral head the curved beam axis starts at an angle 45° to the horizon. It is defined as an arc and it ends at the lower trochanter. (The number of cross-sections shown is not representative)

#### 6.4.2.2 Experimental set-up

A solid three-dimensional model of a proximal femur was developed using SolidWorks2013 (Dassault Systèmes, France) which had cylindrical base for fixation into a loading jig. The shape of the bone model was based on a CT-scan from human cadaveric femur sample from 55 year old male donor (Section 4.2.2.1) which was segmented using ScanIP (Simpleware Ltd., UK). Twelve femur models were built on a Vanguard HS HiQ SLS (Selective Laser Sintering) Rapid Manufacturing machine (3D Systems Corporation, CA) and were manufactured from solid SLS DuraForm PA Nylon.

These twelve femur models were compression tested until fracture using an Instron 3366 single axis tension-compression machine (Instron, Norwood, MA). A metal fixture was used which allowed compression tests at the required angle to analyse stem and neck fractures and the femur model was loaded with a flat platen (Figure 87A). The alignment simulated the approximate loading position during a one leg stand. The *in-vitro* loading correlated with the assumed simplified point loading *in-silico*. The displacement rate was 0.2mm/s.

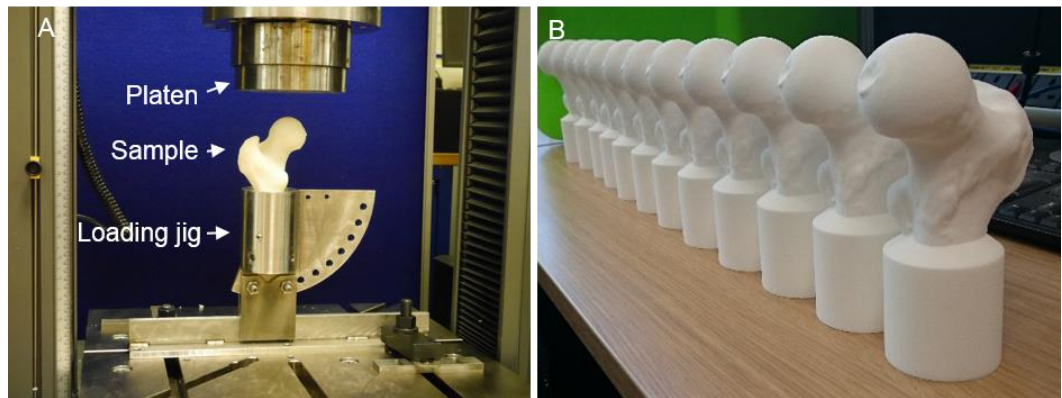


Figure 87 (A) Uniaxial compression test of a proximal femur model. (B) A total of twelve femur models generated by additive manufacturing were tested.

#### 6.4.3 Results

The tool estimated the fracture load at which each respective cross section was likely to fail which was compared to the results of the mechanical testing (Figure 88). The tool identified the femoral neck and the stem as points with increased fracture risk with 9.3kN and 15kN respectively. From twelve *in-vitro* tested femur samples, six fractured at the stem at a mean load of  $12.16 \pm 0.87$  kN (SEM) and six samples fractured at the femoral neck at  $16.50 \pm 0.34$  kN (Appendix E). The predicted fracture load for the femoral stem of the 3D-printed sample was 26% lower than the fracture load that has been seen at *in-vitro* tests. The predicted fracture load for the femoral neck was 35% lower.

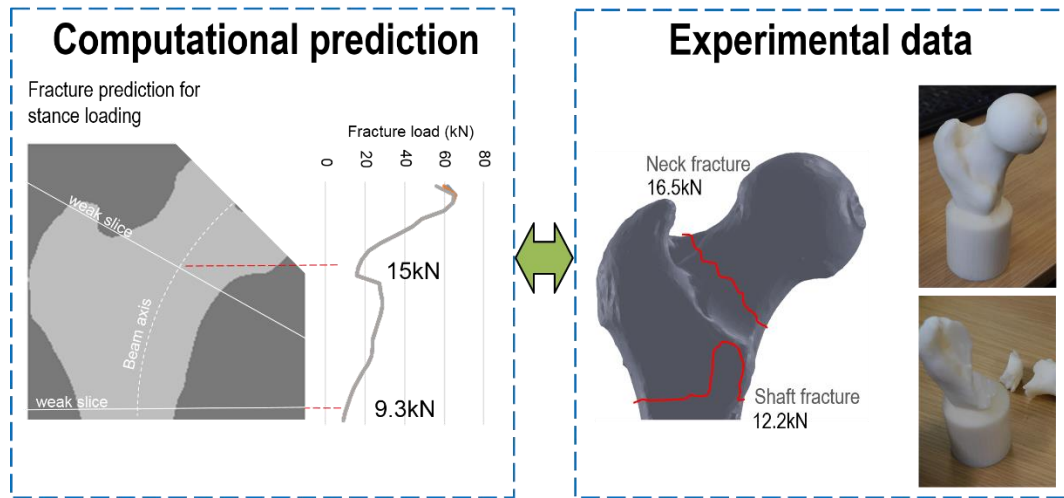


Figure 88 Comparing predicted and experimental results: The computational tool identified the femoral neck and the end of the stem to have the highest fracture risk. The red lines show the typical observed fracture lines from the invitro test which match the computational prediction.

#### 6.4.4 Discussion

The curvature of the intertrochanteric region between head and shaft was successfully acknowledged with a curved beam. The beam axis defined the slicing direction of the cross-sections. Therefore, the beam axis played an important role for the femur beam model.

The cross-section with the lowest predicted fracture load was assumed to be the location where fracture of the entire model initiated. The lower end of the shaft and the end of the femoral neck had similar low predicted fracture loads. The two dips in the fracture curve were clearly identifiable with the stem being slightly higher than the shaft. The lower end of the shaft was therefore assumed to be the point where fracture would initiate however the magnitudes were very similar. When simulating a one-leg stance loading scenario, *in-vitro* compression tests on human femoral heads showed that fracture is likely to initiate at the neck and not at the shaft (Cristofolini et al., 2007). The explanation for this contradiction is likely to be that the human femoral neck is not solid unlike the additive manufactured model of this study.

During the compression test of the proximal femur model half of the samples fractured at the end of the shaft and another half of the same samples fractured at the neck which confirmed the previously predicted fracture sites. Small inhomogeneities in the material of the 3D-printed femur models might explain the two different fracture sites and the slight variations in experimental fracture loads. The magnitude of the predicted fracture load, however, was

higher than predicted indicating that the developed method needed further fine tuning.

This study demonstrated that points within the femur can be identified where fracture was likely to initiate as these match the location of the cross-section which have the lowest predicted fracture load. The fracture prediction tool also had the potential to predict an accurate fracture load for those cross-sections if accurately calibrated.

## 6.5 Summary

The developed analytical fracture prediction method took both material properties and the bone geometry into account. It can potentially identify an increase of the fracture risk caused by a wide array of different bone diseases as most bone disease are linked to either a reduction in the bone material or a change of the bone geometry, or both. If developed into a clinical tool, it can serve as a guideline to give a target for surgical interventions as there is potential for further automation and therefore removing the majority of user bias. The simplicity of beam theory allowed a quick analysis of an entire femur in under 15 minutes which makes it suitable for the clinical environment.

The fracture prediction was successfully verified against compression tests on twelve proximal femur models made from segmented CT-scans and additive manufacturing. Fracture predictions based on CT-scans of healthy human femurs were correlated with failure modes from mechanical testing reported in the literature.

Curved beam theory allowed identification of the fracture risk of the neck and the intertrochanteric area of the femur in contrast to a straight beam approach. The used hyperbolic function between neck and shaft axis was a good compromise between matching the location of the modulus weighted centroids and having a reasonable slicing direction for cross-sections and the flow of stress. A loading model with a single joint reaction force parallel to the shaft axis can give a general indication for the fracture risk *in-vivo* as previously described by Rohlmann *et al.* (1983).

## Chapter 7 Overall discussion and conclusion

### 7.1 Discussion

#### 7.1.1 Introduction

Patient stratification is important for choosing the right treatment option with the best clinical outcome. Current classification systems are not sufficient for this task as they have poor differentiation and reproducibility leading (Schmitt-Sody et al., 2008) to high failure rates of joint-sparing treatment options especially for pre-collapsed AVN. It would be beneficial from a health-economic and welfare perspective to identify patients for whom a conservative treatment is not a viable solution and who would be better served by a hip replacement. On the other hand, not all lesions progress to failure and conservative treatment appears to be relatively successful for patients with a low fracture risk (Ohzono et al., 1992). As patients with AVN are generally younger and have higher functional demands, THA can be problematic (Beaulé and Amstutz, 2004; Hamilton et al., 2009).

#### 7.1.2 Development of a novel fracture prediction tool

This thesis has demonstrated that a fracture prediction tool based on structural mechanics and beam theory has the potential to be a more objective means of stratifying AVN affected femoral heads than existing classification systems. The image based fracture prediction tool was developed and validated against theoretical, physical and clinical disease models. While several studies used FEA to simulate stress within necrotic lesion affected femoral heads (Brown et al., 1981; Anderson, 2015), beam theory has never been used to analyse the impact of AVN. Therefore this was a novel approach compared to previous studies, which simulated fracture within the femoral head. Compared to current classification systems such as ARCO which only quantify the geometry of the lesion, the developed tool took both material and geometrical properties into account. The porcine and human verification study clearly demonstrated the importance of considering material properties for fracture prediction.

As part of the method development in Chapter 3, a theoretical disease model was created. The model was made by altering a CT-scan of a femoral head with simulated necrotic pathology described in the literature. The verification showed that the axial stiffness appeared capable of analysing the mechanical behaviour of the lesion affected femoral heads. Structural stiffness is an

integral part of the beam equation. The axial stiffness described the ability of a beam cross-section to withstand axial loading (Lieberman et al., 2004) which was assumed to be the main loading mode of the upper part of the femoral head (Keyak et al., 2005; Cristofolini et al., 2007; Pauwels, 2012). Structural stiffness has been successfully used to predict bone fracture of the femoral shaft and neck (Snyder et al., 2004; Anez-Bustillos et al., 2014). The direct use of the beam theory equation to calculate exact fracture loads for the femoral head beam model was however unreliable. The load bearing area of the femoral head has a rapidly increasing cross-sectional areas and a short length compared to its thickness. These attributes were in conflict with the assumptions made for the application of beam theory equation that the beam is straight slender and any taper must be slight.

Material properties were assigned to the beam model from CT-scans by using a density-modulus relationship which was an essential step for non-invasive *in-vivo* fracture simulations. A density-modulus conversion model proposed by Morgan et al. (2003) was used and verified against compression tests on human femoral head bone plugs which demonstrated that the calculated Young's modulus delivered reliable results in combination with beam theory.

The density-modulus relationship derived from bone plugs was extrapolated to smaller volume elements defined by the voxel resolution of a CT-scan. The validity of this method was confirmed by analysing the sensitivity of the material model towards the element size. This sensitivity study showed that the material model was relatively resolution stable when calculating structural properties.

The material model could also be applied to AVN affected bone as the validation in Chapter 5 demonstrated that necrotic bone is not only subject to Young's modulus but also density reduction. This contradicted findings by Bobechko & Harris (1960) and Brown et al. (1981) who saw a density increase for necrotic cancellous bone.

### **7.1.3 Effectiveness of developed tool**

A verification study with femoral head disease models generated by additive manufacturing and porcine femoral head disease models confirmed observations by Ohzono et al. (1991) that the fracture risk of femoral heads is dependent on the lesion location. The experimental data showed that a lesion within the subchondral area was statistically more critical for the stability of the femoral head than a lesion located elsewhere. However this study also showed that there was a large variation in measured failure loads among

porcine femoral heads with the same lesion type, despite identical cross-sectional areas of the defect. The additive manufactured models without natural material variation of trabecular bone did not show any significant variations in the fracture load. Therefore, the lesion volume and location did not account for the variation in failure loads and were unsuitable as a good predictor of fracture risk alone. The fracture prediction based on axial stiffness took both material and geometrical properties into account. It was therefore superior in this aspect compared to current classification methods that rely on the identification of the lesion volume and location, an approach that is purely based on geometrical information.

The fracture prediction tool was verified against *in-vitro* tests on explanted human femurs with different simulated AVN pathology. The computationally predicted fracture risk was defined by how the axial stiffness of a sample compared to a reference set of healthy samples in a worst case. There was a good correlation between the simulated fracture risk and the experimental failure loads for the human femoral heads ( $R^2=0.83$ ), which demonstrated the predictive capability of the developed method to identify weak femoral head samples.

The tool was subsequently validated by predicting the fracture risk of femoral heads from patients suffering from AVN. The tool stratified patients according to their predicted fracture risk and the patients were ranked in ascending order. The ranking correlated with the classification and grade of the ARCO standard which indicated that the developed tool had similar good predictive capabilities. The ARCO standard is the current diagnostic gold standard for AVN. While the ARCO classification was purely based on geometrical information such as the lesion volume and location, the fracture prediction method also considered material properties of bone which potentially added predictive capability in terms of the fracture risk.

This study also demonstrated that a comparison against the mean stiffness of a reference set of multiple healthy femurs is potentially more accurate than a comparison against the contralateral femoral head. The contralateral femur might be affected as well or some patients may have a THA. A feasible benchmark is important when developing the tool into a clinical application in the future. Using a global reference may lead to a clinical application where patients are compared against an established fracture risk score based on demographics.

In the second part of Chapter 5 the developed beam tool was compared against another novel fracture prediction tool based on FEA. The comparison

was difficult as both tools had very different methods to predict fracture. A main difference was that the beam tool assigned material properties to the femoral head model based on CT-scans by using a density-modulus relationship while the FEA tool used segmented geometric models with material properties based on empirical tests. Those geometric models could not incorporate the complexity of inhomogeneous bone tissue and the segmentation of lesion models required great user input. FEA model that consider trabecular structure require great computational expense (Van Rietbergen et al., 2003) which is problematic for the clinical setting. The creation of FEA bone models is further complex and the generation of simplified loading conditions is non-trivial in FEA and requires greater user input. While many key steps were similar such as image processing and loading directions, the beam tool was a simpler method.

#### **7.1.4 Future use**

Chapter 6 demonstrated, that the developed analytical tool had the potential to not only stratify patients that suffer from AVN but also a wide range of other bone diseases. It was therefore broaden to other bone diseases in order to increase the commercial interest and also wider impact of the tool. The developed fracture prediction method can be used for an array of other conditions that lead to bone fracture as long as the decrease of structural integrity of the bone is a result of material and/or geometric changes. While AVN most commonly affects the femoral head, other conditions such as osteoporosis or skeletal metastasis can also affect other parts of the femur. The fracture prediction was extended to the rest of the femur. Curved beam theory was used to account for the curved geometry of the intertrochanteric area of the femur. The operability of the tool was tested by utilising clinical CT-scans of human femurs and comparing the predicted fracture loads with fracture loads reported in the literature and by verifying the tool against femur models generated by additive manufacturing. While this is an important step towards proofing the operability of the methodology, an *in-vitro* verification study will be necessary to confirm whether the methodology is able to accurately predict the fracture loads of lesion affected femurs.

#### **7.1.5 Limitations**

The developed tool did not account for biological factors that may weaken the bone structure or factors that are not fracture related but worsen symptoms. Instead it only analysed mechanical risk factors. A surgical intervention can be necessary because of the occurrence of pain or inflammatory responses.

Modelling the femur with a Euler-Bernoulli beam required several simplifications such as that bone is isotropic and linear elastic and that shear deformation is neglected.

The tool also did not consider the dynamic nature of joint loading during gait cycles and the simulated loading on the femur was exclusively static. Repetitive over loading which leads to buckling and fracturing of trabeculae cannot be analysed with this method.

Necrotic lesions were modelled as voids which was a limitation of the verification study. While those voids did not replicate the true appearance of clinical lesions, the simulated lesions provided a method to validate the fracture prediction model in respect of AVN in terms of mechanical behaviour although mechanical implications of AVN lesions are largely unknown.

Only a low number of clinical cases was investigated as part of this thesis and sometimes the CT-scans available were not density calibrated. While results of this study represent a first step in validating the developed method, a follow-up study with a larger number of patients and controlled CT calibration procedures are needed to confirm these promising initial findings.

Finally, the tool assumed that fracture was likely to initiate at the weakest cross-section. Small regions of high stress could indicate regions where individual trabeculae are most likely to yield or be subjected to strain adaptive remodelling but the effect would be limited to a small region because failure of a small number of trabeculae will restore equilibrium in the surrounding bone (Prendergast and Taylor, 1994).

## 7.2 Overall conclusion

The lack of a reliable clinical risk stratification of patients with AVN is a major challenge as success of treatment heavily depends on the correct classification of the disease stage. This thesis approached this issue by developing a novel non-invasive fracture prediction method based on beam theory and structural mechanics. The mechanical risk of an AVN affected femoral head was successfully assessed by comparing relative differences in structural stiffness to intact femoral heads.

Current classification methods have poor differentiation and reproducibility because they rely on the clinician to identify lesion volume and location from tomographic images or plain radiographs. While this risk classification based on lesion volume and location only took geometrical information into account,

the fracture prediction method based on axial stiffness also considered material properties of bone which increased its predictive capabilities. The experimental data confirmed that a lesion within the subchondral area was statistically more critical for the stability of the femoral head. However this study also showed that there was a large variation in measured failure loads among femoral heads even with the same lesion type. Therefore, the lesion volume and location did not account for the variation in failure loads and were unsuitable as a good predictor of fracture risk alone.

Necrotic lesions are often surrounded by a layer of sclerotic bone and therefore the bone appears to be denser while having reduced material properties. This study however suggests that the overall density of AVN affected femurs decreases and that density-modulus can be used to assign material properties to the fracture prediction model to assess the structural deterioration of bone.

Beam theory was chosen because of its simplicity. Even with numerous simplifications, beam theory remains sufficiently accurate to predict the fracture risk and it had the added advantage of being largely automated and therefore removing the majority of user bias. Objectivity is a key problem of current diagnostic classification systems. If introduced as a diagnostic tool in the treatment of AVN, it could improve the effectiveness of diagnostics and subsequent therapeutic responses. The largely automated and simple tool allowed to calculate the fracture risk of the femoral head within several minutes which was its main strength compared to more complex diagnostic approaches. Therefore, the tool has the potential to provide physicians with crucial information for a better-targeted treatment at the point of care. If CT-scans are available, diagnostic strategies can be discussed during patient consultation based on prompt real time access to a fracture risk based diagnosis.

The image based fracture prediction tool has shown promising results when validated against theoretical, physical and clinical disease models and this work may lead to an more effective diagnostic tool which will assist the clinicians to find the most appropriate treatment in the future.

## References

- Aerssens, J., 1998. Interspecies Differences in Bone Composition, Density, and Quality: Potential Implications for in Vivo Bone Research. *Endocrinology* 139, 663–670. doi:10.1210/en.139.2.663
- Agarwala, S., Shah, S.B., 2011. Ten-year follow-up of avascular necrosis of femoral head treated with alendronate for 3 years. *J. Arthroplasty* 26, 1128–34. doi:10.1016/j.arth.2010.11.010
- Ajoku, U., Ajoku, U., Saleh, N., Saleh, N., Hopkinson, N., Hopkinson, N., Hague, R., Hague, R., Erasenthiran, P., Erasenthiran, P., 2006. Investigating mechanical anisotropy and end-Of-Vector effect in laser-Sintered nylon parts. *Proc. Inst. Mech. Eng. Part B J. Eng. Manuf.* 220, 1077–1086. doi:10.1243/09544054JEM537
- AJRR, 2016. Annual Report 2016: Third AJRR Annual Report on Hip and Knee Arthroplasty Data.
- Al Omran, A., 2013. Multiple drilling compared with standard core decompression for avascular necrosis of the femoral head in sickle cell disease patients. *Arch. Orthop. Trauma Surg.* 133, 609–613. doi:10.1007/s00402-013-1714-9
- Anderson, J.A., 2015. In vitro and in silico simulations of femoral heads with avascular necrosis. University of Leeds.
- Anez-Bustillos, L., Derikx, L.C., Verdonschot, N., Calderon, N., Zurakowski, D., Snyder, B.D., Nazarian, A., Tanck, E., 2014. Finite element analysis and CT-based structural rigidity analysis to assess failure load in bones with simulated lytic defects. *Bone* 58, 160–7. doi:10.1016/j.bone.2013.10.009
- Aruwajoye, O.O., Patel, M.K., Allen, M.R., Burr, D.B., Aswath, P.B., Kim, H.K.W., 2013. Microcrack density and nanomechanical properties in the subchondral region of the immature piglet femoral head following ischemic osteonecrosis. *Bone* 52, 632–639. doi:10.1016/j.bone.2012.07.028
- Assouline-Dayan, Y., Chang, C., Greenspan, A., Shoenfeld, Y., Gershwin, M.E., 2002. Pathogenesis and natural history of osteonecrosis. *Semin. Arthritis Rheum.* 32, 94–124. doi:10.1053/sarh.2002.33724b
- Atsumi, T., Kuroki, Y., Yamano, K., 1989. A microangiographic study of idiopathic osteonecrosis of the femoral head. *Clin. Orthop. Relat. Res.* 246, 186–194.
- Aubigné, R.M., Postel, M., Mazabraud, A., Massias, P., Gueguen, J., 1965. Idiopathic Necrosis Of The Femoral Head In Adults. *J. Bone Jt. Jt. Surgery, Br.* Vol. 47-B, 612 LP – 633.

- Aulakh, T.S., Rao, C., Kuiper, J.H., Richardson, J.B., 2010. Hip resurfacing and osteonecrosis: Results from an independent hip resurfacing register. *Arch. Orthop. Trauma Surg.* 130, 841–845. doi:10.1007/s00402-009-0963-0
- Avadi, M.S., 2016. Characterisation and Development of an Experimental Mechanical Model of Avascular Necrosis of the Femoral Head. University of Leeds.
- Bach, C., Baumann, R., 1924. Elastizität und Festigkeit: die für die Technik wichtigsten Sätze und deren erfahrungsmässige Grundlage, 9th ed. Springer-Verlag, Berlin.
- Bae, J.Y., Kwak, D.S., Park, K.S., Jeon, I., 2013. Finite element analysis of the multiple drilling technique for early osteonecrosis of the femoral head. *Ann. Biomed. Eng.* 41, 2528–2537. doi:10.1007/s10439-013-0851-1
- Barker, D.J.P., Hall, A.J., 1986. The epidemiology of Perthes' disease. *Clin. Orthop. Relat. Res.* 209, 89–94.
- Bast, R.C., Croce, C.M., Hait, W.N., Hong, W.K., Kufe, D.W., Piccart-Gebhart, M., Pollock, R.E., Weichselbaum, R.R., Wang, H., Holland, J.F., 2017. *Holland-Frei Cancer Medicine*. Wiley.
- Beaulé, P.E., Amstutz, H.C., 2004. Management of Ficat stage III and IV osteonecrosis of the hip. *J. Am. Acad. Orthop. Surg.* 12, 96–105.
- Beck, T., Mourtada, F., 1998. Experimental testing of a DEXA-derived curved beam model of the proximal femur. *J. ...* 394–398.
- Beck, T.J., Ruff, C.B., 1990. Predicting femoral neck strength from bone mineral data: a structural approach. *Invest. Radiol.* 25, 6–18.
- Belmar, C.J., Steinberg, M.E., Hartman-Sloan, K.M., 2004. Does pain predict outcome in hips with osteonecrosis? *Clin. Orthop. Relat. Res.* 425, 158–162.
- Beltran, J., Knight, C.T., Zuelzer, W.A., Morgan, J.P., Shwendeman, L.J., Chandnani, V.P., Mosure, J.C., Shaffer, P.B., 1990. Core decompression for avascular necrosis of the femoral head: correlation between long-term results and preoperative MR staging. *Radiology* 175, 533–536.
- Bergmann, G., Deuretzbacher, G., Heller, M., Graichen, F., Rohlmann, A., Strauss, J., Duda, G., 2001. Hip contact forces and gait patterns from routine activities. *J. Biomech.* 34, 859–871. doi:10.1016/S0021-9290(01)00040-9
- Bergmann, G., Graichen, F., Rohlmann, A., 1993. Hip joint loading during walking and running, measured in two patients. *J. Biomech.* 26, 969–990.

- Bitzer, E., Grobe, T., Neusser, S., Schneider, a., Dörning, H., Schwartz, F., 2010. Barmer GEK Report Krankenhaus 2010: Trends in der Endoprothetik des Hüft- und Kniegelenks 2010 1–279.
- Blemker, S.S., Asakawa, D.S., Gold, G.E., Delp, S.L., 2007. Image-based musculoskeletal modeling: applications, advances, and future opportunities. *J. Magn. Reson. Imaging* 25, 441–51. doi:10.1002/jmri.20805
- Bobechko, W.P., Harris, W.R., 1960. The Radiographic Density Of Avascular Bone. *J. Bone &amp; Jt. Surgery, Br.* Vol. 42-B, 626 LP – 632.
- Bonney, H., Colston, B.J., Goodman, a. M., 2011. Regional variation in the mechanical properties of cortical bone from the porcine femur. *Med. Eng. Phys.* 33, 513–520. doi:10.1016/j.medengphy.2010.12.002
- Boresi, A.P., Schmidt, R.J., Sidebottom, O.M., 1993. Advanced mechanics of materials. Wiley New York.
- Brodetti, A., 1960. The blood supply of the femoral neck and head in relation to the damaging effects of nails and screws. *J Bone Jt. Surg* 42-B, 794–801.
- Brown, J.P., Josse, R.G., 2002. 2002 clinical practice guidelines for the diagnosis and management of osteoporosis in Canada. *C. Can. Med. Assoc. J.*
- Brown, T., Ferguson, A., 1980. Mechanical property distributions in the cancellous bone of the human proximal femur. *Acta Orthop.* 429–437.
- Brown, T.D., Mutschler, T.A., Ferguson, A.B., 1982. A non-linear finite element analysis of some early collapse processes in femoral head osteonecrosis. *J. Biomech.* 15, 705–715. doi:10.1016/0021-9290(82)90024-0
- Brown, T.D., Shaw, D.T., 1983. In vitro contact stress distributions in the natural human hip. *J. Biomech.* 16, 373–384. doi:10.1016/0021-9290(83)90071-4
- Brown, T.D., Way, M.E., Ferguson, A.B., 1981. Mechanical characteristics of bone in femoral capital aseptic necrosis. *Clin. Orthop. Relat. Res.* 240–7.
- BSI, 2012. ISO Standard 527-2 Determination of tensile properties - Test conditions for moulding and extrusion plastics. London.
- Byrne, D., Mulhall, K., Baker, J., 2010. Anatomy & biomechanics of the hip. *Open Sport. Med.* 51–57.
- Calder, J.D.F., Buttery, L., Revell, P. a., Pearse, M., Polak, J.M., 2004. Apoptosis--a significant cause of bone cell death in osteonecrosis of the

- femoral head. *J. Bone Joint Surg. Br.* 86, 1209–1213. doi:10.1302/0301-620X.86B8.14834
- Camporesi, E.M., Vezzani, G., Bosco, G., Mangar, D., Bernasek, T.L., 2010. Hyperbaric oxygen therapy in femoral head necrosis. *J. Arthroplasty* 25, 118–23. doi:10.1016/j.arth.2010.05.005
- Carpenter, R.D., Saeed, I., Bonaretti, S., Schreck, C., Keyak, J.H., Streeper, T., Harris, T.B., Lang, T.F., 2014. Inter-scanner differences in in vivo QCT measurements of the density and strength of the proximal femur remain after correction with anthropomorphic standardization phantoms. *Med. Eng. Phys.* 36, 1225–1232. doi:10.1016/j.medengphy.2014.06.010
- Carter, D., Hayes, W., 1976. Bone compressive strength: the influence of density and strain rate. *Science* (80-. ). 194, 1174–1176.
- Carter, D.R., Hayes, W.C., 1977. The compressive behavior of bone as a two-phase porous structure. *J. Bone Joint Surg. Am.* 59, 954–962. doi:10.1007/978-1-4471-5451-8\_116
- Chan, V.W.K., Chan, P.K., Chiu, K.Y., Yan, C.H., Ng, F.Y., 2016. Why do hong kong patients need total hip arthroplasty? An analysis of 512 hips from 1998 to 2010. *Hong Kong Med. J.* 22, 11–15. doi:10.12809/hkmj144483
- Chen, W.-M., 2011. Osteonecrosis of the femoral head: Surgical perspective. *Formos. J. Surg.* 44, 131–135. doi:10.1016/j.fjs.2011.08.006
- Cheng, E.Y., Thongtrangan, I., Laorr, A., Saleh, K.J., 2004. Spontaneous Resolution of Osteonecrosis of the Femoral Head. *J. Bone Jt. Surgery-American Vol.* 86, 2594–2599. doi:10.2106/00004623-200412000-00002
- Cheng, X.G., Qu, H., Liu, W., Liu, X., Cheng, K.B., Zhao, T., Li, X.S., Liang, W., Guo, J., 2006. The prevalence of osteonecrosis in 448 SARS patients: a screening study with MRI. *Clin. Imaging* 30, 150. doi:<http://dx.doi.org/10.1016/j.clinimag.2005.12.021>
- Cherian, S.F., Laorr, A., Saleh, K.J., Kuskowski, M.A., Bailey, R.F., Cheng, E.Y., 2003. Quantifying the extent of femoral head involvement in osteonecrosis. *J. Bone Jt. Surgery, Am. Vol.* 309–315.
- Chiu, K., Ng, T., Poon, K., Ho, W., Yau, W., 1998. Primary total hip replacement in Hong Kong Chinese – A review of 647 hips. *Hong Kong J. Orthop. Surg.* 2, 114–119.
- Choi, H.-R., Steinberg, M.E., Y. Cheng, E., 2015. Osteonecrosis of the femoral head: diagnosis and classification systems. *Curr. Rev. Musculoskelet. Med.* 8, 210–220. doi:10.1007/s12178-015-9278-7

- Collier, B.D., Carrera, G.F., Johnson, R.P., Isitman, A.T., Hellman, R.S., Knobel, J., Finger, W.A., Gonyo, J.E., Malloy, P.J., 1985. Detection of femoral head avascular necrosis in adults by SPECT. *J. Nucl. Med.* 26, 979–987.
- Cong, E., Walker, M.D., 2014. The Chinese skeleton: Insights into microstructure that help to explain the epidemiology of fracture. *Bone Res.* 2. doi:10.1038/boneres.2014.9
- Cristofolini, L., Juszczak, M., Martelli, S., Taddei, F., Viceconti, M., 2007. In vitro replication of spontaneous fractures of the proximal human femur. *J. Biomech.* 40, 2837–45. doi:10.1016/j.jbiomech.2007.03.015
- Cristofolini, L., Viceconti, M., Cappello, A., Toni, A., 1996. Mechanical validation of whole bone composite femur models. *J. Biomech.* 29, 525–535. doi:10.1016/0021-9290(95)00084-4
- Cummings, S., Kelsey, J., 1985. Epidemiology of osteoporosis and osteoporotic fractures. *Epidemiol.* ... 7, 178–208.
- Cuppone, M., Seedhom, B.B., Berry, E., Ostell, a E., 2004. The longitudinal Young's modulus of cortical bone in the midshaft of human femur and its correlation with CT scanning data. *Calcif. Tissue Int.* 74, 302–9. doi:10.1007/s00223-002-2123-1
- Currey, J.D., 1969. The mechanical consequences of variation in the mineral content of bone. *J. Biomech.* 2, 1–11. doi:10.1016/0021-9290(69)90036-0
- Dean, M.T., Cabanela, M.E., 1993. Transtrochanteric anterior rotational osteotomy for avascular necrosis of the femoral head. Long-term results. *J. Bone Joint Surg. Br.* 75, 597–601.
- Drake, R., Vogl, A.W., Mitchell, A.W.M., 2009. Gray's Anatomy for Students, Gray's Anatomy. Elsevier Health Sciences.
- Duda, G.N., Schneider, E., Chao, E.Y.S., 1997. Internal forces and moments in the femur during walking. *J. Biomech.* 30, 933–941. doi:10.1016/S0021-9290(97)00057-2
- Euler, L., 1759. Sur la force des colonnes. *Mem. l'academie des Sci. Berlin.*
- Evans, F.G., Lebow, M., 1951. Regional differences in some of the physical properties of the human femur. *J. Appl. Physiol.* 3, 563–72.
- Fazzalari, N.L., Parkinson, I.H., 1996. Fractal dimension and architecture of trabecular bone. *J. Pathol.* 178, 100–105. doi:10.1002/(SICI)1096-9896(199601)178:1<100::AID-PATH429>3.0.CO;2-K
- Felson, D., Anderson, J., 1987. Across-Study Evaluation Of Association Between Steroid Dose And Bolus Steroids And Avascular Necrosis Of Bone. *Lancet* 329, 902–906. doi:10.1016/S0140-6736(87)92870-4

- Ferguson, G.M., Cabanel, M.E., Ilstrup, D.M., 1994. Total hip arthroplasty after failed intertrochanteric osteotomy. *J. Bone Joint Surg. Br.* 76, 252–7.
- Ficat, R.P., 1985. Idiopathic bone necrosis of the femoral head.
- Fisher, D.E., Bickel, W.H., Holley, K.E., Ellefson, R.D., 1972. Corticosteroid-induced Aseptic Necrosis: II. Experimental Study. *Clin. Orthop. Relat. Res.* 84.
- Ford, C.M., Keaveny, T.M., Hospital, B.I., Francisco, S., 1996. The Dependence Of Shear Failure Properties Of Trabecular Bone On Apparent Density And Trabecular Orientation. *Science (80- ).* 29, 1309–1317.
- Fukushima, W., Fujioka, M., Kubo, T., Tamakoshi, A., Nagai, M., Hirota, Y., 2010. Nationwide Epidemiologic Survey of Idiopathic Osteonecrosis of the Femoral Head. *Clin. Orthop. Relat. Res.* EPub ahead of print. doi:10.1007/s11999-010-1292-x
- Galante, J., Rostoker, W., Ray, R.D., 1970. Physical properties of trabecular bone. *Calcif. Tissue Res.* 5, 236–246. doi:10.1007/BF02017552
- Gardeniers, J.W.M., 1993. Report of the Committee of Staging and Nomenclature. ARCO News Letter, in: ARCO Committee on Terminology and Staging: Report on the Committee-Meeting at Santiago de Compostela on Thursday the 14th of October 1993. pp. 79–82.
- Gibson, L.J., 1985. The mechanical behaviour of cancellous bone. *J. Biomech.* 18, 317–328. doi:10.1016/0021-9290(85)90287-8
- Gilroy, A.M., MacPherson, B.R., Ross, L.M., 2008. *Atlas of Anatomy, Thieme Anatomy Series.* Thieme.
- Glimcher, M.J., Kenzora, J.E., 1979. The Biology of Osteonecrosis of the Human Femoral Head and its Clinical Implications: III. Discussion of the Etiology and Genesis of the Pathological Sequelae; Comments on Treatment. *Clin. Orthop. Relat. Res.* 140.
- Goldstein, S.A., 1987. The mechanical properties of trabecular bone: Dependence on anatomic location and function. *J. Biomech.* 20, 1055–1061. doi:10.1016/0021-9290(87)90023-6
- Gray, H., 1919. Anatomy of the Human Body, *The American Journal of the Medical Sciences.*
- Griffith, J.F., Antonio, G.E., Hui, D.S., Ka, J., Wong, T., Joynt, G.M., Ka, A., Wu, L., Yu, A., Cheung, K., Chiu, K.H., Chan, K.M., Leung, P.C., Ahuja, A.T., 2005. Radiology Osteonecrosis of Hip and Knee in Patients with Severe Acute Respiratory Syndrome Treated with Steroids 1.

- Grose, A.W., Gardner, A.W., Sussmann, P.S., Helfet, D.L., Lorich, D., 2008. The surgical anatomy of the blood supply to the femoral head. *J. Bone Jt. Surgery, Br.* Vol. 90-B, 1298–1303. doi:10.1302/0301-620X.90B10.20983
- Guo, K.J., Zhao, F.C., Guo, Y., Li, F.L., Zhu, L., Zheng, W., 2014. The influence of age, gender and treatment with steroids on the incidence of osteonecrosis of the femoral head during the management of severe acute respiratory syndrome: a retrospective study. *Bone Joint J.* 96-B, 259–62. doi:10.1302/0301-620X.96B2.31935
- Ha, Y.-C., Kim, H.J., Kim, S.-Y., Kim, K.-C., Lee, Y.-K., Koo, K.-H., 2011. Effects of age and body mass index on the results of transtrochanteric rotational osteotomy for femoral head osteonecrosis: surgical technique. *J. Bone Joint Surg. Am.* 93 Suppl 1, 75–84. doi:10.2106/JBJS.J.01215
- Haba, Y., Lindner, T., Fritzsche, A., Schiebenhöfer, A., Souffrant, R., Klüss, D., Skripitz, R., Mittelmeier, W., Bader, R., 2012. Relationship between mechanical properties and bone mineral density of human femoral bone retrieved from patients with osteoarthritis. *Open Orthop. J.* 6, 458–63. doi:10.2174/1874325001206010458
- Hall, J.E., 2015. Guyton and Hall textbook of medical physiology. Elsevier Health Sciences.
- Hamilton, T.W., Goodman, S.M., Figgie, M., 2009. SAS weekly rounds: avascular necrosis. *HSS J.* 5, 99–113. doi:10.1007/s11420-009-9107-x
- Havaldar, R., Pilli, S.C., Putti, B.B., 2014. Insights into the effects of tensile and compressive loadings on human femur bone. *Adv. Biomed. Res.* doi:10.4103/2277-9175.129375
- Heimkes, B., Posel, P., Plitz, W., Jansson, V., 1993. Forces acting on the juvenile hip joint in the one-legged stance. *J. Pediatr. Orthop.*
- Helgason, B., Perilli, E., Schileo, E., Taddei, F., Brynjólfsson, S., Viceconti, M., 2008. Mathematical relationships between bone density and mechanical properties: a literature review. *Clin. Biomech. (Bristol, Avon)* 23, 135–46. doi:10.1016/j.clinbiomech.2007.08.024
- Heller, M.O., Bergmann, G., Kassi, J.-P., Claes, L., Haas, N.P., Duda, G.N., 2005. Determination of muscle loading at the hip joint for use in pre-clinical testing. *J. Biomech.* 38, 1155–63. doi:10.1016/j.jbiomech.2004.05.022
- Hernandez, C., Beaupré, G., Keller, T., Carter, D., 2001. The influence of bone volume fraction and ash fraction on bone strength and modulus. *Bone* 29, 74–78. doi:10.1016/S8756-3282(01)00467-7

- Hernigou, P., Poignard, A., Nogier, A., Manicom, O., 2004. Fate of very small asymptomatic stage-I osteonecrotic lesions of the hip. *J. Bone Joint Surg. Am.* 86-A, 2589–93.
- Hipp, J. a, Springfield, D.S., Hayes, W.C., 1995. Predicting pathologic fracture risk in the management of metastatic bone defects. *Clin. Orthop. Relat. Res.* 120–35.
- Hoaglund, F.T., Low, W.D., 1980. Anatomy of the femoral neck and head, with comparative data from Caucasians and Hong Kong Chinese. *Clin. Orthop. Relat. Res.* 10–16. doi:10.1097/00003086-198010000-00003
- Homminga, J., Huiskes, R., Van Rietbergen, B., Rüegsegger, P., Weinans, H., 2001. Introduction and evaluation of a gray-value voxel conversion technique. *J. Biomech.* 34, 513–517. doi:10.1016/S0021-9290(00)00227-X
- Hong, J., Cabe, G.D., Tedrow, J.R., Hipp, J. a, Snyder, B.D., 2004. Failure of trabecular bone with simulated lytic defects can be predicted non-invasively by structural analysis. *J. Orthop. Res.* 22, 479–86. doi:10.1016/j.orthres.2003.09.006
- Hong, N., Du, X.K., 2004. Avascular necrosis of bone in severe acute respiratory syndrome. *Clin. Radiol.* 59, 602–608. doi:10.1016/j.crad.2003.12.008
- Hougum, P.A., 2016. Therapeutic Exercise for Musculoskeletal Injuries 4th Edition. Human Kinetics.
- Huiskes, R., 1984. Principles and methods of solid biomechanics. *Funct. Behav. Orthop. Biomater.* 1.
- Huiskes, R., 1982. On the modelling of long bones in structural analyses. *J. Biomech.* 15, 65–69. doi:10.1016/0021-9290(82)90036-7
- Huiskes, R., Janssen, J., Slooff, T., 1981. A detailed comparison of experimental and theoretical stress-analyses of a human femur. *Mech. Prop. Bone.*
- Hungerford, D.S., Zizic, T.M., 1978. Alcoholism associated ischemic necrosis of the femoral head. Early diagnosis and treatment. *Clin Orthop Relat Res* 144–153.
- Issa, K., Pivec, R., Kapadia, B.H., Banerjee, S., Mont, M. a., 2013. Osteonecrosis of the femoral head: the total hip replacement solution. *Bone Joint J.* 95 B, 46–50. doi:10.1302/0301-620X.95B11.32644
- Ito, H., Matsuno, T., Kaneda, K., 2000. Bipolar Hemiarthroplasty for Osteonecrosis of the Femoral Head. *Clin. Orthop. Relat. Res.* 374, 201–211. doi:10.1097/00003086-200005000-00019
- Ito, H., Tanino, H., Yamanaka, Y., Nakamura, T., Takahashi, D., Minami, a, Matsuno, T., 2012. Long-term results of conventional varus half-wedge

- proximal femoral osteotomy for the treatment of osteonecrosis of the femoral head. *J. Bone Joint Surg. Br.* 94, 308–314. doi:10.1302/0301-620X.94B3.27814
- Jacobs, B., 1978. Epidemiology of traumatic and nontraumatic osteonecrosis. *Clin Orthop Relat Res* 51–67.
- Johannson, H.R., Zywiel, M.G., Marker, D.R., Jones, L.C., McGrath, M.S., Mont, M. a., 2011. Osteonecrosis is not a predictor of poor outcomes in primary total hip arthroplasty: A systematic literature review. *Int. Orthop.* 35, 465–473. doi:10.1007/s00264-010-0979-7
- Jones, J.P., Engleman, E.P., 1966. Osseous avascular necrosis associated with systemic abnormalities. *Arthritis Rheum.* 9, 728–736. doi:10.1002/art.1780090511
- Kafka, V., 1983. On hydraulic strengthening of bones. *Biorheology* 20, 789–793.
- Kaneko, T.S., Bell, J.S., Pejcic, M.R., Tehrzanadeh, J., Keyak, J.H., 2004. Mechanical properties, density and quantitative CT scan data of trabecular bone with and without metastases. *J. Biomech.* 37, 523–530. doi:10.1016/j.jbiomech.2003.08.010
- Kaneko, T.S., Pejcic, M.R., Tehrzanadeh, J., Keyak, J.H., 2003. Relationships between material properties and CT scan data of cortical bone with and without metastatic lesions. *Med. Eng. Phys.* 25, 445–454. doi:10.1016/S1350-4533(03)00030-4
- Kaushik, A.P., Das, A., Cui, Q., 2012. Osteonecrosis of the femoral head: An update in year 2012. *World J. Orthop.* 3, 49–57. doi:10.5312/wjo.v3.i5.49
- Kay, R.M., Lieberman, J.R., Dorey, F.J., Seeger, L.L., 1994. Inter- and intraobserver variation in staging patients with proven avascular necrosis of the hip. *Clin. Orthop. Relat. Res.* 124–9.
- Keaveny, T.M., Borchers, R.E., Gibson, L.J., Hayes, W.C., 1993. Trabecular bone modulus and strength can depend on specimen geometry. *J. Biomech.* 26. doi:10.1016/0021-9290(93)90059-N
- Keaveny, T.M., Guo, X.E., Wachtel, E.F., McMahon, T.A., Hayes, W.C., 1994a. Trabecular bone exhibits fully linear elastic behavior and yields at low strains. *J. Biomech.* 27. doi:10.1016/0021-9290(94)90053-1
- Keaveny, T.M., Morgan, E.F., Niebur, G.L., Yeh, O.C., 2001. Biomechanics of trabecular bone. *Annu. Rev. Biomed. Eng.* 3, 307–333. doi:10.1146/annurev.bioeng.3.1.307
- Keaveny, T.M., Pinilla, T.P., Crawford, R.P., Kopperdahl, D.L., Lou, a., 1997. Systematic and random errors in compression testing of trabecular bone. *J. Orthop. Res.* 15, 101–110. doi:10.1002/jor.1100150115

- Keaveny, T.M., Wachtel, E.F., Ford, C.M., Hayes, W.C., 1994b. Differences between the tensile and compressive strengths of bovine tibial trabecular bone depend on modulus. *J. Biomech.* 27, 1137–1146. doi:10.1016/0021-9290(94)90054-X
- Keller, T.S., 1994. Predicting the compressive mechanical behavior of bone. *J. Biomech.* 27, 1159–1168. doi:10.1016/0021-9290(94)90056-6
- Kerboul, M., Thomine, J., Postel, M., Merle D'Aubigne, R., 1974. The conservative surgical treatment of idiopathic aseptic necrosis of the femoral head. *J. Bone Jt. Surg. Br.* Vol. 56, 291–6.
- Keyak, J.H., Kaneko, T.S., Tehrzanadeh, J., Skinner, H.B., 2005. Predicting proximal femoral strength using structural engineering models. *Clin. Orthop. Relat. Res. &NA;*, 219–228. doi:10.1097/01.blo.0000164400.37905.22
- Keyak, J.H., Lee, I.Y., Skinner, H.B., 1994. Correlations between orthogonal mechanical properties and density of trabecular bone: Use of different densitometric measures. *J. Biomed. Mater. Res.* 28, 1329–1336. doi:10.1002/jbm.82028111
- Keyak, J.H., Skinner, H.B., Fleming, J. a., 2001. Effect of force direction on femoral fracture load for two types of loading conditions. *J. Orthop. Res.* 19, 539–544. doi:10.1016/S0736-0266(00)00046-2
- Kim, S.-Y., Rubash, H.E., 2007. *The Adult Hip, The Adult Hip.* Lippincott Williams & Wilkins.
- Kim, Y.H., Choi, Y., Kim, J.S., 2011. Cementless Total Hip Arthroplasty With Alumina-on-Highly Cross-Linked Polyethylene Bearing in Young Patients With Femoral Head Osteonecrosis. *J. Arthroplasty* 26, 218–223. doi:10.1016/j.arth.2010.03.010
- Kim, Y.M., Ahn, J.H., Kang, H.S., Kim, H.J., 1998. Estimation of the extent of osteonecrosis of the femoral head using MRI. *J. Bone Joint Surg. Br.* 80, 954–8.
- Knauss, P., 1981. Materialkennwerte und Festigkeitsverhalten des spongiösen Knochengewebes am coxalen Human-Femur / Material Properties and Strength Behavioor of Spongy Bone Tissue at the Coxal Human Femur. *Biomed. Tech.* 26, 200–210.
- Koch, J.C., 1917. The laws of bone architecture. *Am. J. Anat.* 21, 177–298. doi:10.1002/aja.1000210202
- Koo, K., Kim, R., 1995. Quantifying the extent of osteonecrosis of the femoral head. *J. Bone Jt. Surgery, Br.* Vol. 77, 875–875.
- Koo, K., Kim, R., Ko, G., Song, H., Jeong, S., 1995. Preventing collapse in early necrosis of the femoral head. *J. Bone Jt. Surgery, Br.* Vol. 77-B, 870–874.

- Koob, T.J., Pringle, D., Gedbaw, E., Meredith, J., Berrios, R., Kim, H.K.W., 2007. Biomechanical properties of bone and cartilage in growing femoral head following ischemic osteonecrosis. *J. Orthop. Res.* 25, 750–757.
- Koren, L., Ginesin, E., Melamed, Y., Norman, D., Levin, D., Peled, E., 2015. Hyperbaric Oxygen for Stage I and II Femoral Head Osteonecrosis. *Orthopedics* 38, e200–e205. doi:10.3928/01477447-20150305-57
- Lai, K.-A., Shen, W.-J., Yang, C.-Y., Shao, C.-J., Hsu, J.-T., Lin, R.-M., 2005. The use of alendronate to prevent early collapse of the femoral head in patients with nontraumatic osteonecrosis. A randomized clinical study. *J. Bone Joint Surg. Am.* 87, 2155–2159. doi:10.2106/JBJS.D.02959
- Lai, Y.S., Wei, H.W., Cheng, C.K., 2008. Incidence of hip replacement among national health insurance enrollees in Taiwan. *J. Orthop. Surg. Res.* 3, 42. doi:10.1186/1749-799X-3-42
- Lavernia, C.J., Sierra, R.J., Grieco, F.R., 1999. Osteonecrosis of the femoral head. *J. Am. Acad. Orthop. Surg.* 7, 250–61.
- Lee, C., 2014. Osteonecrosis more common in men than women in Korea. *Korean Her.*
- Lee, M.H., Moon, D.H., Na, H.W., 1992. Diagnosis of femoral head avascular necrosis by triple head high resolution. *J Nucl Med* 33, 936.
- Lee, M.J., Corrigan, J., Stack, J.P., Ennis, J.T., 1990. A comparison of modern imaging modalities in osteonecrosis of the femoral head. *Clin. Radiol.* 42, 427–432. doi:10.1016/S0009-9260(05)80900-6
- Li, B., Aspden, R.M., 1997. Composition and mechanical properties of cancellous bone from the femoral head of patients with osteoporosis or osteoarthritis. *J. Bone Miner. Res.* 12, 641–51. doi:10.1359/jbmr.1997.12.4.641
- Lieberman, D.E., Polk, J.D., Demes, B., 2004. Predicting Long Bone Loading from Cross-Sectional Geometry. *Am. J. Phys. Anthropol.* 123, 156–171. doi:10.1002/ajpa.10316
- Lieberman, J.R., Berry, D.J., Mont, M.A., Aaron, R.K., Callaghan, J.J., Rajadhyaksha, A.D., Urbaniak, J.R., 2003. Osteonecrosis of the hip: management in the 21st century. *Instr. Course Lect.* 52, 337–355. doi:10.1007/s00132-007-1082-7
- Linde, F., Hvid, I., Madsen, F., 1992. The effect of specimen geometry on the mechanical behaviour of trabecular bone specimens. *J. Biomech.* 25, 359–368. doi:10.1016/0021-9290(92)90255-Y

- Linde, F., Sørensen, H.C.F., 1993. The effect of different storage methods on the mechanical properties of trabecular bone. *J. Biomech.* 26, 1249–1252. doi:10.1016/0021-9290(93)90072-M
- Lindsey, D., Beaupre, G., 2009. Apparent Differences in Mineral Concentration in Bone Calibration Phantoms are Caused by Differences in microCT Scanners and Scanner Protocols. *56Th Annu. Meet. Orthop. Res. Soc.* 54, 94304.
- Liu, X.S., Walker, M.D., McMahon, D.J., Udesky, J., Liu, G., Bilezikian, J.P., Guo, X.E., 2011. Better Skeletal Microstructure Confers Greater Mechanical Advantages in Chinese-American Women Versus White Women. *J. Bone Miner. Res.* doi:10.1002/jbm.378
- Lotz, J., Gerhart, T., Hayes, W., 1990. Mechanical properties of trabecular bone from the proximal femur: a quantitative CT study. *J. Comput. Assist. ....*
- Lotz, J.C., Cheal, E.J., Hayes, W.C., 1991. Fracture prediction for the proximal femur using finite element models: Part I--Linear analysis. *J. Biomech. Eng.* 113, 353–360. doi:10.1115/1.2895412
- Lotz, J.C., Hayes, W.C., 1991. Fracture Prediction for the Proximal Femur Using Finite Element Models : Part II — Nonlinear Analysis 113, 353–360.
- Lv, H., De Vlas, S.J., Liu, W., Wang, T.B., Cao, Z.Y., Li, C.P., Cao, W.C., Richardus, J.H., 2009. Avascular osteonecrosis after treatment of SARS: A 3-year longitudinal study. *Trop. Med. Int. Heal.* 14, 79–84. doi:10.1111/j.1365-3156.2008.02187.x
- Malizos, K.N., Karantanas, A.H., Varitimidis, S.E., Dailiana, Z.H., Bargiotas, K., Maris, T., 2007. Osteonecrosis of the femoral head: etiology, imaging and treatment. *Eur. J. Radiol.* 63, 16–28. doi:10.1016/j.ejrad.2007.03.019
- Mankin, H.J., 1992. Nontraumatic Necrosis of Bone (Osteonecrosis). *N. Engl. J. Med.* 326, 1473–1479. doi:10.1056/NEJM199205283262206
- Marcus, N.D., Enneking, W.F., Massam, R. a, 1973. The Silent Hip in Idiopathic Aseptic Necrosis. *J. Bone & Jt. Surg.* 55, 1351–1366.
- Marker, D.R., Seyler, T.M., Ulrich, S.D., Srivastava, S., Mont, M.A., 2008. Do Modern Techniques Improve Core Decompression Outcomes for Hip Osteonecrosis? *Clin. Orthop. Relat. Res.* 466, 1093–1103.
- McGrory, B.J., York, S.C., Iorio, R., Macaulay, W., Pelker, R.R., Parsley, B.S., Teeny, S.M., 2007. Current practices of AAHKS members in the treatment of adult osteonecrosis of the femoral head. *J Bone Jt. Surg Am* 89, 1194–1204. doi:10.2106/JBJS.F.00302

- Meier, R., Kraus, T.M., Schaeffeler, C., Torka, S., Schlitter, A.M., Specht, K., Haller, B., Waldt, S., Rechl, H., Rummeny, E.J., Woertler, K., 2014. Bone marrow oedema on MR imaging indicates ARCO stage 3 disease in patients with AVN of the femoral head. *Eur. Radiol.* 24, 2271–2278. doi:10.1007/s00330-014-3216-8
- Melton, L.J., 1996. Epidemiology of hip fractures: Implications of the exponential increase with age. *Bone* 18, S121–S125. doi:10.1016/8756-3282(95)00492-0
- Metselaar, H.J., Van Steenberge, E.J., Bijnen, a B., Jeekel, J.J., Van Linge, B., Weimar, W., 1985. Incidence of osteonecrosis after renal transplantation. *Acta Orthop. Scand.* 56, 413–415. doi:10.3109/17453678508994360
- Mitchell, D.G., Steinberg, M.E., Dalinka, M.K., Rao, V.M., Fallon, M., Kressel, H.Y., 1989. Magnetic Resonance Imaging of the Ischemic Hip alterations within the osteonecrotic, viable, and reactive zones. *Clin. Orthop. Relat. Res.* 244, 60–77.
- Mont, M., Carbone, J., Fairbank, A., 1996. Core decompression versus nonoperative management for osteonecrosis of the hip. *Clin. Orthop. Relat. Res.* 324, 169.
- Mont, M., Jones, L.C., Einhorn, T.A., 1998. Osteonecrosis of the Femoral Head. *Clin. Orthop. Relat. Res.* 314S–335S.
- Mont, M.A., Cherian, J.J., Sierra, R.J., Jones, L.C., Lieberman, J.R., 2015. Nontraumatic Osteonecrosis of the Femoral Head: Where Do We Stand Today? A Ten-Year Update. *J. Bone Joint Surg. Am.* 97, 1604–27. doi:10.2106/JBJS.O.00071
- Mont, M.A., Fairbank, A., Krackow, K., Hungerford, D., 1996. Corrective osteotomy for osteonecrosis of the femoral head. *J. Bone Joint Surg. Am.* 78, 1032–1038.
- Mont, M.A., Hungerford, D., 1995. Non-traumatic avascular necrosis of the femoral head. *J. Bone Jt. Surgery, Am. Vol.* 77, 459–474.
- Mont, M.A., Marulanda, G.A., Jones, L.C., Saleh, K.J., Gordon, N., Hungerford, D.S., Steinberg, M.E., 2006. Systematic analysis of classification systems for osteonecrosis of the femoral head. *J. bone Jt. surgery.American Vol.* 88 Suppl 3, 16–26. doi:88/suppl\_3/16 [pii]
- Morgan, E.F., Bayraktar, H.H., Keaveny, T.M., 2003. Trabecular bone modulus–density relationships depend on anatomic site. *J. Biomech.* 36, 897–904. doi:10.1016/S0021-9290(03)00071-X
- Morgan, E.F., Keaveny, T.M., 2001. Dependence of yield strain of human trabecular bone on anatomic site. *J. Biomech.* 34, 569–577. doi:10.1016/S0021-9290(01)00011-2

- Motomura, G., Yamamoto, T., Yamaguchi, R., Ikemura, S., Nakashima, Y., Mawatari, T., Iwamoto, Y., 2011. Morphological analysis of collapsed regions in osteonecrosis of the femoral head. *J. Bone Jt. Surgery, Br.* Vol. 93-B, 184–187. doi:10.1302/0301-620X.93B2
- Mourtada, F., Beck, T., 1996. Curved beam model of the proximal femur for estimating stress using dual-energy x-ray absorptiometry derived structural geometry. *J. Orthop. Res.* 14, 483–492.
- Musso, E.S., Mitchell, S.N., Schink-Ascani, M., Bassett, C., 1986. Results of Conservative Management of Osteonecrosis of the Femoral Head A Retrospective Review. *Clin. Orthop. Relat. Res.* 207, 209–215.
- Nakamura, J., Harada, Y., Oinuma, K., Iida, S., Kishida, S., Takahashi, K., 2010. Spontaneous repair of asymptomatic osteonecrosis associated with corticosteroid therapy in systemic lupus erythematosus: 10-year minimum follow-up with MRI. *Lupus* 19, 1307–1314.
- Nakamura, T., Matsumoto, T., Nishino, M., Tomita, K., Kadoya, M., 1997. Early magnetic resonance imaging and histologic findings in a model of femoral head necrosis. *Clin. Orthop. Relat. Res.*
- Nam, K.W., Kim, Y.L., Yoo, J.J., Koo, K.-H., Yoon, K.S., Kim, H.J., 2008. Fate of untreated asymptomatic osteonecrosis of the femoral head. *J. Bone Joint Surg. Am.* 90, 477–484. doi:10.2106/JBJS.F.01582
- National Joint Registry, 2015. National Joint Registry: 12th Annual Report 2015, National Joint Registry. Hemel Hempstead.
- National Joint Registry, 2013. National Joint Registry: 10th Annual Report 2013. Hemel Hempstead.
- National Joint Registry, 2007. National Joint Registry: 5th Annual Report 2007. Hemel Hempstead.
- National joint replacement registry, 2016. Annual Report 2016.
- National Osteoporosis Society, 2015. The Osteoporosis Agenda England Improving the lives of people with osteoporosis and fragility fractures.
- Nazarian, A., Muller, J., Zurakowski, D., Müller, R., Snyder, B.D., 2007. Densitometric, morphometric and mechanical distributions in the human proximal femur. *J. Biomech.* 40, 2573–9. doi:10.1016/j.jbiomech.2006.11.022
- Nazarian, A., Snyder, B.D., Zurakowski, D., Müller, R., 2008a. Quantitative micro-computed tomography: A non-invasive method to assess equivalent bone mineral density. *Bone* 43, 302–311. doi:10.1016/j.bone.2008.04.009
- Nazarian, A., von Stechow, D., Zurakowski, D., Müller, R., Snyder, B.D., 2008b. Bone volume fraction explains the variation in strength and stiffness of cancellous bone affected by metastatic cancer and

- osteoporosis. *Calcif. Tissue Int.* 83, 368–79. doi:10.1007/s00223-008-9174-x
- Nelissen, R., Schreurs, W., 2015. Blik op Uitkomsten. Jaarrapportage Landelijke Registratie Orthopedische Implantaten 2015.
- Oftadeh, R., Karimi, Z., Villa-Camacho, J., Tanck, E., Verdonschot, N., Goebel, R., Snyder, B.D., Hashemi, H.N., Vaziri, A., Nazarian, A., 2016. Curved Beam Computed Tomography based Structural Rigidity Analysis of Bones with Simulated Lytic Defect: A Comparative Study with Finite Element Analysis. *Sci. Rep.* 6, 32397. doi:10.1038/srep32397
- Öhman, C., Baleani, M., Perilli, E., Dall'Ara, E., Tassani, S., Baruffaldi, F., Viceconti, M., 2007. Mechanical testing of cancellous bone from the femoral head: Experimental errors due to off-axis measurements. *J. Biomech.* 40, 2426–2433. doi:10.1016/j.jbiomech.2006.11.020
- Ohzono, K., Saito, M., Sugano, N., Takaoka, K., Ono, K., 1992. The fate of nontraumatic avascular necrosis of the femoral head: A radiologic classification to formulate prognosis. *Clin. Orthop. Relat. Res.* 277, 73.
- Ohzono, K., Saito, M., Takaoka, K., 1991. Natural history of nontraumatic avascular necrosis of the femoral head. *J. Bone ...* 73-B, 68–72.
- Openstax college, 2013. Anatomy and Physiology, Anatomy and physiology. doi:10.1037/e565512011-001
- Ortiguera, C.J., Pulliam, I.T., Cabanela, M.E., 1999. Total hip arthroplasty for osteonecrosis. *J. Arthroplasty* 14, 21–28. doi:10.1016/S0883-5403(99)90197-3
- Pachore, J.A., Vaidya, S. V., Thakkar, C.J., Bhalodia, H.K.P., Wakankar, H.M., 2013. ISHKS joint registry: A preliminary report. *Indian J. Orthop.* doi:10.4103/0019-5413.118208
- Pankaj, P., 2013. Patient specific modelling of bone and bone implant systems: the challenges. *Int. j. numer. method. biomed. eng.* 29, 233–249. doi:10.1002/cnm.2536
- Patel, P.S.D., Shepherd, D.E.T., Hukins, D.W.L., 2008. Compressive properties of commercially available polyurethane foams as mechanical models for osteoporotic human cancellous bone. *BMC Musculoskelet. Disord.* 9, 5–11. doi:10.1186/1471-2474-9-137
- Patterson, R.J., Bickel, W.H., Dahlin, D.C., 1964. Idiopathic Avascular Necrosis of the Head of the Femur. A Study of fifty-two Cases. *J. Bone Joint Surg. Am.* 46, 267–82.
- Paul, J., 1967. Paper 8: Forces Transmitted by Joints in the Human Body. *Proc. Inst. Mech. Eng.* doi:10.1243/PIME

- Pauwels, F., 2012. Biomechanics of the Normal and Diseased Hip: Theoretical Foundation, Technique and Results of Treatment An Atlas. Springer Science & Business Media.
- Pauwels, F., 1965. Die Bedeutung der Bauprinzipien des Stütz- und Bewegungsapparates für die Beanspruchung der Röhrenknochen, in: Gesammelte Abhandlungen Zur Funktionellen Anatomie Des Bewegungsapparates. Springer Berlin Heidelberg, Berlin, Heidelberg, pp. 197–235. doi:10.1007/978-3-642-86841-2\_4
- Peng, L., Bai, J., Zeng, X., Zhou, Y., 2006. Comparison of isotropic and orthotropic material property assignments on femoral finite element models under two loading conditions. *Med. Eng. Phys.* 28, 227–233. doi:10.1016/j.medengphy.2005.06.003
- Perry, D.C., Bruce, C.E., Pope, D., Dangerfield, P., Platt, M.J., Hall, A.J., 2012. Legg-Calvé-Perthes disease in the UK: Geographic and temporal trends in incidence reflecting differences in degree of deprivation in childhood. *Arthritis Rheum.* 64, 1673–1679. doi:10.1002/art.34316
- Plakseychuk, A.Y., Shah, M., Varitimidis, S.E., Rubash, H.E., Sotereanos, D., 2001. Classification of Osteonecrosis of the Femoral Head: Reliability, Reproducibility, and Prognostic Value. *Clin. Orthop. Relat. Res.* 386.
- Prendergast, P.J., Taylor, D., 1994. Prediction of bone adaptation using damage accumulation. *J. Biomech.* 27, 1067–1076. doi:10.1016/0021-9290(94)90223-2
- Pringle, D., Koob, T.J., Kim, H.K.W., 2004. Indentation properties of growing femoral head following ischemic necrosis. *J. Orthop. Res.* 22, 122–30.
- Pritchett, J.W., 2001. Statin therapy decreases the risk of osteonecrosis in patients receiving steroids. *Clin. Orthop. Relat. Res.* 173–178.
- Raftopoulos, D.D., Qassem, W., 1987. Three-dimensional curved beam stress analysis of the human femur. *J. Biomed. Eng.* 9, 356–366. doi:10.1016/0141-5425(87)90085-9
- Reilly, D.T., Burstein, A.H., 1975. The elastic and ultimate properties of compact bone tissue. *J. Biomech.* 8. doi:10.1016/0021-9290(75)90075-5
- Reis, N.D., Schwartz, O., Militianu, D., Ramon, Y., Levin, D., Norman, D., Melamed, Y., Shupak, A., Goldsher, D., Zinman, C., 2003. Hyperbaric oxygen therapy as a treatment for stage-I avascular necrosis of the femoral head. *J. Bone Jt. Surgery, Br.* Vol. 85, 371–375.
- Renders, G. a P., Mulder, L., van Ruijven, L.J., van Eijden, T.M.G.J., 2007. Porosity of human mandibular condylar bone. *J. Anat.* 210, 239–48. doi:10.1111/j.1469-7580.2007.00693.x

- Resnick, D., Niwayama, G., 1995. Osteonecrosis: diagnostic techniques, specific situations, and complications. *Diagnosis bone Jt. Disord.* 3rd ed. Philadelphia, Pa Saunders 3495–3515.
- Rho, J.Y., Hobatho, M.C., Ashman, R.B., 1995. Relations of mechanical properties to density and CT numbers in human bone. *Med. Eng. Phys.* 17, 347–355. doi:10.1016/1350-4533(95)97314-F
- Rho, J.Y., Hobatho, M.C., Ashman, R.B., 1995. Relations of mechanical properties to density and CT numbers in human bone. *Med. Eng. Phys.* 17, 347–355. doi:10.1016/1350-4533(95)97314-F
- Richmond, B.G., Wright, B.W., Grosse, I., Dechow, P.C., Ross, C.F., Spencer, M. a, Strait, D.S., 2005. Finite element analysis in functional morphology. *Anat. Rec. A. Discov. Mol. Cell. Evol. Biol.* 283, 259–274. doi:10.1002/ar.a.20169
- Rico, H., Gomez-Castresana, F., Cabranes, J. a., Almoguera, I., Lopez Duran, L., Matute, J. a., 1985. Increased blood cortisol in alcoholic patients with aseptic necrosis of the femoral head. *Calcif. Tissue Int.* 37, 585–587. doi:10.1007/BF02554910
- Ridler, T., Calvard, S., 1978. Picture thresholding using an iterative selection method. *IEEE Trans. Syst. Man ...* 630–632.
- Roach, K., Miles, T., 1991. Normal hip and knee active range of motion: the relationship to age. *Phys. Ther.*
- Rodan, G.A., 1992. Introduction to bone biology. *Bone* 13, S3–S6.
- Rohlmann, a., Mössner, U., Bergmann, G., Kölbel, R., 1983. Finite-element-analysis and experimental investigation in a femur with hip endoprosthesis. *J. Biomech.* 16, 727–742. doi:10.1016/0021-9290(83)90082-9
- Rybicki, E.F., Simonen, F.A., Weis, E.B., 1972. On the mathematical analysis of stress in the human femur. *J. Biomech.* 5, 203–215. doi:10.1016/0021-9290(72)90056-5
- Saini, A., Saifuddin, A., 2004. MRI of osteonecrosis. *Clin. Radiol.* 59, 1079–93. doi:10.1016/j.crad.2004.04.014
- Salathe, E., Arangio, G., 1989. An application of beam theory to determine the stress and deformation of long bones. *J. Biomech.* 22.
- Savvidis, E., Stabrey, H., 1997. Erste werkstoffangepaßte Anstrengungshypothese zur Berechnung der Vergleichsspannung an humanen Femura The First Material-Adapted Strength Hypothesis for Calculating the Equivalent Stress in Human Femora. *Biomed. Tech.* 42, 276–279.
- Schileo, E., Dall'Ara, E., Taddei, F., Malandrino, A., Schotkamp, T., Baleani, M., Viceconti, M., 2008a. An accurate estimation of bone density

- improves the accuracy of subject-specific finite element models. *J. Biomech.* 41, 2483–2491. doi:10.1016/j.jbiomech.2008.05.017
- Schileo, E., Taddei, F., Cristofolini, L., Viceconti, M., 2008b. Subject-specific finite element models implementing a maximum principal strain criterion are able to estimate failure risk and fracture location on human femurs tested in vitro. *J. Biomech.* 41, 356–67.  
doi:10.1016/j.jbiomech.2007.09.009
- Schileo, E., Taddei, F., Cristofolini, L., Viceconti, M., 2008c. Subject-specific finite element models implementing a maximum principal strain criterion are able to estimate failure risk and fracture location on human femurs tested in vitro. *J. Biomech.* 41, 356–67.  
doi:10.1016/j.jbiomech.2007.09.009
- Schmitt-Sody, M., Kirchhoff, C., Mayer, W., Goebel, M., Jansson, V., 2008. Avascular necrosis of the femoral head : inter- and intraobserver variations of Ficat and ARCO classifications. *Int. Orthop.* 32, 283–287.
- Schweizerisches Implantatregister, 2014. Jahresbericht 2014.  
doi:10.5089/9781498350891.017
- Seireg, A., Arvikar, R., 1975. The prediction of muscular load sharing and joint forces in the lower extremities during walking. *J. Biomech.*
- Shannon, B.D., Trousdale, R.T., 2004. Femoral osteotomies for avascular necrosis of the femoral head. *Clin. Orthop. Relat. Res.* 55905, 34–40.
- Simoes, J.A., Vaz, M.A., Blatcher, S., Taylor, M., 2000. Influence of head constraint and muscle forces on the strain distribution within the intact femur. *Med. Eng. Phys.* 22, 453–459.
- Smith, S.W., Meyer, R. a, Connor, P.M., Smith, S.E., Hanley, E.N., 1996. Interobserver reliability and intraobserver reproducibility of the modified Ficat classification system of osteonecrosis of the femoral head. *J. Bone Joint Surg. Am.* 78, 1702–6.
- Snyder, B., Hipp, J., Nazarian, A., 2004. Non-Invasive Prediction of Fracture Risk Due to Metastatic Skeletal Defects. *Orthop. J. Harvard Med. Sch.* 6, 88–94.
- Snyder, B.D., Hauser-Kara, D.A., Hipp, J.A., Zurakowski, D., Hecht, A.C., Gebhardt, M.C., 2006. Predicting fracture through benign skeletal lesions with quantitative computed tomography. *J Bone Jt. Surg Am* 88, 55–70.
- Snyder, S., Schneider, E., 1991. Estimation of mechanical properties of cortical bone by computed tomography. *J. Orthop. Res.* 422–431.
- Song, W.S., Yoo, J.J., Kim, Y.-M., Kim, H.J., 2007. Results of multiple drilling compared with those of conventional methods of core

- decompression. *Clin. Orthop. Relat. Res.* 454, 139–46.  
doi:10.1097/01.blo.0000229342.96103.73
- Steinberg, D.R., Steinberg, M.E., Garino, J.P., Dalinka, M., Udupa, J.K., 2006. Determining lesion size in osteonecrosis of the femoral head. *J. Bone Jt. Surgery, Am. Vol.* 88 Suppl. , 27–34.
- Steinberg, M.E., Bands, R.E., Parry, S., Hoffman, E., Chan, T., Hartman, K.M., 1999. Does lesion size affect the outcome in avascular necrosis? *Clin. Orthop. Relat. Res.* 367, 262–271.
- Steinberg, M.E., Brighton, C., Steinberg, D.R., Tooze, S.E., Hayken, G.D., 1984. Treatment of Avascular Necrosis of the Femoral Head by a Combination of Bone Grafting, Decompression, and Electrical Stimulation. *Clin. Orthop. Relat. Res.* 186, 137–153.
- Steinberg, M.E., Hayken, G.D., Steinberg, D.R., 1995. A quantitative system for staging avascular necrosis. *J. Bone Jt. Surgery, Am. Vol.* 77-B, 34–41.
- Steinberg, M.E., Larcom, P.G., Strafford, B., Hosick, W.B., Corces, A., BANDS, R.O.Y.E., Hartman, K.E., 2001. Core decompression with bone grafting for osteonecrosis of the femoral head. *Clin. Orthop. Relat. Res.* 386, 71–78.
- Steinberg, M.E., Steinberg, D.R., 2014. Osteonecrosis: Historical Perspective, in: Koo, K.-H., Mont, M.A., Jones, L.C. (Eds.), *Osteonecrosis*. Springer Berlin Heidelberg, Berlin, Heidelberg, pp. 3–15. doi:10.1007/978-3-642-35767-1\_1
- Steinberg, M.E., Steinberg, D.R., 2004. Classification systems for osteonecrosis: An overview. *Orthop. Clin. North Am.* 35, 273–283. doi:10.1016/j.ocl.2004.02.005
- Stoica, Z., Dumitrescu, D., Popescu, M., 2009. Imaging of avascular necrosis of femoral head: familiar methods and newer trends. *Curr. Heal. Sci.* 35, 23–28.
- Sugano, N., Atsumi, T., Ohzono, K., Kubo, T., Hotokebuchi, T., Takaoka, K., 2002. The 2001 revised criteria for diagnosis, classification, and staging of idiopathic osteonecrosis of the femoral head. *J. Orthop. Sci.* 7, 601–605. doi:<http://dx.doi.org/10.1007/s007760200108>
- Sugioka, Y., 1978. Transtrochanteric Anterior Rotational Osteotomy of the Femoral Head in the Treatment of Osteonecrosis Affecting the Hip. *Clin. Orthop. Relat. Res.* 191–201. doi:10.1097/00003086-197801000-00019
- Sugioka, Y., Hotokebuchi, T., Tsutsui, H., 1992. Transtrochanteric anterior rotational osteotomy for idiopathic and steroid-induced necrosis of the femoral head. Indications and long-term results. *Clin. Orthop. Relat. Res.* 111–20.

Swedish Hip Arthroplasty Register, 2014. The Swedish Hip Arthroplasty Register: Annual Report 2014. Gothenburg.

Szabó, M.E., Taylor, M., Thurner, P.J., 2011. Mechanical properties of single bovine trabeculae are unaffected by strain rate. *J. Biomech.* 44, 962–7. doi:10.1016/j.jbiomech.2010.12.008

Tanck, E., van Aken, J.B., van der Linden, Y.M., Schreuder, H.W.B., Binkowski, M., Huizenga, H., Verdonschot, N., 2009. Pathological fracture prediction in patients with metastatic lesions can be improved with quantitative computed tomography based computer models. *Bone* 45, 777–783. doi:10.1016/j.bone.2009.06.009

Taylor, M.E., Tanner, K.E., Freeman, M. a R., Yettram, a. L., 1996. Stress and strain distribution within the intact femur: Compression or bending? *Med. Eng. Phys.* 18, 122–131. doi:10.1016/1350-4533(95)00031-3

Taylor, S.D., Tsiridis, E., Ingham, E., Jin, Z., Fisher, J., Williams, S., 2011. Comparison of human and animal femoral head chondral properties and geometries. *Proc. Inst. Mech. Eng. Part H J. Eng. Med.* 226, 55–62. doi:10.1177/0954411911428717

Timoshenko, S.P., 1922. X. On the transverse vibrations of bars of uniform cross-section. *Philos. Mag. Ser.* 6 43, 125–131. doi:10.1080/14786442208633855

Tingart, M., Bäthis, H., Perlick, L., Lerch, K., Lüring, C., Grifka, J., 2004. Die Therapie der Osteonekrose des Femurkopfes: Ergebnisse einer bundesweiten Umfrage. *Zeitschrift für Orthopädie* 142, 553–558. doi:10.1055/s-2004-822819

Toridis, T.G., 1969. Stress analysis of the femur. *J. Biomech.* 2, 163–174. doi:10.1016/0021-9290(69)90028-1

Townsend, P.R., Rose, R.M., Radin, E.L., 1975. Buckling studies of single human trabeculae. *J. Biomech.* 8. doi:10.1016/0021-9290(75)90025-1

Trueta, J., Harrison, M., 1953. The normal vascular anatomy of the femoral head in adult man. *J Bone Jt. Surg Br* 35-B, 442–461.

Turner, C.H., Cowin, S.C., 1988. Errors Induced by Off-Axis Measurement of the Elastic Properties of Bone. *J Biomech Eng* 110, 213–215. doi:10.1115/1.3108433

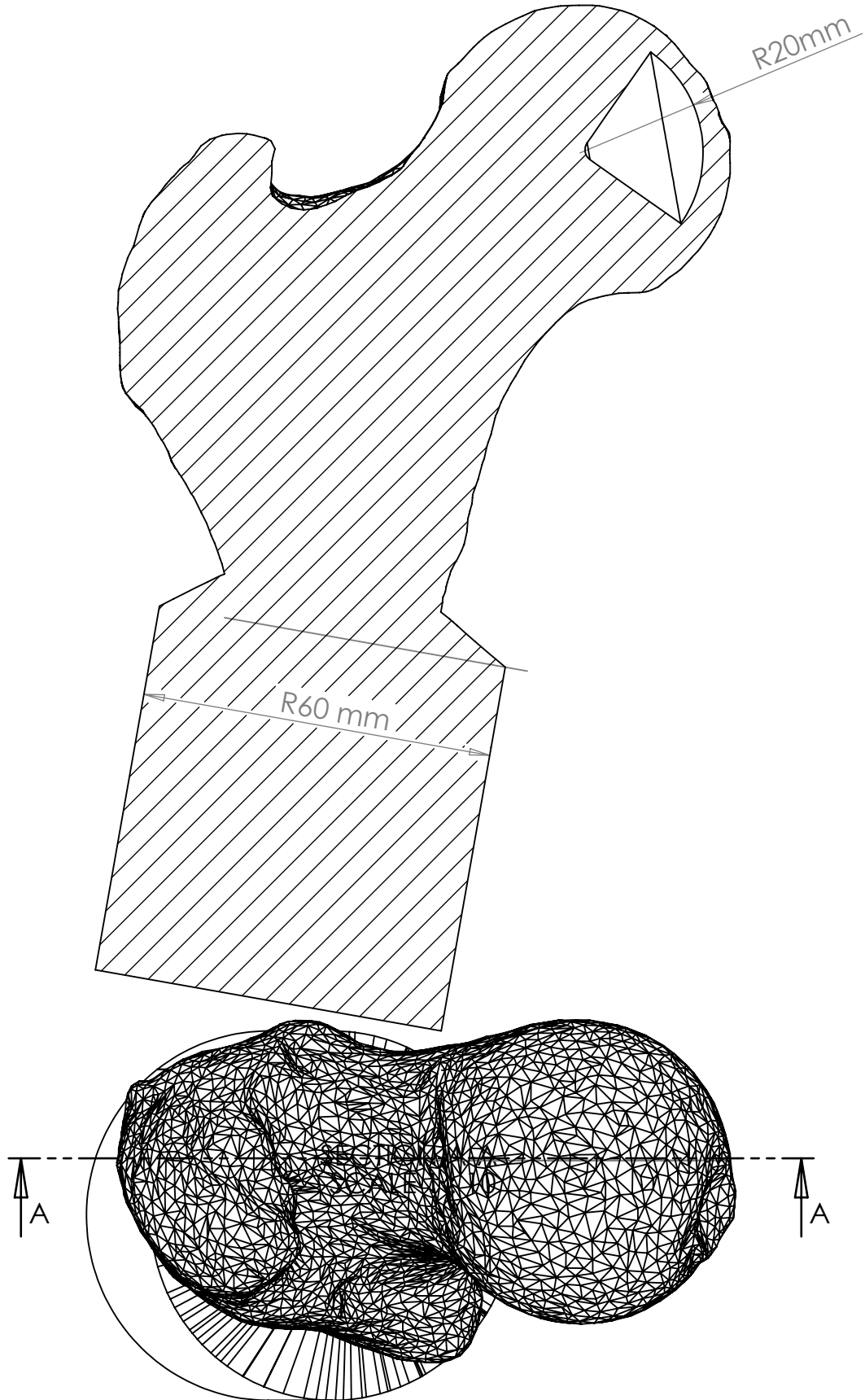
Turner, C.H., Rho, J., Takano, Y., Tsui, T.Y., Pharr, G.M., 1999. The elastic properties of trabecular and cortical bone tissues are similar: Results from two microscopic measurement techniques. *J. Biomech.* 32, 437–441. doi:10.1016/S0021-9290(98)00177-8

Turner, D.A., Templeton, A.C., Selzer, P.M., Rosenberg, A.G., Petasnick, J.P., 1989. Femoral capital osteonecrosis: MR finding of diffuse marrow abnormalities without focal lesions. *Radiology* 171, 135–140.

- Urbaniak, J.R., Coogan, P.G., Gunneson, E.B., Nunley, J.A., 1995. Treatment of osteonecrosis of the femoral head with free vascularized fibular grafting. A long-term follow-up study of one hundred and three hips. *J. Bone & Joint Surg.* 77, 681 LP – 694.
- Von Mises, R., 1928. Mechanik der plastischen Formanderung von Kristallen. *Z. Angew. Math. Mech.* 8, 161–185.  
doi:10.1002/zamm.19280080302
- Vose, G.P., Kubala, A.L., 1959. Bone strength—its relationship to X-ray-determined ash content. *Hum. Biol.* 31, 261–270.
- Wang, C., Wang, J., Zhang, Y., Yuan, C., Liu, D., Pei, Y., Li, X., Wu, Z., Li, Y., Guo, Z., 2013. A canine model of femoral head osteonecrosis induced by an ethanol injection navigated by a novel template. *Int. J. Med. Sci.* 10, 1451–8. doi:10.7150/ijms.6314
- Wang, C., Wang, X., Xu, X., Yuan, X., Gou, W., Wang, A., Guo, Q., Peng, J., Lu, S., 2014. Bone microstructure and regional distribution of osteoblast and osteoclast activity in the osteonecrotic femoral head. *PLoS One* 9, e96361. doi:10.1371/journal.pone.0096361
- Wehrli, F.W., 2007. Structural and functional assessment of trabecular and cortical bone by micro magnetic resonance imaging. *J. Magn. Reson. Imaging* 25, 390–409. doi:10.1002/jmri.20807
- Weinstein, R.S., Jilka, R.L., Michael Parfitt, a., Manolagas, S.C., 1998. Inhibition of osteoblastogenesis and promotion of apoptosis of osteoblasts and osteocytes by glucocorticoids potential mechanisms of their deleterious effects on bone. *J. Clin. Invest.* 102, 274–282.  
doi:10.1172/JCI2799
- Whealan, K., Kwak, S., Tedrow, J., 2000. Noninvasive Imaging Predicts Failure Load of the Spine with Simulated Osteolytic Defects. *J. Bone ...* 82-A, 1240–1251.
- Winkler, E., 1867. Die Lehre von der Elasticitaet und Festigkeit: mit besonderer Rücksicht auf ihre Anwendung in der Technik für polytechnische Schulen, Bauakademien, Ingenieure, Maschinenbauer, Architecten, etc. Dominicus, Prag.
- Wirtz, D.C., Schiffers, N., Pandorf, T., Radermacher, K., Weichert, D., Forst, R., 2000. Critical evaluation of known bone material properties to realize anisotropic FE-simulation of the proximal femur. *J. Biomech.* 33, 1325–1330. doi:10.1016/S0021-9290(00)00069-5
- Wolff, J., Maquet, P., Furlong, R., 1986. The law of bone remodelling. Springer-Verlag.

- World Health Organisation, 2003. Prevention and management of osteoporosis. World Health Organ. Tech. Rep. Ser. 921, 1–164, back cover.
- Wright, D., Whyne, C., Hardisty, M., Kreder, H.J., Lubovsky, O., 2011. Functional and anatomic orientation of the femoral head. Clin. Orthop. Relat. Res. 469, 2583–2589. doi:10.1007/s11999-010-1754-1
- Yamada, H., Evans, F.G., 1970. Strength of biological materials. Williams & Wilkins.
- Yamashita, T., 1996. Analysis of Anisotropic Material. doi:10.1017/CBO9781107415324.004
- Yang, L., Palermo, L., Black, D.M., Eastell, R., 2014. Prediction of incident hip fracture with the estimated femoral strength by finite element analysis of DXA Scans in the study of osteoporotic fractures. J. Bone Miner. Res. 29, 2594–600. doi:10.1002/jbmr.2291
- Zhao, D.W., Yu, X.B., 2015. Core decompression treatment of early-stage osteonecrosis of femoral head resulted from venous stasis or artery blood supply insufficiency. J. Surg. Res. 194, 614–621. doi:10.1016/j.jss.2014.12.007
- Zizic, T.M., Marcoux, C., Hungerford, D.S., Dansereau, J. V, Stevens, M.B., 1985. Corticosteroid therapy associated with ischemic necrosis of bone in systemic lupus erythematosus. Am. J. Med. 79, 596–604.
- Zizic, T.M., Marcoux, C., Hungerford, D.S., Stevens, M.B., 1986. The early diagnosis of ischemic necrosis of bone. Arthritis Rheum. 29, 1177–1186.
- Zoroofi, R.A., Nishii, T., Sato, Y., Sugano, N., Yoshikawa, H., Tamura, S., 2001. Segmentation of avascular necrosis of the femoral head using 3-D MR images. Comput. Med. Imaging Graph. 25, 511–21.
- Zurlo, J., 1999. The Double-Line Sign 1. Radiology 212, 1998–1999.

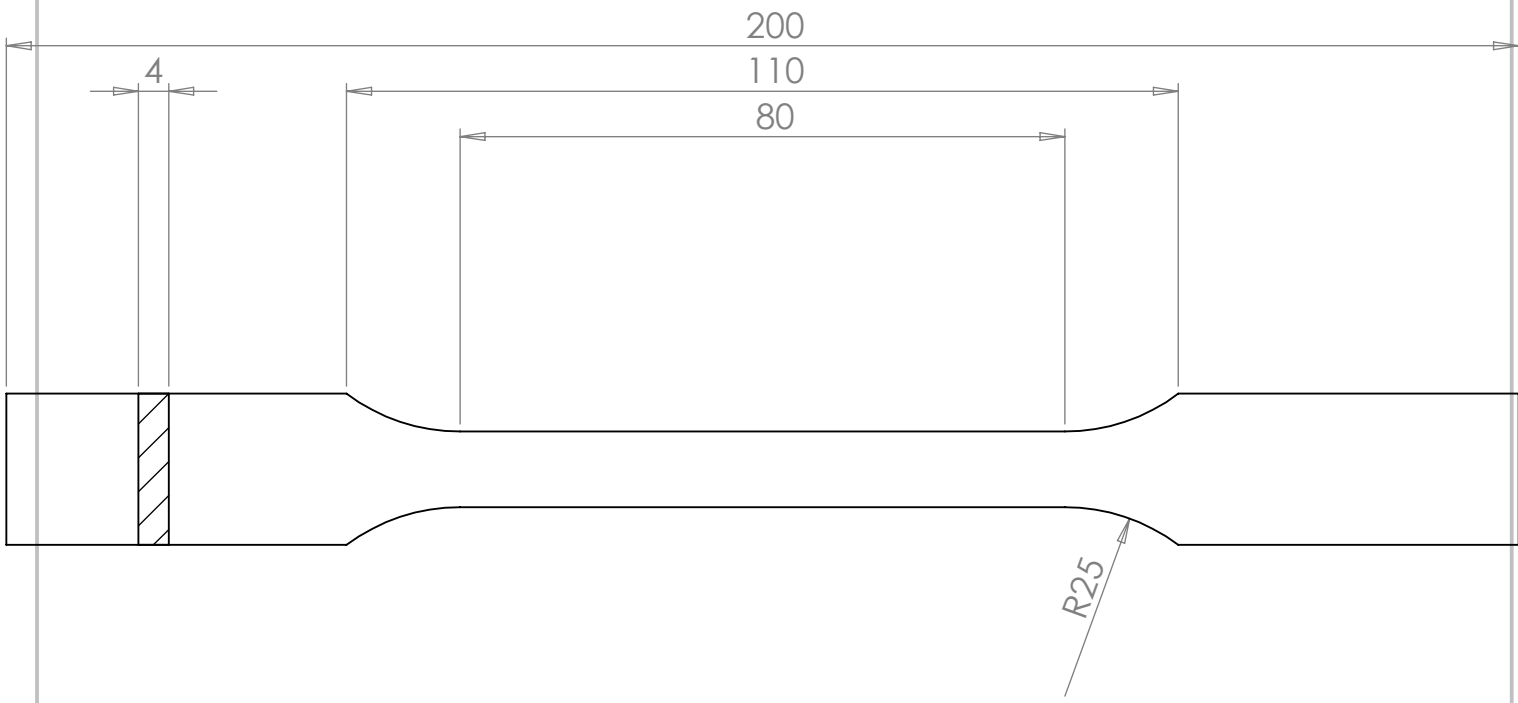
**Appendix A**  
**Proximal femur model with simulated cone shaped AVN**  
**Lesion**



|   |                       |           |            |                                   |                      |              |
|---|-----------------------|-----------|------------|-----------------------------------|----------------------|--------------|
| UNLESS OTHERWISE SPECIFIED:<br>DIMENSIONS ARE IN MILLIMETERS<br>SURFACE FINISH:<br>TOLERANCES:<br>LINEAR:<br>ANGULAR: |                       | FINISH:   |            | DEBUR AND<br>BREAK SHARP<br>EDGES | XtremeCT scan 076_RF | REVISION: v1 |
| DRAWN   | Martin Preutenborbeck | SIGNATURE | DATE       |                                   |                      |              |
| CHK'D   |                       |           | 16/09/2015 |                                   |                      |              |
| APP'D   |                       |           |            |                                   |                      |              |
| MFG   |                       |           |            |                                   |                      |              |
| Q.A   |                       |           |            | MATERIAL:                         | DWG NO.              |              |
|   |                       |           |            |                                   |                      | A4           |
|   |                       |           |            | WEIGHT:                           | SCALE:1:1            | SHEET 1 OF 1 |

Upper femur with simulated  
wedge shaped AVN Lesion

**Appendix B**  
**Drawing Tensile bar ISO527**



UNLESS OTHERWISE SPECIFIED:  
DIMENSIONS ARE IN MILLIMETRES  
SURFACE FINISH:

TOLERANCES:  
LINEAR:  
ANGULAR:

FINISH:

DEBUR AND  
BREAK SHARP  
EDGES

DO NOT SCALE DRAWING

REVISION

|       |                |           |            |  |  |
|-------|----------------|-----------|------------|--|--|
| DRAWN | NAME           | SIGNATURE | DATE       |  |  |
| M     | Preutenborbeck |           | 21/10/2015 |  |  |

CHK'D

APP'D

MFG

Q.A

TITLE:

# Tensilebar ISO527

MATERIAL: SLS DuraForm Nylon PA

DWG NO.

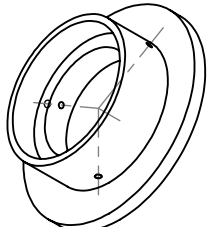
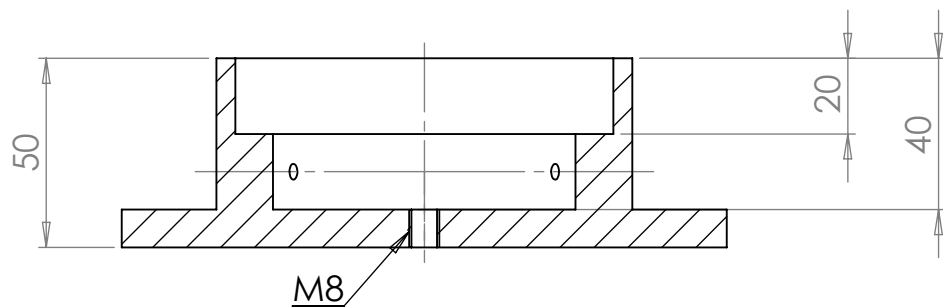
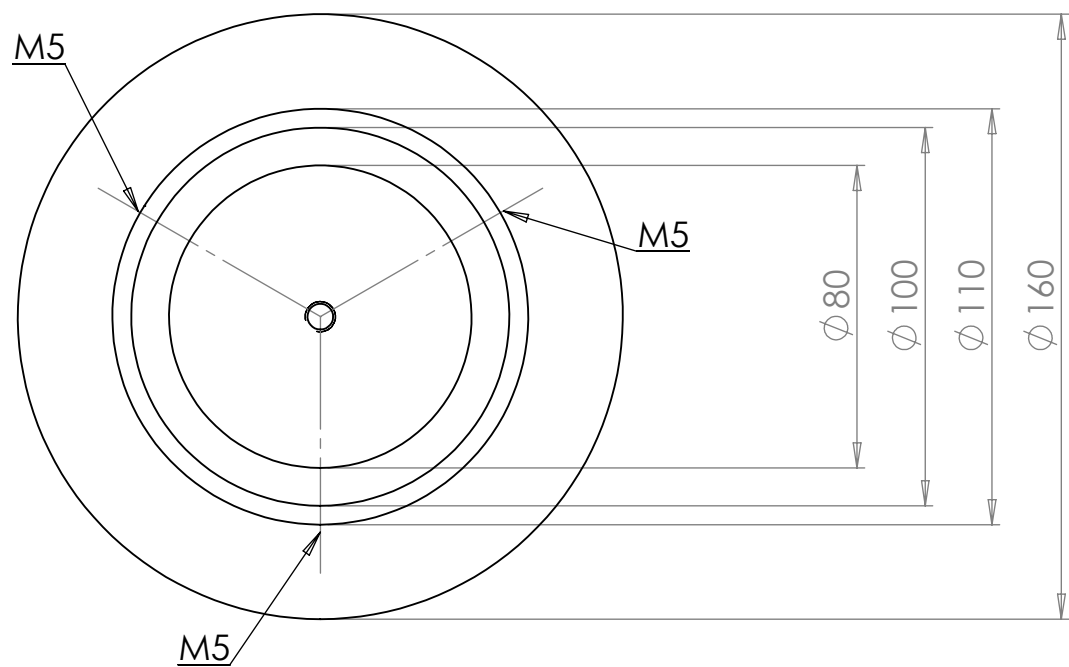
A4

WEIGHT:

SCALE:1:1

SHEET 1 OF 1

**Appendix C**  
**Drawing Instron Cement Mould**



UNLESS OTHERWISE SPECIFIED:  
DIMENSIONS ARE IN MILLIMETRES  
TOLERANCES: ISO 2768

University of Leeds  
School of Mechanical  
Engineering

REVISION v1

DRAWN M Preutenborbeck

23/10/2015

TITLE:

CementMould

CHK'D

APP'D

MFG

Q.A

MATERIAL:

Delrin

DWG NO.

A4

WEIGHT:

SCALE: 1:2

SHEET 1 OF 1

**Appendix D**

**SOP.07.17 Standard Operating Protocol. Simulating an AVN-  
lesion within an in-vitro porcine model**

## **SOP.07.17 Standard Operating Protocol**

### **Simulating an AVN-lesion within an in-vitro porcine model**

**Author:** Martin Preutenborbeck

**Date:** 14/01/2016

**Revision:** v1

#### **1.0 RATIONALE**

The hip is the most prevalent site for avascular necrosis (AVN). AVN is a bone affecting disease which is caused by blockages of blood vessels inside the femoral head. This leads to a loss of structural integrity of the femoral head. It is necessary to validate a developed fracture prediction method against in-vitro tests on porcine tissue. Due to the limited access to AVN femurs, AVN lesions are simulated with a mechanical instrument by cutting a void into the femoral head.

This standard operating procedure applied to the The procedures outlined in this document should be carried out in the preparation room of the Tissue Engineering Laboratory or Bioengineering laboratory, School of Mechanical Engineering, University of Leeds.

#### **2.0 RESPONSIBILITY**

It is the responsibility of the researcher to ensure that all test procedures outlined in this document are carried out in accordance with these instruction.

This procedure involves working with Cement, Drill, Instrons and Animal tissue. The researcher should ensure they are familiar with all the procedures, particularly the SOPs for mounting cemented animal bone, compression testing animal tissue on an Instron, drilling holes into animal tissue and disposal techniques. Contact a member of iMBE technical support to arrange demonstration or to seek assistance.

#### **3.0 ASSOCIATED DOCUMENTS**

This SOP is just a record to keep track of the conducted tests and how they were done. All procedures described here are standard procedures. Please refer to SOPs already in place within the tissue Engineering Laboratory for mounting cemented animal bone, compression testing animal tissue on an Instron, and drilling holes into animal tissue!

Project Specification: 'Validation of a fracture prediction tool based on beam theory against in-vitro testing.'

## 4.0 MATERIALS

Porcine tissue

Cement

## 5.0 EQUIPMENT

### Equipment needed:

Drill

Flexible metal rail

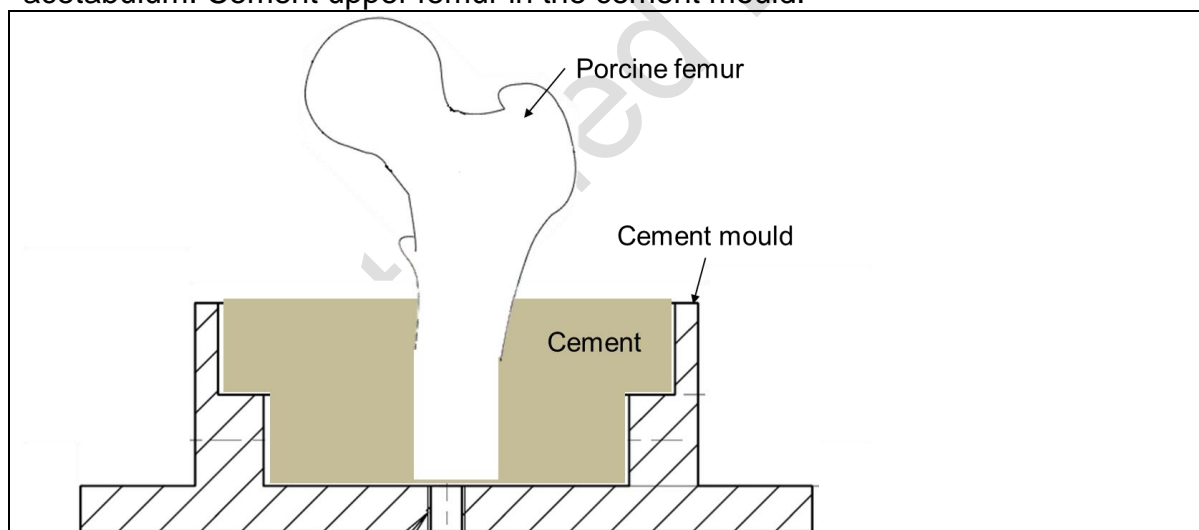
Tape and zip ties

Distance bar

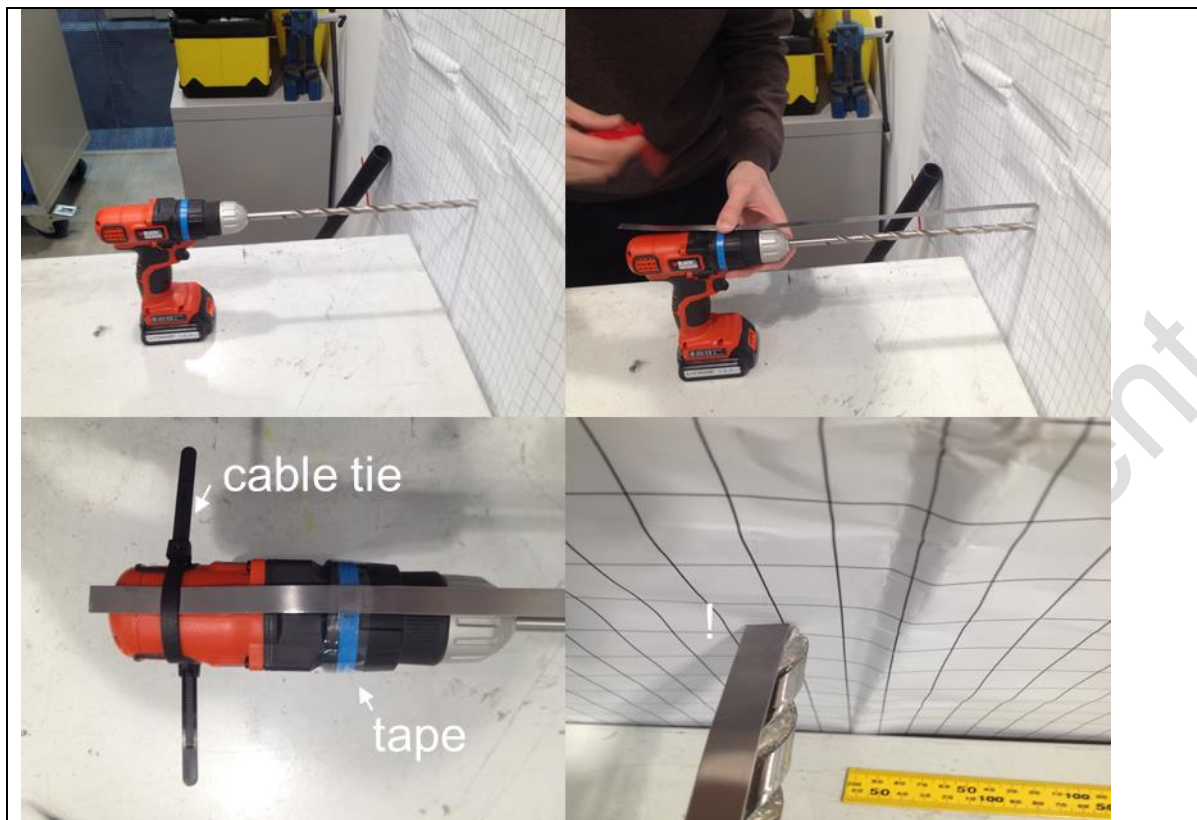
Porcine legs

### Preparing equipment

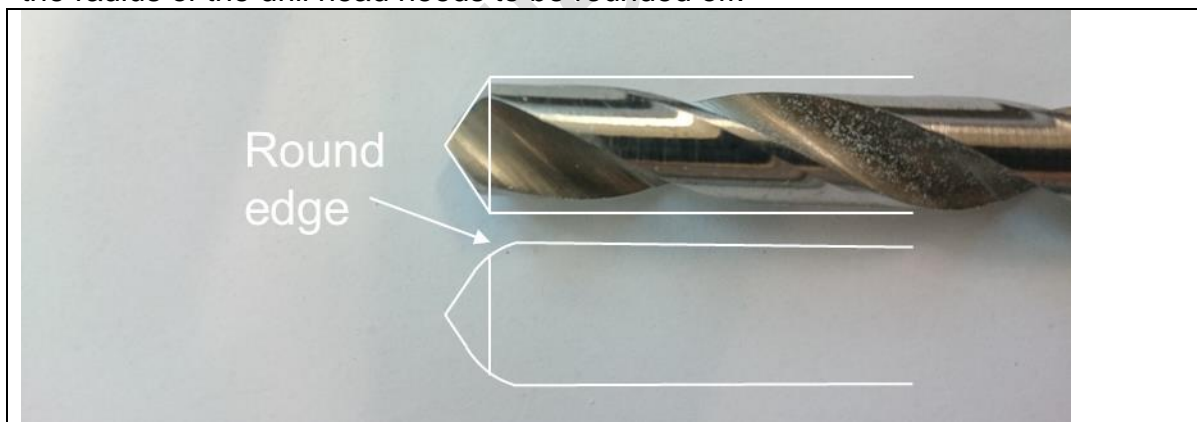
Dissect porcine leg: Remove soft tissue from the femur and remove the attached acetabulum. Cement upper femur in the cement mould.



Attach flexible metal rail to the drill so that it is in parallel to the drill bit. Use a zip tie to attach the rail to the drill and subsequently use tape to fix the rail in the final position. The end of the drill should match the end of the rail.



Sharp edges increase the likelihood of fracture. The shape of a hole placed with a drill has such edges at the top end of the hole due to the shape of the drill head. Therefore the radius of the drill head needs to be rounded off.

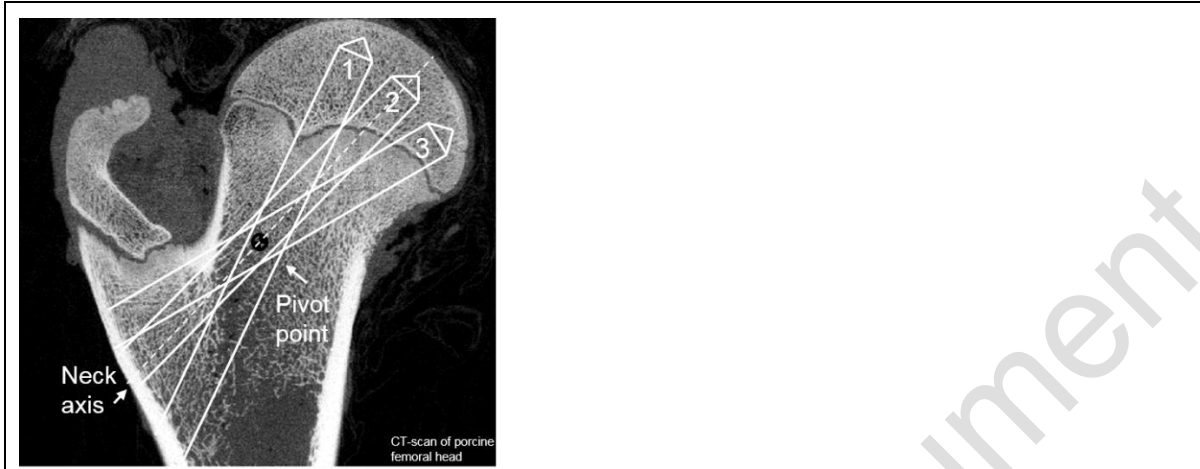


## 6.0 PROCEDURE

Lab coats and gloves must be worn throughout this procedure.

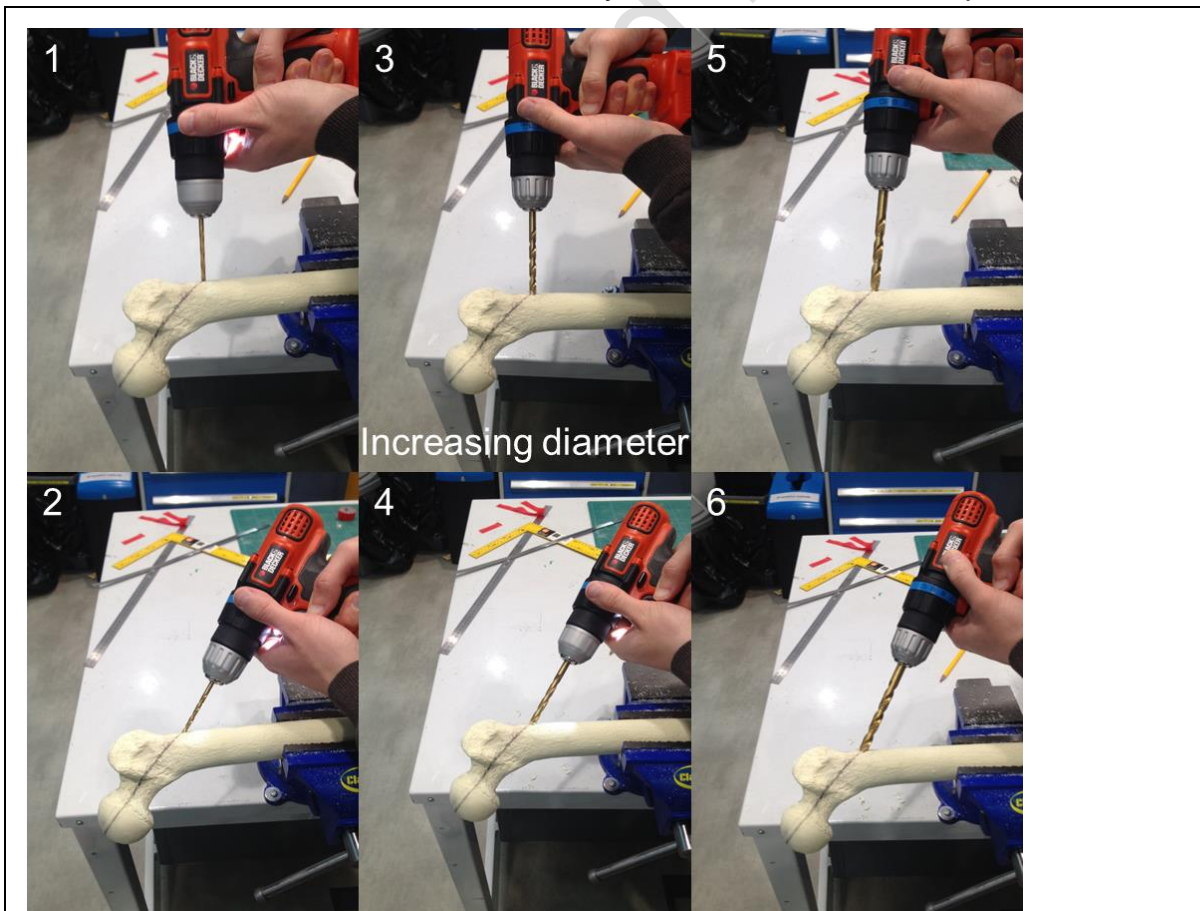
Step1:

Choose where the hole needs to be placed within the femoral head (1,2, or 3). Identify the point where the neck axis pierces the bone surfaces. The pivot point lies between those two points. All holes will go through this point.



### Step2:

Drill a pilot hole into the bone and subsequently drill into the desired direction for ca. 15 mm. Repeat this with increasing drill diameters (ie. 3). The metal rail fixates one degree of freedom so that it is easier to accurately drill the hole into the required direction.



## Step3:

Use the final drill bit to drill half the distance to the bone surface of the femoral head.  
Use the distance bar to check the distance to the bone surface and the top of the drill.  
Mark the distance on the drill bit with a marker or tape.



## Step4:

Carefully drill until the mark on the drill bit reaches the bone surface. Check whether the dimensions and the position of the drilled hole are acceptable. Do amendments if possible and needed.



Subsequently, the upper femur will be CT-scanned on the Xtreme CT. The femoral head in its cement mould will be compression tested on an Instron machine within the tissue lab. Prior tests on porcine femurs had a fracture load of well below 5kN.

## 7.0 Revision traceability table

| Revision | Date       | Section | Change made / Further comments |
|----------|------------|---------|--------------------------------|
|          | XX/XX/XXXX |         |                                |

## 8.0 APPROVAL

Author: Martin Preutenborbeck

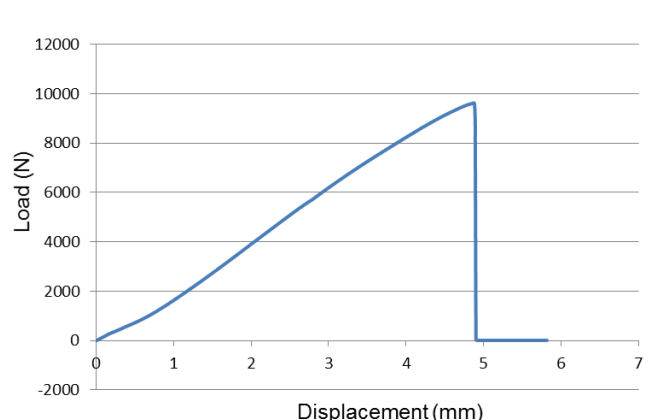
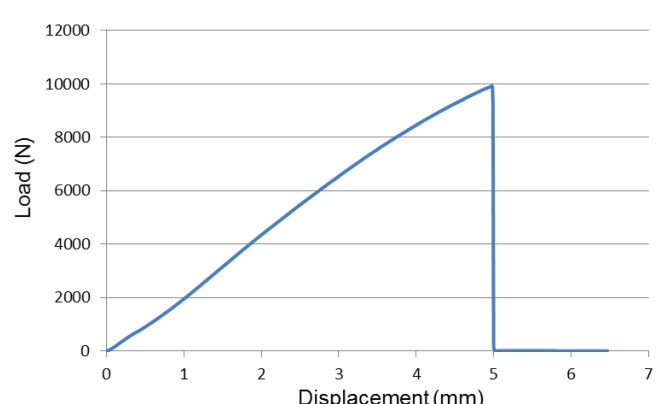
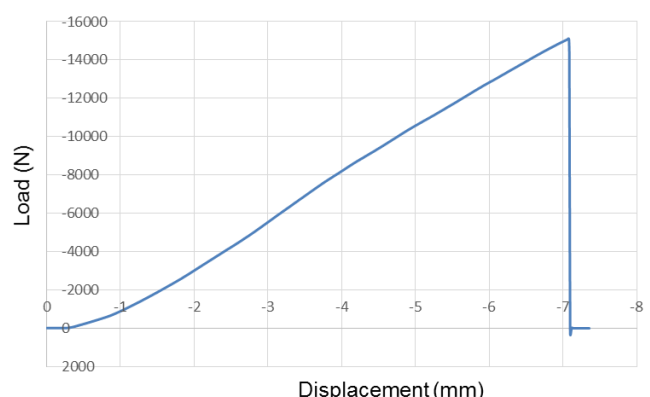
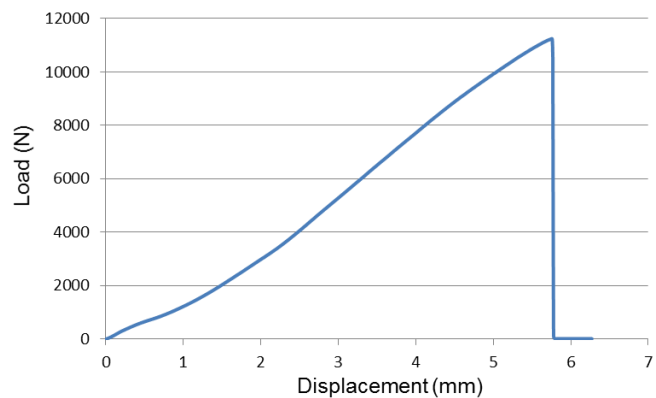
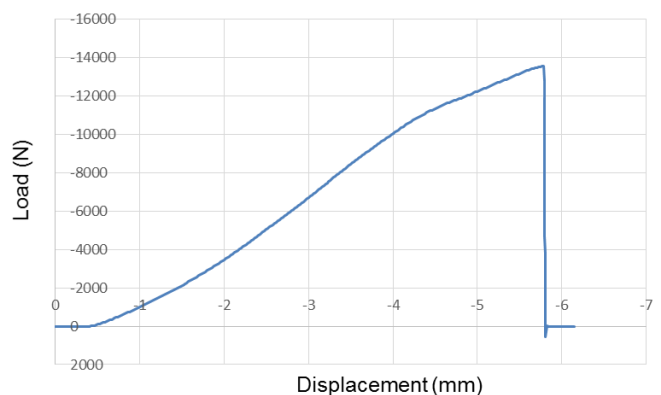
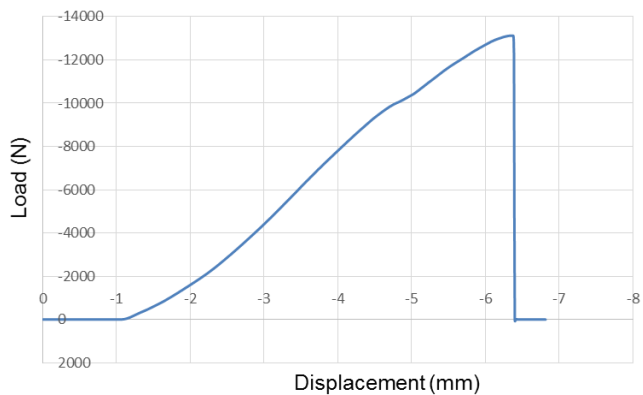
Date

Laboratory Director: Dr Louise Jennings

Date

**Appendix E**  
**Compression data additive manufactured proximal femur**  
**models**

## Load-Displacement curve for stem fracture



## Load-Displacement curve for neck fracture

